AN ABSTRACT OF THE DISSERTATION OF

Renellys C. Perez for the degree of Doctor of Philosophy in Oceanography presented on October 31, 2005.

Title: Numerical and Assimilative Studies of the Equatorial Pacific Cold Tongue.

Abstract approved: Redacted for Privacy

Robert N. Miller

Numerical model and assimilation experiments were conducted in the tropical Pacific Ocean to obtain a better understanding of the processes that control the cold tongue surface mixed layer temperature balance during August 1999 to July 2004. The numerical model was first applied to test two hypotheses (asymmetric background currents and asymmetric wind forcing) for the observed asymmetry of annual equatorial Rossby waves. The model with asymmetric background currents perturbed with symmetric annually-varying winds consistently produced asymmetric Rossby waves, and simulations with symmetric background currents perturbed by asymmetric annually-varying winds failed to produce the observed Rossby wave structure unless the perturbation winds were strong enough for nonlinear interactions to become important. The observed latitudinal asymmetry of the westward phase speed was found to be critically dependent on the inclusion of realistic coastline boundaries. To measure the cold tongue sensitivity to errors in wind forcing, the next study compared the seasonal cycle response of the model driven by different wind stress products. The FSU wind stress produced the least realistic cold tongue,

and both the ECMWF and QuikSCAT wind stress driven model runs exhibited cold tongue annual cycles, tropical instability waves, and annual equatorial Rossby waves that compared well with observations. The highest realism, however, was obtained with QuikSCAT wind forcing. In the final modeling study, mean dynamic height biases resulting from climatological drift away from the Levitus initialization were discovered in the waveguide.

The assimilation experiments combined the model driven by 5-day QuikSCAT winds with 5-day Tropical Atmosphere Ocean dynamic height anomalies via a reduced state space Kalman filter. Assimilation improved the interannual and intraseasonal variability of sea surface height, reduced the cold tongue bias in the waveguide, increased the core strength of the Equatorial Undercurrent, and produced more realistic albeit weak tropical instability waves. An autoregressive model added to the innovation sequence further optimized the assimilation scheme, but did not correct the pre-existing cold tongue thermal biases. Despite the decrease in positive (warming) high-frequency horizontal advection associated with TIWs, the assimilation run with the autoregressive model did not alter the mean balance significantly as there was a compensatory decrease in magnitude of the cooling by the low-frequency horizontal advection. Based on comparisons with observations, the annual cycle of the model tendency was too weak in the eastern Pacific giving rise to sea surface temperatures that were too cold in the spring and summer months and during the 2002-2003 El Niño event. Errors in the simulated net surface heat flux, vertical entrainment, and diffusion were identified as sources for the unrealistically low annual amplitudes of sea surface temperature and tendency in the model cold tongue.

Numerical and Assimilative Studies of the Equatorial Pacific Cold Tongue

by

Renellys C. Perez

A DISSERTATION

submitted to

Oregon State University

in partial fulfillment of
the requirements for the
degree of

Doctor of Philosophy

Presented October 31, 2005
Commencement June 2006

Doctor of Philosophy dissertation of Renellys C. Perez presented on October 31, 2005.

APPROVED:

Redacted for Privacy

Major Professor, representing Oceanography

Redacted for Privacy

Dean of the College of Oceanic and Atmospheric Sciences

Redacted for Privacy

Dean of the Graduate School

I understand that my dissertation will become part of the permanent collection of Oregon State University libraries. My signature below authorizes release of my dissertation to any reader upon request.

Redacted for Privacy

Renellys C. Perez, Author

ACKNOWLEDGMENTS

I would like to thank Robert N. Miller for being an excellent advisor, mentor, and friend during my doctorate. Many thanks to Dudley B. Chelton who served as a surrogate advisor in the middle of my degree and enabled my dissertation to have a broader focus. I also thank John S. Allen for challenging me with high research expectations and the rest of my committee Robert Higdon and Stel Walker for their invaluable input and support. Their advice and suggestions enhanced the quality and focus of my research.

It is impossible to thank everyone who provided assistance during the course of my dissertation. I am truly grateful to the people who kept my computer running, supplied me with observations, and provided research or coding advice: Eric Beals, Jim Beauchamp, Brandy Cervantes, Roland de Szoeke, Laura Ehret, Eric Hackert, Billy Kessler, Jay McCreary, Ragu Murtugudde, Larry O'Neill, Tim Pugh, Michael G. Schlax, Nicolai Thum, Guillaume Vernieres, and the Computer Gurus.

My friends here in Corvallis and back home in Miami sustained me throughout my tenure as a graduate student. They were incredibly supportive and incredibly distracting and I am lucky to know them. Brandy Cervantes, Jennifer Simeon, Debbie Colbert, Sheila O'Keefe, Cidney Howard, Leah Bandstra, Laura Snow, my West-coast-mother Irma Delson, Guillaume Vernieres, Nicolai Thum, Larry O'Neill, Antonio Fetter, Craig Risien, Eric Beals, FORMS, the list goes on. Thank you for all of the great memories, sanity checks, and coffee breaks.

Merci mille fois! to my husband, Bertrand Dano, who never ceases to make me smile and is always there to provide balance and support. His unlimited enthusiasm for research and education will always inspire me. My amazing parents, Antonio and Renellys Perez, and my incredible sister Rebecca Perez (aka Dr. Perez) deserve a multitude of thanks for their love, patience, support, and endless encouragement. My in-laws, Raymond and Nicole Dano, also deserve my thanks for their support of both of us throughout the years and the wonderful care packages filled with French chocolate.

CONTRIBUTION OF AUTHORS

Dr. Dudley B. Chelton was involved with the numerical experiment design and writing for Chapters 2 and 3.

TABLE OF CONTENTS

TABLE OF CONTENTS (Continued)

TABLE OF CONTENTS (Continued)

TABLE OF CONTENTS (Continued)

LIST OF FIGURES

LIST OF FIGURES (Continued)

LIST OF FIGURES (Continued)

LIST OF FIGURES (Continued)

LIST OF FIGURES (Continued)

LIST OF FIGURES (Continued)

LIST OF FIGURES (Continued)

LIST OF FIGURES (Continued)

LIST OF FIGURES (Continued)

LIST OF TABLES

LIST OF TABLES (Continued)

Numerical and Assimilative Studies of the Equatorial Pacific Cold Tongue

1 Introduction

A series of numerical and data assimilation experiments are performed in the tropical Pacific Ocean with a focus on the physical processes that affect the equatorial Pacific cold tongue from August 1999 to July 2004. Data assimilation is a means of converting a sparse set of observations into a highly resolved estimate of the state of the system using a numerical model as a dynamic interpolator. The numerical model of choice is the nonlinear, reduced gravity equatorial β-plane model designed by Gent and Cane (1989) and the data assimilation method applied to the model is the Kalman filter. The Kalman filter provides an optimal estimate of the present state of the system, albeit at computational expense proportional to the cube of the number of model state variables. Application of the Kalman filter, therefore, necessitates a system which can be easily represented by a simple numerical model. Over the past three decades, the tropical Pacific Ocean has provided a natural testing ground for Kalman filtering techniques as the large scale, low frequency equatorial dynamics governing sea surface height (SSH), thermocline depths, and zonal currents in the upper 500 m of the water column can be simulated realistically with low-order numerical models (e.g., Busalacchi and O'Brien 1980; Cane and Patton 1984; Miller and Cane 1996).

These low order models were based on linear theory in which disturbances were assumed small and the background currents were neglected. In contrast to the

equatorially symmetric structure predicted by classical linear theory (Matsuno 1966; Moore 1968; Moore and Philander 1977), observations of annual equatorial Rossby waves in the Pacific Ocean consistently show asymmetric latitudinal structure in the equatorial waveguide (Chelton et al. 2003 and references therein). A benchmark model run determined that the observed Rossby wave asymmetry could be simulated with the nonlinear Gent and Cane model driven by high-resolution winds from SeaWinds scatterometer aboard the QuikSCAT satellite (Chelton and Freilich 2005). In Chapter 2, a series of numerical experiments are performed using the Gent and Cane model to investigate whether the observed asymmetry of the equatorial Rossby waves is due to asymmetry of the background equatorial current system (ECS) or the asymmetry of the time-varying wind forcing. The computational efficiency of the numerical model allows for various hypotheses for the Rossby wave asymmetry to be explored. In addition, the range of amplitudes of time-varying winds for which the model responds linearly can be tested.

Data assimilation requires knowledge of the errors in the wind forcing as it is typically assumed to be the largest source of model forecast error (e.g., Miller and Cane 1989; Miller et al. 1995; Cane et al. 1996). In a second Gent and Cane modeling study detailed in Chapter 3, the sensitivity of the equatorial Pacific cold tongue to three different wind products was explored using seasonal cycle winds generated from a two-year time period when La Niña conditions prevailed. Specifically, the sensitivity of cold tongue annual cycle of sea surface temperature (SST), the annual cycle of the ECS, and the tropical instability waves (TIWs) to the wind forcing are analyzed. The wind comparison results are used to determine the

best available wind stress product for the cold tongue data assimilation experiments presented in Chapters 5 and 6.

For the planned data assimilation experiments, it was necessary to upgrade the Gent and Cane model surface heat flux formulation and increase the horizontal and vertical resolution in the equatorial waveguide. The horizontal resolution was increased to improve the simulation of the asymmetric meridional shear of the ECS that generates TIWs (Lyman et al. 2005a and references therein). As the goal of this project is to assimilate seasonal cycle anomalies of dynamic height (DH) relative to 500 decibars, Chapter 4 studies the sensitivity of the model DH and the ECS to the parameters that define the vertical resolution in the upper 500 m of the water column. The ability to simulate the thermocline and subthermocline ocean with adequate realism and keep the size of the model state space manageable for the data assimilation experiments in Chapters 5 and 6 are the criteria used to determine the best vertical resolution configuration. This chapter also explores significant biases in the model DH that result from climatological drift from the initial thermohaline structure specified from Levitus (1994) climatology in the waveguide. These biases were previously undocumented for the Gent and Cane model since previous model validation and assimilation experiments focused on sea level height anomalies.

In Chapter 5, a nearly optimal Kalman filter scheme is designed and implemented which builds on the results from the wind and resolution sensitivity studies in Chapters 3 and 4. The goal of this study is to investigate whether the assimilation of seasonal cycle anomalies of DH in the equatorial waveguide can improve the structure of temperature and zonal currents in the cold tongue on interannual to intraseasonal timescales and simultaneously improve the statistics of the simulated

TIWs. The limitations of anomaly-for-anomaly assimilation in a model whose seasonal cycle may be biased or out-of-phase in the cold tongue will also be explored.

The last modeling and assimilation study (Chapter 6) explores the impact of data assimilation on the temperature budget of the cold tongue surface mixed layer. The importance of the TIWs in the model heat balance is quantified for both the unassimilated and assimilated model runs. The error statistics generated by the Kalman filter are used to diagnose whether the model temperature fluxes are significantly different from observed temperature fluxes. This comparison will aid in developing an understanding of the cause of SST biases in the model and the unrealistically low variability which characterizes the model cold tongue in the eastern Pacific. Concluding remarks along with comments on future directions for assimilation studies in the equatorial Pacific are presented in Chapter 7.

2 The effects of wind forcing and background currents on the latitudinal structure of equatorial Rossby waves

Renellys C. Perez, Dudley B. Chelton, and R. N. Miller

Journal of Physical Oceanography

45 Beacon Street, Boston, MA 02108-3693

Vol. 35, No. 5, May 2005

2.1 Abstract

The latitudinal structure of annual equatorial Rossby waves in the tropical Pacific based on sea surface height (SSH) and thermocline depth observations is equatorially asymmetric, which differs from the structure of the linear waves of classical theory that are often presumed to dominate the variability. The nature of this asymmetry is such that the northern SSH maximum (along 5.5°N) is roughly twice that of the southern maximum (along 6.5°S). In addition, the observed westward phase speeds are roughly half the predicted speed of 90 $cm\ s^{-1}$ and are also asymmetric with the northern phase speeds about 25% faster than the southern phase speeds. One hypothesized mechanism for the observed annual equatorial Rossby wave amplitude asymmetry is modification of the meridional structure by the asymmetric meridional shears associated with the equatorial current system. Another hypothesis is the asymmetry of the annually-varying wind forcing, which is stronger north of the equator.

A reduced gravity, nonlinear, β-plane model with rectangular basin geometry forced by idealized QuikSCAT wind stress is used to test these two mechanisms. The model with an asymmetric background mean current system perturbed with symmetric annually-varying winds consistently produces asymmetric Rossby waves with a northern maximum (4.7°N) that is 1.6 times larger than the southern maximum (5.2°S), and westward phase speeds of approximately $53 \pm 13\ cm\ s^{-1}$ along both latitudes. Simulations with a symmetric background mean current system perturbed by asymmetric annually-varying winds fail to produce the observed Rossby wave structure unless the perturbation winds become strong enough for nonlinear interactions to produce asymmetry in the background mean current

system. The observed latitudinal asymmetry of the phase speed is found to be critically dependent on the inclusion of realistic coastline boundaries.

2.2 Introduction

Sea surface height (SSH) and thermocline depth observations of equatorial Rossby waves in the Pacific Ocean consistently show asymmetric latitudinal structure in the equatorial waveguide (Chelton et al. 2003 and references therein). It is often presumed that the vertical mode *1*, meridional mode *1* Rossby waves of classical theory in which zero background mean flow is assumed (Matsuno 1966; Moore 1968; Moore and Philander 1977) dominate the seasonal to interannual variability in the tropical Pacific. The observed equatorial Rossby wave structure, however, differs from the symmetric structure of the baroclinic, meridional mode *1* Rossby waves. Baroclinic gravity wave speeds, c_1, based on hydrographic data (e.g., Eriksen et al. 1983; Chelton et al. 1998) in the equatorial Pacific range from 2.3 $m\ s^{-1}$ near the Galapagos Islands to 3.0 $m\ s^{-1}$ near the dateline (Eriksen et al. 1983) and the western boundary currents (Chelton et al. 1998). Given a characteristic c_1 of about 2.6 $m\ s^{-1}$, the first meridional mode for SSH has symmetric local maxima along 3.7°N and 3.7°S and a local minimum along the equator (solid line, Figure 1). The observed maxima, however, are located along higher latitudes than this and are asymmetric with larger amplitude north of the equator. Classical theory also predicts a phase speed of 90 $cm\ s^{-1}$, whereas the estimated phase speeds from observations are 30 to 50% slower. The primary objective of this paper is to simulate the latitudinal structure of equatorial Rossby waves in the Pacific Ocean with a series of numerical experiments designed to investigate the mechanism for the mismatch

between the observed and theoretical structure. We also investigate some aspects of the discrepancies between the observed and theoretical phase speeds.

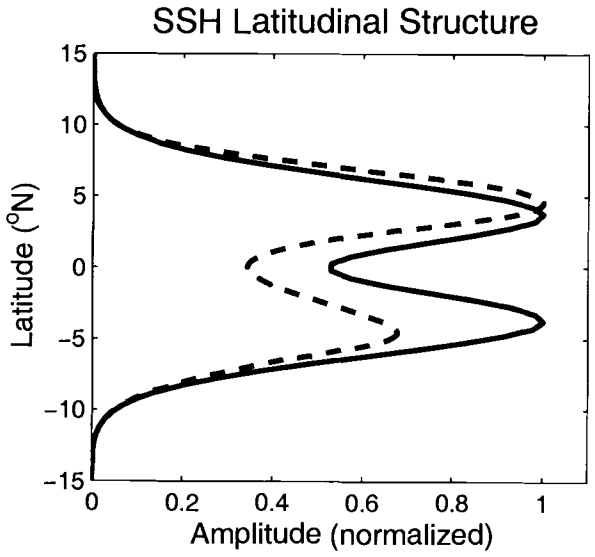

Figure 1. Latitudinal structure function for SSH meridional mode *1*, vertical mode *1* Rossby waves as predicted by classical theory (solid line) and by the shear-modified theory (dashed line) of *Chelton et al. (2003)*.

The asymmetric latitudinal structure of equatorial Rossby waves has been documented from subsurface thermal data (Meyers 1979; Lukas and Firing 1985; Kessler 1990; Kessler and McCreary 1993; Yu and McPhaden 1999) and from altimeter data (Delcroix et al. 1991; Fu et al. 1991; Delcroix et al. 1994; Susanto et al. 1998). The most recent analysis by Chelton et al. (2003) from 8.5 years of TOPEX/Poseidon measurements of SSH provides a thorough description of the latitudinally asymmetric structure of broad-banded Rossby waves. The observed local maxima along 5.5°N are roughly twice those along 5.5°S. The same asymmetry is observed when the annual cycle amplitude and phase are isolated during August 1999 to July 2001 in the TOPEX/Poseidon data set (Figure 2). This asymmetric

latitudinal structure is maintained over much of the Pacific basin, with only small zonal variations (upper left panel, Figure 2). The northern maximum along 5.5°N as determined by a zonal average between 170°E and 240°E is 1.8 times larger than the southern maximum along 6.5°S (upper right panel, Figure 2) and the estimated westward phase speeds of annual Rossby waves along these latitudes are 55.0 ± 14.2 and 43.3 ± 6.8 $cm\ s^{-1}$, respectively (see Section 2.3.3 for methodology). Within the uncertainties of these estimates, these phase speeds of annual variability are consistent with the latitudinally asymmetric phase speed estimates obtained by Chelton et al. (2003) from broad-banded variability.

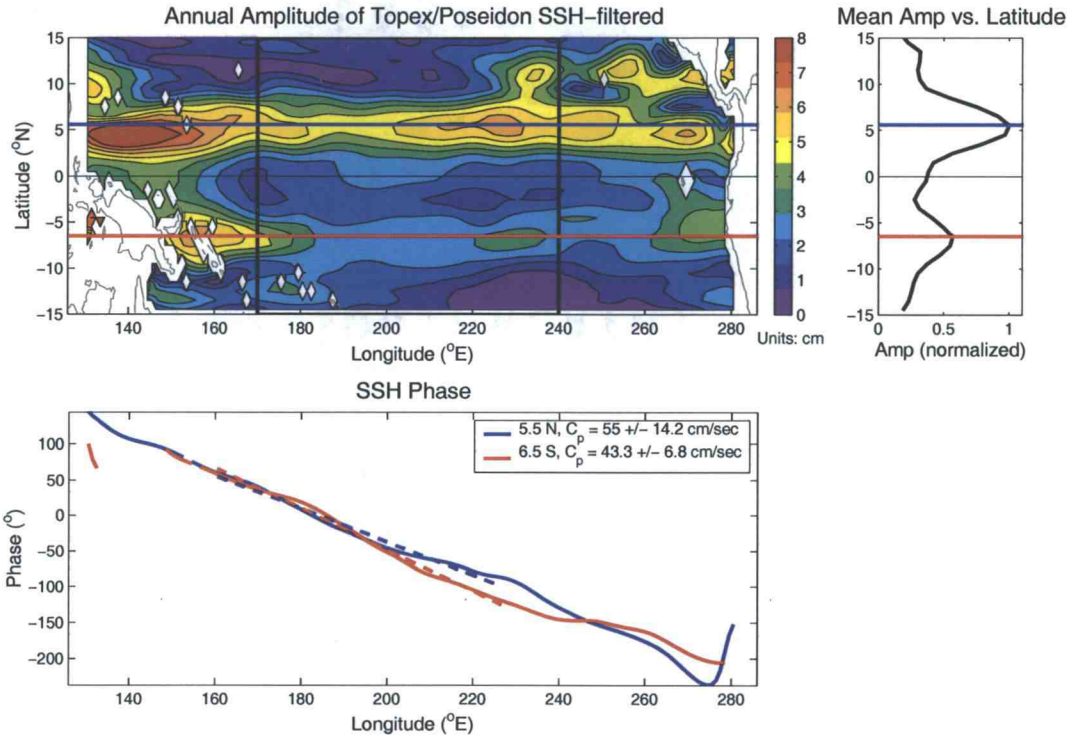

Figure 2. SSH from August 1999 to July 2001 TOPEX/Poseidon measurements filtered to isolate Rossby wave signatures. Upper left: SSH annual amplitude (cm). Upper right: zonally averaged variability from 170° E to 240° E. Bottom: phase as a function of longitude along 6.5° S (red) and 5.5° N (blue).

Various hypotheses have been put forth to explain the observed equatorial asymmetry, including superposition of meridional Rossby wave modes, asymmetries in the time-varying wind forcing, and asymmetries in the background mean currents (cf Section 2 of Chelton et al. 2003). Since each meridional mode has a corresponding phase speed that is inversely proportional to the mode number, it is unlikely that a superposition of more than one meridional mode could produce the observed asymmetric latitudinal structure across the large zonal distance over which it is observed. A modeling study by Kessler and McCreary (1993) suggests that asymmetric time-varying wind forcing of a linear model with zero mean background currents also cannot produce latitudinally asymmetric Rossby waves.

From consideration of the eigensolutions of a simple 1.5-layer, unforced equatorial β-plane model linearized about a symmetric Equatorial Undercurrent (EUC), Philander (1979) showed that the Rossby wave maxima shift to higher latitudes, but the influence of the complete equatorial current system (ECS) on the structure of the waves was not analyzed in that study. Chelton et al. (2003) linearized the same model about the observed mean currents along seven longitudes in the Pacific and concluded that meridional shears in the background currents and associated modification of the meridional potential vorticity gradient are sufficient to generate asymmetric Rossby wave amplitudes (dashed line, Figure 1) and reduce the westward phase speeds by 20% (71 $cm\ s^{-1}$). The slower westward phase speeds in the presence of equatorially asymmetric background shear had previously been documented from eigensolutions for an idealized mean ECS by Chang and Philander (1989) and Zheng et al. (1994). The effects of the background shear on the latitudinal structure of the eigenfunctions was not considered in these earlier studies.

In this study, we investigate numerically the importance of wind forcing and background currents in explaining the observed equatorial Rossby wave asymmetry. In Section 2.3, the numerical model, wind forcing, and methodology of the hypothesis tests are detailed. A benchmark model run is compared to available satellite altimetry data in Section 2.4. We perform a series of model runs detailed in Sections 2.5 and 2.6 to investigate whether the observed asymmetry of the Rossby waves is due to asymmetry of the background mean currents, or to asymmetry of the time-varying wind forcing. Since the background mean flow of the ECS is created by the asymmetric mean forcing of the NE and SE Trades, it is a challenge to distinguish between these two hypotheses. For the present discussion, we evaluate whether either source is individually sufficient to generate the observed Rossby wave asymmetry. In Section 2.5, the Rossby waves forced by symmetric annual cycle perturbation winds are analyzed in the presence of asymmetric mean currents set up by steady, asymmetric wind forcing. Conversely, Section 2.6 analyzes the structure of Rossby waves forced by asymmetric annual cycle perturbation winds in the presence of symmetric currents set up by steady, symmetric wind forcing. By changing the magnitude of the perturbation winds relative to the background mean winds, we test the linearity of the system response and possible scales at which the perturbation begins to alter the background mean currents significantly. To quantify the subsurface effects of asymmetric currents on the Rossby waves, vertical structure and the modal decompositions of the model zonal velocity are also analyzed in Section 2.5. The results of the numerical experiments and conclusions from the hypothesis tests are summarized in Section 2.7.

Table 1. Parameter choices for different numerical experiments.

Parameter	Benchmark	Hypothesis 1	Hypothesis 2
Background Wind	$(\overline{\tau}^x, \overline{\tau}^y)$	AS[a] $(\overline{\tau}^x, 0)$	SS[b] $(\overline{\tau}^x_s, 0)$
Perturbation Wind	Seasonal cycle	Annual cycle	Annual cycle
	Asymmetric	Symmetric	Asymmetric
	$\epsilon = 1$	$0.01 \leq \epsilon \leq 0.10$	$0.01 \leq \epsilon \leq 0.10$
Surface Heat Flux	Seasonal cycle	AS[a]	SS[b]
Relaxation to Levitus	Seasonal cycle	AS[a]	SS[b]
Coastlines	Included[c]	Rectangular basin	Rectangular basin

[a]AS indicates asymmetric, smoothed, mean fields (e.g., (1) in Section 2.5).

[b]SS indicates symmetric, smoothed, mean fields (e.g., (5) in Section 2.6).

[c]See Figure 5 for the coastline representation on the model grid between 15°S and 15°N.

2.3 The Model as a Hypothesis Tester

2.3.1 Gent-Cane Model. The Gent and Cane (1989) reduced gravity, nonlinear, β-plane model (hereafter the Gent-Cane model) and its evolution over the past two decades have been extensively documented. The model in this study is similar to the version detailed in Chen et al. (1994a,b) with the inclusion of salinity which was found to be important to tropical ocean dynamics and thermodynamics (Murtugudde and Busalacchi 1998). This model has demonstrated its ability to reproduce the annual cycle of SST, mixed layer depth, thermocline depth, and zonal currents at TAO (Tropical Atmosphere-Ocean) moorings along 110°W (Kessler et al. 1998; Hackert et al. 2001). It has been used to evaluate wind stress products as forcing fields (Hackert et al. 2001), incorporated as a component of advanced data assimilation systems (Verron et al. 1999), and been applied to study all three tropical ocean basins (Murtugudde et al. 1996; Murtugudde et al. 2002 and references therein).

The model domain covers the entire longitudinal extent of the Pacific Ocean (126° to 286°E) and ranges from 30°S to 30°N. The dynamical model is a reduced gravity model with a uniform surface mixed layer above an active layer divided into six σ-like layers relative to the bottom of the subthermocline active region defined by T_{bottom} = 11°C and S_{bottom} = 34.5 psu (nominally at 400 meters). Increased resolution of the subthermocline ocean can be achieved by changing the number of layers (NZ), bottom temperature and salinity as in Hackert et al. (2001) where NZ = 20, T_{bottom} = 6°C, and S_{bottom} = 35 psu for tropical Pacific simulations. Along the equator, the simulated variability above the thermocline (the thermocline mean

depth ranged from approximately 150 meters at 140°E to 50 meters at 95°W) is not notably stronger than TAO (Hackert et al. 2001).

The dynamic variables of the model are zonal velocity, meridional velocity, layer thickness, salinity, and temperature (u, v, h, S, T). At each hourly time step, these fields are calculated at 80 x 60 horizontal gridpoints, 3810 of which are ocean gridpoints when Pacific basin coastlines are included. The stretched horizontal grid has highest meridional resolution (ca. 0.6°) in the equatorial waveguide and gradually stretches to 3.3° at 30° latitude. The highest zonal resolution (ca. 0.8°) is located at the eastern and western boundaries with 2.4° resolution in the model interior. A hybrid mixing scheme designed by Chen et al. (1994a), which defines the dynamics of the surface mixed layer and allows for entrainment or detrainment between the layers, combines the Kraus and Turner (1967) mixed layer model with the Price et al. (1986) dynamical instability model.

Table 1 summarizes the model parameters selected for the benchmark run presented in Section 2.4 and each hypothesis test (see Section 2.5 and 2.6 for detailed descriptions). In all of the cases discussed in this paper, the nonlinear advection terms are retained. For all model runs, no-slip conditions are imposed at the zonal and meridional boundaries. Experiments with free-slip boundary conditions were performed and little difference was observed. Coastlines are retained for the benchmark run described in Section 2.4. For the hypothesis tests (Section 2.5 and 2.6), coastlines are removed to avoid boundary-induced asymmetries. To avoid introducing additional asymmetric forcing to experiments where symmetric background currents are desired, heat flux and precipitation at the model boundaries

are symmetrized as a function of latitude with respect to the equator as described in Section 2.6.

2.3.2 Wind Forcing and Background Mean Currents.

2.3.2.1 QuikSCAT Wind Forcing: The SeaWinds scatterometer aboard the QuikSCAT satellite was launched 19 June 1999 (Freilich et al. 1994). The two years beginning in August 1999 are of particular interest in this study because they include the most recent La Niña event. La Niña conditions are characterized by anomalously strong tradewinds and strong wind stress divergence and curl over the northern front of the equatorial Pacific cold tongue (Chelton et al. 2001), amplifying latitudinal asymmetries in the climatological average wind field and in the ECS.

For this study, QuikSCAT monthly mean wind stresses from August 1999 to July 2001 are binned onto a 1° x 1° grid. The wind stresses are smoothed zonally using a one-dimensional loess smoother (Schlax and Chelton 1992) with a half span of 10^o longitude which corresponds to a 5^o longitude block average. QuikSCAT mean wind stress resolves the well-known features in the tropical wind field, including the NE and SE tradewinds and the wind jets through gaps in the Sierra Madre mountains (upper left panel, Figure 3). There is high variability over the Intertropical Convergence Zone (ITCZ), near New Guinea, and in the western Pacific between 15° and 30°N (upper right panel, Figure 3). QuikSCAT winds capture an intense zonal band of divergence over the northern front of the cold tongue (lower left panel, Figure 3). This enhanced divergence near the equator is thought to be an important driver for equatorial upwelling (De Szoeke and Chelton 2004). There is also positive wind stress curl just north of the equator (lower right panel, Figure 3), which is present in scatterometer wind products such as ERS-1 and

QuikSCAT, but weak or absent in coarser resolution wind products such as FSU, NCEP, and ECMWF (Kessler et al. 2003; Chelton 2004).

To force the benchmark model run summarized in Section 2.4, we fit these wind stresses to an annual cycle and three higher harmonics to generate a "seasonal cycle" during La Niña conditions. This seasonal cycle differs from that which would be obtained from a longer data record. The La Niña conditions during the first two years of the QuikSCAT mission are advantageous for the present purposes because of the amplified asymmetry in the background wind forcing which is believed to play an essential role in the asymmetry of equatorial Rossby waves.

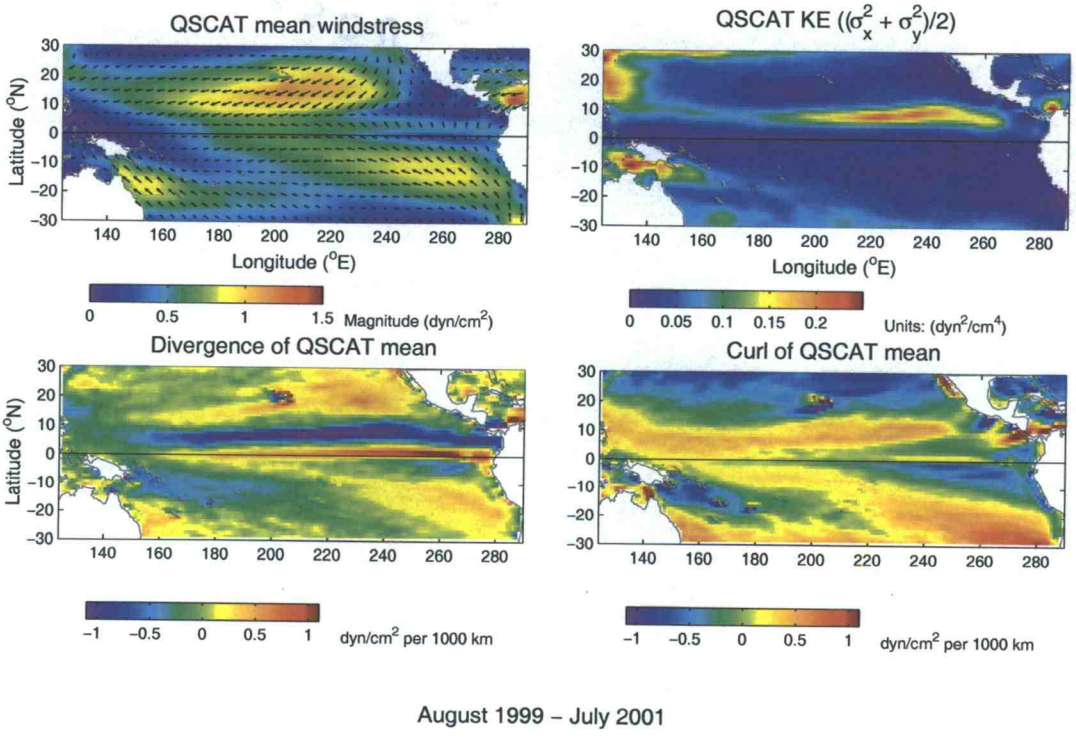

Figure 3. Mean (upper left), kinetic energy of the variance (upper right), divergence (lower left), and curl (lower right) of QuikSCAT windstress during August 1999 - July 2001.

2.3.2.1 Background Mean Currents: The observed meridional structure of the mean (years 1985 to 2000) ECS along 140°W estimated from ADCP/CTD transects by Johnson et al. (2002) is shown in the upper left panel of Figure 4. There is an equatorial asymmetry in the meridional shear due to the eastward flowing North Equatorial Counter Current (NECC) adjacent to the westward flowing northern branch of the South Equatorial Current (SECN).

The benchmark run with realistic coastlines and forced with the QuikSCAT seasonal cycle winds (Section 2.4) reproduces the salient features of the mean EUC and the mean NECC - SECN shear (upper right panel, Figure 4). The model NECC and SEC are somewhat weak, however, and the SEC is lacking in detail. Forcing the model with the spatially-varying, two-year mean QuikSCAT wind stress (upper left panel, Figure 3) produces a mean NECC - SECN structure that appears similar to observations (lower left panel, Figure 4). The model mean EUC partially surfaces, however, and alters the sign of the simulated mixed layer currents at 141°W, producing larger meridional shears near the equator. This partial surfacing of the EUC is due to the lack of vertical shear within the surface mixed layer of the Gent-Cane model (Chen et. al. 1994a). The background mean wind stress applied in the experiments described in Section 2.5 is a modified version of the two-year QuikSCAT mean and produces the mean zonal currents shown in the lower right panel of Figure 4.

The winds during the La Niña condition considered here produce a model ECS with stronger shear than during neutral or El Niño conditions. Despite the stronger forcing, we find that model meridional shears are somewhat weaker than those of the 15-year mean zonal currents constructed from ADCP data by Johnson et al. (2002).

Some of this discrepancy is due to aliasing of the ADCP data by Tropical Instability Waves (TIWs), which result from the meridional and vertical shears in the ECS (Philander 1978; Cox 1980). Given this uncertainty, the meridional structure of the simulated ECS (lower right panel of Figure 4) will suffice to test the role of asymmetric mean currents in establishing the asymmetric latitudinal structure of equatorial Rossby waves (see Section 2.5).

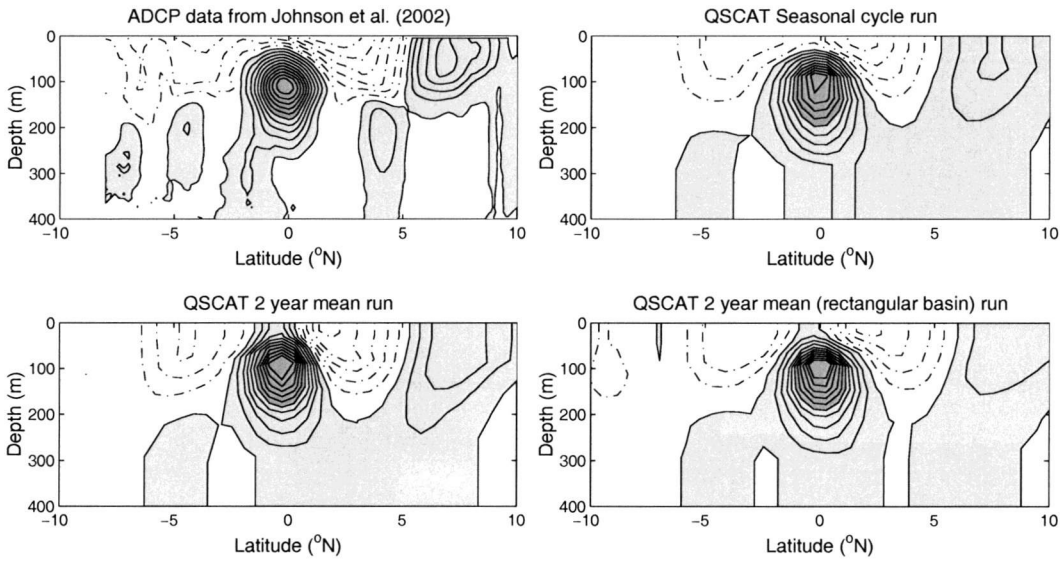

Figure 4. ADCP mean zonal currents at 140°W (upper left) from *Johnson et al. (2002)*. Model background mean z onal currents at 141°W resulting from forcing with seasonal cycle QuikSCAT windstress (upper right), QuikSCAT 2-year mean windstress (lower left), and QuikSCAT 2-year mean zonal windstress modified to a rectangular basin (lower right) . Contour interval is 10 $cm\ s^{-1}$.

2.3.3 Extraction of the Rossby Wave Signal. The five years of model output analyzed for each simulation are stored as three-day averages for each variable at all model locations. All of the model runs performed for this study generate TIWs with wave periods of about 35 days and zonal wavelengths of about 1600 km, which are consistent with the kinematic features of TIWs in numerous observational studies (e.g., Qiao and Weisberg 1995). The spatial and temporal resolution of the model is therefore sufficient to produce TIWs. Note that increased horizontal resolution in the Gent-Cane model increases the realism of the TIW statistics (Kessler et al. 1998).

To extract the Rossby wave signal for each experiment, the model SSH is filtered in a sequence of stages designed to mimic the processing applied by Chelton et al. (2003) to the satellite altimeter data. First, a zonal average across the full basin is removed from each grid location at each time step in an effort to eliminate the response from Ekman pumping with large zonal scales, thus isolating the propagating wave signals. A temporal low-pass filter is then applied to remove high-frequency processes, most notably Kelvin waves and the aforementioned TIWs. The low-pass filter consists of two passes of the data through a 150-day running mean. Finally, an annual cycle is fit to the filtered SSH. The SSH Figures 2, 5, 7, 11 and 14 in the sections that follow show the amplitude for the annual cycle regression between 15°S and 15°N and the phase along the northern and southern latitudes where the zonally averaged amplitudes are largest in the equatorial waveguide. The zonal wavelength λ is computed by fitting a straight line to the longitudinal variation of the annual phase (dashed lines in lower left panels of the figures) and estimating the wavelength from the slope s by $\lambda = 2\pi s^{-1}$. Since the period (T) is annual, the westward phase

speed estimate is just $|\lambda/T|$. The errors associated with these speeds are estimated by computing the phase speeds for smaller overlapping segments (30° zonal segments every 5° of longitude within the longitudinal range of the original straight line fit) and taking the standard deviation as the error bounds (Table 2).

2.4 Benchmark Run

The Gent-Cane model forced with the seasonal cycle QuikSCAT winds computed from two years of QuikSCAT (Section 2.3.2.1) is able to simulate the salient features of the observed equatorial asymmetry with annual SSH amplitudes along 5.2°N more than twice those along 5.2°S (Figure 5). East of 250°E along 5° and 10°N, there are patches of high SSH variability in both the TOPEX/Poseidon data and the benchmark run (Figure 2 and 5, respectively), apparently due to local Ekman pumping in the lee of the Sierra Madre mountains (Ducet et al. 2000; Kelly and Thompson 2002). While very similar in geographical structure, the model northern maximum is 25% weaker than the TOPEX/Poseidon maximum. In the central Pacific, a stronger latitudinal asymmetry is present in the benchmark run due to a weaker southern SSH maximum (Figure 5). Simple kinematic arguments show that meridional shear in the mean zonal currents alters the meridional gradient of potential vorticity which sets up the amplitude of the Rossby waves. We find that the maxima in SSH amplitude are collocated with maxima in the meridional gradient of potential vorticity. The overall weaker southern maximum therefore results from the weaker meridional shear in the benchmark SEC in the central Pacific (upper right panel of Figure 4). Note that the combination of asymmetries in the mean and time-varying wind forcing used in the benchmark run may amplify the Rossby wave

asymmetry in a way not readily explained by these simple kinematic arguments. The Rossby wave phase speeds along 5.2°N/S are similar to those estimated from observations with faster speeds in the north than in the south ($55.4 \pm 2.3\ cm\ s^{-1}$ compared with $48.9 \pm 3.4\ cm\ s^{-1}$).

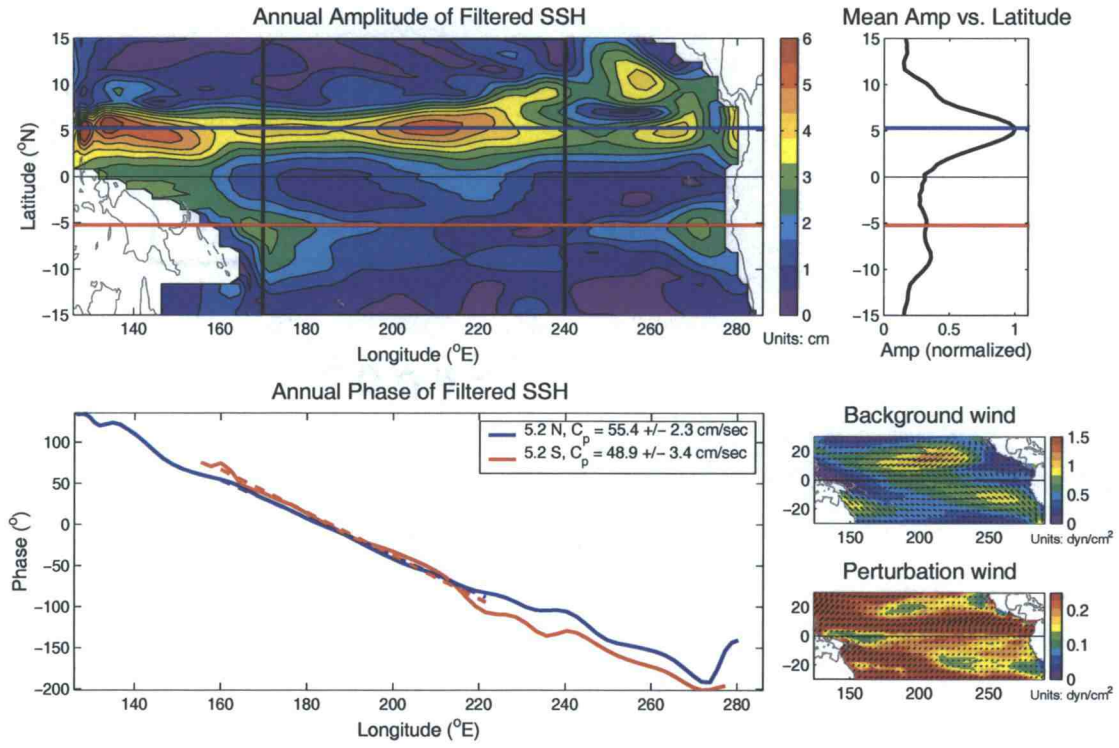

Figure 5. SSH from the Gent-Cane model forced by seasonal QuikSCAT windstress (benchmark run) and filtered to isolate Rossby wave signatures. Upper left: SSH annual amplitude (cm). Upper right: zonally averaged amplitude from 170°E to 240°E. Bottom left: phase as a function of longitude along 5.2°S (red) and 5.2°N (blue). Bottom right: structure of the steady (mean) wind and standard deviation of the perturbation windstress ($dyn\ cm^{-2}$).

Depth-averaged (layer 4 to 7) zonal and meridional velocity annual amplitude (not shown) are in qualitative agreement with the geostrophic velocities estimated from altimeter measurements (Delcroix et al. 1994; Chelton et al. 2003). Layers 4 to 7 are chosen because they capture the modal structure in a more computationally stable fashion. The first Empirical Orthogonal Functions (EOFs) for sea surface height and depth-averaged zonal and meridional velocity are plotted along six meridional transects as the thick solid lines in Figure 6. The SSH EOF structures agree well with the first SSH EOFs from TOPEX/Poseidon data (thin solid lines) and the eigensolutions from 1.5-layer shear-modified theory (dashed lines) reproduced from Figures 24 and 26 in Chelton et al. (2003). Although the simulated southern maximum is somewhat weak in the central Pacific compared to the observed and theoretical maxima, there is good agreement west of the dateline. The structures of the zonal velocity EOF 1 also compare well with the observed and theoretical structures with the maximum shifted north of the equator by 1 to 2°. The meridional velocity comparisons are less clear, probably because the meridional velocity is so weak (generally $< 3\ cm\ s^{-1}$; see Figure 13 of Chelton et al. 2003) and therefore difficult to isolate from noise. The locations of the northern maximum (near 4°N) and southern minimum (near 2°S) differ among the model, observations, and theory. The model meridional velocity has structure near the equator that can not be validated with altimeter-based estimates as geostrophy fails near the equator. Except for the westernmost section, however, the latitudinal structure of meridional velocity near the equator in the model is quite similar to the eigensolutions of the 1.5-layer shear-modified theory.

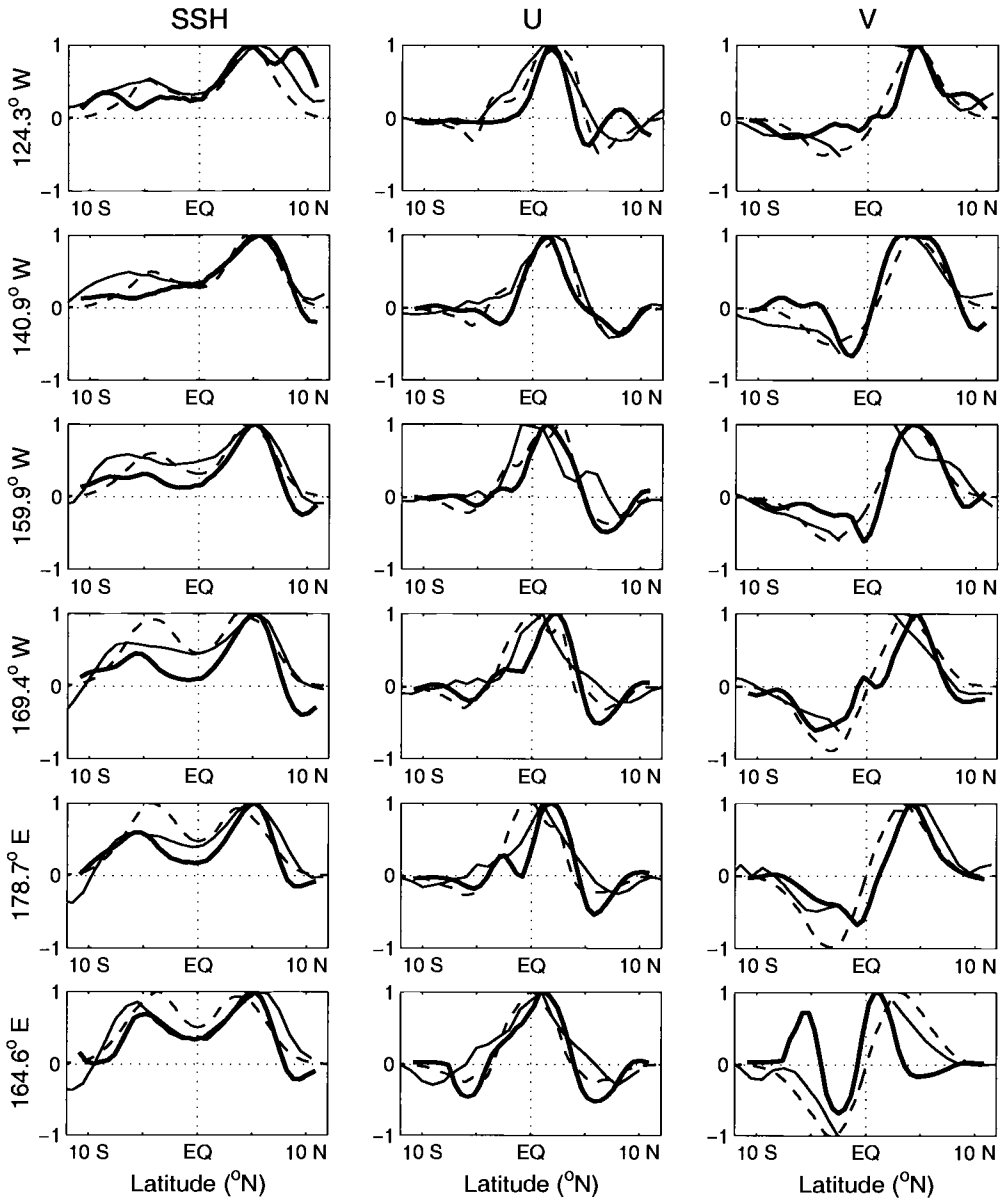

Figure 6. First EOF of SSH (left panel), depth-averaged (layers 4 to 7) zonal (center panel) and meridional (right panel) velocity along model transects nearest to 125°W, 140°W, 155°W, 170°W, 180°W, and 165°E. The thick solid line are EOF amplitudes computed from the benchmark run. TOPEX/Poseidon EOF amplitudes (thin solid lines) and the shear-modified theory eigensolutions (dashed lines) from *Chelton et al. (2003)* Figure 24 and 26.

Hydrographic observations in the tropical Pacific have found evidence of vertical Rossby wave propagation (Lukas and Firing 1985; Kessler and McCreary 1993). This raises the question of the suitability of the Gent-Cane model for Rossby wave process studies in the tropics. The lack of downward energy flux associated with vertically propagating baroclinic Rossby waves (as in the modeling study of Dewitte and Reverdin 2000) might be expected to trap energy in the upper ocean of the Gent-Cane model and produce anomalously large signals in the western Pacific. Neither are found to be the case here. Kessler and McCreary (1993) argued that resolving the low-frequency variations of the thermocline is sufficient to predict the subthermocline response to the wind forcing and that the vertical propagation they observed can be modeled with only a few baroclinic modes. The Gent-Cane model, which resolves the low-frequency variations of the thermocline (Hackert et al. 2001), reproduces the observed asymmetry of equatorial Rossby wave amplitudes and phase speeds in the benchmark run with acceptable realism. We therefore conclude that the Gent-Cane model is appropriate for testing hypotheses for the asymmetry of equatorial Rossby waves.

2.5 Hypothesis 1: Asymmetric Background Zonal Currents

In the first set of experiments, we spun up the model with steady, equatorially asymmetric winds (a modification of the QuikSCAT two-year mean shown in Figure 3) to obtain an asymmetric background mean ECS in a rectangular basin (lower right panel, Figure 4). The goal is to generate a latitudinally asymmetric mean circulation that possesses the general features of the Pacific Ocean (e.g.,

an equatorial Pacific cold tongue, warm pool, and NECC-SECN shear) without introducing boundary-induced asymmetry through coastline geometry.

The background meridional winds are set to zero everywhere for this set of experiments. Numerical experiments (not shown here) with non-zero mean meridional winds demonstrated that they do not significantly alter the symmetry of the eigensolutions or the phase speeds of the Rossby waves. The background wind field for the rectangular ocean basin considered here is generated by bilinearly interpolating the two-year mean QuikSCAT zonal wind stress over the continents and setting the interpolated mean zonal wind stress to zero over the Gulf of Mexico and surrounding coastlines. The interpolated mean zonal wind stress is then smoothed to further reduce spurious winds over land boundaries by fitting at each latitude a low-order Fourier representation (two harmonics of the basin width, X_E) of the form

$$\overline{\tau}^x(x,y) = a_0(y) + a_1(y)\cos(\frac{\pi x}{X_E}) + a_2(y)\sin(\frac{\pi x}{X_E}) + a_3(y)\cos(\frac{2\pi x}{X_E}) + a_4(y)\sin(\frac{2\pi x}{X_E}). \quad (1)$$

From comparison of the lower right panel of Figures 5 and 7, this fit captures the general features of the mean tropical Pacific winds.

Constant in time, but spatially varying precipitation and heat flux forcing are applied at the surface to avoid introducing buoyancy-forced temporal variability. The mean surface heat flux is computed via the bulk formula of Seager et al. (1988) based on the mean cloud coverage from the International Satellite Cloud Climatology Project climatology (Rossow and Schiffer 1991), the mean wind speed, and constant solar fluxes. Following Chen et al. (1994a,b), the model solutions away from the

equatorial region are restored to a Levitus (1982) mean state (h, S, and T) in a sponge layer from 20° to 30° of latitude. The above interpolation and smoothing steps are repeated with the precipitation, cloud cover, and Levitus climatology to produce fluxes of heat and moisture over the rectangular basin.

The steady-forced model converges to an asymmetric mean state within 20 years of run time. For the Hypothesis 1 tests, we then apply idealized equatorially symmetric, annually-varying winds as a small perturbation to the steady asymmetric winds. The small perturbation is generated by fitting an annual harmonic to the two years of monthly mean QuikSCAT wind stress and symmetrizing the winds about the equator. At each gridpoint and time, the symmetrized windfield is defined by

$$\begin{pmatrix} \tau'_{x,s}(x,y,t) \\ \tau'_{y,s}(x,y,t) \end{pmatrix} = 0.5\epsilon \begin{pmatrix} \tau'_x(x,y,t) + \tau'_x(x,-y,t) \\ \tau'_y(x,y,t) + \tau'_y(x,-y,t) \end{pmatrix}. \quad (2)$$

In an effort to avoid contamination from terrestrial winds, the perturbation domain is defined to be 165°E to 240°E and 10°S to 10°N. Outside of this domain, the perturbation winds are tapered by a Gaussian function to zero at the model boundaries in all directions. The decay scales chosen for the taper are 40° of longitude and 20° of latitude. The model is then run for 15 years with this perturbation wind stress forcing, with several values of ϵ chosen to test the linearity of the system response, and the model solutions are analyzed from the years 31 to 35. The use of small values for ϵ avoids significant alteration of the asymmetry of the background currents.

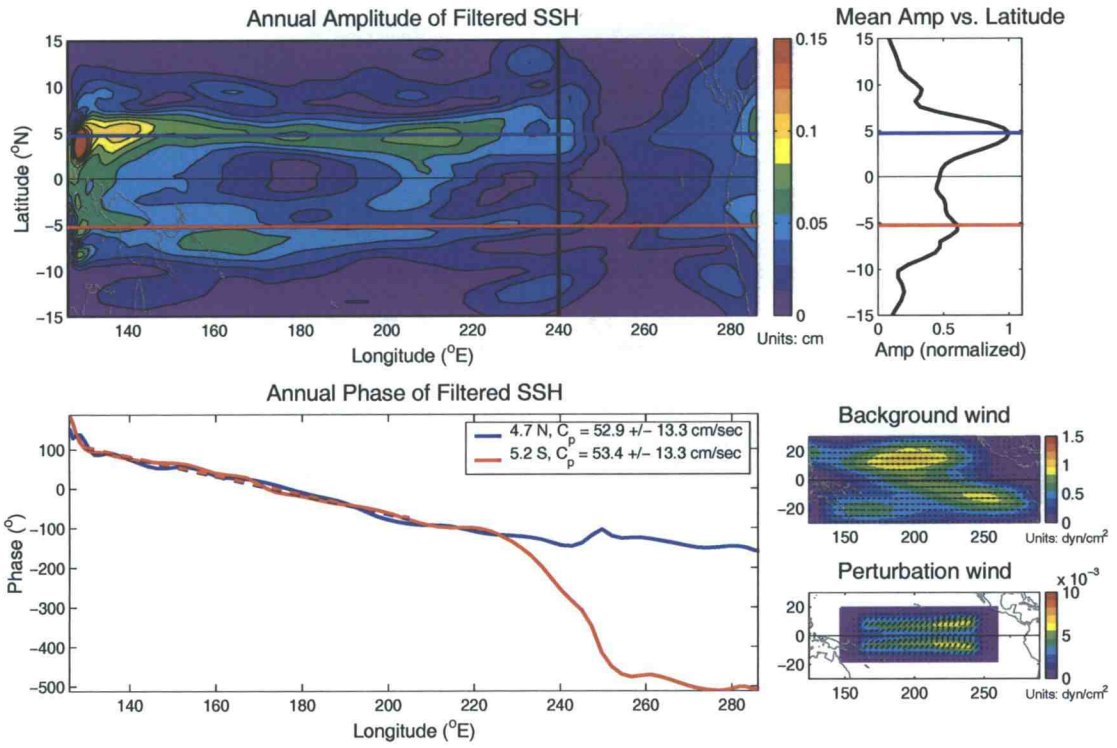

Figure 7. Similar to Figure 5, but SSH from the Gent-Cane model with a rectangular basin forced with 2-year mean zonal wind plus symmetric perturbation winds ($\epsilon = 0.02$) derived from QuikSCAT windstress as described in the text. Zonally averaged amplitudes between 126° and 240°E. Phase lines along 5.2°S and 4.7°N are shown in red and blue, respectively.

2.5.1 SSH Amplitude and Zonal Phase Speed. When forced by symmetric, annually-varying perturbation wind stress with $\epsilon = 0.02$, the model with asymmetric background mean currents generates asymmetric Rossby waves (Figure 7). The northern and southern maxima of SSH span nearly the entire Pacific in the TOPEX/Poseidon observations (upper left panel, Figure 2). The simulated northern and southern maxima of SSH are negligible east of 240°E (upper left panel, Figure 7), which is the direct result of choosing 240°E as the eastern boundary of the wind perturbation domain. Zonal averaging of the amplitudes between the western boundary (126°E) and the eastern edge of the perturbation domain

(240°E) shows that the northern maximum along 4.7°N is 1.7 times larger than the southern maximum along 5.2°S (upper right panel, Figure 7). The westward phase speeds of 52.9 ± 13.3 and 53.4 ± 13.3 $cm\ s^{-1}$ along the northern and southern maxima, respectively, are nearly equal. The SSH structure in Figure 7 supports the hypothesis that the observed wave amplitude asymmetry is due to the asymmetry of the background mean flow. The equatorial symmetry of the model phase speeds, however, indicates that another mechanism is evidently responsible for the approximately 25% faster observed phase speeds in the north than in the south.

There are curious local maxima near 12°N/S in the model SSH amplitudes in the central Pacific. A similar peak is present along 12°N in the TOPEX/Poseidon observations (Figure 2) and in the benchmark run (Figures 5 and 6). The northern peak results from the superposition of local annual forcing with a travelling annual Rossby wave originating in the eastern Pacific (White 1977) and can be seen in $x - t$ diagrams of model SSH (not shown here). The southern peak in the model SSH results from the symmetrized perturbation winds used here to force the model. The Gaussian tapering of wind stress used here to restrict the perturbation winds to the equatorial waveguide artificially enhances the wind stress curl poleward of 10° of latitude and provides intensified local forcing of this real feature. The intensity of the peak increases linearly as the magnitude of the perturbation (ϵ) increases. Experiments with different tapers (e.g., a linear taper) successfully eliminate the spurious amplification of these peaks, but this is not pursued further since our focus is on the structure of the variability within the equatorial waveguide between about 8°S and 8°N.

2.5.2 Vertical Structure and Modal Decomposition. The existence of background currents alters the meridional structure of equatorial Rossby waves (Chelton et al. 2003; and Figure 7). To quantify the subsurface effects of the ECS on the Rossby waves, we construct the meridional and vertical (y, z) structures for zonal velocity which we interpret as representative of the first two shear-modified meridional Rossby wave modes for our Hypothesis 1 simulation with $\epsilon = 0.02$. Here the model zonal velocity is treated in terms of (y, s) space, where s is the vertical layer, and then converted to (y, z) space for graphical display. We seek a separated representation of the zonal velocity annual signal (filtered as in Section 2.3.3), u, of the form

$$u(x, y, s, t) = B_{u,1}(x, t)F_{u,1}(y, s) + B_{u,2}(x, t)F_{u,2}(y, s) \tag{3}$$

where we specify the spatial modes $F_{u,i}(y, s)$ as

$$F_{u,i}(y, s) = u(x_0, y, s, t_i). \tag{4}$$

The temporally varying amplitudes $B_{u,i}(x, t)$ of these spatial modes are obtained by computing the linear regression of $u(x, y, s, t)$ onto the spatial structures $F_{u,1}(y, s)$ and $F_{u,2}(y, s)$, where the t_1 and t_2 in (4) represent times when the zonal velocity is dominated by modes 1 and 2, respectively, as described below.

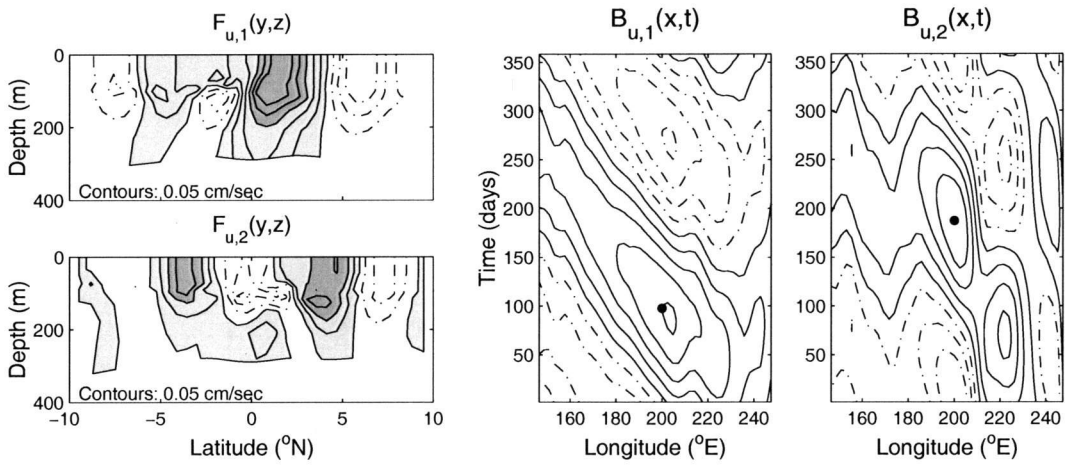

Figure 8. Left panels show (y,z) structure functions of the zonal velocity annual signal for mode 1 and 2 of the Gent-Cane model with rectangular basin forced with 2-year mean zonal winds plus symmetric perturbation winds ($\epsilon = 0.02$). Center and right panels show regression coefficients as a function of longitude and time for mode 1 and mode 2, respectively, which demonstrate westward propagation. The contour interval is 0.25, dash-dot lines depict negative contours, and the dots indicate (x_0, t_1) and (x_0, t_2).

The location x_0 is chosen to be 200.1°E in order to avoid the influence of TIWs in the eastern Pacific, and the times, t_1 and t_2, are chosen based on the temporal variability of the depth-averaged (layer 4 to 7) zonal velocity EOF 1 at 200.1°E, computed as in Section 2.4 except for the Hypothesis 1 simulation with $\epsilon = 0.02$. The maximum in the EOF 1 amplitude time series occurs on day $t_1 = 99$, and the following zero crossing in this time series occurs on day $t_2 = 189$. Because the first zonal velocity EOF mode has the structure of meridional mode 1 Rossby wave modified by the model ECS (as in center panels of Figure 6), the structure at t_2 should represent ECS modified meridional mode 2 structure.

As expected, (y, s) structures of the zonal velocity for t_1 and t_2 projected onto (y, z) space (left panels of Figure 8) are latitudinally asymmetric with meridional structures in the upper layer that resemble mode 1 and 2 modified by asymmetric

background currents (lower right panel, Figure 4). Except near 2°S, the vertical structures of both $F_{u,1}(y,z)$ and $F_{u,2}(y,z)$ indicate vertical mode 1 Rossby waves; near 2°S, the vertical structures are somewhat less clear, especially for $F_{u,1}(y,z)$.

The linear regression coefficients, $B_{u,1}(x,t)$ and $B_{u,2}(x,t)$ (center and right panels of Figure 8) exhibit westward propagation with phase speeds on the order of 45 and 30 $cm\ s^{-1}$ for mode 1 and 2, respectively. The westward phase speed found for $B_{u,1}(x,t)$ is consistent with the phase speed determined from SSH in Section 2.5.1. In the absence of an analytical representation of the subsurface effects of background currents on the Rossby waves in a nonlinear system, we have obtained empirically a separable structure for u with clear westward propagation.

2.5.3 Sensitivity to ϵ. To determine whether waves generated in the nonlinear Gent-Cane model behave linearly, we study the sensitivity of the Hypothesis 1 experiments to the magnitude of the symmetric perturbation winds by running the model with $\epsilon = 0.01, 0.02, 0.05$, and 0.10. The measures utilized to highlight the sensitivity of the model runs to ϵ include U_ϵ, the five-year model mean (years 31 to 35), depth-averaged (layers 1 to 7) zonal velocity along 141°W (Figure 9), and the zonally averaged SSH amplitude maxima (between 126°E and 240°E) and westward phase speeds along 4.7°N and 5.2°S (Figure 10).

The extent to which nonlinearities in the Gent-Cane model are important can be inferred from the differences between U_ϵ and U_0, the depth-averaged zonal velocity in the absence of perturbation winds (upper panel, Figure 9). As ϵ decreases, the difference between U_ϵ and U_0 decreases as expected (lower panel, Figure 9). Though small, the latitudinal structure of $U_\epsilon - U_0$ is asymmetric for all values of ϵ, evidence of weak nonlinear interactions between the asymmetric background mean circulation

and the symmetric annually-varying perturbation. The small differences between U_ϵ and U_0 relative to U_0 indicate that symmetric perturbations with ϵ as high as 0.10 are insufficient to significantly alter the asymmetry of the background mean flow and shear. Thus, the Hypothesis 1 assumption of asymmetric background flow holds.

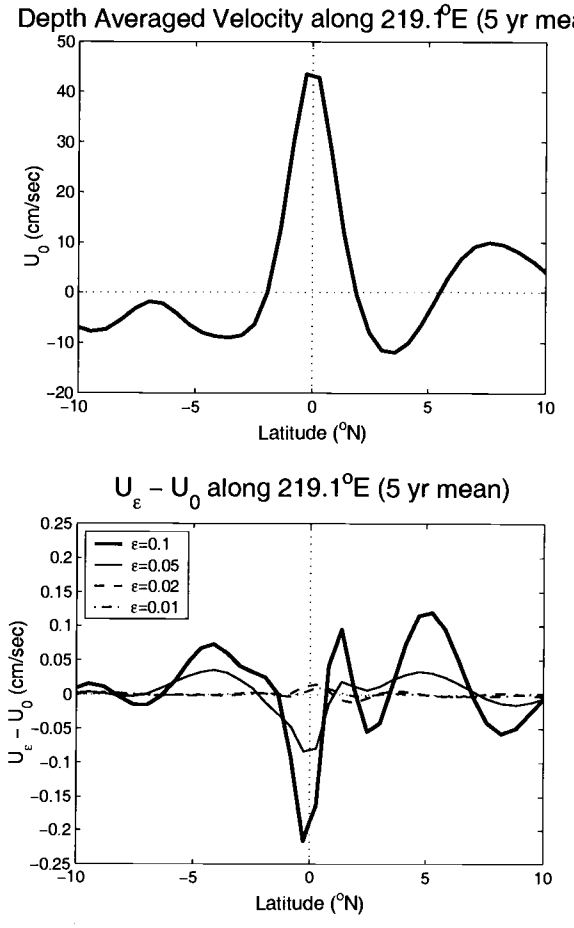

Figure 9. Dependence of the five-year model mean (years 31 to 35) depth-averaged (layers 1 to 7) zonal velocity, U_ϵ, along 219°E (141°W) on ϵ for the Gent-Cane model forced with 2-year mean zonal wind plus symmetric perturbation winds. Upper panel: Zero perturbation depth-averaged zonal velocity, U_0. Lower panel: U_ϵ - U_0 for ϵ = 0.01 (dash-dot line), 0.02 (dashed line), 0.05 (thin solid line), and 0.10 (thick solid line).

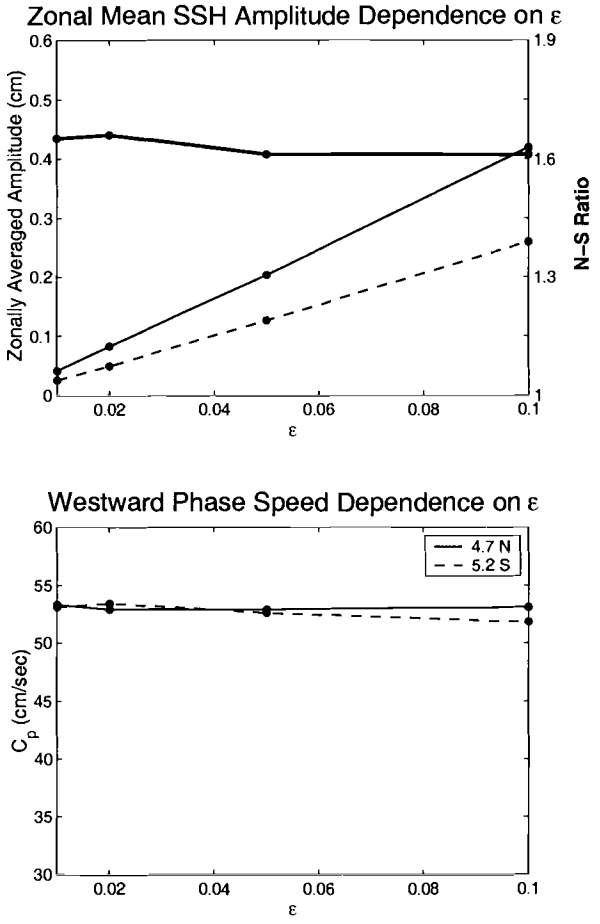

Figure 10. The zonally averaged (126° to 240°E) SSH amplitude (upper panel) and westward phase speeds (lower panel) along 4.7°N (thin solid line) and 5.2°S (dashed line), and the ratio of the northern values to the southern values (thick solid line on right y-axis scale) as functions of the perturbation wind amplitude ϵ for the Gent-Cane model forced with 2-year mean zonal wind plus symmetric perturbation winds. The smallest value of ϵ tested was 0.01.

For linear waves, the amplitudes of the SSH maxima are expected to increase linearly as the magnitude of the perturbation forcing (ϵ) increases, and the phase speeds are not expected to change. The SSH maxima for the Hypothesis 1 experiments (upper panel, Figure 10) do increase linearly with increasing ϵ. The ratio of the northern maximum to the southern maximum is nearly a constant value,

1.6, essentially independent of ϵ. The westward phase speeds of about 53 $cm\ s^{-1}$ along 4.7°N and 5.2°S are also independent of ϵ (lower panel, Figure 10). The ratio of the northern phase speed to the southern phase speed is approximately 1.0 for all values of ϵ. The asymmetry of the Rossby wave SSH amplitudes and the symmetry of the estimated phase speeds are therefore robust features in this set of experiments where the background mean flow is asymmetric.

2.6 Hypothesis 2: Asymmetric Wind Forcing

In the second set of experiments, we perturb the model about a symmetrized background mean state. The goal is to produce a latitudinally symmetric mean circulation that possesses symmetrized versions of the general features of the Pacific Ocean. The background zonal wind stress is similar to that of (1) in Section 2.5, but is symmetrized with respect to latitude such that

$$\overline{\tau}_s^x(x,y) = 0.5[\overline{\tau}^x(x,y) + \overline{\tau}^x(x,-y)]. \tag{5}$$

The heat and moisture fluxes used in Section 2.5 are symmetrized with respect to latitude in the same manner. The model is run for twenty years under these conditions, by which time it converges to a steady, symmetric mean state.

The time-varying wind stress perturbation in the model runs for testing Hypothesis 2 consists of idealized equatorially asymmetric, annually-varying winds generated by fitting an annual harmonic to the two years of QuikSCAT wind stress and allowing the winds to retain the observed asymmetric structure about the equator,

$$\begin{pmatrix} \tau'_{x,a}(x,y,t) \\ \tau'_{y,a}(x,y,t) \end{pmatrix} = \epsilon \begin{pmatrix} \tau'_{x}(x,y,t) \\ \tau'_{y}(x,y,t) \end{pmatrix}. \tag{6}$$

The strength of the perturbation winds (ϵ), the domain over which the perturbation winds are applied, and the Gaussian taper outside of the domain are the same as in the previous numerical experiments described in Section 2.5. (Additional values of ϵ are included to resolve curious behavior near $\epsilon = 0.05$ in Section 2.6.2.) The model is then run for an additional 15 years with the perturbation wind stress forcing, and model solutions are analyzed from years 31 to 35.

2.6.1 SSH Amplitude and Zonal Phase Speed. The model forced by asymmetric annually-varying perturbation winds about a symmetric mean state with $\epsilon = 0.02$ generates essentially symmetric Rossby waves (Figure 11). The zonally averaged (between 126°E and 240°E) SSH maxima are along 6.4°N and 7.0°S, which differs from the 3.7°N/S maxima of classical theory (solid line, Figure 1) but presents a nearly symmetric pattern about the equator. The EUC in the Hypothesis 2 experiments (not shown) is slightly stronger than the EUC of the Hypothesis 1 experiments, which is consistent with the shift of the SSH maxima from 4.7°N and 5.2°S to the higher latitudes of 6.4°N and 7.0°S (Philander 1979). The westward phase speeds of 39.4 ± 8.6 and 35.5 ± 6.0 $cm\ s^{-1}$ along 6.4°N and 7.0°S, respectively, are somewhat smaller than those observed but are not significantly different on the two sides of the equator. This model run suggests that asymmetric wind forcing does not generate latitudinally asymmetric Rossby waves without an asymmetric background mean flow.

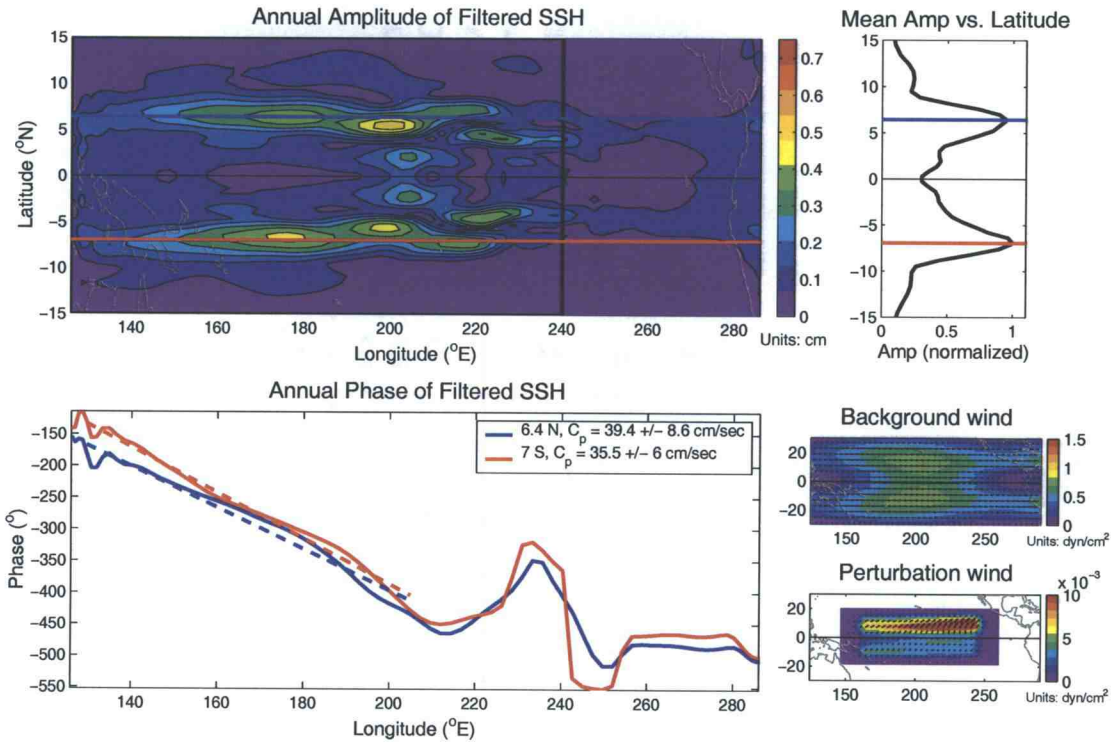

Figure 11. Similar to Figure 7, but SSH from the Gent-Cane model with a rectangular basin forced with symmetric 2-year zonal mean wind plus asymmetric perturbation winds ($\epsilon = 0.02$) derived from QuikSCAT windstress as described in the text. Phase lines along 7.0°S and 6.4°N are shown in red and blue, respectively.

The 12°N peak previously described in Section 2.5 (Hypothesis 1) is again present and increases in strength as the magnitude of the perturbation winds ϵ increases (see Section 2.6.2). Since the perturbation winds are not symmetrized for the model runs for testing Hypothesis 2, there is no matching peak along 12°S.

2.6.2 Sensitivity to ϵ. The dependence of the Hypothesis 2 numerical experiments on the magnitude of the asymmetric perturbation winds is explored by running the model with $\epsilon = 0.01, 0.02, 0.04, 0.05, 0.06, 0.08$ and 0.10. We evaluate the linearity of the system response and observe the changes in the depth- and time-averaged zonal velocities as the value of ϵ increases.

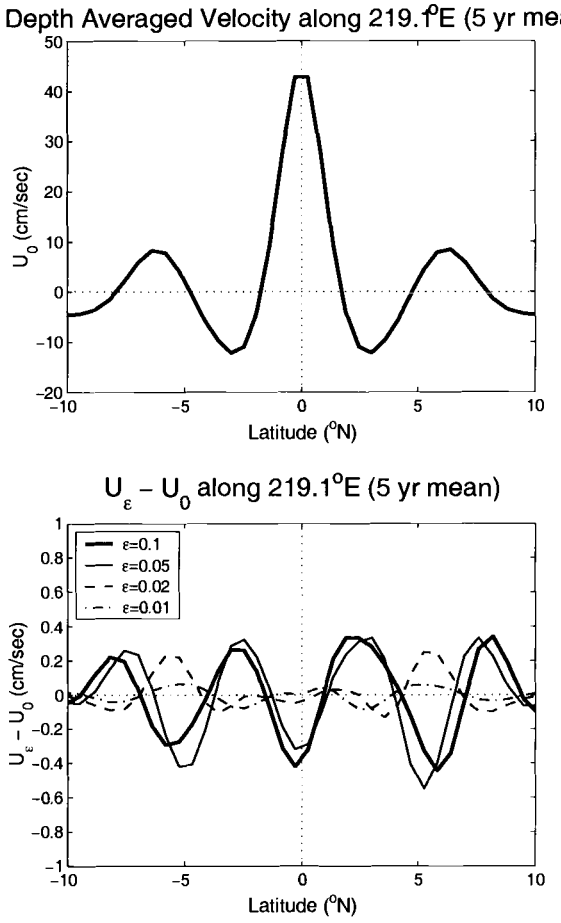

Figure 12. Similar to Figure 9: dependence of the five-year model mean (years 31 to 35) depth-averaged (layers 1 to 7) zonal velocity, U_ϵ, along 219°E (141°W) on ϵ for the Gent-Cane model forced with symmetric mean plus asymmetric perturbation winds. Upper panel: Zero perturbation depth-averaged zonal velocity, U_0. Lower panel: U_ϵ - U_0 given $\epsilon = 0.01$ (dash-dot line), 0.02 (dashed line), 0.05 (thin solid line), and 0.10 (thick solid line).

In the Hypothesis 1 experiments (Section 2.5.3), the background shear is strongly asymmetric and symmetric perturbations winds with ϵ as high as 0.10 are unable to significantly alter the asymmetry of the background currents (lower panel, Figure 9). In this set of experiments, to test Hypothesis 2, U_0 is latitudinally symmetric (upper panel, Figure 12) and the latitudinal structure of $U_\epsilon - U_0$ (lower

panel, Figure 12) remains nearly symmetric for $\epsilon < 0.05$. For $\epsilon \geq 0.05$, the mean flow becomes increasingly asymmetric and $U_\epsilon - U_0$ does not vary linearly with ϵ.

In contrast to the results obtained in Section 2.5.3, the amplitudes of the SSH maxima do not increase monotonically beyond $\epsilon = 0.04$ for this set of experiments (upper panel, Figure 13). The latitudes of the zonally averaged (between 126°E and 240°E) SSH amplitude maxima range from 5.2° to 7.0°, depending on ϵ, so we select a median latitude, 5.8°, to carry out the analysis. For $0.01 \leq \epsilon \leq 0.05$, the ratios of the amplitudes of the northern and southern maxima are very close to 1. The northern maximum increases to approximately 1.3 times the southern maximum for $\epsilon > 0.05$. The westward phase speeds along 5.8°N/S increase from 35 to 54 $cm\ s^{-1}$ as ϵ increases from 0.01 to 0.05 but then decreases to 40 $cm\ s^{-1}$ for $\epsilon \geq 0.08$ (lower panel, Figure 13). For all values of ϵ considered, the ratio of the northern phase speed to the southern phase speed is close to 1.0.

The near symmetry of the Rossby wave SSH amplitudes and the depth- and time-averaged zonal velocity are maintained for $\epsilon < 0.05$. For $\epsilon \geq 0.05$, the asymmetric wind perturbation becomes large enough to upset the underlying symmetry of the background flow and thus generate significantly asymmetric Rossby waves, as apparent from the SSH amplitudes when $\epsilon = 0.10$ (Figure 14). The structure of the SSH amplitude under these conditions (upper left panel, Figure 14) differs from the observed structure as the simulated southern maximum extends farther into the central Pacific than is observed from TOPEX/Poseidon (upper left panel, Figure 2). This is probably due to the unrealistic and possibly unstable symmetric background circulation and the lack of coastlines (i.e., the rectangular basin in the model runs considered here).

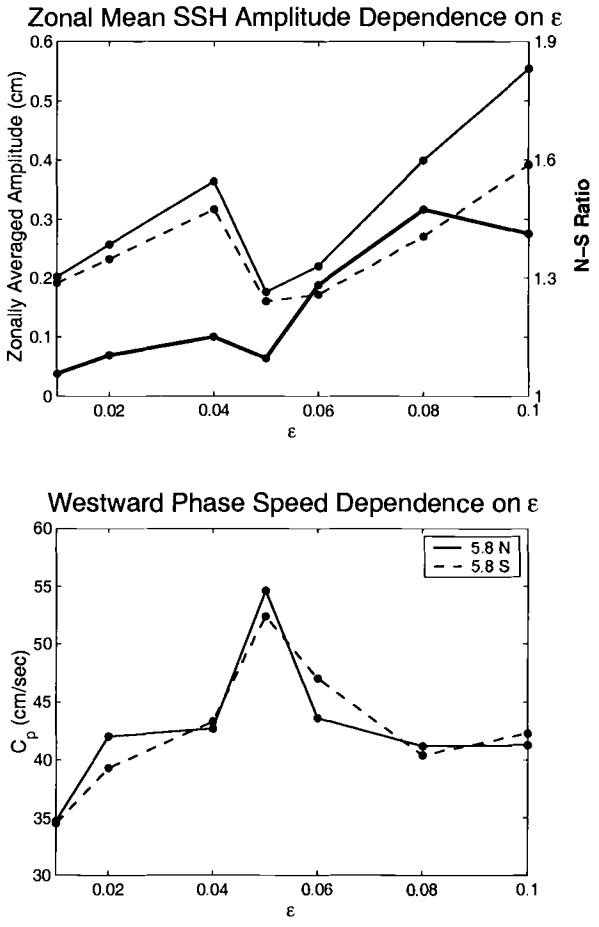

Figure 13. Similar to Figure 10: zonally averaged SSH amplitude (upper panel) and westward phase speeds (lower panel) along 5.8°N (thin solid line) and 5.8°S (dashed line), and the ratio of the northern values to the southern values (thick solid line on right y-axis scale) as functions of the perturbation wind amplitude ϵ for the Gent-Cane model forced with symmetric mean plus asymmetric perturbation winds. Additional values of ϵ ($\epsilon = 0.04$, 0.06, and 0.08) were tested.

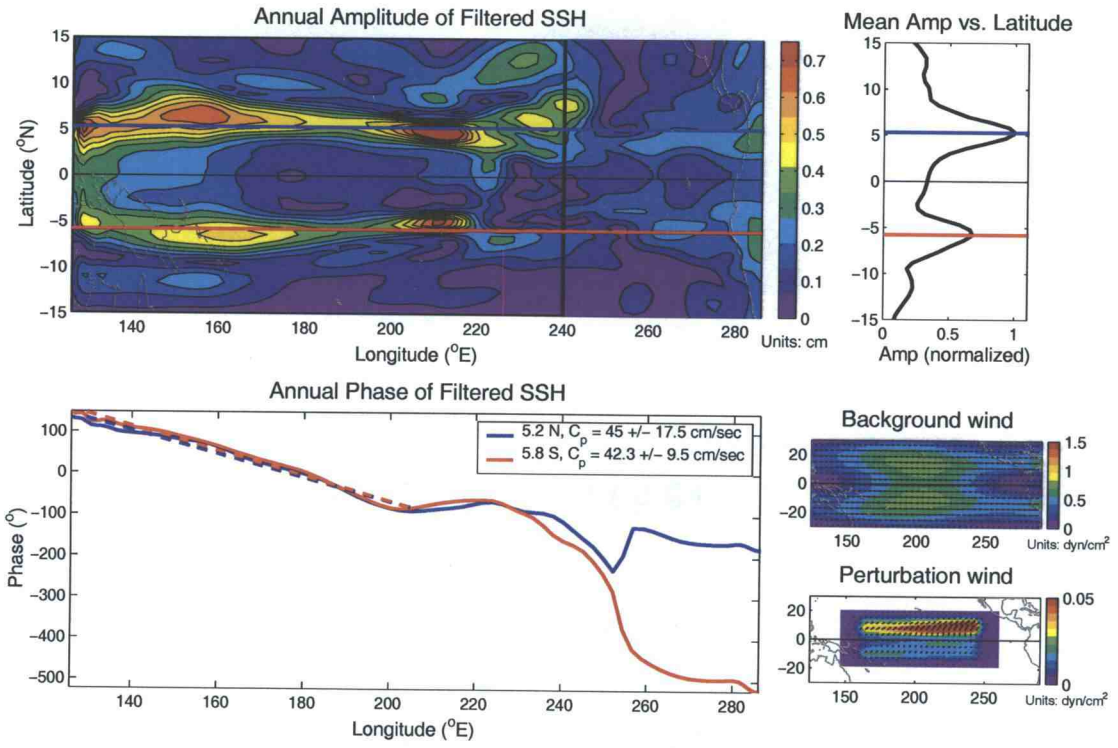

Figure 14. Similar to Figure 11, except for $\epsilon = 0.10$. Phase lines along 5.8°S and 5.2°N are shown in red and blue, respectively.

In our Hypothesis 2 experiments, we thus find that $\epsilon \geq 0.05$ is sufficient to alter the symmetry of the background mean flow via nonlinear interactions. Consistent with the Hypothesis 1 results, the asymmetrization of the Hypothesis 2 mean flow for $\epsilon \geq 0.05$ produces asymmetric Rossby waves.

2.7 Summary and Conclusions

The Gent-Cane model was used in this study to test two potential mechanisms for the asymmetry of annual equatorial Rossby waves and the discrepancy between the predicted and observed westward phase speeds. The two mechanisms tested were asymmetry of the background mean currents (Hypothesis 1) and asymmetric annually-varying wind forcing (Hypothesis 2). We considered rectangular basins to avoid introducing asymmetries due to coastline geometry.

The Gent-Cane model with asymmetric background mean currents perturbed by symmetric annually-varying winds generated asymmetric annual equatorial Rossby waves with latitudinal structure similar to the observed asymmetry (Figure 7), independent of the amplitude of the symmetric perturbation winds (Figure 10). Vertical structure and modal decomposition were used to gain insight into the modification of the Rossby waves by the background ECS (Figure 8). In the presence of asymmetric background currents, simulated waves were found to have a separable structure, i.e., the annual deviations from the mean were well described by westward propagating waves of the form given by (3) in Section 2.5.2. In lieu of analytical solutions, this provides a quantitative description of the subsurface effects of the ECS on the propagating waves.

The model with symmetric mean currents perturbed by asymmetric annually-varying winds generated symmetric equatorial Rossby waves when the magnitude of the annually-varying wind stress was sufficiently small ($\epsilon < 0.05$) relative to the background wind stress (Figure 11 and 13). Because this system behaves nonlinearly, asymmetric Rossby waves resulted when the magnitude of the asymmetric wind perturbation became sufficiently large ($\epsilon \geq 0.05$), as shown in Figure 13 and 14. For

these larger values of ϵ, nonlinearity caused the five-year mean, depth-averaged zonal currents, U_ϵ, to deviate from the unperturbed symmetric background current, U_0 (lower panel, Figure 12), and thus destroyed the symmetry of the mean circulation.

The model runs for testing Hypothesis 2 thus indicate that asymmetric wind forcing in the absence of an asymmetric background mean ECS does not generate asymmetric Rossby waves. This is consistent with the results obtained by Kessler and McCreary (1993) from a linear model with $U_0 = 0$. Therefore, the numerical experiments in Section 2.5 and 2.6 demonstrate that the primary mechanism for the observed asymmetric latitudinal structure of equatorial Rossby waves is asymmetric meridional shears in the background flow (Hypothesis 1). Asymmetric time-varying wind forcing serves as a secondary and weaker mechanism in the presence of an asymmetric ECS.

As in the observations, the model-derived westward phase speeds in the presence of non-zero background currents were slower than the theoretical phase speeds. Table 2 compares phase speeds derived from observations, analytic theory, and a subset of the numerical experiments conducted for this study. Hypothesis 1 experiments succeeded in producing westward phase speeds with magnitudes similar to the observed phase speeds. In general, the Hypothesis 2 experiments produced phase speeds that were significantly slower than observed. In both sets of experiments, the ratio of the phase speed along the northern maximum to the phase speed along the southern maximum was very nearly equal to 1.0. Phase speeds estimated from observations, however, found a northern phase speed that was slightly faster (by about 25%) than the southern phase speed.

Table 2. Westward phase speeds derived from observations, analytical theory, and Gent-Cane modeling experiments along latitudes of local SSH amplitude maxima.

Description	Latitude	c_p $(cm\ s^{-1})$	Latitude	c_p $(cm\ s^{-1})$
Classical Theory (m=1,n=1)	3.7°S	90	3.7°N	90
Shear-modified Theory[a]	5.5°S	71	5.5°N	71
Broad-band TOPEX/Poseidon[a]	5.5°S	48 ± 10	5.5°N	60 ± 15
Annual TOPEX/Poseidon	6.5°S	43.3 ± 6.8	5.5°N	55.0 ± 14.2
Benchmark Gent-Cane run	5.2°S	48.9 ± 3.4	5.2°N	55.4 ± 2.3
Hypothesis 1:				
ϵ=0.02	5.2°S	53.4 ± 13.3	4.7°N	52.9 ± 13.3
ϵ=0.10	5.2°S	51.8 ± 4.4	4.7°N	53.1 ± 12.7
Hypothesis 2:				
ϵ=0.02	7.0°S	35.5 ± 6.0	6.4°N	39.4 ± 8.6
ϵ=0.10	5.8°S	42.3 ± 9.5	5.2°N	45.0 ± 17.5

[a]Values from Chelton et al. (2003)

Although the shear-modified eigensolutions in Chelton et al. (2003) yielded slower Rossby wave phase speeds than the classical theory, they were still about 20% faster than the observed phase speeds. The eigenvalue solutions for the phase speeds were calculated locally along selected longitudes. The resulting shear-modified phase speeds were therefore independent of latitude and oblivious to the effects of coastline geometry and time-varying wind forcing.

Since neither asymmetric background zonal currents (Hypothesis 1) nor asymmetric wind forcing (Hypothesis 2) suceeded at reproducing the observed Rossby wave phase speed asymmetry, the role of the asymmetric coastlines bounding the Pacific Ocean should be explored. The benchmark run forced by observed seasonal varying winds discussed in Section 2.4 was able to capture a north-south phase speed difference of roughly 13%. Aside from the different time-varying wind forcing, the two significant differences in the benchmark run were the inclusion of coastline geometry and asymmetries in both the mean and time-varying wind forcing. Numerical experiments (not shown here) indicate that the combined asymmetry of the background and perturbation winds do not play a role in the phase speed asymmetry. In contrast, experiments with asymmetric background shear (lower left panel in Figure 4), realistic coastlines, and symmetric perturbations ϵ (also not shown here) produced phase speeds that were roughly 23% faster along 5.2°N than along 5.2°S (50.1 and 40.7 $cm\ s^{-1}$, respectively). Comparing these numbers with the model basin width, X_E, along each of those latitudes, we find that $X_{E,5.2N}$ is approximately 27% larger than $X_{E,5.2S}$ remarkably similar to the 23% phase speed differences. Annual Rossby wave phase speeds in the equatorial waveguide evidently depend on the width of the basin. A detailed analysis of the effect of coastline geometry on the ECS and the phase speeds of annual equatorial Rossby waves will be the focus of a future study.

2.8 Acknowledgments

We thank Roland de Szoeke for helpful discussions during the course of this study and Michael G. Schlax for preparing the TOPEX/Poseidon and QuikSCAT data used in this study. We also thank Billy Kessler, Jay McCreary, and our anonymous reviewers for insightful comments that improved the final draft. RCP and RNM were supported by the National Oceanic and Atmospheric Administration Office of Global Programs under award NA16GP2016. DBC was supported by the National Aeronautics and Space Administration under contracts 1206715 and 1217722 from the Jet Propulsion Laboratory.

2.9 References

Chang, P., and S. G. H. Philander, 1989: Rossby wave packets in baroclinic mean currents. *Deep Sea Res.*, **36,** 17-37.

Chelton, D. B., 2004: The impact of SST specification on ECMWF surface wind stress fields in the eastern tropical Pacific. *J. Climate, in press.*

Chelton, D. B., R. A. De Szoeke, M. G. Schlax, K. El Naggar, and N. Siwertz, 1998: Geographical variability of the first baroclinic Rossby radius of deformation. *J. Phys. Oceanogr.*, **28,** 443-460.

Chelton, D. B., and Coauthors, 2001: Observations of coupling between surface wind stress and sea surface temparature in the eastern tropical Pacific. *J. Climate,* **14,** 1479-1498.

Chelton, D. B., M. G. Schlax, J. M. Lyman, and G. C. Johnson, 2003: Equatorially trapped waves in the presence of meridionally sheared baroclinic flow in the Pacific Ocean. *Prog. Oceanogr.*, **56,** 323-380.

Chen, D., L. M. Rothstein, and A. J. Busalacchi, 1994a: A hybrid vertical mixing scheme and its application to tropical ocean models. *J. Phys. Oceanogr.*, **24,** 2156-2179.

Chen, D., A. J. Busalacchi, and L. M. Rothstein, 1994b: The roles of vertical mixing, solar radiation, and wind stress in a model simulation of the sea surface temperature seasonal cycle in the tropical Pacific Ocean. *J. Geophys. Res.*, **99,** 20 345-20 359.

Cox, M. D., 1980: Generation and propagation of 30-day waves in a numerical model of the Pacific. *J. Phys. Oceanogr.*, **10,** 1168-1186.

Delcroix, T., J. Picaut, and G. Eldin, 1991: Equatorial Kelvin and Rossby waves evidenced in the Pacific Ocean through Geosat sea level and surface current anomalies. *J. Geophys. Res.*, **96 Suppl.,** 3249-3262.

Delcroix, T., J.-P. Boulanger, F. Masia, and C. Menkes, 1994: Geosat-derived sea level and surface current anomalies in the equatorial Pacific during the 1986-1989 El Niño and La Niña. *J. Geophys. Res.*, **99,** 25 093-25 107.

De Szoeke, R. A., and D. B. Chelton, 2004: On the wind-driven vertical velocity at the equator. *In preparation for J. Phys. Oceanogr.*

Dewitte, B., and G. Reverdin, 2000: Vertically propagating annual and interannual variability in an OGCM simulation of the tropical Pacific Ocean in 1985-94. *J. Phys. Oceanogr.,* **30,** 1562-1581.

Ducet, N., P. Y. Le Traon, and G. Reverdin, 2000: Global high-resolution mapping of ocean circulation from TOPEX/Poseidon and ERS-1 and -2. *J. Geophys. Res.,* **105,** 19 477-19 498.

Eriksen, C. C., M. B. Blumethal, S. P. Hayes, and P. Ripa, 1983: Wind-generated equatorial Kelvin waves observed across the Pacific Ocean. *J. Phys. Oceanogr.,* **13,** 1622-1640.

Freilich, M. H., D. G. Long, and M. W. Spencer, 1994: SeaWinds: A scanning scatterometer for ADEOS II - science overview. *Proc. Int. Geosci. Rem. Sens. Symposium,* Vol. II, Pasadena, CA, August 8-12, 960-963.

Fu, L.-L., J. Vazquez, and C. Perigaud, 1991: Fitting dynamic models to the Geosat sea level observations in the tropical Pacific ocean. Part I: A free wave model. *J. Phys. Oceanogr.,* **21,** 798-809.

Gent, P. R., and M. A. Cane, 1989: A reduced gravity, primitive equation model of the upper equatorial ocean. *J. Comp. Physics,* **81,** 444-480.

Hackert, E. C., A. J. Busalacchi, and R. Murtugudde, 2001: A wind comparison study using an ocean general circulation model for the 1997-1998 El Niño. *J. Geophys. Res.,* **106,** 2345-2362.

Johnson, G. C., B. M. Sloyan, W. S. Kessler, and K. E. McTaggart, 2002: Direct measurements of upper ocean currents and water properties across the tropical Pacific Ocean during the 1990s. *Prog. Oceanogr.,* **52,** 31-61.

Kelly, K. A., and L. Thompson, 2002: Scatterometer winds explain damped Rossby waves. *Geophys. Res. Lett.,* **29,** 52,1-4, doi:10.129/2002GL015595.

Kessler, W. S., 1990: Observations of long Rossby waves in the northern tropical Pacific. *J. Geophys. Res.,* **95,** 5183-5217.

Kessler, W. S., and J. P. McCreary, 1993: The annual wind-driven Rossby wave in the subthermocline equatorial Pacific. *J. Phys. Oceanogr.,* **23,** 1192-1207.

Kessler, W. S., L. M. Rothstein, and D. Chen, 1998: The annual cycle of SST in the eastern tropical Pacific, diagnosed in an ocean GCM. *J. Climate,* **11,** 777-799.

Kessler, W. S., G. C. Johnson, and D. W. Moore, 2003: Sverdrup and nonlinear dynamics of the Pacific Equatorial Currents. *J. Phys. Oceanogr.,* **33,** 994-1008.

Kraus, E. B., and J. S. Turner, 1967: A one-dimensional model of the seasonal thermocline. Part II. The general theory and its consequences. *Tellus,* **19,** 98-105.

Levitus, S., 1982: *Climatological atlas of the world ocean.* National Oceanic and Atmospheric Administration, 173 pp.

Lukas, R., and E. Firing, 1985: The annual Rossby wave in the central equatorial Pacific Ocean. *J. Phys. Oceanogr.,* **15,** 55-67.

Matsuno, T., 1966: Quasi-geostrophic motions in the equatorial area. *J. Meteorol. Soc. Jpn.,* **44,** 25-43.

Meyers, G., 1979: On the annual Rossby wave in the tropical North Pacific. *J. Phys. Oceanogr.,* **9,** 663-674.

Moore, D. W., 1968: Rossby waves in an equatorial ocean. Ph.D. dissertation, Harvard University, Cambridge, MA, 207 pp.

Moore, D. W., and S. G. H. Philander, 1977: Modeling of the tropical oceanic circulation. *The Sea,* E. D. Goldberg, I. N. McCave, J. J. O'Brien, and J. H. Steele, Eds., Vol. 6, Wiley-Interscience, 319-361.

Murtugudde, R., and A. J. Busalacchi, 1998: Salinity effects in a tropical ocean model. *J. Geophys. Res.,* **103,** 3283-3300.

Murtugudde, R., R. Seager, and A. J. Busalacchi, 1996: Simulation of the tropical oceans with an ocean GCM coupled to an atmospheric mixed-layer model. *J. Climate,* **9,** 1795-1815.

Murtugudde, R., J. Beauchamp, C. R. McClain, M. Lewis, and A. J. Busalacchi, 2002: Effects of penetrative radiation on the upper tropical ocean circulation. *J. Climate,* **15,** 470-486.

Philander, S. G. H., 1978: Instabilities of zonal equatorial currents, Part 2. *J. Geophys. Res.,* **83,** 3679-3682.

Philander, S. G. H., 1979: Equatorial waves in the presence of the equatorial undercurrent. *J. Phys. Oceanogr.,* **9,** 254-262.

Price, J. F., R. A. Weller, and R. Pinkel, 1986: Diurnal cycling: Observations and models of the upper ocean response to diurnal heating, cooling, and wind mixing. *J. Geophys. Res.,* **91,** 8411-8427.

Qiao, L., and R. H. Weisberg, 1995: Tropical instability wave kinematics: Observations from the Tropical Instability Wave Experiment. *J. Geophys. Res.,* **100,** 8677-8693.

Rossow, W. B., and R. A. Schiffer, 1991: ISCCP cloud data products. *Bull. Am. Meteorol. Soc.,* **72,** 2-20.

Schlax, M. G., and D. B. Chelton, 1992: Frequency domain diagnostics for linear smoothers. *J. Amer. Stat. Assoc.,* **87,** 1070-1081.

Seager, R., S. E. Zebiak, and M. A. Cane, 1988: A model of the tropical Pacific sea surface temperature climatology. *J. Geophys. Res.,* **93,** 1265-1280.

Susanto, R. D., Q. Zheng, and X.-H. Yan, 1998: Complex singular value decomposition analysis of equatorial waves in the Pacific observed by TOPEX/Poseidon altimeter. *J. Atmos. Oceanic Technol.,* **15,** 764-774.

Verron, J., L. Gourdeau, D. T. Pham, R. Murtugudde, and A. J. Busalacchi, 1999: An extended Kalman filter to assimilate satellite altimeter data into a nonlinear numerical model of the tropical Pacific Ocean: method and validation. *J. Geophys. Res.,* **104,** 5441-5458.

White, W. B., 1977: Annual forcing of baroclinic long waves in the tropical North Pacific Ocean. *J. Phys. Oceanogr.,* **7,** 50-61.

Yu, X., and M. J. McPhaden, 1999: Seasonal variability in the equatorial Pacific. *J. Phys. Oceanogr.,* **29,** 925-947.

Zheng, Q., X. -H. Yan, C. -R. Ho, and C. -K. Tai, 1994: The effects of shear flow on propagation of Rossby waves in the equatorial oceans. *J. Phys. Oceanogr.,* **24,** 1680-1686.

3 Response of a Tropical Pacific Ocean General Circulation Model to La Niña Condition Wind Forcing

Renellys C. Perez, R. N. Miller, and Dudley B. Chelton

Unpublished Manuscript.

3.1 Abstract

Wind forcing errors are typically assumed to be the largest source of model forecast error. To measure the sensitivity of the Gent and Cane (1989) nonlinear, reduced-gravity, equatorial β-plane model to errors in wind forcing, the seasonal cycle response of the model driven by three different wind stress products is analyzed in the equatorial Pacific cold tongue region. The wind stress products are obtained from Florida State University (FSU) wind analyses, the European Centre for Medium-Range Weather Forecasts (ECMWF) global wind analyses, and winds from the SeaWinds scatterometer aboard the QuikSCAT satellite (QuikSCAT). A seasonal cycle is constructed for each wind product during two years when La Niña conditions prevail in the tropical Pacific (August 1999 to July 2001).

Significant sensitivity was found in the model cold tongue response to wind forcing on both annual and monthly time scales. The FSU wind stress produced the least realistic cold tongue due to anomalous meridional banding of the wind stress which generated spurious wind stress curl in the equatorial waveguide. Both the ECMWF and QuikSCAT wind stress driven model runs exhibited cold tongue annual cycles, tropical instability waves, and annual equatorial Rossby waves that compared well with measurements from the Tropical Rainfall Measuring Mission Microwave Imager, merged altimetry, the Tropical Atmosphere-Ocean (TAO) mooring array, and surface current reanalyses; however, the highest realism was obtained with QuikSCAT wind forcing.

3.2 Introduction

During La Niña conditions, the eastern equatorial Pacific is characterized by colder than average sea surface temperatures (SST) and increased equatorial upwelling. Consequently, the equatorial "cold tongue" of water which seasonally extends westward from South America along the equator to the central Pacific (Mitchell and Wallace 1992) finds its strongest expression during La Niña events (Wallace et al. 1989; Deser and Wallace 1990). The surface wind fields are characterized by stronger trade winds and there is stronger wind stress divergence and curl over the northern boundary of the cold tongue (Chelton et al. 2001). La Niña conditions strengthen the South Equatorial Current (SEC) and Equatorial Undercurrent (EUC) (Johnson et al. 2002) which generate enhanced latitudinal shear between the eastward flowing North Equatorial Countercurrent (NECC) and the north branch of the westward flowing SEC (SECN) and increased vertical shear between the SEC and the eastward flowing EUC. Tropical instability waves (TIWs), which likely result from the meridional and vertical shears in the equatorial current system (ECS; see Lyman et al. 2005b for a review of TIW literature), are most active during La Niña and nearly supressed during El Niño (Baturin and Niiler 1997). TIWs play an important role in the cold tongue heat balance as they produce equatorward oceanic eddy heat flux on par with the Ekman heat flux away from the equator (Hansen and Paul 1984; Bryden and Brady 1989; Baturin and Niiler 1997; Wang and McPhaden 1999; Swenson and Hansen 1999).

In this modeling study, seasonal cycle winds generated from a period when La Niña conditions prevail are used to investigate the sensitivity of an ocean general circulation model (GCM) to different wind products. The ocean GCM and

parameters are described in Section 3.3. Section 3.4 describes the wind products used to force the model and the data products used for model-data comparisons. In Section 3.5, the sensitivity of the GCM annual cycle, TIWs, and annual equatorial Rossby waves to the various wind products is analyzed. These results are also put into the context of available observations in Section 3.5. Finally, the results of the sensitivity study are summarized and implications for equatorial Pacific cold tongue modeling and data assimilation are discussed in Section 3.6.

3.3 Gent-Cane Model

The ocean general circulation model used for this study is the Gent and Cane (1989) model of the tropical Pacific, hereafter the Gent-Cane model. The dynamical model is a nonlinear, reduced-gravity, β-plane model with a uniform surface mixed layer above an active layer divided into six sigma layers relative to the bottom of the active region. The five dynamic variables are zonal velocity, meridional velocity, layer thickness, salinity, and temperature (u, v, h, S, T). At each hourly time step, the five fields are calculated at 80 x 60 horizontal gridpoints. The horizontal grid is a stretched grid that affords highest resolution near the equator and zonal boundaries. The nominal resolution of the horizontal grid in the equatorial waveguide is 2.4° longitude by 0.6° latitude. The turbulence model designed by Chen et al. (1994) consists of a Kraus and Turner (1967) mixed layer model and a Price (1986) dynamical instability model. Heat flux is parameterized by the Seager et al. (1988) bulk formulation where heat flux depends on multiple atmospheric quantities (temperature, clouds, relative humidity, and wind speed). A more detailed

description of this particular implementation of the Gent-Cane model is given in Perez et al. (2005) and references therein.

3.4 Wind and Data Products

Various wind products are used to force the Gent-Cane model in this sensitivity study. The Florida State University (FSU) wind analyses (Legler and O'Brien 1988) and European Centre for Medium-Range Weather Forecasts (ECMWF) global wind analyses (ECMWF 1994) were chosen to extend the 1997/1998 El Niño study of Hackert et al. (2001) to La Niña wind conditions. The Hackert et al. (2001) study focused on model means and variances over the three year period from January 1996 to December 1998. In this La Niña study, the focus is on the cold tongue response on time scales ranging from TIW periods of 20 to 40 days (e.g., Qiao and Weisberg 1995) to the annual cycle. The third wind product was obtained from the SeaWinds scatterometer aboard the QuikSCAT satellite (Chelton and Freilich 2005) which was launched June 19, 1999. Fortunately, the QuikSCAT satellite was operational during a significant portion of the sustained La Niña conditions that commenced in the summer 1998 and terminated in the spring of 2001.

FSU monthly mean pseudostress is available on a 2° x 2° grid from January 1960 to present. The ECMWF monthly mean wind stress was binned onto a 1° x 1° grid and is available from July 1985 to the present. The QuikSCAT monthly mean wind stress was also binned onto a 1° x 1° grid and is available from August 1999 to the present. A 10° zonal loess smoother (Schlax and Chelton 1992), which has a half-power filter cutoff analogous to that of a 5° zonal block average, was applied to the QuikSCAT winds. To generate a common La Niña wind record only ECMWF,

QuikSCAT, and FSU monthly mean wind stress fields from the 2 year time period beginning in August 1999 and ending July 2001 are used.

3.4.1 Comparison of Wind Features. The three mean wind stress fields during the two year period August 1999 to July 2001 reproduce well-known tropical Pacific wind features such as the northeast and southeast trade winds and the intertropical convergence zone (ITCZ; Figure 15). The ECMWF and QuikSCAT products are also able to resolve features like the wind jets through gaps in the Sierra Madres off of the southwest coast of Mexico. Both QuikSCAT and FSU have stronger wind stress magnitude than ECMWF in the central Pacific band between 10°N and 20°N and the eastern Pacific band between 10°S and 20°S. This bias in the ECMWF wind stress magnitude is due to a systematic low bias of about $0.5\ m\ s^{-1}$ in the ECMWF $10-m$ wind fields (Chelton and Freilich 2005). Chelton and Freilich (2005) estimate that this bias could lead to a wind stress magnitude bias of $10\% - 20\%$. Note the presence of spuriously low FSU wind stress in the eastern and western portions of the equatorial waveguide (Figure 15). This anomalous wind stress banding yields artificial wind stress curls and divergences in the central equatorial Pacific (Figure 16).

All three wind products have high variability over the ITCZ and in the western Pacific between 15°N and 30°N (Figure 15). The variability over the ITCZ is strongest in the QuikSCAT observations. The spatial pattern of the ECMWF variability is very similar to that of QuikSCAT, albeit with weaker magnitudes. FSU produces patches of anomalously high variability in the southern Pacific (east of the dateline between 15°S to 30°S), possibly due to undersampling.

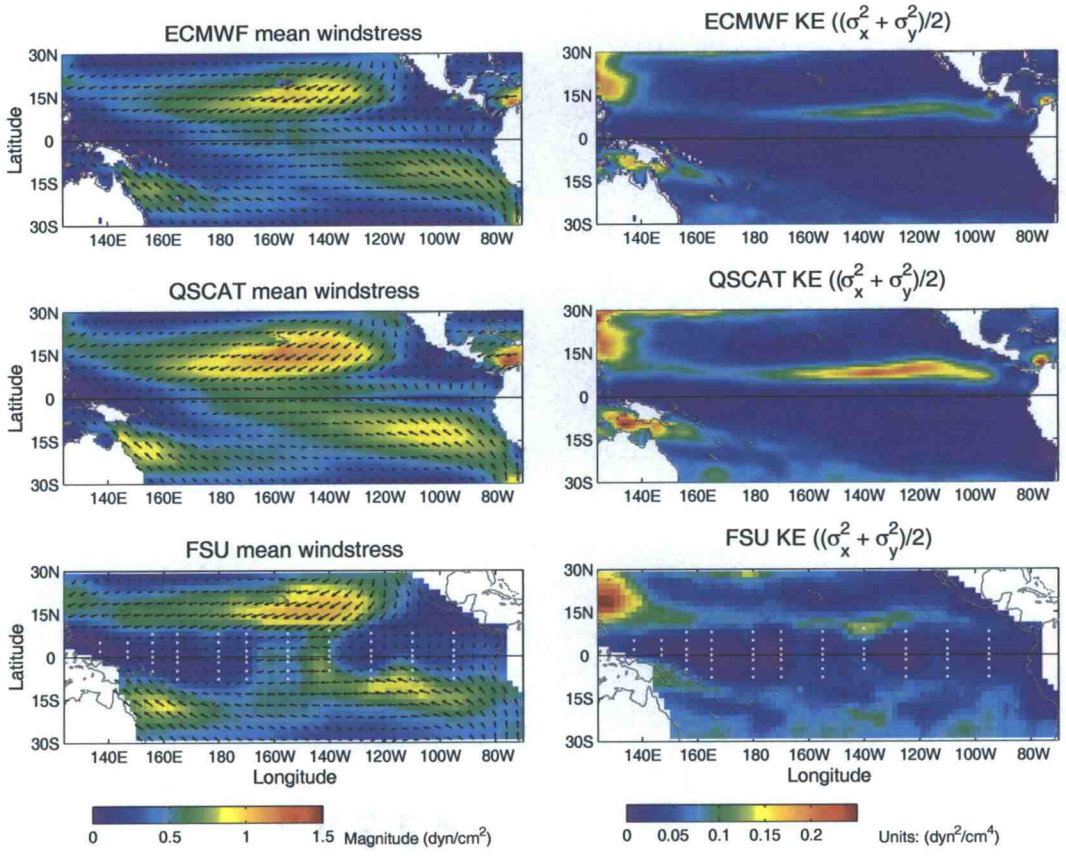

Figure 15. Mean (left panels) and kinetic energy of the variance (right panels) of the ECMWF (top), QuikSCAT (center), and FSU (bottom) wind stress during August 1999 - July 2001. The location of the TAO moorings are superimposed on the FSU panels.

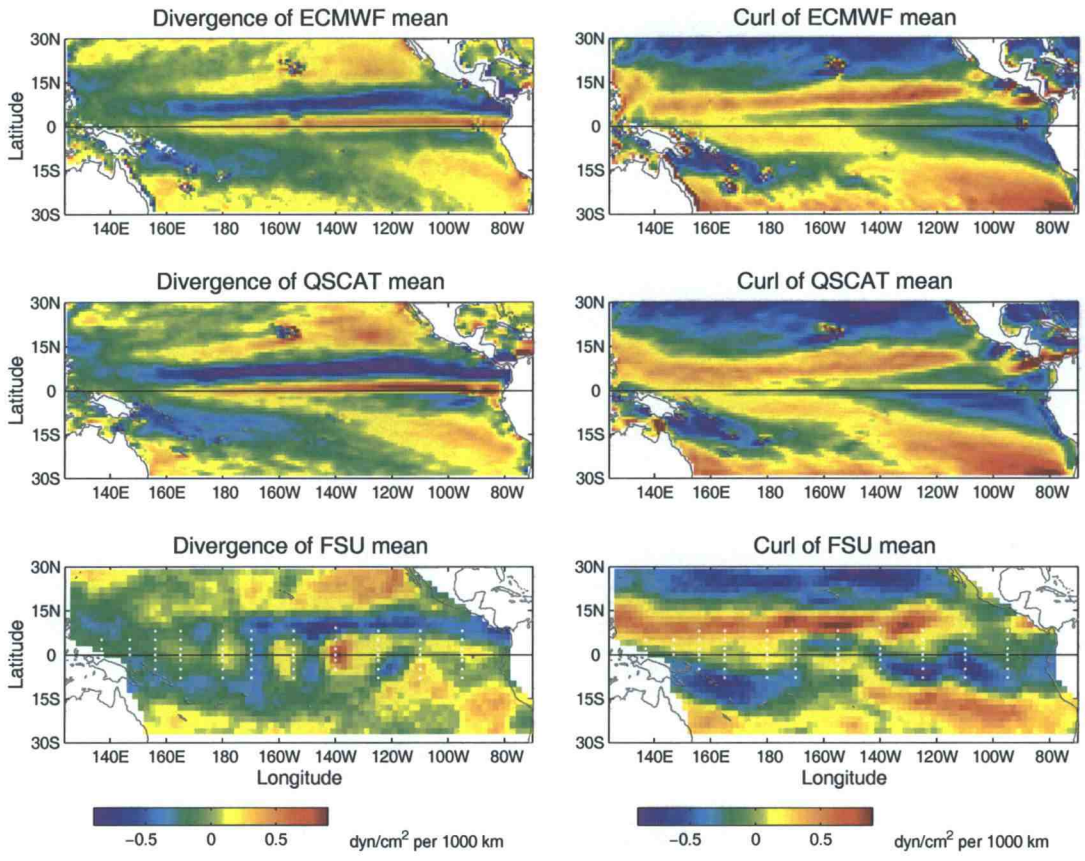

Figure 16. Divergence (left panels) and curl (right panels) of the ECMWF (top), QuikSCAT (center), and FSU (bottom) mean wind stress during August 1999 - July 2001. The location of the TAO moorings are superimposed on the FSU panels.

The divergence and curl of the mean wind stress during the same two year period are shown in Figure 16. All three wind products show negative wind stress divergence over the ITCZ and positive wind stress divergence just north of the equator, however the magnitude of these divergences is largest in the QuikSCAT observations and smallest in the FSU winds. QuikSCAT also shows a narrow band of positive wind stress curl just north of the equator, which is weakly resolved by the ECMWF product and absent in the FSU product, consistent with the findings of Kessler et al. (2003) and Chelton (2005). FSU also has artificial curls and

divergences which occasionally align with the longitudes of Tropical Atmosphere Ocean (TAO; Hayes et al. 1991; McPhaden 1993) project moorings (lower panels in Figure 16). TAO wind measurements were incorporated into the FSU analyses and the artificial curls and divergences likely relate to the subjective interpolation procedure used to map the wind stress fields. This problem has been rectified in the new objectively interpolated version of the FSU winds (Bourassa et al. 2001).

3.4.2 Wind Sensitivity Experiment and Observations. To investigate the maximum sensitivity of the simulated cold tongue to different wind forcing, we fit a seasonal cycle with 4 harmonics of the annual cycle, to generate "seasonal cycles" of ECMWF, QuikSCAT, and FSU winds during the La Niña conditions of August 1999 - July 2001. This seasonal cycle captures on average over 70% (QuikSCAT, ECMWF) and 60% (FSU) of the variability present in each data set. In each simulation, the model spins-up for 11 years to a converged La Niña state and three-day averages from year 12 to 16 are analyzed in detail. The fourteenth year is considered to represent the La Niña condition seasonal cycle and bracketing years are used to generate continuous $x - t$ diagrams and to avoid losing data when temporal filters are applied. The ability of the model runs to simulate the low-frequency evolution of the cold tongue, TIWs, and annual equatorial Rossby waves is investigated.

Model results will be compared to measurements of the 20°C isotherm depth estimated from TAO temperature profiles and SST from the Tropical Rainfall Measuring Mission Microwave Imager (TMI; Kummerow et al. 1998; Chelton et al. 2001) to analyze the sensitivity of the cold tongue evolution to the different wind forcing. Surface currents obtained from the NOAA Ocean Surface Current Analyses

- Real time (OSCAR; Lagerloef et al. 1999; Bonjean and Lagerloef 2002) will allow us to evaluate the ECS seasonal cycle. Merged altimetric sea level anomalies (MSLA) produced by Ssalto/Duacs as part of the Environment and Climate EU Enact project (EVK2-CT2001-00117) and distributed by the Archiving, Validation and Interpretation of Satellite Oceanographic data (AVISO) program, with support from the French Space Agency are used along with the TMI and TAO data to examine the model TIWs. The TOPEX/Poseidon sea surface height (SSH) estimates of annual equatorial Rossby wave amplitude, phase, and westward phase speed from Perez et al. (2005) are reproduced here to evaluate the sensitivity of the model Rossby waves to wind forcing.

The 20°C isotherm depths are daily averaged fields produced by TAO by linearly interpolating temperature profiles with depth. Small gaps in coverage (on the order of days) were filled in by spatial-temporal interpolation for the $x-t$ diagrams. Daily averages of TMI SST were obtained along select latitudes at $\Delta x = 0.25°$ intervals (for the $x-t$ diagrams, every fourth data point in space and every third data point in time are plotted). The OSCAR surface zonal velocities were obtained as filtered, five-day average fields on a 1° x 1° grid. Although the OSCAR product is an amalgam of model and observations, the surface zonal velocities are treated as data to enhance the suite of model-data comparisons. The AVISO MSLA is available as 7-day averages on a 0.33° x 0.33° grid, and every third data point in space is used for $x-t$ diagrams.

3.5 Sensitivity of the Gent-Cane Model to Wind Forcing

3.5.1 Low-Frequency Cold Tongue Evolution. In this section, the low-frequency cold tongue evolution, as marked by the model surface mixed layer temperature, 20°C isotherm depth, and surface zonal currents, is compared for the three wind-driven model runs between the date line and 74°W.

In Figure 17, select monthly means (January, April, July, and October) of surface mixed layer temperatures are compared for the ECMWF, QuikSCAT, and FSU driven model runs. The differences between the QuikSCAT surface mixed layer temperatures and those of ECMWF and FSU are plotted in Figure 18. For all three model runs, the monthly mean surface layer temperatures demonstrate the decline of the cold tongue in April, its intensification in July, its westward penetration in October, and its persistence thereafter until the following spring (Figure 17). The spatial structures of the QuikSCAT and ECMWF driven monthly mean temperatures are very similar, although the QuikSCAT cold tongue penetrates farther into the central Pacific (Figure 17) and the QuikSCAT temperatures tend to be colder in the equatorial waveguide (Figure 18). This difference may relate to the low bias of the ECMWF wind stresses discussed in Section 3.4. The FSU driven monthly mean surface mixed layer temperatures are significantly warmer than those of QuikSCAT in the waveguide (Figure 18), due to weaker cold tongue penetration (Figure 17). Some of the most pronounced QuikSCAT-FSU differences are coincident with TAO mooring locations (Figure 18), which may relate to the sampling issues discussed in Section 3.4. Outside of the equatorial band (latitudes greater than 10°), the differences in monthly mean surface mixed layer temperatures between QuikSCAT-ECMWF and QuikSCAT-FSU are small (Figure 18).

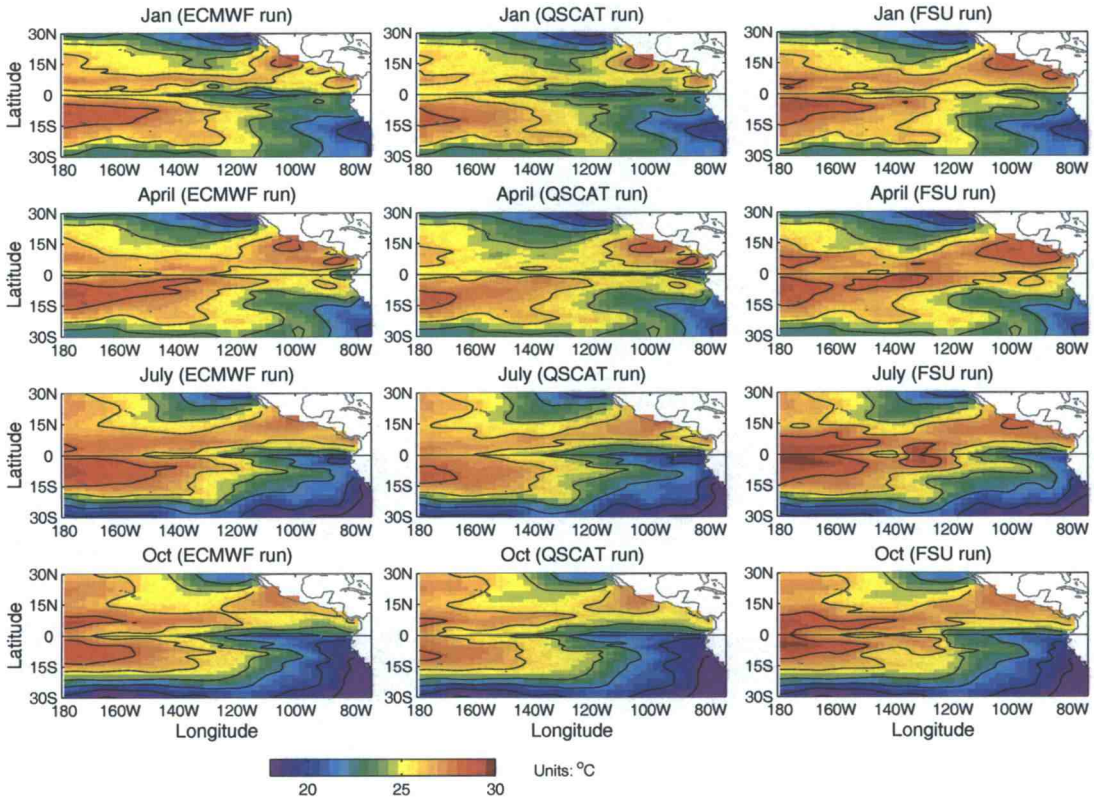

Figure 17. Select monthly means of the surface mixed layer temperature for the Gent-Cane simulations forced by seasonal ECMWF (left panels), QuikSCAT (center panels), and FSU (right panels) wind stress.

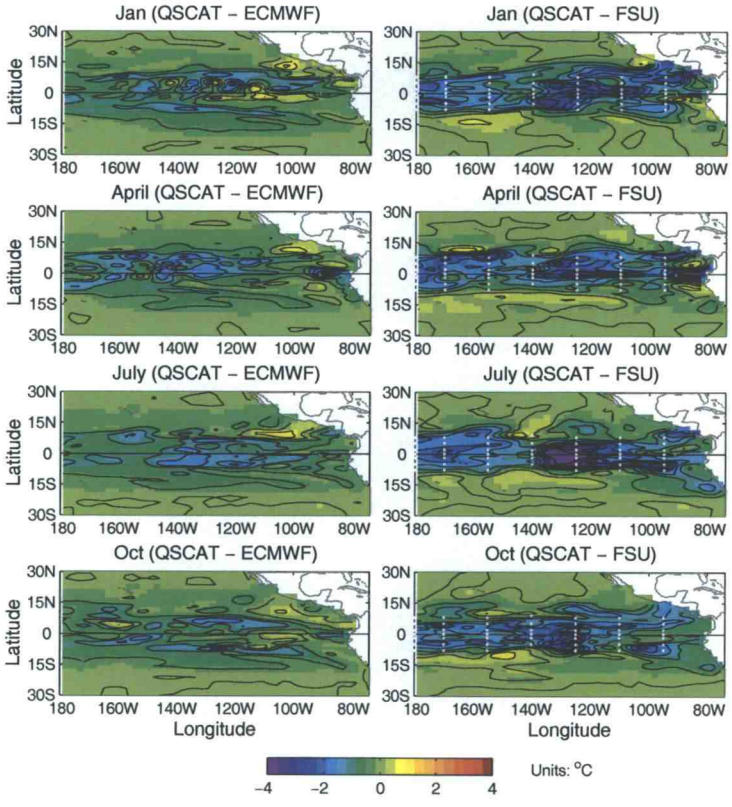

Figure 18. Select monthly means of the difference between the QuikSCAT driven surface mixed layer temperature in Figure 17 and those of ECWMF (left panels) and FSU (right panels).

Another quantity which can be used to describe the cold tongue evolution is the monthly mean 20°C isotherm depth (Figure 19). Since the model has vertically homogenous temperatures in each layer, the depth of the midpoint of each layer is computed and temperatures are linearly interpolated between layers to find the approximate 20°C isotherm depth. The isotherm depths were set to zero (identified by purple shading in Figure 19) whenever the surface mixed layer temperatures were cooler than 20°C. The QuikSCAT and ECMWF driven model runs produce very similar monthly mean 20°C isotherm depth patterns (Figure 19); however, there are significant differences along the boundaries of the cold tongue (Figure 20). The

20°C isotherm outcrops further west in the QuikSCAT driven run and the 20°C isotherm is deeper in the central Pacific between 5°N and 10°N. There are dramatic differences between the QuikSCAT and FSU monthly mean 20°C isotherm depths (Figures 19 and 20). Specifically, the QuikSCAT 20°C isotherm is deeper than that of FSU in the central Pacific between 10°S - 5°S and 5°N - 10°N, and is in contrast shallower in the cold tongue (Figure 20).

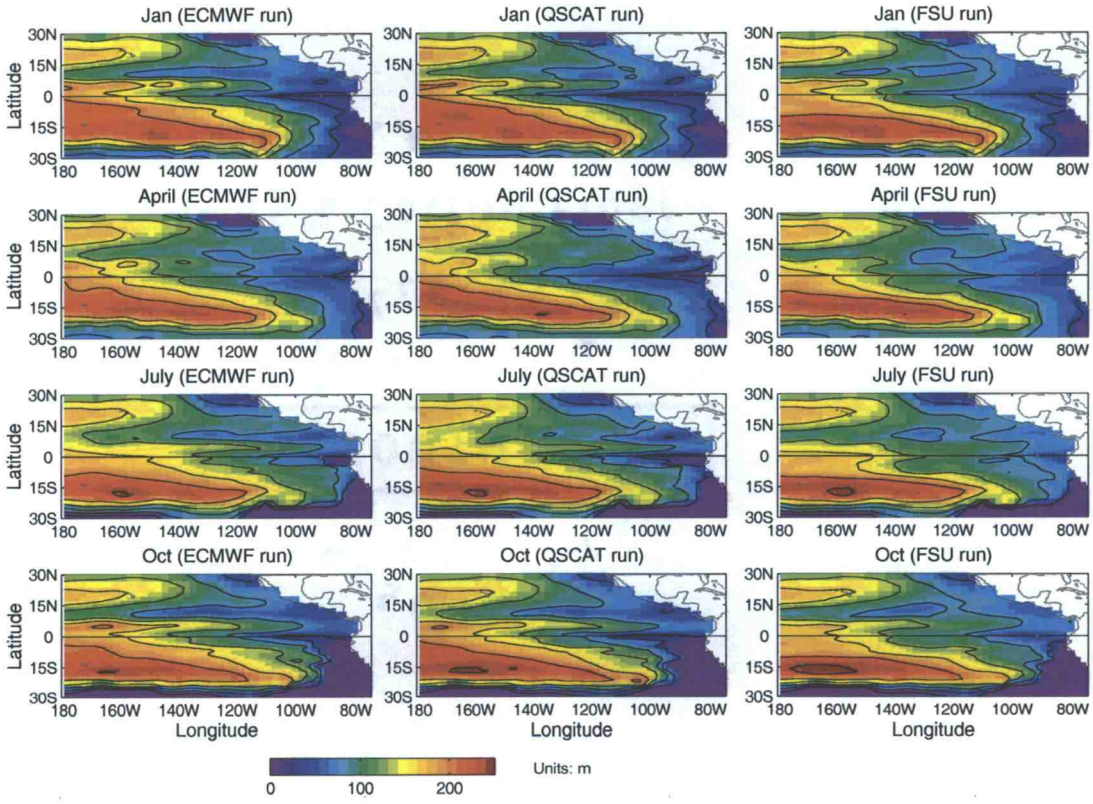

Figure 19. Select monthly means of the 20°C isotherm depth for the Gent-Cane simulations forced by seasonal ECMWF (left panels), QuikSCAT (center panels), and FSU (right panels) wind stress. Purple shading indicates the surface mixed layer temperature is colder than 20°C.

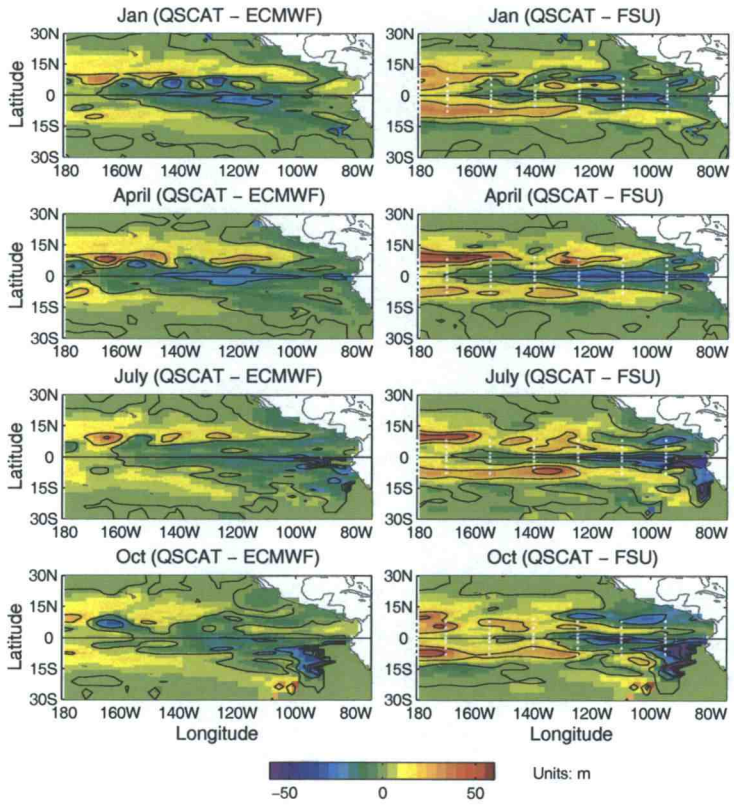

Figure 20. Select monthly means of the difference between the QuikSCAT driven 20°C isotherm depth in Figure 19 and those of ECWMF (left panels) and FSU (right panels).

To develop a sense of the seasonal evolution of the ECS under varied wind forcing, the monthly mean surface zonal velocity between 15°S and 15°N are examined (Figure 21). As before, the differences between the QuikSCAT driven monthly mean surface zonal velocities and those of ECMWF and FSU are provided in Figure 22. These currents are difficult to interpret as the monthly means are somewhat noisy from the effects of TIWs with periods between 20 and 40 days. In all of the model runs, the well-known equatorial surface currents, the NECC, both branches of the SEC, and the South Equatorial Countercurrent (SECC) are present (Figure 21). The EUC surfaces during April and July when the cold tongue

subsides. The surfacing of the EUC is not an uncommon feature in this model which has no vertical shear within a given layer (Chen et al. 1994; Perez et al. 2005). Moreover, the surfacing has been observed before in TAO ADCP transects in the spring and summer months and during La Niña events (Johnson et al. 2002). On average, the QuikSCAT driven model run has weaker countercurrents in the central Pacific than do the ECMWF and FSU model runs (Figure 21) consistent with weaker meridional gradients in the 20°C isotherm depths (not shown). Large differences between QuikSCAT and ECMWF surface zonal velocities in January also seem to be associated with the TIWs on the northern flank of the cold tongue and reflect the difference in the phasing of the ECMWF and QuikSCAT TIWs (Figure 22). Note these QuikSCAT-ECMWF phasing differences are present in the surface layer temperatures in Figure 18 and the 20°C isotherm depths in Figure 20. The differences in the QuikSCAT and FSU driven monthly mean surface currents have broad zonal length scales in the equatorial waveguide (e.g., zonal bands of alternating positive and negative differences between 10°S and 10°N in the July panel of Figure 22).

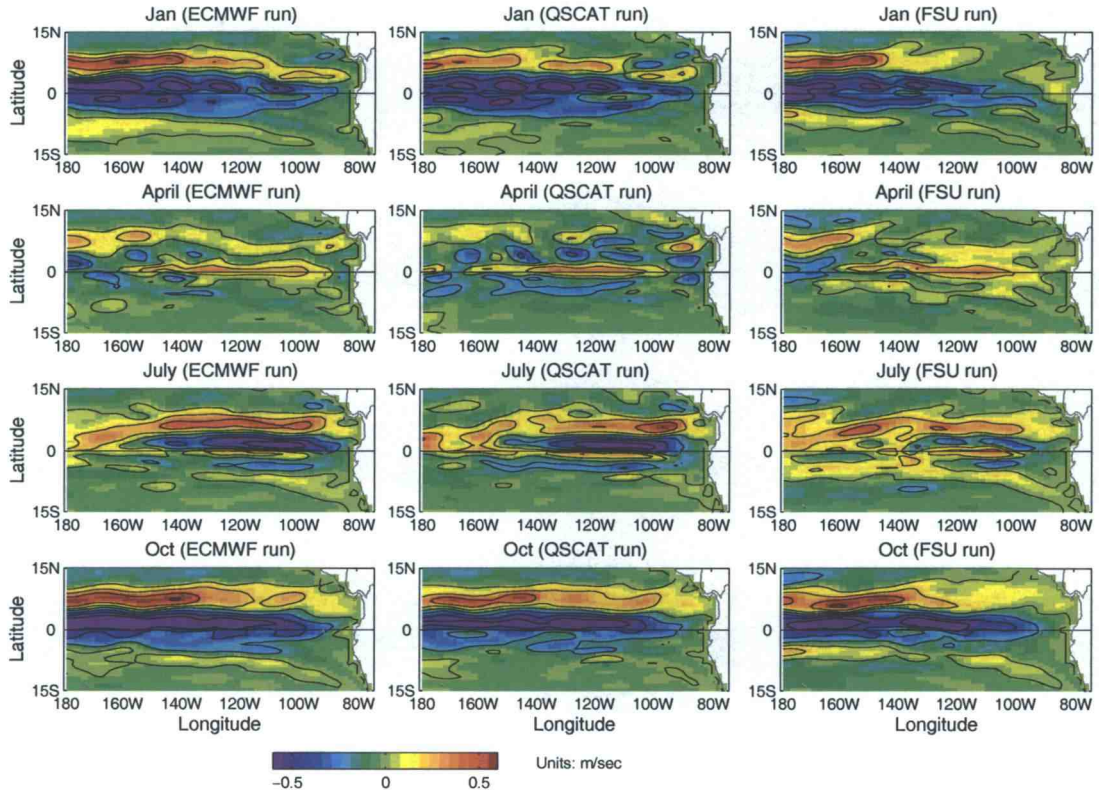

Figure 21. Select monthly means of the surface zonal velocity for the Gent-Cane simulations forced by seasonal ECMWF (left panels), QuikSCAT (center panels), and FSU (right panels) wind stress.

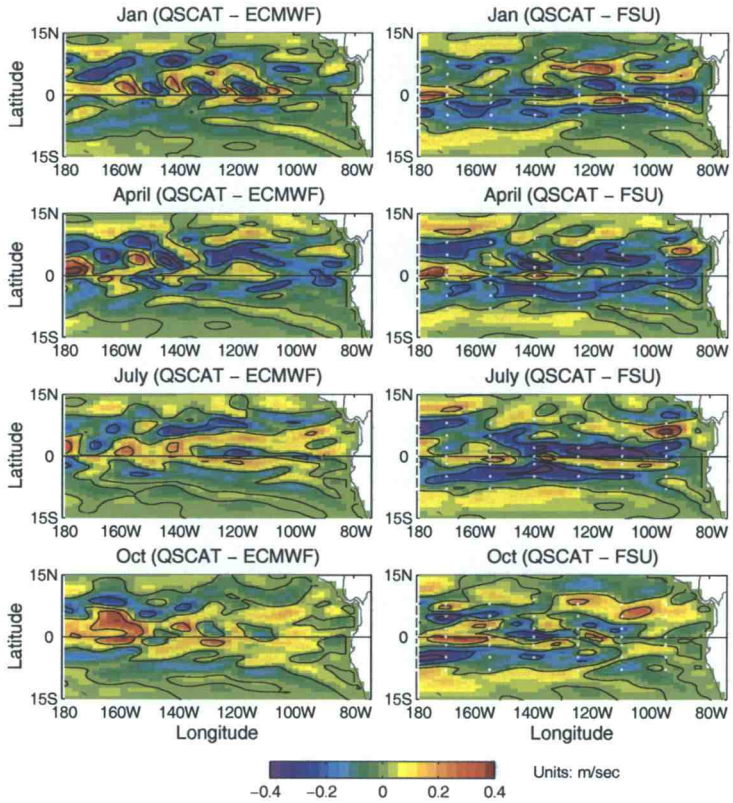

Figure 22. Select monthly means of the difference between the QuikSCAT driven surface zonal velocity in Figure 21 and those of ECWMF (left panels) and FSU (right panels).

The annual evolution of the model cold tongue is evaluated by plotting $x - t$ diagrams of the simulated low-frequency (30-day low-pass filtered) surface mixed layer temperatures, 20°C isotherm depths, and surface zonal currents for years 14 and 15 along the model latitude nearest the equator, 0.3°N (Figures 23, 24, and 25). The simulated cold tongue evolution is compared to a variety of measurements along the equator from June 1999 to May 2001 (see Section 3.4.2). These measurements were obtained during La Niña conditions and should compare well with our simulated La Niña condition seasonal cycle.

Comparison of model surface mixed layer temperature with TMI SST is at most qualitative since the model mixed layer can span tens of meters and TMI SST is a measurement of skin temperature. We can nonetheless gain insight by comparing the patterns (Figure 23). The QuikSCAT and ECMWF driven model runs do a better job of matching the spatial structure and time evolution of the observed cold tongue surface temperature. Both runs are colder on average than the observed surface temperature during the three months when the cold tongue subsides (March to May). Clearly there is a model cold bias, but it is difficult to quantify this bias since the TMI skin temperature is not easily related to the surface mixed layer temperature. This cold tongue cold bias, documented in various Gent-Cane modeling studies, presents a serious challenge to tropical Pacific assimilation studies (as discussed in Perez and Miller 2005). The surface mixed layer temperature for the FSU driven run has the appropriate range of cold tongue temperatures when the cold tongue subsides, but it is too warm when the cold tongue is present (June to February). The FSU driven run also has anomalously cold SSTs between 150°W and 140°W adjacent to anomalously warm SSTs between 140°W and 120°W. These features persist throughout the year and are coincident with the anomalous structures found in the FSU wind stress fields (Figure 15) and the divergences and curls (Figure 16) in the region.

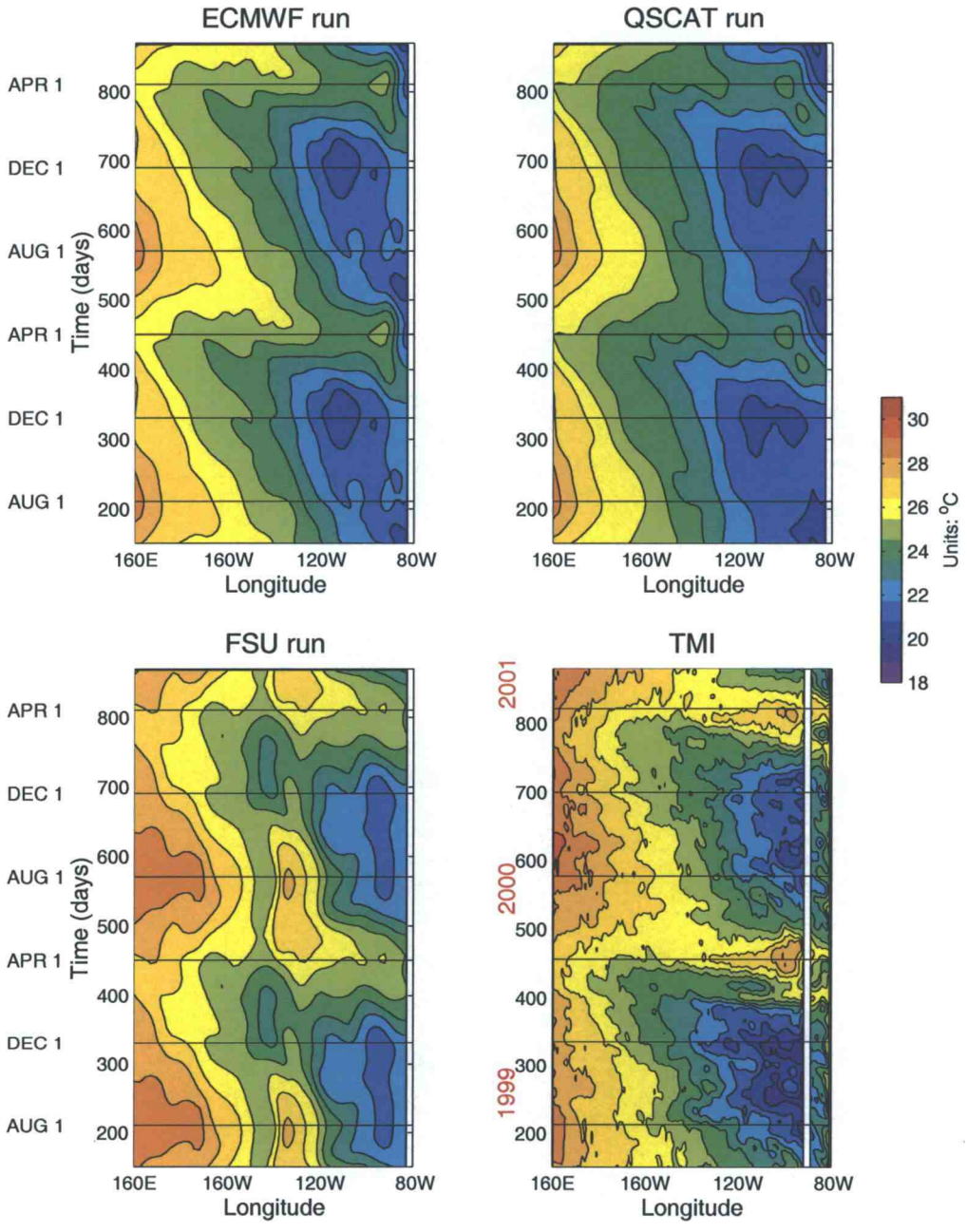

Figure 23. 30-day low-pass filtered Gent-Cane surface mixed layer temperature along 0.3°N forced by seasonal ECMWF (upper left panel), QuikSCAT (upper right panel), and FSU (lower left panel) wind stress. Low-pass filtered TMI SST along 0° from June 1999 - May 2001 is plotted in the lower right panel.

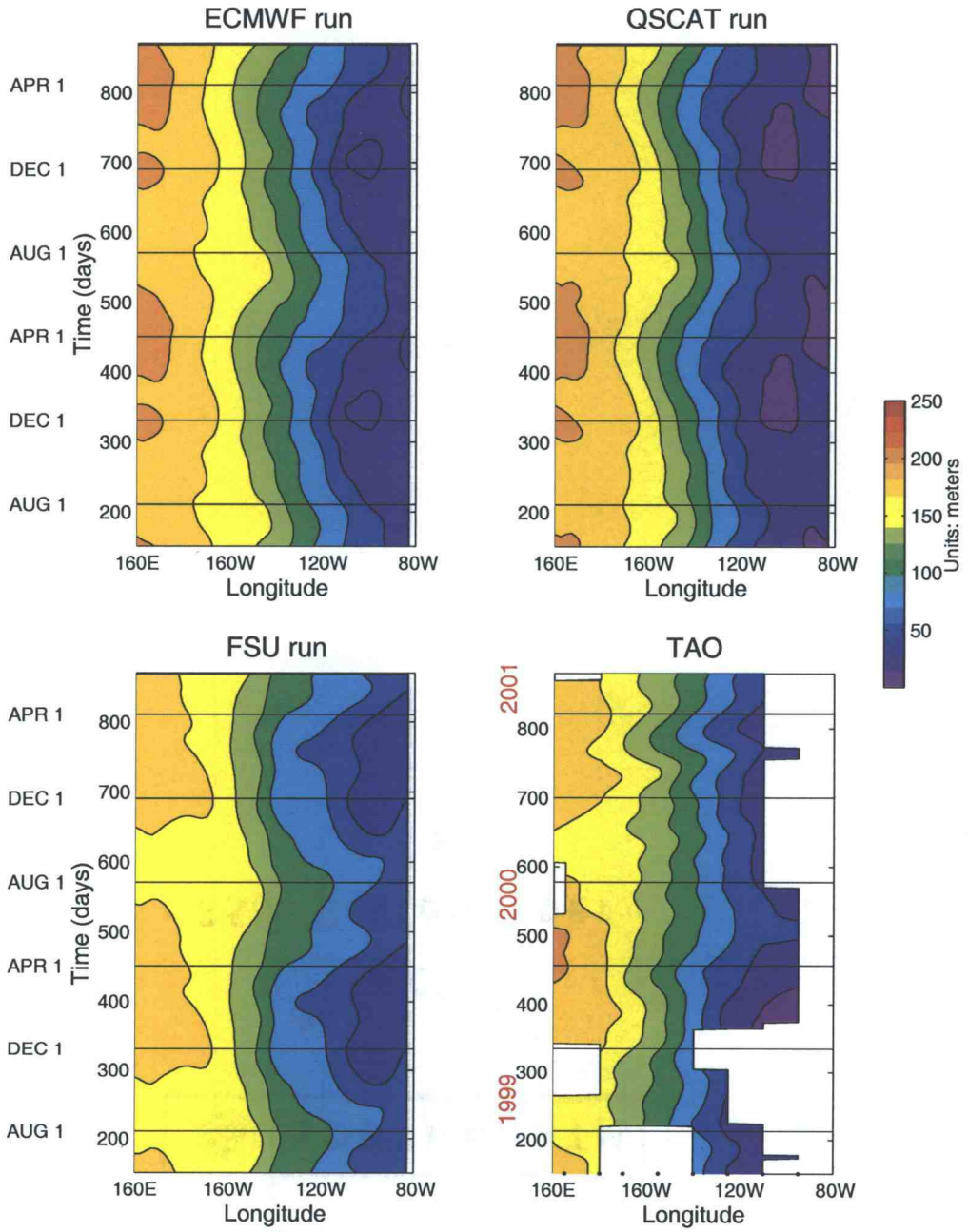

Figure 24. 30-day low-pass filtered Gent-Cane 20°C isotherm depth along 0.3°N forced by seasonal ECMWF (upper left panel), QuikSCAT (upper right panel), and FSU (lower left panel) wind stress. Low-pass filtered TAO 20°C isotherm depth along 0° from June 1999 - May 2001 is plotted in the lower right panel.

Comparison of the low-frequency evolution of the 20°C isotherm depth with TAO estimates along the equator provides a means to evaluate the subsurface thermal structure (Figure 24). Here all of the model runs look fairly similar, although the east-west isotherm depth gradient in the FSU driven run is too weak with 20°C isotherms too shallow near 160°E and too deep in the eastern Pacific. As shown in Figures 19 and 20, the 20°C isotherm depth outcrops most in the QuikSCAT driven run. Unfortunately, we cannot validate this as the TAO array ends at 95°W and there are gaps in the TAO data records in the eastern Pacific during this time period. Comparison of the August 1999 - July 2001 mean 20°C isotherm depth reveals significant model-TAO biases of 15.2 (ECMWF), 15.6 (QuikSCAT), and -4.6 m (FSU) along 160°E and 26.6 (ECMWF), 7.9 (QuikSCAT), and 14.7 m (FSU) along 140°W.

Surface zonal velocity along the equator can give insight into the low-frequency evolution of the SEC and instances when the EUC surfaces (Figure 25). The observed and simulated surface zonal currents demonstrate clear westward propagation. During the spring and summer, the EUC surfaces in both the model runs and the OSCAR data as marked by a change in the sign of zonal velocity around day 500 and 850. The FSU surface zonal velocities are generally weaker than those of ECMWF and QuikSCAT and have a minimum near 140°W which is coincident with the anomalous surface mixed layer temperature features noted in Figure 23.

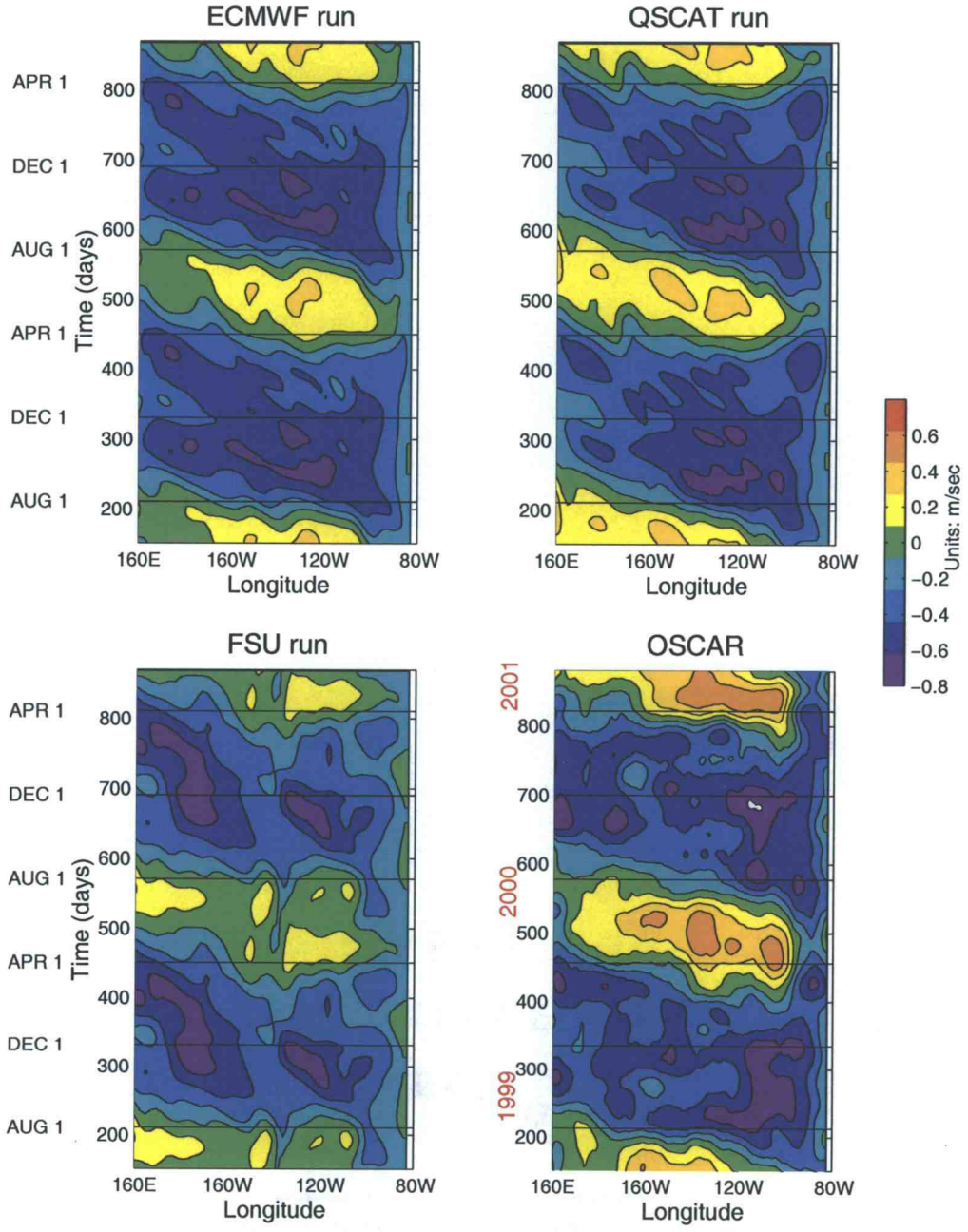

Figure 25. 30-day low-pass filtered Gent-Cane surface zonal velocity along 0.3°N forced by seasonal ECMWF (upper left panel), QuikSCAT (upper right panel), and FSU (lower left panel) wind stress. Low-pass filtered OSCAR surface zonal velocity along 0.5°N from June 1999 - May 2001 is plotted in the lower right panel.

3.5.2 High-Frequency Cold Tongue Evolution. Despite the coarse resolution of this particular implementation of the Gent-Cane model, all three simulations produce TIW-like features. As argued by Lyman et al. (2005b), TIWs can be viewed as two different instabilities, one with near equator signals and period of about 17 days, which is similar to a Yanai wave, and the other near 5°N with period of about 33 days, which is an unstable first merdional mode Rossby wave. The annual evolution of the model TIWs is therefore evaluated near the equator by plotting $x - t$ diagrams of the simulated high-frequency (50-day high-pass filtered) surface mixed layer temperature for year 14 and 15 of the model runs along 1.9°N and TMI SST along 2°N (Figure 26). In addition, the simulated high-frequency TIW evolution is examined farther north by looking at 20°C isotherm depths (Figure 27) and SSH anomalies (SSHA; Figure 28) near 5°N and comparing with TAO isotherm depths and AVISO MSLA. The data were filtered in similar manner to the model output, the only difference being the application of a low-pass four-day filter to the TMI SST to remove some of the noise.

Overall, the strength of the near equator TIW signature is much stronger in the TMI SST observations and dominated by shorter wave periods (ca. 28-32 days) than the simulated mixed layer temperature which has wave periods on the order of 35 to 40 days (Figure 26). Our ability to simulate TIWs correctly is likely limited by the coarse resolution chosen for this study (Kessler et al. 1998; Jochum and Murtugudde 2004). The observed TIW season commences around June, whereas the model TIW season lags this by approximately one month. The duration of the TIW season is apparently too long for the model runs forced by ECMWF and QuikSCAT (until April) when compared with TMI observations (until February). Both the ECMWF

and QuikSCAT surface mixed layer temperatures produce a pattern of TIW onset which extends eastward to 90°W and then shifts westward between 120°W and 115°W. The observed TIWs exhibit a similar pattern with a westward shift to 100°W rather than 120°W. The FSU driven TIW SST signal does not intensify until 130°W and looks the least like the observed signal.

Farther north, the TIW signal is present in the 20°C isotherm depth (Figure 27) and SSHA (Figure 28) near 5°N. All of the model simulations demonstrate clear westward propagation of the waves (Figures 27 and 28). Although the periodicity of the model waves better matches the observed periodicity farther north, westward propagation is less evident in the available observations of TAO 20°C isotherm depth. As discussed in Perez and Miller (2005), the TAO zonal spacing of 15° is too coarse to detect the westward propagation of the TIWs. The westward propagation of TIWs, however, is clear in AVISO MSLA near 5°N (Figure 28) and agrees well with the ECMWF and QuikSCAT SSHA. The FSU TIW signal is again weak compared to those of ECMWF and QuikSCAT (Figures 27 and 28).

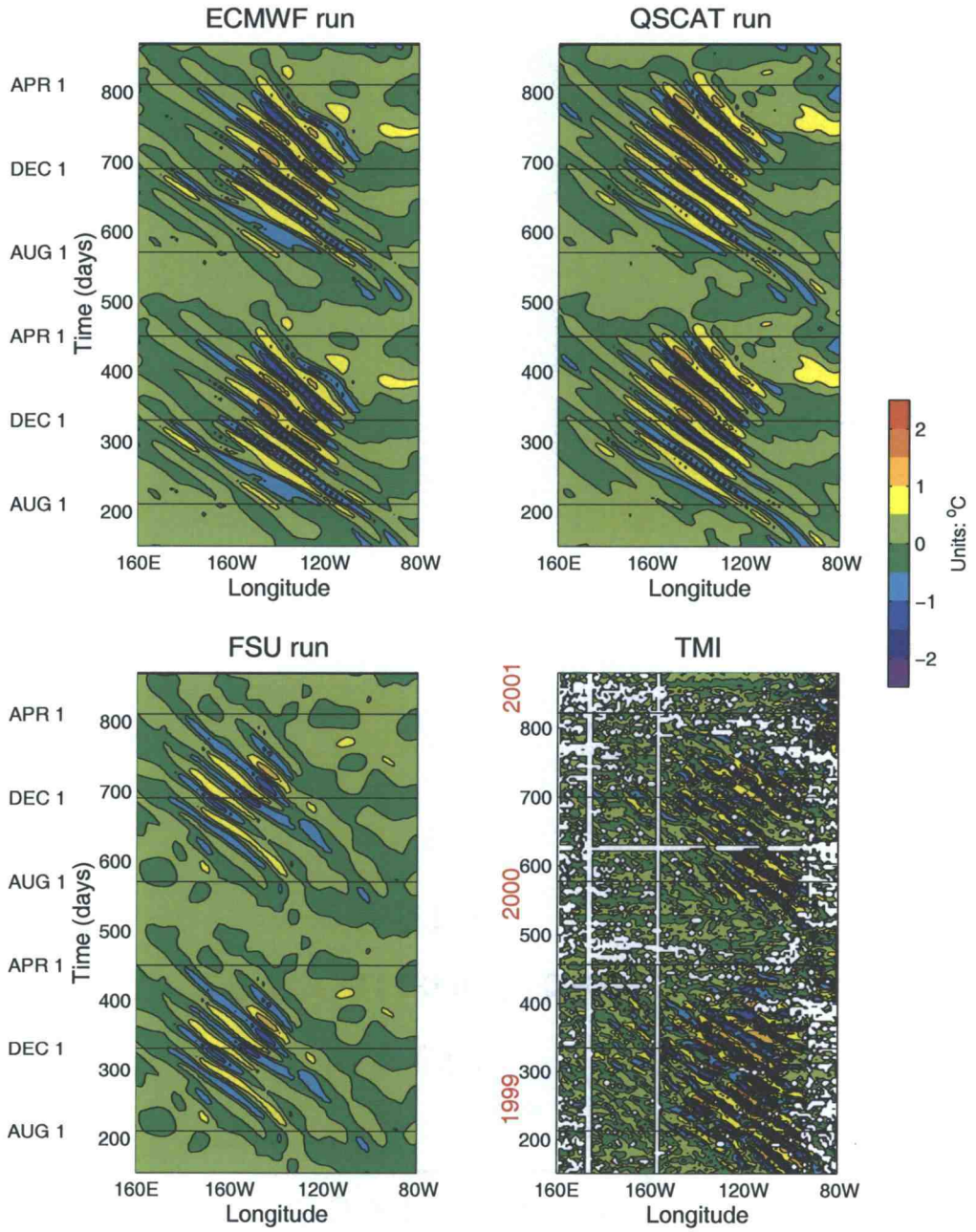

Figure 26. 50-day high-pass filtered Gent-Cane surface mixed layer temperature along 1.9°N forced by seasonal ECMWF (upper left panel), QuikSCAT (upper right panel), and FSU (lower left panel) wind stress. High-pass filtered TMI SST along 2.0°N from June 1999 - May 2001 is plotted in the lower right panel.

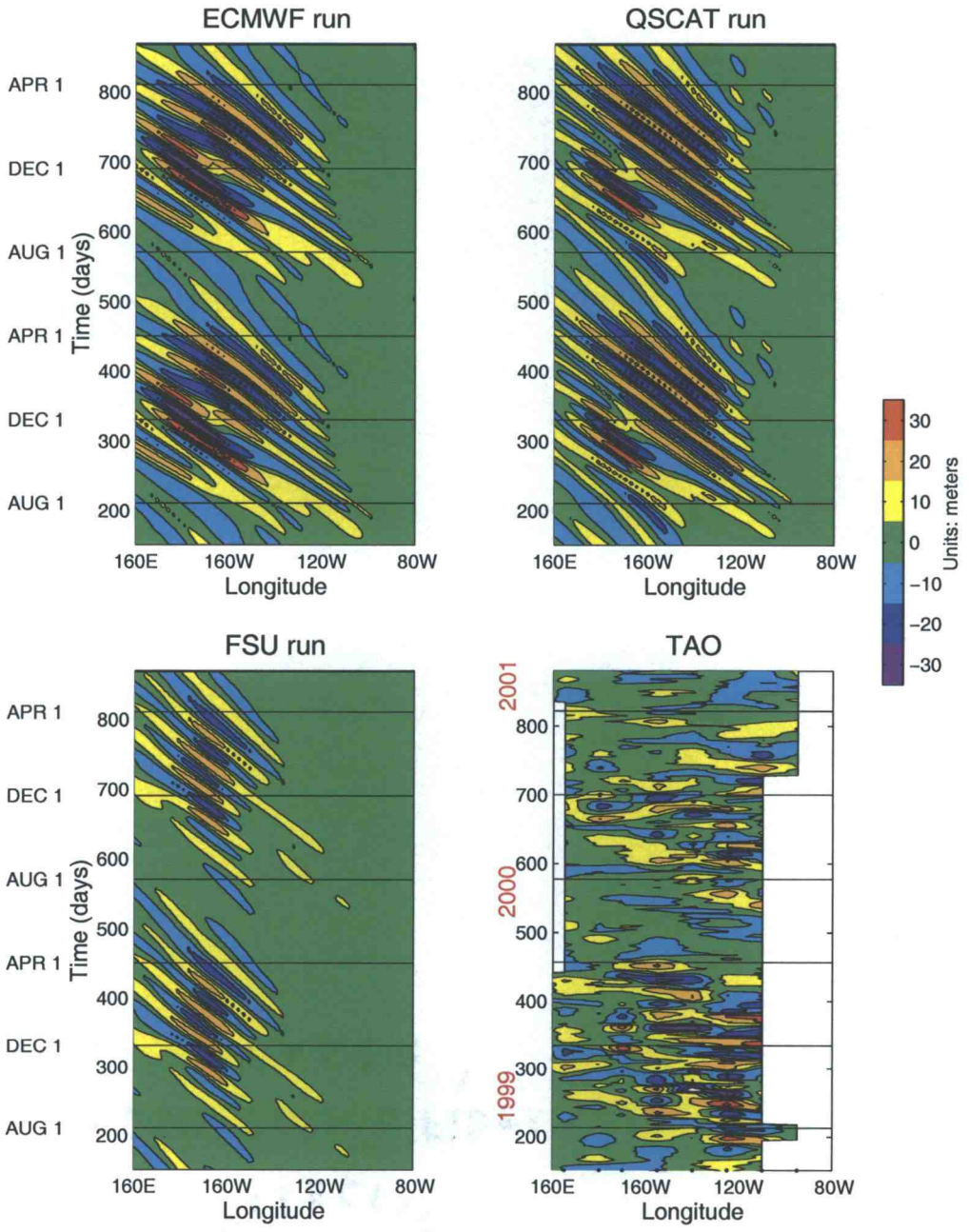

Figure 27. 50-day high-pass filtered Gent-Cane 20°C isotherm depth along 5.2°N forced by seasonal ECMWF (upper left panel), QuikSCAT (upper right panel), and FSU (lower left panel) wind stress. High-pass filtered TAO 20°C isotherm depth along 5.0°N from June 1999 - May 2001 is plotted in the lower right panel.

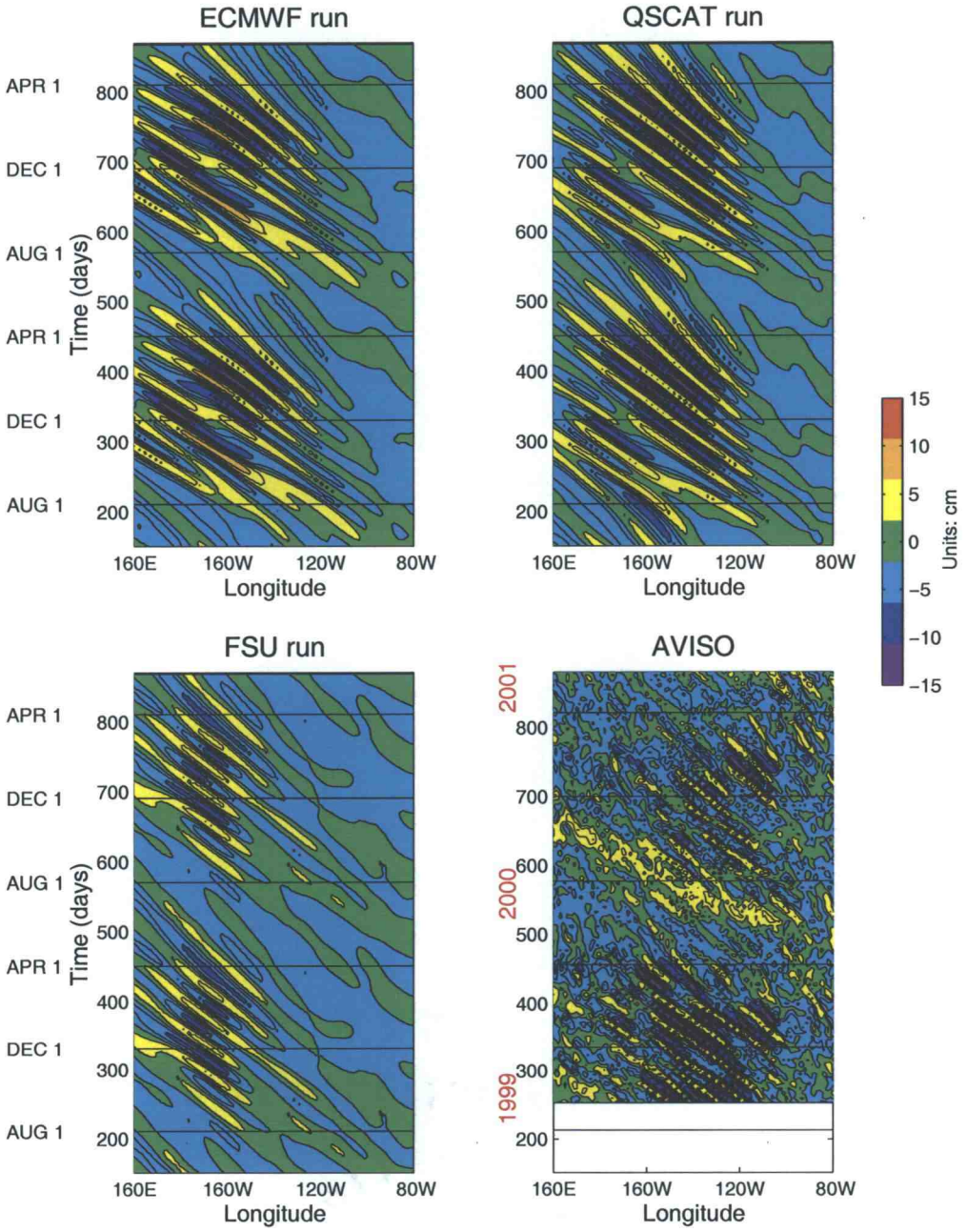

Figure 28. 50-day high-pass filtered Gent-Cane SSH along 5.2°N forced by seasonal ECMWF (upper left panel), QuikSCAT (upper right panel), and FSU (lower left panel) wind stress. High-pass filtered AVISO merged sea level anomalies along 4.9°N from August 1999 - May 2001 is plotted in the lower right panel.

To address the question of why the TIWs generated by seasonal QuikSCAT and ECMWF wind stress forcing are more energetic and appear at the correct longitudes, whereas the TIWs generated by FSU winds do not, the meridional and vertical structure of the zonal velocity generated by these three model runs are described. Figure 29 compares y-z slices of November monthly mean zonal currents (November is near the peak of the TIW season) along 140°W and 120°W. Along the 140°W transect, the three runs have EUC, SECN, and NECC of comparable strength. Therefore, all three model runs have comparable meridional shear in the zonal currents on the northern flank of the cold tongue at this longitude. Farther east along 120°W, the model SECN and NECC generated with QuikSCAT and ECMWF wind forcing are stronger than those generated by FSU wind stress forcing. Consequently, the merdional shear of the FSU driven zonal currents at 5°N, 120°W is weaker than the QuikSCAT and ECMWF shear. Previous modeling studies (see Lyman et al. 2005a,b and references therein) indicate the importance of either the NECC-SECN background shear (Philander 1978; Cox 1980; Donohue and Wimbush 1998; Lyman et al. 2005a) or the SEC-EUC background shear (McCreary and Yu 1992) in setting up TIWs on the northern flank of the cold tongue. The weaker FSU TIWs are therefore consistent with the weak NECC-SECN meridional shear.

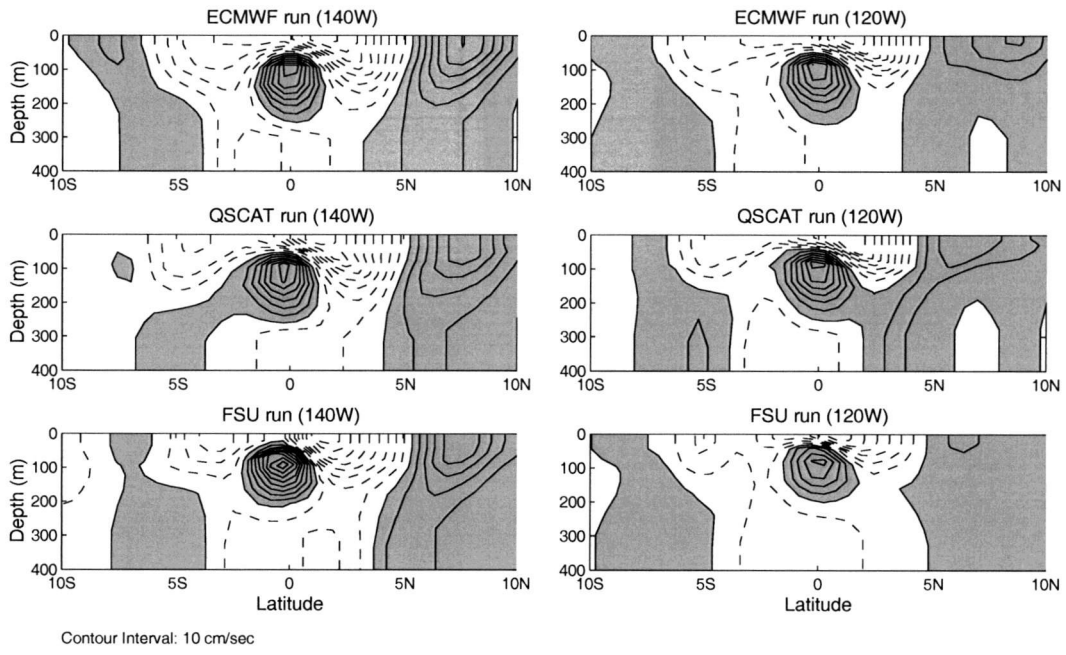

Figure 29. November mean zonal velocity for year 14 of the Gent-Cane model forced by seasonal ECMWF, QuikSCAT, and FSU wind stress along the model grid point nearest 140° (left panels) and 120°W (right panels). The gray shaded contours indicate positive or eastward zonal velocity.

Another way to analyze the variability associated with TIWs is to compute the standard deviation of 50-day high-pass filtered surface mixed layer temperatures for model year 14 (Figure 30). Both QuikSCAT and ECMWF runs have highest variability just north of the equator between 160°W and 115°W. The FSU run has high variability farther west between 170°W and 130°W and is significantly less energetic than the other two runs. Note that the equatorial asymmetry of the meridional shear present in all three model runs (Figure 29) matches the strong equatorial asymmetry in TIW variability (Figure 30).

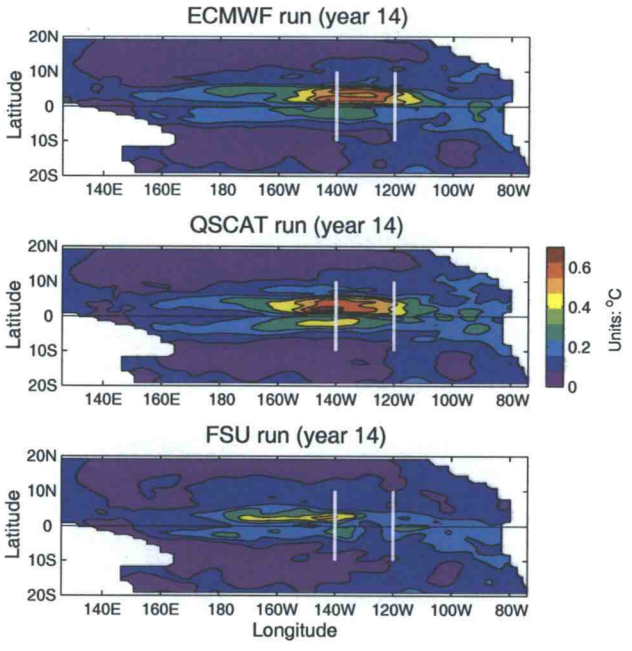

Figure 30. Variability associated with TIWs as measured by the standard deviation of 50-day high-pass filtered Gent-Cane surface mixed layer temperature driven by ECMWF (top), QuikSCAT (center), and FSU (bottom) wind stress. The transects from Figure 29 are marked by white lines.

3.5.3 Annual Rossby Waves. As described in Perez et al. (2005), this implementation of the Gent-Cane model can be used to study annual equatorial Rossby waves. SSH and thermocline depth observations of equatorial Rossby waves in the tropical Pacific have consistently found waves which are latitudinally asymmetric in amplitude and westward phase propagation (Chelton et al. 2003 and references therein). An example of this asymmetry is shown in the lower right panel of Figure 31, where the annual Rossby wave signal has been isolated in the August 1999 to July 2001 TOPEX/Poseidon SSH data from Perez et al. (2005). The observed amplitude of the northern maximum along 5.5°N is approximately 1.8 times larger than the southern maximum along 5.5°S (lower right panel of Figure 31), with

westward phase speeds 55.0 ± 14.2 and 43.3 ± 6.8 $cm\ s^{-1}$, respectively (Table 3). The processing applied to the TOPEX/Poseidon data and model SSH to isolate the annual Rossby signal is described in detail in Chelton et al. (2003) and Perez et al. (2005), respectively.

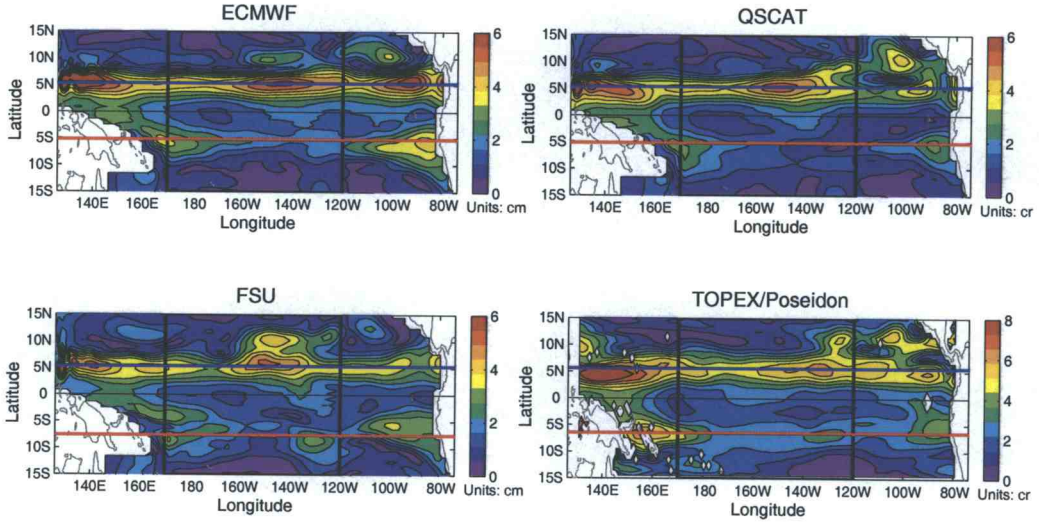

Figure 31. SSH annual Rossby wave amplitude for the Gent-Cane model forced by seasonal ECMWF (upper left), QuikSCAT (upper right), and FSU (lower left) wind stress, and TOPEX/Poseidon data (lower right). Blue and red lines indicate zonally averaged northern and southern maxima, respectively, within the box between 170°E and 120°W.

Table 3. Comparison of Rossby wave SSH amplitudes and westward phase speeds ($cm\ s^{-1}$) along latitudes identified on Figure 31 by the blue and red lines.

Wind product	Amplitude Ratio	$C_{p,S}$	$C_{p,N}$	C_p Ratio
ECMWF run	2.19	58.1 ± 3.4	62.8 ± 3.3	1.08
FSU run	1.98	42.7 ± 50.4	60.1 ± 8.0	1.41
QuikSCAT run	3.08	48.9 ± 3.4	55.4 ± 2.3	1.13
TOPEX/Poseidon	1.76	43.3 ± 6.8	55.0 ± 14.2	1.27

Here we compare the observed annual SSH signal with that of the Gent-Cane model forced by seasonal ECMWF, QuikSCAT, and FSU wind stress (Figure 31). The QuikSCAT driven run corresponds to the benchmark run in Section 3 of Perez et al. (2005). As is apparent from Figure 31, all three model runs manifest significant equatorial asymmetry in the Rossby wave amplitudes. The FSU Rossby wave signal is least like observed; most notably, the southern maximum is replaced by two distinct maxima. The ECMWF and QuikSCAT meridional structures both closely resemble the observed structure, although the northern maximum for both runs is approximately 25% weaker than observed (Figure 31). The amplitude ratio of the north to south maxima are given in Table 3 for the model runs and observations. We see that the ECMWF and surprisingly FSU ratios match the observed ratio best. The QuikSCAT ratio is too large but is consistent with a strong mean meridional gradient of potential vorticity, Q_y (Figure 32), which is believed to be the primary

mechanism for the meridional asymmetry of Rossby wave SSH amplitudes (Chelton et al. 2003). A secondary mechanism is time-variability of the wind forcing, which was also found to be stronger in the QuikSCAT winds (Figure 1). Note that there is enhanced meridional asymmetry in the standard deviation of the QuikSCAT Q_y (Figure 33). The ECMWF asymmetry would likely intensify if the ECMWF wind stresses were appropriately adjusted to eliminate the bias described in Section 3.4.1.

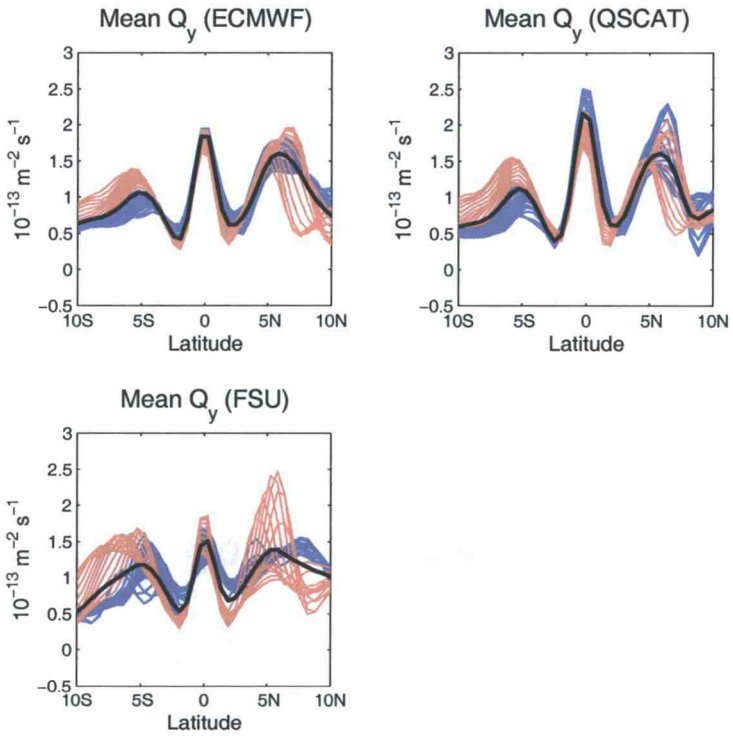

Figure 32. Five-year mean of the meridional potential vorticity gradient (Q_y) computed from layers 4 to 7 of the Gent-Cane model forced by seasonal ECMWF (upper left), QuikSCAT (upper right), and FSU (lower left) wind stress. Blue and red lines denote $\mu(Q_y)$ along longitudes between 170°E - 150°W and 150°W - 120°W, respectively. The thick black line represents the zonal average between 170°E and 120°W.

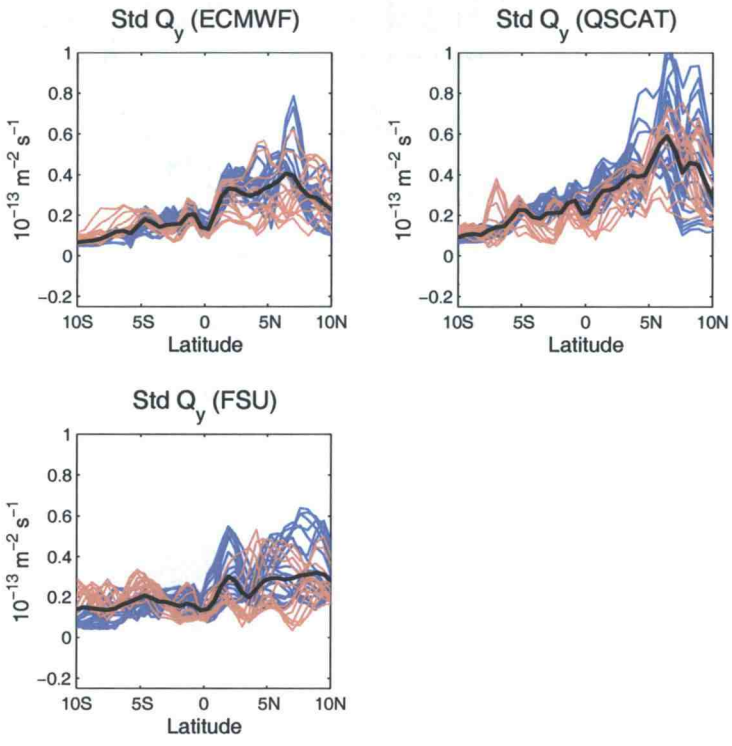

Figure 33. Five-year standard deviation of the meridional potential vorticity gradient (Q_y) computed from layers 4 to 7 of the Gent-Cane model forced by seasonal ECMWF (upper left), QuikSCAT (upper right), and FSU (lower left) wind stress. Blue and red lines denote $\sigma(Q_y)$ along longitudes between 170°E - 150°W and 150°W - 120°W, respectively. The thick black line represents the zonal average between 170°E and 120°W.

Table 3 also shows the westward phase speeds (computed as described in Perez et al. 2005) along the northern and southern maxima. All of the model runs produce a north-south phase speed asymmetry. Due to the split in the southern maximum, the FSU estimates have error bars as large as the phase speeds themselves, which renders the north-south phase speed ratio of 1.41 highly suspect. The ECMWF and QuikSCAT phase speeds, however, have much smaller error bars and we note that they produce a north-south phase speed asymmetry of 1.08 and 1.13, respectively, which compare well with the observed asymmetry of 1.27.

3.6 Summary and Conclusions

We found significant sensitivity in the Gent-Cane model equatorial Pacific cold tongue to wind forcing on seasonal and TIW time scales. The poorest performance occurred when FSU wind stress was used due to the anomalous meridional banding of the wind stress in the central equatorial Pacific (Figure 15). Upgrades to the FSU analysis may improve the response of the model cold tongue to FSU wind forcing (Bourassa et al. 2001). The ECMWF and QuikSCAT wind stress produced cold tongue seasonal cycles, TIWs, and annual equatorial Rossby waves that compared well with available observations from the TMI, merged altimetry, the TAO mooring array, and the OSCAR reanalyses; however, the highest realism was obtained with QuikSCAT wind forcing.

The long time records of the ECMWF and FSU wind analyses make them an attractive choice for cold tongue modeling studies and data assimilation experiments. However, upgrades and incorporation of new sources of observations lead to time dependent wind errors in these analyses. For example, the forecasts produced by ECMWF were based on different SST boundary conditions before and after 9 May 2001. This change had a dramatic effect on the ECMWF wind stress fields in this region (Chelton 2005). Moreover, ECMWF began assimilating QuikSCAT windstress on 22 January 2002 (Chelton and Freilich 2005), and FSU currently incorporates Seawinds scatterometer data into their new winds (Bourassa et al. 2002). Data assimilation requires knowledge of the errors in the wind forcing as it is typically assumed to be the largest source of model forecast error (Miller and Cane 1989; Miller et al. 1995; Cane et al. 1996). Given that FSU and ECMWF have errors which change dramatically in time, it seems that QuikSCAT is the optimal

choice to incorporate into four dimensional data assimilation schemes. Despite the relatively short QuikSCAT record (six full years at present time), the consistency of the error statistics over time and the high quality of the wind stress forcing make the QuikSCAT winds the best available choice for modeling studies and data assimilation experiments in the cold tongue region.

3.7 References

Baturin, N. G., and P. P. Niiler, 1997: Effects of instability waves in the mixed layer of the equatorial Pacific. *J. Geophys. Res.,* **102,** 27 771- 27 793.

Bonjean F., and G. S. E. Lagerloef, 2002: Diagnostic model and analysis of the surface currents in the tropical Pacific ocean. *J. Phys. Oceanogr.,* **32,** 2938-2954.

Bourassa, M. A., S. R. Smith, and J. J. O'Brien, 2001: A new FSU winds and flux climatology. 11th Conference on Interations of the Sea and Atmosphere, San Diego, CA, Amer. Meteor. Soc., 912.

Bourassa, M. A., S. R. Smith, and J. J. O'Brien, 2002: Assimilation of scatterometer and in situ winds for regularly gridded products. 6th Symposium on Integrated Observing Systems, Orlando, FL, Amer. Meteor. Soc., xx.

Bryden, H., and E. C. Brady, 1989: Eddy momentum and heat fluxes and their effects on the circulation of the equatorial Pacific Ocean. *J. Mar. Res.,* **47,** 55-79.

Cane, M. A., A. Kaplan, R. N. Miller, B. Tang, E. C. Hackert, and A. J. Busalacchi, 1996: Mapping tropical Pacific sea level: Data assimilation via a reduced state space Kalman filter. *J. Geophys. Res.,* **101,** 22 599-22 617.

Chelton, D. B., 2005: The impact of SST specification on ECMWF surface wind stress fields in the eastern tropical Pacific. *J. Climate,* **18,** 530-550.

Chelton, D. B., and M. H. Freilich, 2005: Scatterometer-based assessment of 10-m wind analyses from the operational ECMWF and NCEP numerical weather prediction models. *Mon. Wea. Rev.,* **133,** 409-429.

Chelton, D. B., M. G. Schlax, J. M. Lyman, and G. C. Johnson, 2003: Equatorially trapped waves in the presence of meridionally sheared baroclinic flow in the Pacific Ocean. *Prog. Oceanogr.,* **56,** 323-380.

Chelton, D. B., and Coauthors, 2001: Observations of coupling between surface wind stress and sea surface temparature in the eastern tropical Pacific. *J. Climate,* **14,** 1479-1498.

Chen, D., L. M. Rothstein, and A. J. Busalacchi, 1994: A hybrid vertical mixing scheme and its application to tropical ocean models. *J. Phys. Oceanogr.*, **24,** 2156-2179.

Cox, M. D., 1980: Generation and propagation of 30-day waves in a numerical model of the Pacific. *J. Phys. Oceanogr.*, **10,** 1168-1186.

Deser, C. S., and J. M. Wallace, 1990: Large-scale atmospheric circulation features of warm and cold episodes in the tropical Pacific. *J. Climate,* **3,** 1254-1281.

Donohue, K. A., and M. Wimbush, 1998: Model results of flow instabilities in the tropical Pacific Ocean. *J. Geophys. Res.,* **103,** 21 401 - 21 412.

European Centre for Medium-Range Weather Forecasts (ECMWF), 1994: The description of the ECMWF/WCRP Level III-A Global Atmospheric Data Archive, *Tech. Attach.,* 72 pp., Reading, England, U. K.

Freilich, M. H., D. G. Long, and M. W. Spencer, 1994: SeaWinds: A scanning scatterometer for ADEOS II - science overview. *Proc. Int. Geosci. Rem. Sens. Symposium,* Vol. II, Pasadena, CA, August 8-12, IEEE No. 94CH3378-7, 960-963.

Gent, P. R., and M. A. Cane, 1989: A reduced gravity, primitive equation model of the upper equatorial ocean. *J. Comp. Physics,* **81,** 444-480.

Hackert, E. C., A. J. Busalacchi, and R. Murtugudde, 2001: A wind comparison study using an ocean general circulation model for the 1997-1998 El Niño. *J. Geophys. Res.,* **106,** 2345-2362.

Hansen, D. V., and C. A. Paul, 1984: Genesis and effects of long waves in the equatorial Pacific. *J. Geophys. Res.,* **89,** 10 431-10 440.

Hayes, S. P., L. J. Mangum, J. Picaut, A. Sumi, and K. Takeuchi, 1991: TOGA-TAO: A moored array for real-time measurements in the tropical Pacific Ocean. *Bull. Amer. Meteor. Soc.,* **72,** 339-347.

Jochum, M., and R. Murtugudde, 2004: Internal variability of the tropical Pacific Ocean. *Geophys. Res. Lett.,* 31, L14309, doi: 10.1029/2004GL020488.

Johnson, G. C., B. M. Sloyan, W. S. Kessler, and K. E. McTaggart, 2002: Direct measurements of upper ocean currents and water properties across the tropical Pacific Ocean during the 1990s. *Prog. Oceanogr.,* **52,** 31-61.

Kessler, W. S., L. M. Rothstein, and D. Chen, 1998: The annual cycle of SST in the eastern tropical Pacific, diagnosed in an ocean GCM. *J. Climate,* **11,** 777-799.

Kessler, W. S., G. C. Johnson, and D. W. Moore, 2003: Sverdrup and nonlinear dynamics of the Pacific Equatorial Currents. *J. Phys. Oceanogr.,* **33,** 994-1008.

Kraus, E. B., and J. S. Turner, 1967: A one-dimensional model of the seasonal thermocline. Part II. The general theory and its consequences. *Tellus,* **19,** 98-105.

Kummerow, C., W. Barnes, T. Kozu, J. Shiue, and J. Simpson, 1998: The Tropical Rainfall Measuring Mission (TRMM) sensor package. *J. Atmos. Oceanic Technol.,* **15,** 808-816.

Lagerloef, G. S. E., G. T. Mitchum, R. B. Lukas, and P. P. Niiler, 1999: Tropical Pacific near-surface currents estimated from altimeter, wind and drifter data. *J. Geophys. Res.,* **104,** 23 313-23 326.

Large, W. G., and S. Pond, 1982: Sensible and latent heat flux measurements over the ocean. *J. Phys. Oceanogr.,* **12,** 464-482.

Legler, D.M., and J.J. O'Brien, 1988: Tropical Pacific wind stress analysis for TOGA, IOC Time series of ocean measurements, IOC Technical Series 33, Volume 4, UNESCO.

Lyman, J. M., D. B. Chelton, R. A. deSzoeke, and R. M. Samelson, 2005a: Tropical instability waves as a resonance between equatorial Rossby waves. *J. Phys. Oceanogr.,* **35,** 232-254.

Lyman, J. M., G. C. Johnson, and W. S. Kessler, 2005b: Structure of 17-day versus 33-day tropical instability waves in the equatorial Pacific. *J. Phys. Oceanogr.,* revised.

McCreary, J. P., and Z. Yu, 1992: Equatorial dynamics in a 2.5-layer model. *Prog. Oceanogr.*, **29,** 61-132.

McPhaden, M. J., 1993: TOGA-TAO and the 1991-93 El Niño-Southern Oscillation event. *Oceanography,* **6,** 36-44.

Miller, R. N., and M. A. Cane, 1989: A Kalman filter analysis of sea level heights in the tropical Pacific. *J. Phys. Oceanogr.*, **19,** 773-790.

Miller, R. N., A. J. Busalacchi, and E. C. Hackert, 1995: Sea surface topography fields of the tropical Pacific from data assimilation. *J. Geophys. Res.*, **100,** 13 389-13 425.

Mitchell, T. P., and J. M. Wallace, 1992: The annual cycle in equatorial convection and sea surface temperature. *J. Climate,* **5,** 1140-1156.

Perez, R. C., and R. N. Miller, 2005: Impact of a reduced state space Kalman filter on the equatorial Pacific cold tongue and tropical instability waves. *Submitted to J. Geophys. Res.*

Perez, R. C., D. B. Chelton, and R. N. Miller, 2005: The effects of wind forcing and background mean currents on the latitudinal structure of equatorial Rossby waves. *J. Phys. Oceanogr.*, **35,** 666-682.

Philander, S. G. H., 1978: Instabilities of zonal equatorial currents, Part 2. *J. Geophys. Res.*, **83,** 3679-3682.

Price, J. F., R. A. Weller, and R. Pinkel, 1986: Diurnal cycling: Observations and models of the upper ocean response to diurnal heating, cooling, and wind mixing. *J. Geophys. Res.*, **91,** 8411-8427.

Qiao, L., and R. H. Weisberg, 1995: Tropical instability wave kinematics: Observations from the Tropical Instability Wave Experiment. *J. Geophys. Res.*, **100,** 8677-8693.

Schlax, M. G., and D. B. Chelton, 1992: Frequency domain diagnostics for linear smoothers. *J. Amer. Stat. Assoc.*, **87,** 1070-1081.

Seager, R., S. E. Zebiak, and M. A. Cane, 1988: A model of the tropical Pacific sea surface temperature climatology. *J. Geophys. Res.*, **93,** 1265-1280.

Swenson, M. S., and D. V. Hansen, 1999: Tropical Pacific Ocean mixed layer heat budget: The Pacific cold tongue. *J. Phys. Oceanogr.*, **29,** 69-81.

Wallace, J. M., T. P. Mitchell, and C. S. Deser, 1989: The influence of sea surface temperature on surface wind in the eastern equatorial Pacific: Seasonal and interannual variability. *J. Climate,* **2,** 1492-1499.

Wang, W., and M. J. McPhaden, 1999: The surface-layer heat balance in the equatorial Pacific Ocean. Part I: The mean seasonal cycle. *J. Phys. Oceanogr.*, **29,** 1812-1831.

4 Vertical Resolution Study in a Reduced Gravity Model of the Tropical Pacific

Renellys C. Perez and R. N. Miller

Unpublished Manuscript.

4.1 Introduction

For numerical and assimilative studies of the equatorial Pacific cold tongue dynamics and thermodynamics, it is necessary to upgrade the numerical model used in Chapter 2 (Perez et al. 2005) and 3. The updated version of the Gent and Cane (1989) nonlinear, reduced gravity, β-plane model was coupled to the Seager et al. (1995) advective atmospheric mixed layer model by Murtugudde et al. (1996). This mixed layer model requires the input of solar radiation, cloud cover, wind speed, and sea level air temperature and humidity from climatological data sets. We'll refer to the version of the Gent and Cane (1989) model used in Perez et al. (2005) and Chapter 3 as the GC model and the new version with the advective atmospheric mixed layer as the GCAML model. For additional GCAML model configuration details see Chapter 5 (Perez and Miller 2005).

In the GC simulations of Perez et al. (2005), a relatively coarse horizontal (approximately 2.5° zonal x 0.6° meridional in the waveguide) and vertical grid (7 layers in the upper 400 m) were used to study the meridional asymmetry of annual Rossby waves in the equatorial Pacific. Increased horizontal and vertical resolution, however, are needed to obtain a realistic representation of the cold tongue thermal structure above and below the thermocline, the equatorial current system (ECS), and the meridional and vertical shears that generate tropical instability waves (TIWs; Philander 1978; Cox 1980; McCreary and Yu 1992; Donohue and Wimbush 1998; Lyman et al. 2005b). Given that TIWs have zonal wavelengths of 1000 to 2000 km (Qiao and Weisberg 1995), a uniform zonal grid spacing of 1^o is chosen. Meridional resolution of 0.25^o to 0.4^o in the equatorial waveguide was found to be sufficient to produce realistic TIWs with the GC (Kessler et al. 1998) and GCAML (Jochum and

Murtugudde 2004) model. Hence, the meridional grid has 0.33^o resolution in the equatorial waveguide and stretches to 1^o resolution at the poleward boundaries. This horizontal resolution is comparable to that of recent GC and GCAML studies in the tropical Pacific (Table 4) and is applied to the cold tongue and TIW assimilation experiments of Perez and Miller (2005).

The model active region is defined by specifying the density at the base of the active region, ρ_{btm}, by selecting the bottom temperature (T_{btm}) and salinity (S_{btm}). As $\sigma_{btm} = \rho_{btm} - 1000\ kg\ m^{-3}$ is increased, the slope of the active layer base decreases and the lower layers approach z-levels, penetrate deeper into the water column, and become decoupled from the prevailing winds. A deeper active layer base requires an increase of NZ, the number of layers, to maintain sufficient vertical resolution in the upper ocean. The maximum density used in GCAML simulations of the tropical Pacific is $\rho_{btm} = 1027.55\ kg\ m^{-3}$ corresponding to $T_{btm} = 6^o$ C, $S_{btm} = 35$ psu, and a nominal depth of 1500 m (Table 4). Even with $NZ = 20$ vertical layers, this configuration may not adequately resolve the upper 500 m of the water column.

As 5-day seasonal cycle anomalies of dynamic height (DH) relative to 500 decibars (db) are assimilated into the GCAML model in Perez and Miller (2005), this paper studies the sensitivity of the GCAML DH and ECS to the parameters that define the vertical resolution in the active region. The ability to adequately resolve the thermocline and subthermocline ocean and keep the size of the model state space manageable for the data assimilation experiments in Perez and Miller (2005) and Chapter 6 are the criteria used to determine the best vertical configuration.

Table 4. Comparison of grid resolution in recent GC and GCAML simulations of the tropical Pacific.

Study	Δx	Δy	NZ	$T_{btm}(°C)$	$S_{btm}(psu)$
Chen et al. 1994a,b	1°*	0.3°*	9	10	NS
Chen et al. 1999	1°*	0.5°*	7		
Gourdeau et al. 2000	1°*	0.3°*	9	9	NS
Hackert et al. 2001	1°	0.33°*	20	6	35.0
Jochum and Murtugudde 2004	0.25°	0.25°	12		
Kessler et al. 1998	1.1°*	0.37°*	9		NS
Kessler et al. 2003	1.1°*	0.37°*	9		NS
Murtugudde et al. 1996	1°*	0.33°*	12		NS
Murtugudde and Busalacchi 1998	1°*	0.33°*	12	9	34.5
Murtugudde et al. 2002	1°	0.33°*	20	6	35.0
Perez et al. 2005	2.5°*	0.6°*	7	11	34.5
Seager et al. 2003	0.5°	0.5°	15		
Verron et al. 1999	1°*	0.3°*	9	9	NS

* Indicates a stretched grid (e.g., Hackert et al. 2001 has a stretched meridional grid but uniform zonal grid) where Δx and Δy correspond to values in the waveguide interior.

NS means that the model is run with an equation of state that depends only on temperature.

An empty cell means that the article did not provide the numeric value.

Table 5. Different choices for the bottom of the active region.

$\sigma_{btm}(kg\ m^{-3})$	$T_{btm}(°C)$	$S_{btm}(psu)$	Nominal Thickness (m)
26.28	12.0	34.6	200
26.80	10.0	34.8	400
27.00	9.0	34.85	600
27.20	8.0	34.9	800
27.55	6.0	35.0	1500

4.2 Vertical Resolution Experiments

The GCAML model is forced by monthly climatological winds from European Center for Medium Range Weather Forecasting (ECMWF 1994) for the vertical resolution experiments. Surface heat and rain fluxes are computed using Interannual Satellite Cloud Climatology Project (ISCCP) cloud cover data, Earth Radiation Budget Experiment (ERBE) solar radiation, Oberhuber (1988) precipitation, and ECMWF estimates of wind speed, sea level air temperature and humidity. Levitus temperature and salinity (Levitus et al. 1994) provide forcing at the lateral boundaries. All climatological fields are available monthly on a 2° zonal x 2° meridional grid.

Table 6. Initial layer distributions.

$h_{k=1,11}$	$s_{k=1,11}$	$h_{k=1,15}$	$s_{k=1,15}$	$h_{k=1,20}$	$s_{k=1,20}$
50		50		50	
10	0.0286	10	0.0286	5	0.0143
				5	0.0143
10	0.0286	10	0.0286	5	0.0143
				5	0.0143
10	0.0286	10	0.0286	5	0.0143
				5	0.0143
20	0.0571	10	0.0286	10	0.0286
		10	0.0286	10	0.0286
20	0.0571	10	0.0286	10	0.0286
		10	0.0286	10	0.0286
40	0.1143	20	0.0571	20	0.0571
		20	0.0571	20	0.0571
40	0.1143	40	0.1143	20	0.0571
				20	0.0571
60	0.1714			30	0.0857
		40	0.1143	30	0.0857

Table 6. (continued)

$h_{k=1,11}$	$s_{k=1,11}$	$h_{k=1,15}$	$s_{k=1,15}$	$h_{k=1,20}$	$s_{k=1,20}$
60	0.1714	40	0.1143	30	0.0857
		60	0.1714	30	0.0857
80	0.2286	60	0.1714	80	0.2286

The values of σ_{btm} used to define the bottom of the active region were $26.28, 26.80, 27.00, 27.20$, and $27.55\ kg\ m^{-3}$. These density choices correspond to nominal active layer depths of $200, 400, 600, 800$, and $1500\ m$, respectively (see Table 5 for corresponding T_{btm} and S_{btm}). The fixed ratios of the k^{th} layer thickness to total active layer thickness, $s_k = h_k / \Sigma_{k=2}^{NZ} h_k$, for $k > 1$ are provided in Table 6. Given a nominal active layer thickness of $400\ m$ and $NZ = 11$, the initial layer distribution is $50, 10, 10, 10, 20, 20, 40, 40, 60, 60$, and $80\ m$. NZ is then increased to 15 and 20 layers by bisecting some of the active layers (Table 6). Using more than 20 vertical layers was deemed computationally impractical for the planned assimilation experiments.

For each configuration, the model is initialized from Levitus climatology projected onto the vertical grid (Hackert et al. 2001 and references therein) and run for ten years. Monthly results from year 11 are analyzed and monthly Levitus climatology are used to demonstrate the climatological drift of the model from its initialization.

4.3 ECS

We focus first on the sensitivity of the eastward flowing Equatorial Undercurrent (EUC), the northern branch of the westward flowing South Equatorial Current (SECN), and the eastward flowing North Equatorial Countercurrent (NECC) to the choice of ρ_{btm}. The vertical structure of EUC is sensitive to the parameters chosen to define the model active region (Figure 34). By comparing the model mean zonal velocity with mean $1988 - 2004$ TAO ADCP zonal velocity along the equator at 147°E, 165°E, 170°W, 140°W, and 110°W, optimal values for σ_{btm} and NZ can be determined. Note that this is not an attempt to validate the climatology driven model run; rather, it is a means to establish which parameters best resolve the EUC vertical structure when all else is held equal. Fixing $NZ = 11$ layers, the five values for σ_{btm} are compared (upper panel of Figure 34). Although the EUC is strongest in the $\sigma_{btm} = 26.28\ kg\ m^{-3}$ simulation, it is largely truncated by this simulation whose nominal depth is 200 m. West of the dateline and at 170°W, runs with $\sigma_{btm} \geq 26.80\ kg\ m^{-3}$ produce similar EUC vertical structure with a shallower EUC core than observed by TAO; however, the core is deeper than the $\sigma_{btm} = 26.28\ kg\ m^{-3}$ run (upper panel of Figure 34). In the eastern Pacific, large values of σ_{btm} (e.g., 27.20 and 27.55 $kg\ m^{-3}$) produce a narrower EUC as fewer layers are placed in the EUC core region. With the exception of 140°W, the runs with $\sigma_{btm} = 26.80$ and $27.00\ kg\ m^{-3}$ produce similar EUC vertical structure. Increasing the number of layers from 11 to 15 for $\sigma_{btm} = 27.00\ kg\ m^{-3}$ improves the vertical structure of the EUC (lower panel of Figure 34). Specifically, the strength, vertical extent, and depth of the EUC core increases as NZ changes from 11 to 15 layers (lower panel in Figure 34). The profiles are essentially identical for $NZ = 15$ and

$NZ = 20$ layers at the TAO moorings west of 110°W. At 110°W, the $NZ = 20$ run is indistinguishable from the $NZ = 11$ run, and the EUC core is strongest for $NZ = 15$.

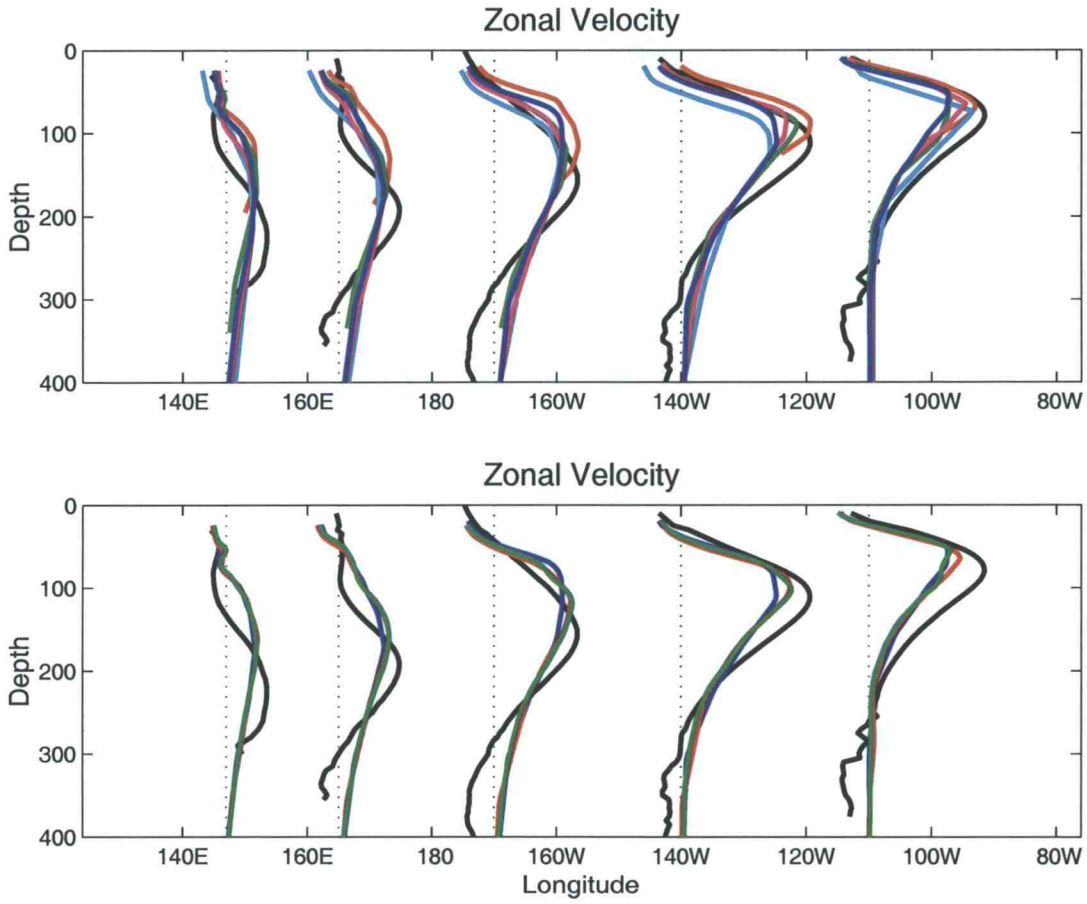

Figure 34. Mean 1988-2004 TAO ADCP zonal velocity along the equator at 147°E, 165°E, 170°W, 140°W, and 110°W (solid black line) compared with ECMWF climatology driven model mean zonal velocity. Upper panel: the red, green, blue, magenta, and cyan lines correspond to $\sigma_{btm} = 26.28, 26.80, 27.00, 27.20$, and $27.55\ kg\ m^{-3}$ and $NZ = 11$. Lower panel: the blue, red, and green lines correspond to $\sigma_{btm} = 27.00\ kg\ m^{-3}$ and $NZ = 11, 15$, and 20. Zonal velocity is scaled so that $100\ cm\ s^{-1}$ corresponds to 20° longitude.

Overall, the largest variability along the equator is obtained with the $\sigma_{btm} = 27.00\ kg\ m^{-3}$ run (blue line in the upper panel of Figure 35). As expected, the daily TAO zonal velocities have larger variability than the monthly model currents driven by climatology. For $\sigma_{btm} = 27.00\ kg\ m^{-3}$, the variability is not modified significantly by increasing NZ to 15 and 20 layers (lower panel of Figure 35).

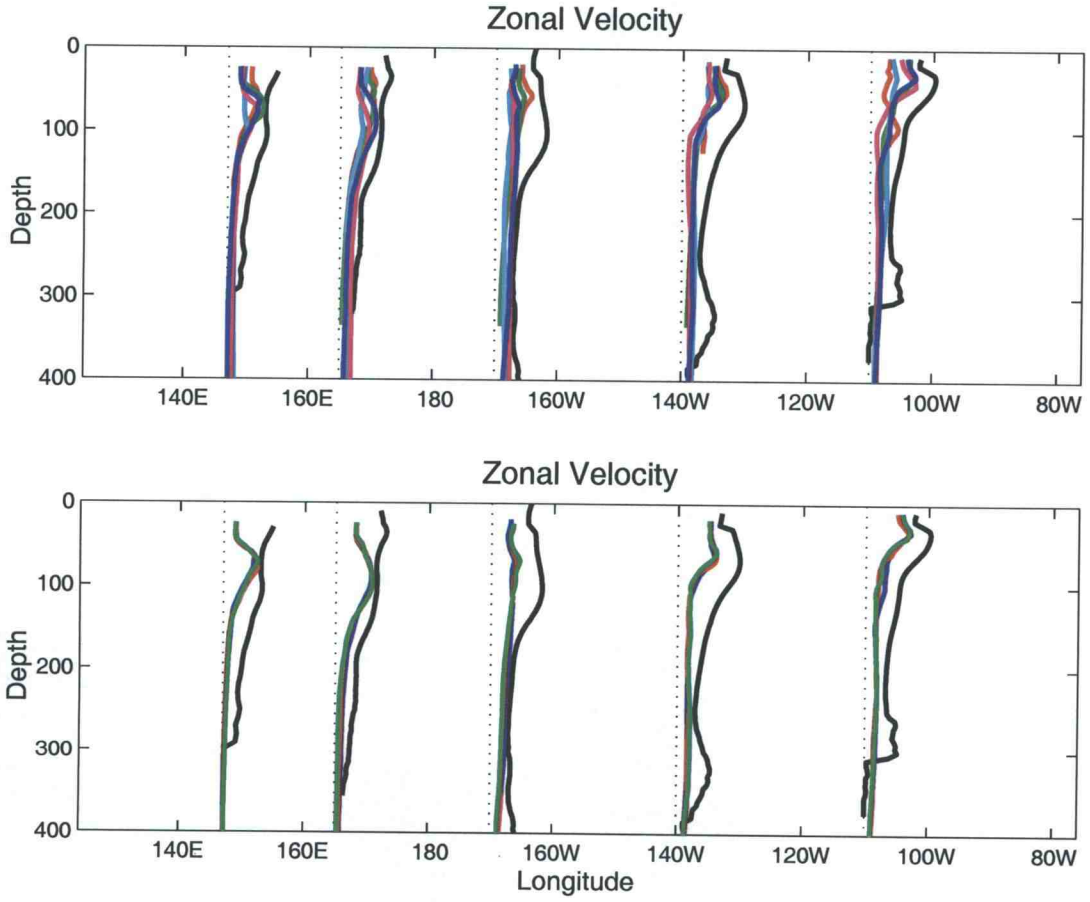

Figure 35. Similar to Figure 34, except for the standard deviation of zonal velocity.

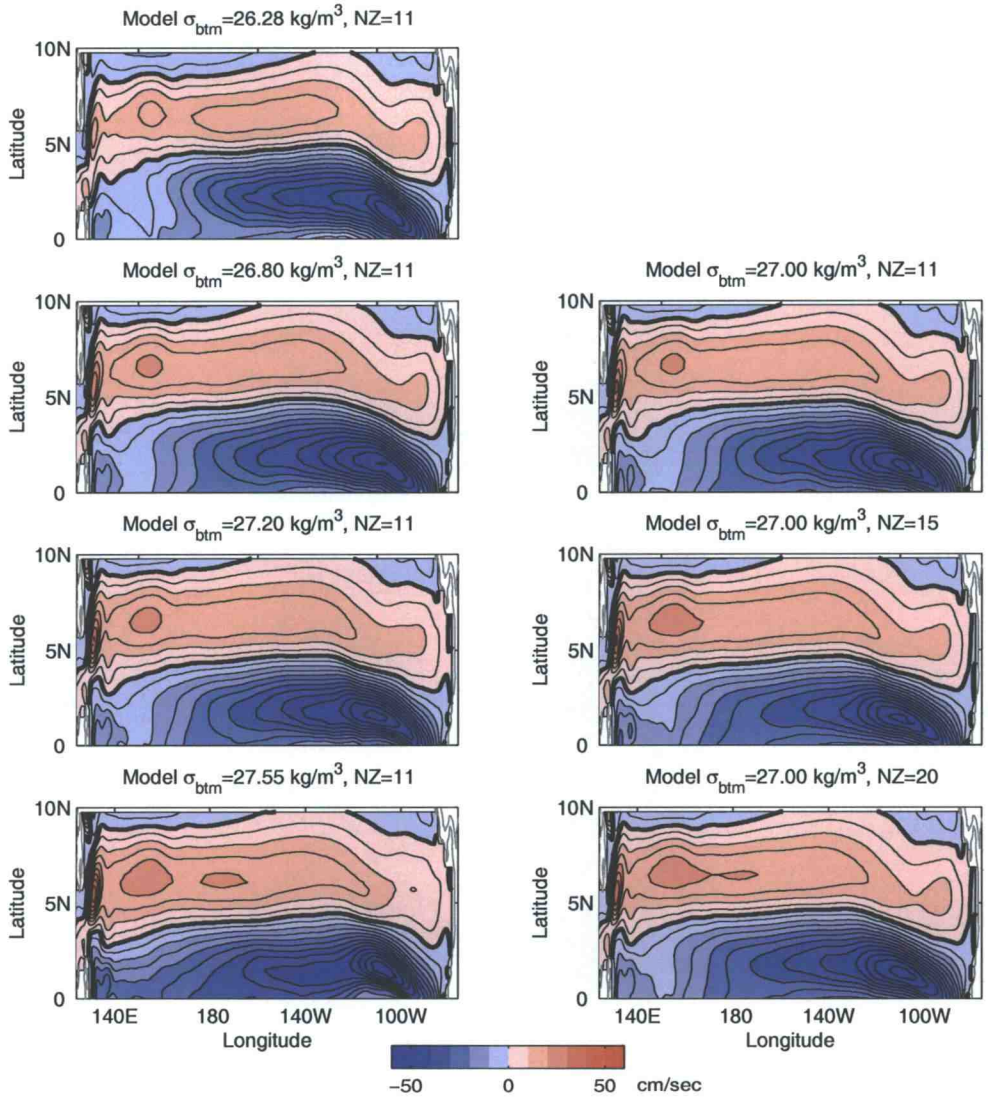

Figure 36. Model mean surface mixed layer zonal velocity between 0° and 10°N for several values of σ_{btm} and NZ. The contour interval is 5 $cm\ s^{-1}$ with red and blue colors indicating eastward and westward velocities, respectively, and the thick black line indicates the zero contour.

Little sensitivity was found in the strength of the equatorial currents whose cores lie above the thermocline, specifically the NECC along 7°N and the SECN along 2°N, to the choice of σ_{btm} and NZ. As σ_{btm} increases from 26.28 to 27.55 $kg\ m^{-3}$ for $NZ = 11$, the magnitude of the surface mixed layer zonal velocity in the NECC

and the SECN (Figure 36) increases slightly (ca. 5 $cm\ s^{-1}$). As a consequence, the SECN-NECC meridional shear of mean surface zonal velocity averaged over all longitudes is increased with increasing σ_{btm} between 1.5 and 4°N (Figure 37). The strengthening of the SECN-NECC shear should increase the amplitudes of simulated TIWs on the northern flank of the cold tongue (Lyman et al. 2005a). The largest variability in the surface mixed layer zonal velocity is found for $\sigma_{btm} = 27.00\ kg\ m^{-3}$ between the equator and 3°N (Figure 38). There is little modification to the standard deviation as NZ is increased to 15 and 20 layers for $\sigma_{btm} = 27.00\ kg\ m^{-3}$.

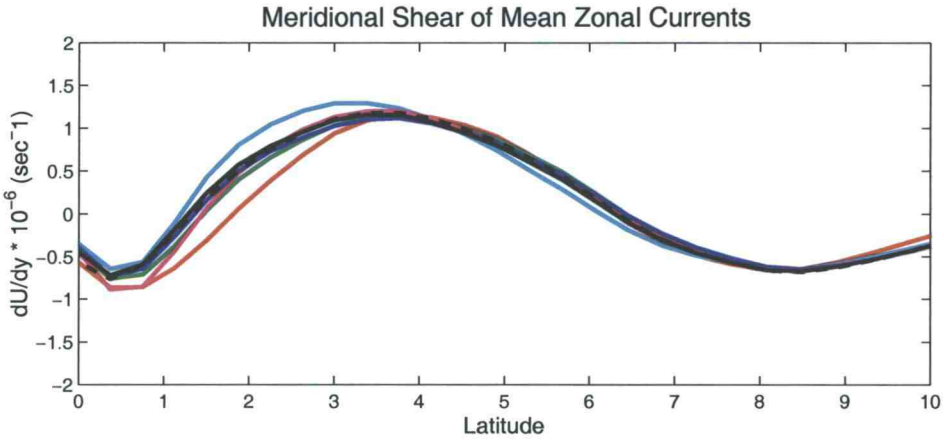

Figure 37. Model meridional shear of mean surface mixed layer zonal velocity averaged over all longitudes. The red, green, blue, magenta, and cyan lines correspond to $\sigma_{btm} = 26.28, 26.80, 27.00, 27.20$, and $27.55\ kg\ m^{-3}$ and $NZ = 11$. The solid and dashed black lines correspond to $\sigma_{btm} = 27.00\ kg\ m^{-3}$ and $NZ = 15$ and 20.

The Tsuchiya jet cores that flank the EUC core near the $1026.5\ kg\ m^{-3}$ isopycnal (Johnson and McPhaden 1999), were present, albeit weak, in simulations with $\sigma_{btm} \geq 27.00\ kg\ m^{-3}$ (not shown). Realistic Tsuchiya jets, however, are not expected as this model lacks the Pacific interocean circulation (IOC) which has been identified as the source of the Tsuchiya jets in modeling studies such as McCreary et al. (2002) and are beyond the scope of this project.

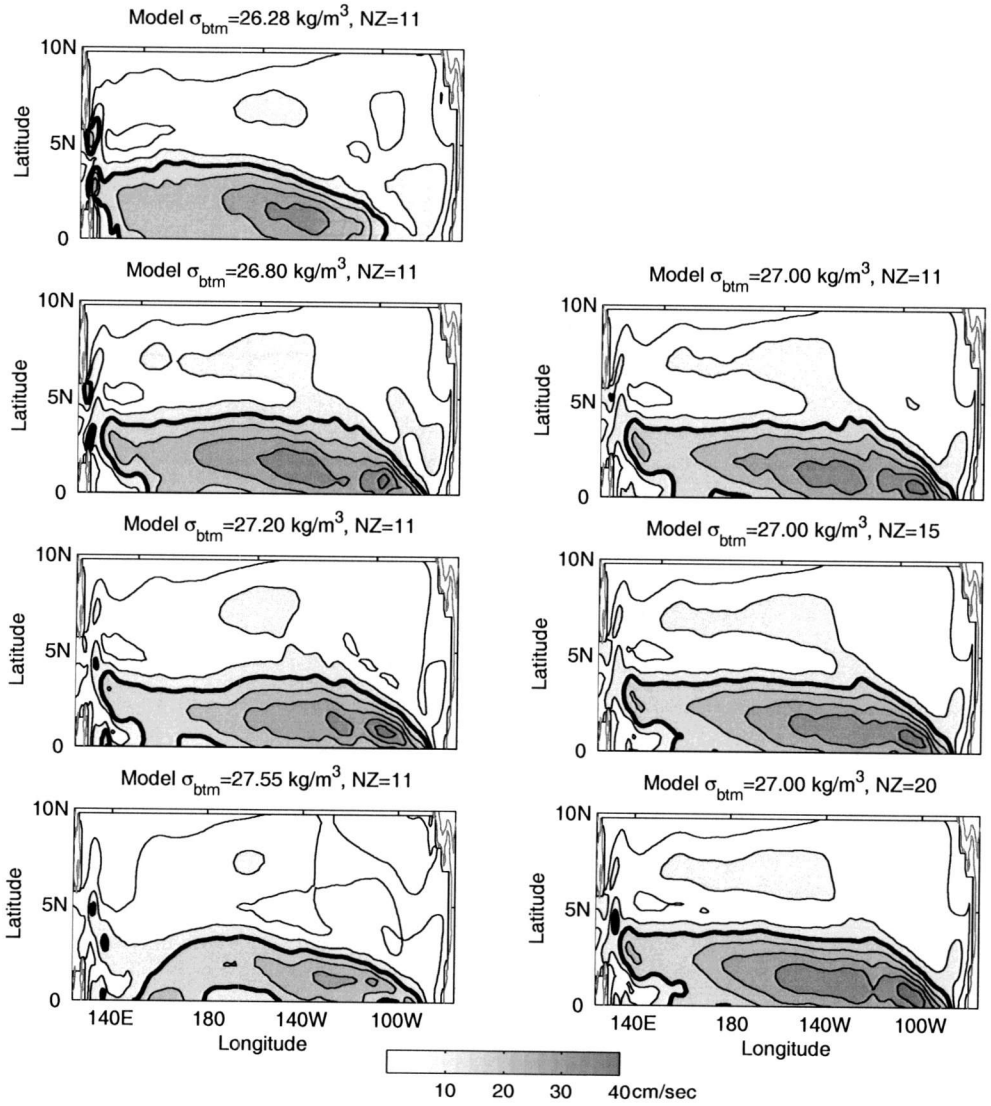

Figure 38. Similar to Figure 36, except for the standard deviation of the surface mixed layer zonal velocity. The contour interval is 5 $cm\ s^{-1}$ with darker colors indicating incresed variability and the thick black line indicates the 15 $cm\ s^{-1}$ contour.

4.4 Dynamic Height

As DH anomalies (DHA) will be used in the assimilation experiments discussed in Perez and Miller (2005) and Chapter 6, the spatial structure of the mean and standard deviations of DH in the equatorial waveguide are meaningful diagnostics

for the specification of σ_{btm} and NZ. Model DHs are compared to TAO DH estimates from August 1999 to July 2004 at the locations specified by white dots in Figure 39. Using the UNESCO equation of state for seawater (Millero and Poisson 1981), TAO estimates daily specific volume anomalies based on vertical profiles of temperature and inferred profiles of salinity obtained from local temperature-salinity (T-S) profiles (Conkright et al. 2002). The daily specific volume anomalies are vertically integrated to generate DH relative to 500 db at the TAO moorings. Model DHs are computed for each vertical configuration using model profiles of monthly temperature and salinity. For values of σ_{btm} where the base of the active region is shallower than 500 db, T_{btm} and S_{btm} are used to compute the specific volume anomaly between the base of the active region and the 500 db isobar.

Comparison of the mean DHs at the TAO stations demonstrates the presence of an overall positive model-TAO bias that exceeds 10 dynamic cm (dyn cm) for all the values of σ_{btm} and NZ tested (Figure 39). The mean DH bias is largest when $\sigma_{btm} = 27.55\ kg\ m^{-3}$ and smallest for $\sigma_{btm} = 26.80\ kg\ m^{-3}$ and does not vary significantly with increasing NZ. RMS errors in the TAO DHs stemming from the use of T-S relationships, the limited resolution of the thermistor chain moorings, and gap filling through regression analysis of missing data between 300 and 500 m depth range from 3 to 4 dyn cm in the west and 2 to 3 dyn cm in the east (Johnson and McPhaden 1993; Busalacchi et al. 1994) and are too small to explain this bias. The elevated model DH at the TAO moorings implies that the model thermocline is too deep or the upper ocean water column is too fresh relative to the Levitus initialization.

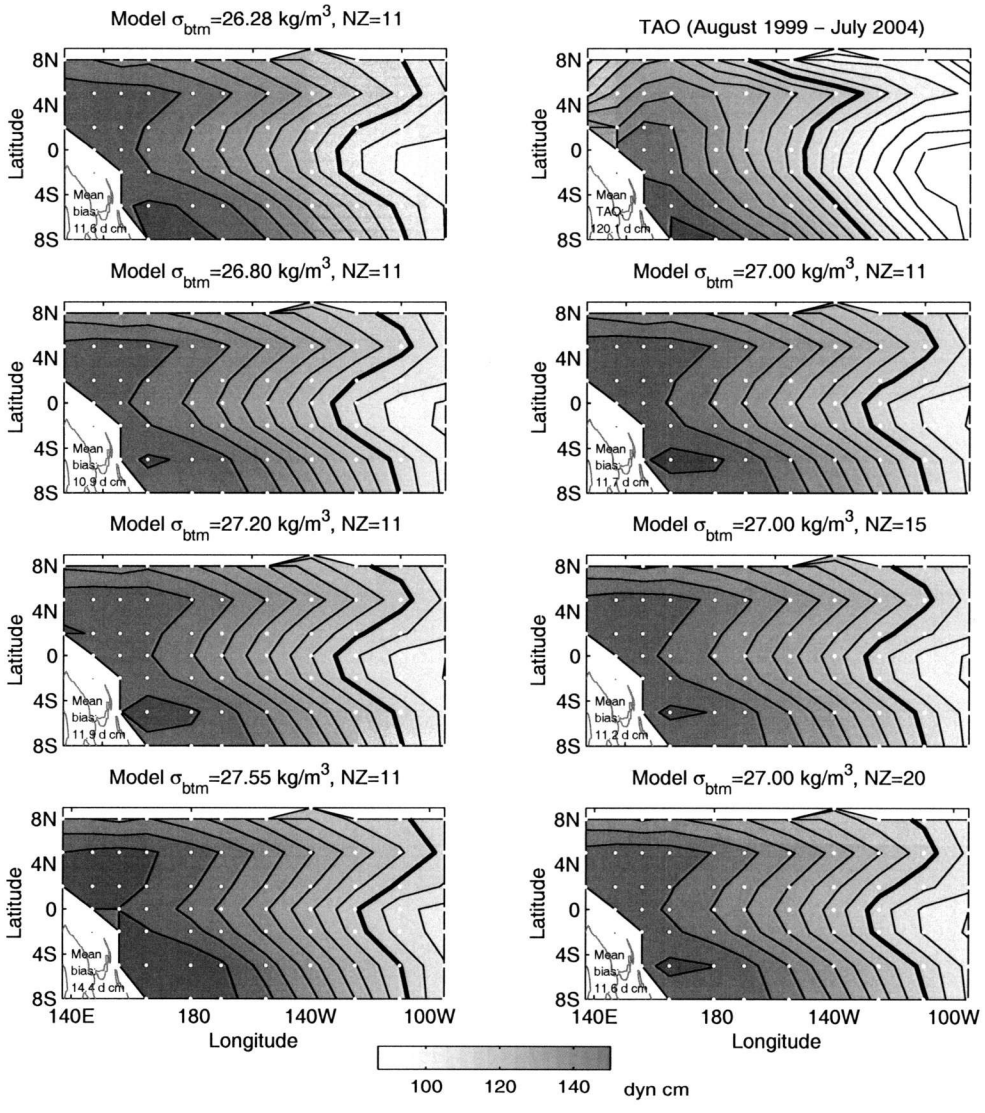

Figure 39. Model mean DH for several values of σ_{btm} and NZ compared with TAO mean DH from August 1999 to July 2004. Model values are only plotted at TAO locations which are indicated by the white dots. The contour interval is 4 dyn cm with thick black contour indicating 115 dyn cm. The mean model-TAO bias is identified on each panel.

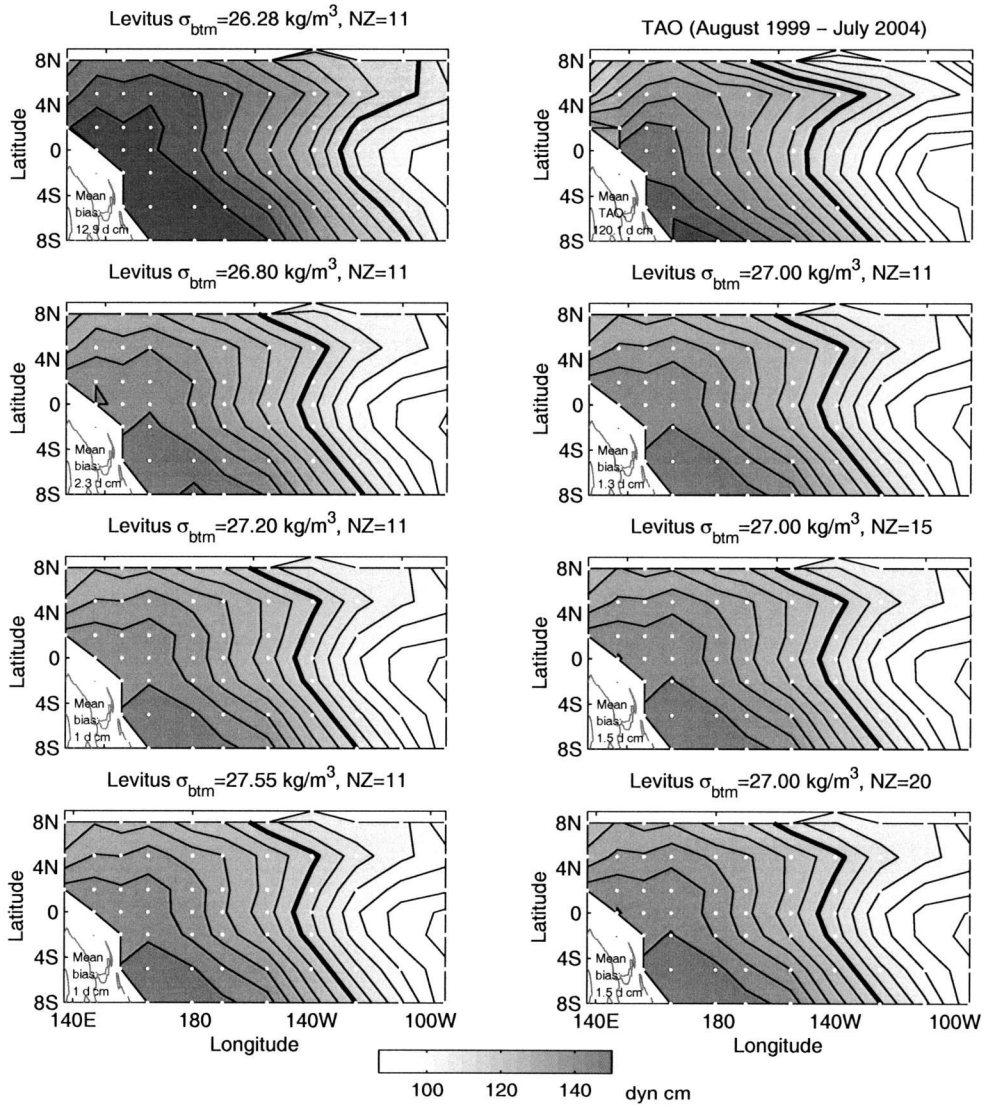

Figure 40. Similar to Figure 39, except for Levitus mean DH. (Levitus climatology is projected onto model layer configuration.)

DHs are computed from the monthly Levitus temperature and salinity projected onto the model layer configurations to examine whether the initial DHs are biased. Overall, the horizontal structure and range of values in the mean Levitus DHs match the TAO estimates for the values of σ_{btm} and NZ tested (Figure 40). However, the $\sigma_{btm} = 26.28\ kg\ m^{-3}$ and $NZ = 11$ run produces positively biased DHs along the northern TAO latitudes and in the cold tongue associated with weaker cold tongue penetration. The cold tongue DH bias is essentially removed for $\sigma_{btm} \geq 26.80\ kg\ m^{-3}$; however, the northern bias is only removed (to within 1.5 dyn cm) for $\sigma_{btm} \geq 27.00\ kg\ m^{-3}$. Increasing the number of layers to 15 and 20 for $\sigma_{btm} = 27.00\ kg\ m^{-3}$ doesn't modify the spatial structure of the mean Levitus DHs significantly.

As the mean Levitus DHs are essentially unbiased for $\sigma_{btm} = 27.00\ kg\ m^{-3}$ and $NZ = 15$, the Levitus temperature and salinity climatology can be used to diagnose whether climatological drift in the model temperature or salinity is responsible for the mean DH bias. The monthly model and Levitus salinity and temperature are linearly interpolated from the layer coordinates into 5 m vertical bins that span the upper 500 m of the water column. DHs are computed using the mean model salinity and mean Levitus temperature (S_m, T_L) and mean Levitus salinity and mean model temperature (S_L, T_m) to estimate the individual contributions of the salinity and temperature bias to the DH bias (upper panels of Figure 41). Model-Levitus salinity and temperature biases account for 5.8 and 7.5 dyn cm of the overall model-TAO DH bias. The percent bias explained by the drift of the model temperature and salinity from Levitus initialization varies spatially (lower panels of Figure 41). The

salinity bias plays a larger role south of the ITCZ (8°S to 2°N) and west of 140°W and the thermal biases are more important in the eastern Pacific and north of 5°N.

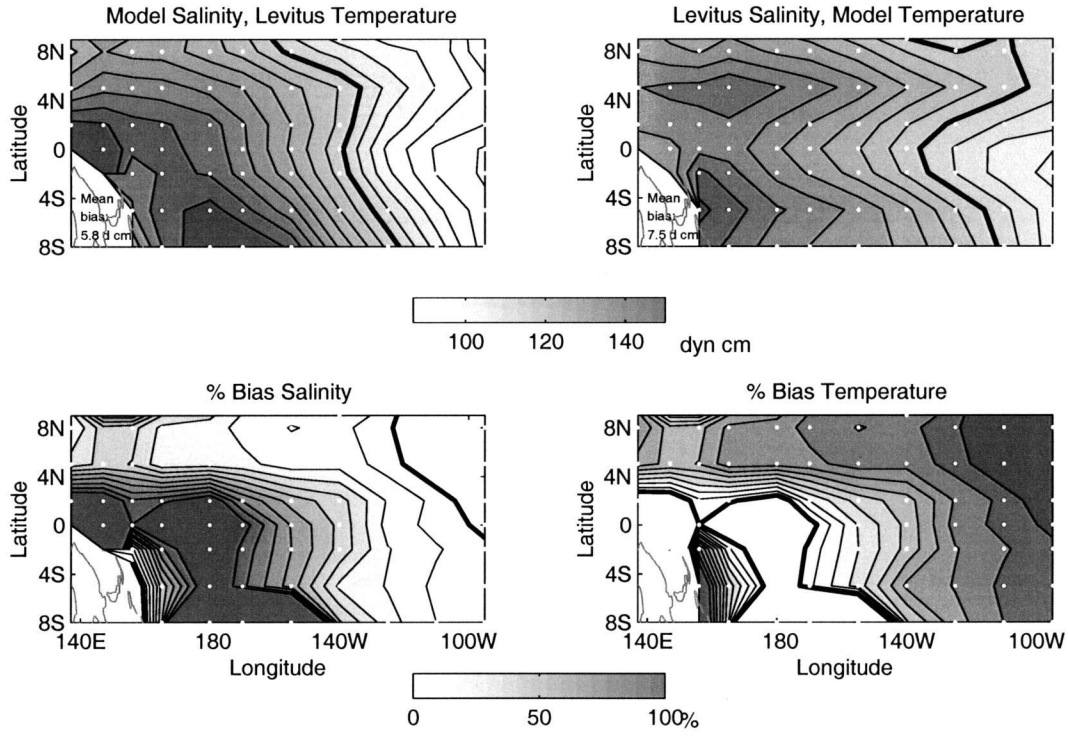

Figure 41. Estimate of DH bias relative to TAO obtained by computing the DH with mean model salinity and mean Levitus temperature (5.8 dyn cm) and mean Levitus salinity and mean model temperature (7.5 dyn cm) for the $\sigma_{btm} = 27.00\ kg\ m^{-3}$ and $NZ = 15$ layer configuration. The percent bias explained by each are plotted on the lower panels at 10 percent contour intervals (zero contour given by thick black contour).

The mean 20°C isotherm depths (here a proxy for the depth of the thermocline), plotted for the model and Levitus given $\sigma_{btm} = 27.00\ kg\ m^{-3}$ and $NZ = 15$ are compared with the mean of daily TAO isotherm depths from August 1999 - July 2004 (Figure 42). Areas with large DH biases due to thermal biases (lower right panel of Figure 41) are coincident with areas where the mean model 20°C isotherm depths are too deep or positively biased relative to Levitus (lower panel of Figure 42). In regions where the model mean 20°C isotherm depths are negatively biased compared

to the Levitus mean isotherm depths (e.g., too shallow), the salinity bias plays a larger role in producing the positive DH bias (lower left panel of Figure 41).

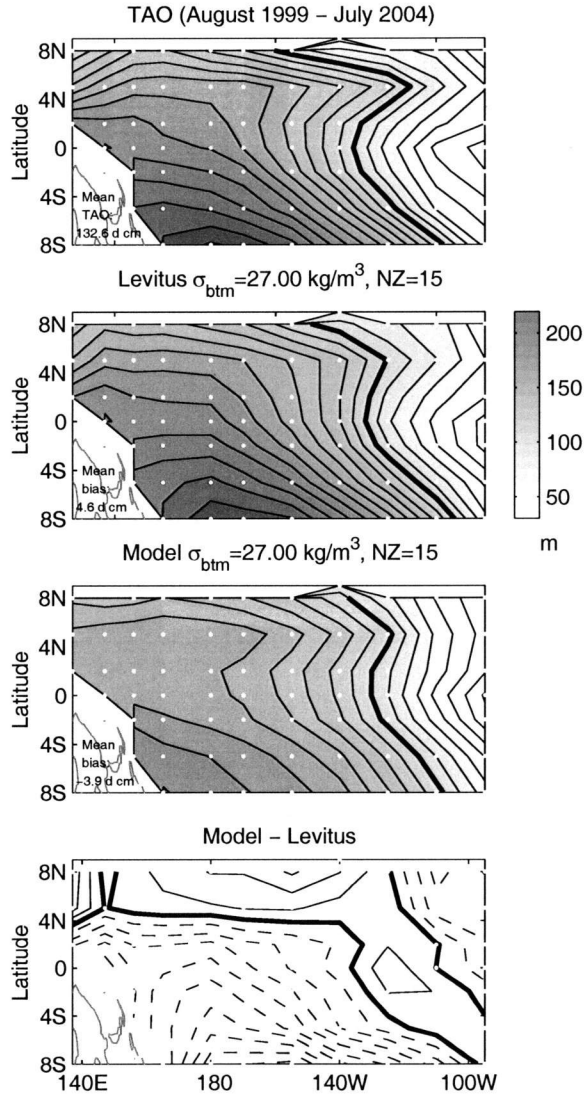

Figure 42. Levitus and model mean 20°C isotherm depth for $\sigma_{btm} = 27.00\ kg\ m^{-3}$ and $NZ = 15$ compared with TAO depths from August 1999 to July 2004. The contour interval is 10 m with thick black contour indicating 100 m and depths increasing westward. The bottom panel show the spatial bias between the model and Levitus mean 20°C isotherm depth. The contour interval is 5 m and the solid and dashed contours indicate positive and negative values, respectively.

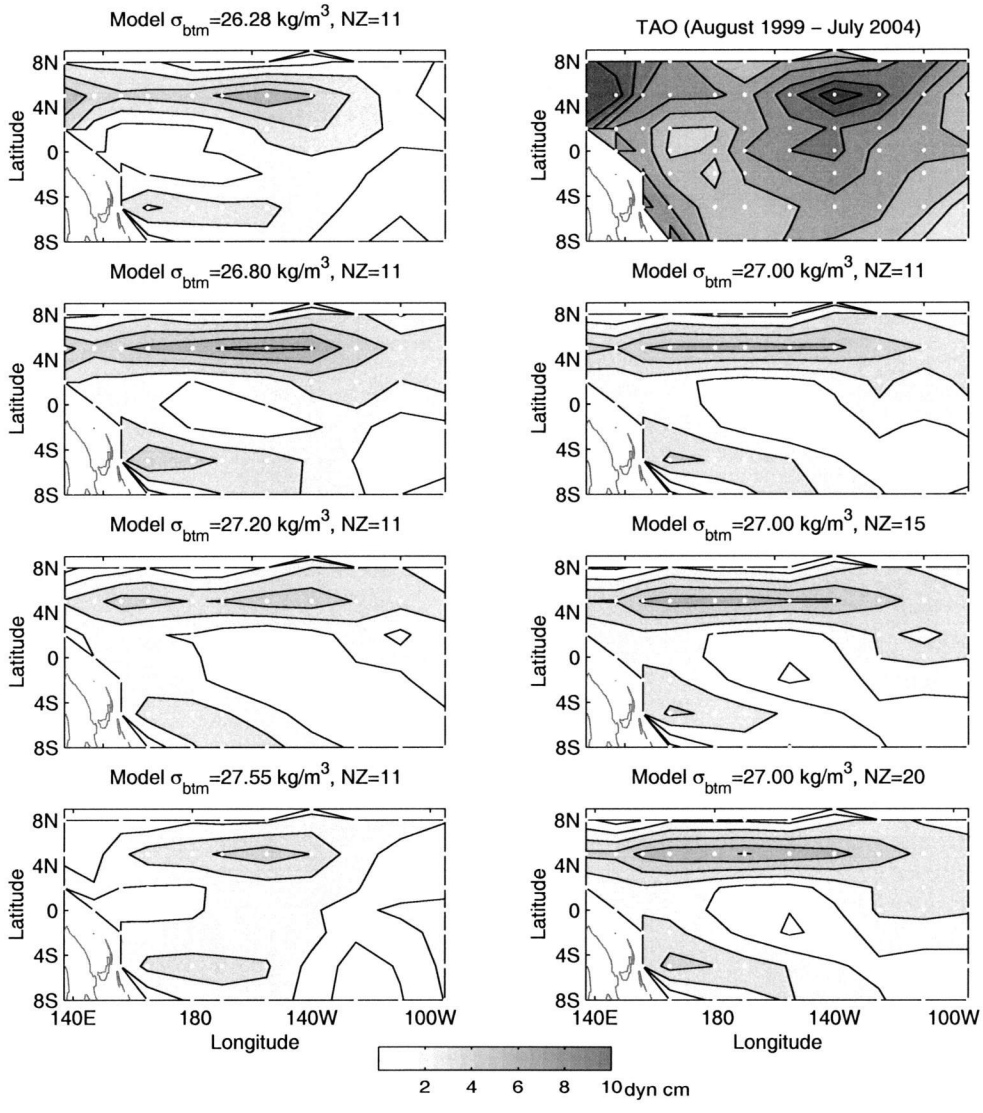

Figure 43. Similar to Figure 39, except the standard deviation of model DH for several values of σ_{btm} and NZ compared with TAO mean DH from August 1999 to July 2004. Model values are only plotted at TAO locations which are indicated by the white dots. The contour interval is 1 dyn cm.

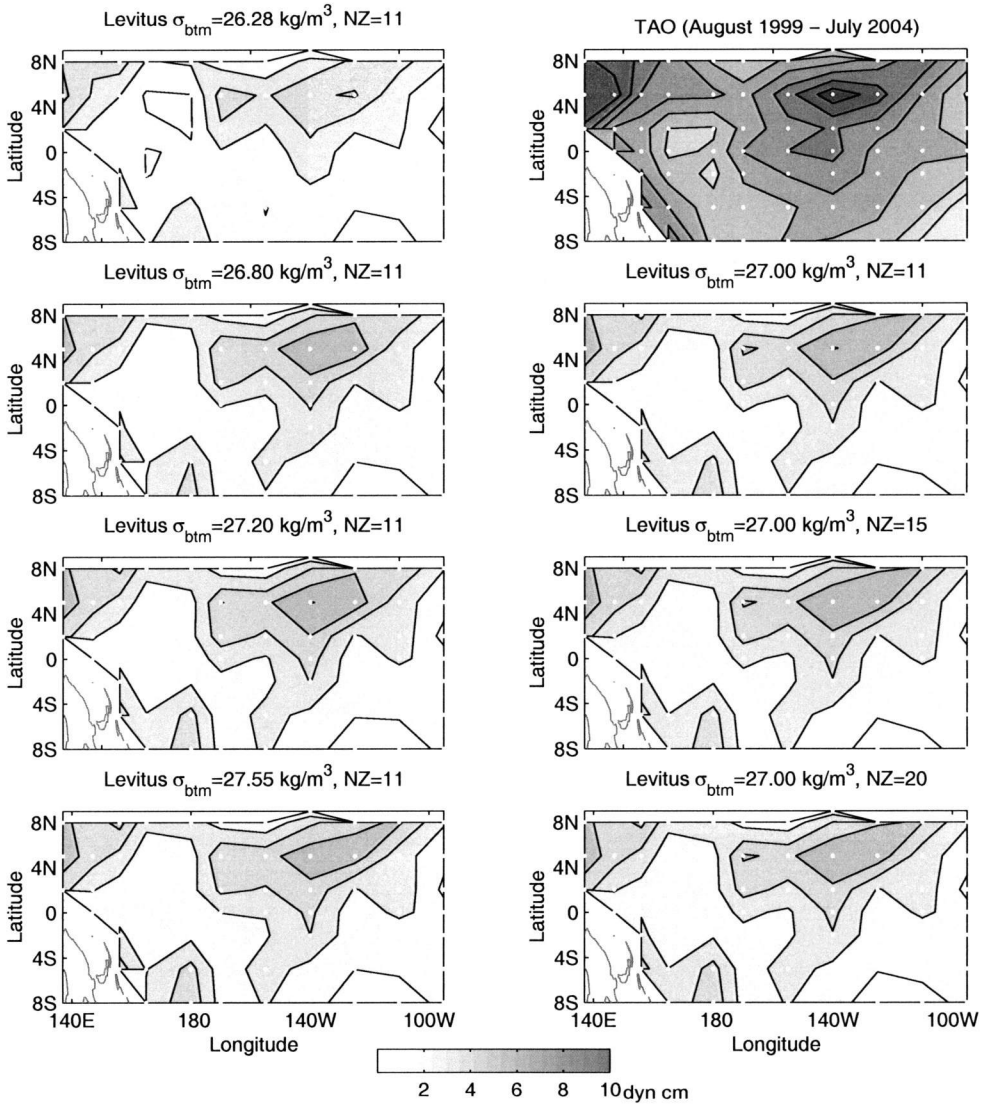

Figure 44. Similar to Figure 42, except for Levitus standard deviation of DH.

The standard deviations of model and Levitus DHs for $NZ = 11$ are largest when $26.80 \leq \sigma_{btm} \leq 27.20\ kg\ m^{-3}$ (Figures 43 and 44). For $\sigma_{btm} = 27.00\ kg\ m^{-3}$, the model DH variability increases slightly for $NZ = 20$ layers. As expected, the magnitudes of the standard deviations of the monthly model and Levitus fields are much smaller than those of the daily TAO measurements. While the spatial structure of the Levitus and TAO DH standard deviations have high agreement, the spatial structure of the ECMWF driven model DH standard deviations is very different from the observed structure. Note that the highly resolved QuikSCAT winds used to drive the GCAML model in the assimilation studies of Perez and Miller (2005) produce much higher agreement to the TAO DH observations than the above simulations with climatological wind forcing.

4.5 Summary and Conclusions

This vertical resolution study was designed to analyze the sensitivity of the GCAML model to the parameters that define the base of the active region and the distribution of the vertical layers. Given the above DH and ECS comparisons, $\rho_{btm} = 1027.00\ kg\ m^{-3}$ (nominal depth of 600 m) is a suitable density value with which to define the active region in the GCAML model. Due to the lack of sensitivity of the DHs and ECS to increasing from 15 to 20 layers, 15 vertical layers are chosen. This allows realistic simulation of the ECS and DHs in the equatorial Pacific while keeping the size of the model state space relatively small for data assimilation purposes (Perez and Miller 2005; Chapter 6).

The positive model mean DH bias is not removed for any of the active layer configurations tested here and is still present in GCAML runs with improved wind

forcing (Perez and Miller 2005). Forced by climatological heat and salt fluxes, the model drifts away from the Levitus initialization and develops significant biases in temperature and salinity such that the thermocline is too deep or the water column is too fresh in the equatorial waveguide. As was discovered in Perez and Miller (2005) and Chapter 6, these biases limit the success of anomaly-for-anomaly assimilation in the tropics.

4.6 References

Busalacchi, A. J., M. J. McPhaden, J. Picaut, 1994: Variability in the equatorial Pacific sea surface topography during the verification phase of the TOPEX/Poseidon mission. *J. Geophys. Res.,* **99,** 24 725-24 738.

Chen, D., L. M. Rothstein, and A. J. Busalacchi, 1994a: A hybrid vertical mixing scheme and its application to tropical ocean models. *J. Phys. Oceanogr.,* **24,** 2156-2179.

Chen, D., A. J. Busalacchi, and L. M. Rothstein, 1994b: The roles of vertical mixing, solar radiation, and wind stress in a model simulation of the sea surface temperature seasonal cycle in the tropical Pacific Ocean. *J. Geophys. Res.,* **99,** 20 345-20 359.

Chen, D., W. T. Liu, S. E. Zebiak, M. A. Cane, Y. Kushnir, and D. Witter, 1999: Sensitivity of the tropical Pacific Ocean simulation to the temporal and spatial resolution of wind forcing. *J. Geophys. Res.,* **104,** 11 261-11 271.

Conkright, M. E., R. A. Locarnini, and H. E. Garcia 2002: *World ocean atlas 2001: Objective analyses, data statistics, and figure, CD Rom documentation,* National Oceanographic Data Center, Silver Spring, MD.

Cox, M. D., 1980: Generation and propagation of 30-day waves in a numerical model of the Pacific. *J. Phys. Oceanogr.,* **10,** 1168-1186.

Donohue, K. A., and M. Wimbush, 1998: Model results of flow instabilities in the tropical Pacific Ocean. *J. Geophys. Res.,* **103,** 21 401-21 412.

European Centre for Medium-Range Weather Forecasts (ECMWF), 1994: The description of the ECMWF/WCRP Level III-A Global Atmospheric Data Archive, *Tech. Attach.,* 72 pp., Reading, England, U. K.

Gent, P. R., and M. A. Cane, 1989: A reduced gravity, primitive equation model of the upper equatorial ocean. *J. Comp. Physics,* **81,** 444-480.

Gourdeau, L., J. Verron, T. Delcroix, A. J. Busalacchi, and R. Murtugudde, 2000. Assimilation of TOPEX/Poseidon altimetric data in a primitive equation model of the tropical Pacific Ocean during the 1992-1996 El Niño Southern Oscillation period. *J. Geophys. Res.,* **105,** 8473-8488.

Hackert, E. C., A. J. Busalacchi, and R. Murtugudde, 2001: A wind comparison study using an ocean general circulation model for the 1997-1998 El Niño. *J. Geophys. Res.,* **106,** 2345-2362.

Jochum, M., and R. Murtugudde, 2004: Internal variability of the tropical Pacific Ocean. *Geophys. Res. Lett.,* **31**, L14309, doi: 10.1029/2004GL020488.

Johnson, G. C., and M. J. McPhaden, 1999: Interior pycnocline flow from the subtropical to the equatorial Pacific Ocean. *J. Phys. Oceanogr.,* **29,** 3073-3089.

Kessler, W. S., L. M. Rothstein, and D. Chen, 1998: The annual cycle of SST in the eastern tropical Pacific, diagnosed in an ocean GCM. *J. Climate,* **11,** 777-799.

Kessler, W. S., G. C. Johnson, and D. W. Moore, 2003: Sverdrup and nonlinear dynamics of the Pacific Equatorial Currents. *J. Phys. Oceanogr.,* **33,** 994-1008.

Levitus, S., T. Boyer, J. Antonov, R. Burgett, 1994: *World ocean atlas 1994, Temperature, NOAA Atlas NESDIS,* vol. 4, 129 pp., Natl. Oceanic and Atmos. Admin., Silver Spring, MD.

Lyman, J. M., D. B. Chelton, R. A. deSzoeke, and R. M. Samelson, 2005a: Tropical instability waves as a resonance between equatorial Rossby waves. *J. Phys. Oceanogr.,* **35,** 232-254.

Lyman, J. M., G. C. Johnson, and W. S. Kessler, 2005b: Structure of 17-day versus 33-day tropical instability waves in the equatorial Pacific. *J. Phys. Oceanogr.,* revised.

McCreary, J. P, and Z. Yu, 1992: Equatorial dynamics in a 2.5-layer model. *Prog. Oceanogr.,* **29,** 61-132.

McCreary, J. P., P. Lu, and Z. Yu, 2002: Dynamics of the Pacific subsurface countercurrents. *J. Phys. Oceanogr.,* **32,** 2379-2404.

Millero, F. J., and A. Poisson, 1981: International one-atmosphere equation of state of seawater. *Deep-Sea Res.,* **28,** 625-629.

Murtugudde, R., and A. J. Busalacchi, 1998: Salinity effects in a tropical ocean model. *J. Geophys. Res.,* **103,** 3283-3300.

Murtugudde, R., R. Seager, and A. J. Busalacchi, 1996: Simulation of the tropical oceans with an ocean GCM coupled to an atmospheric mixed-layer model. *J. Climate,* **9,** 1795-1815.

Murtugudde, R., J. Beauchamp, C. R. McClain, M. Lewis, and A. J. Busalacchi, 2002: Effects of penetrative radiation on the upper tropical ocean circulation. *J. Climate,* **15,** 470-486.

Oberhuber, J., 1988: An atlas based on 'COADS' Data Set, *Rep. 15.,* Max-Planck-Inst. für Meterol., Hamburg, Germany.

Perez, R. C., and R. N. Miller, 2005: Impact of a reduced state space Kalman filter on the equatorial Pacific cold tongue and tropical instability waves. *Submitted to J. Geophys. Res.*

Perez, R. C., D. B. Chelton, and R. N. Miller, 2005: The effects of wind forcing and background mean currents on the latitudinal structure of equatorial Rossby waves. *J. Phys. Oceanogr.,* **35,** 666-682.

Philander, S. G. H., 1978: Instabilities of zonal equatorial currents, Part 2. *J. Geophys. Res.,* **83,** 3679-3682.

Qiao, L., and R. H. Weisberg, 1995: Tropical instability wave kinematics: Observations from the Tropical Instability Wave Experiment. *J. Geophys. Res.,* **100,** 8677-8693.

Seager, R., M. Blumenthal, and Y. Kushnir, 1995: An advective atmospheric mixed layer model for ocean modeling purposes: Global simulation of surface heat fluxes. *J. Climate,* **8,** 1951-1964.

Seager, R., R. Murtugudde, A. Clement, C. Herweijer, 2003: Why is there an evaporative minimum at the equator? *J. Climate,* **16,** 3793-3802.

Verron, J., L. Gourdeau, D. T. Pham, R. Murtugudde, and A. J. Busalacchi, 1999: An extended Kalman filter to assimilate satellite altimeter data into a nonlinear numerical model of the tropical Pacific Ocean: method and validation. *J. Geophys. Res.,* **104,** 5441-5458.

5 Impact of a reduced state space Kalman filter on the equatorial Pacific cold tongue and tropical instability waves

Renellys C. Perez, and R. N. Miller

Submitted to the

Journal of Geophysical Research, Oceans

2000 Florida Avenue, N.W., Washington, D.C. 20009

5.1 Abstract

A four-dimensional multivariate data assimilation scheme has been developed to determine whether assimilation of dynamic height data can improve the model structure of temperature and zonal currents in the cold tongue on interannual to intraseasonal timescales and the statistics of simulated tropical instability waves (TIWs) during August 1999 to July 2004. The assimilation scheme combines a reduced gravity, nonlinear, equatorial β-plane model with Tropical Atmosphere Ocean (TAO) dynamic height anomalies (DHA) via a reduced state space Kalman filter (RKF). The model is forced by QuikSCAT satellite winds and a 5-day assimilation cycle is chosen to resolve and correct TIWs.

A Monte Carlo Markov Chain model is used to construct a forecast error model in a reduced state space spanned by Empirical Orthogonal Functions. Statistical hypothesis tests, comparisons to withheld observations, and analysis of prior and posterior errors were used to evaluate the performance of the RKF. The assimilation of TAO DHA improves the interannual and intraseasonal variability of sea surface height, reduces the cold tongue bias in the waveguide, and increases the core strength of the Equatorial Undercurrent. The ability of the assimilation to improve the cold tongue evolution is limited by the skill of the model cold tongue seasonal cycle. In the assimilated runs, the seasonality, zonal structure, phase, and spectral properties of the TIWs were better correlated with the observed TIWs, but the amplitudes were reduced and the westward phase speeds increased. An autoregressive model added to the innovation sequence produced a nearly optimal RKF and improved the overall performance of the assimilation scheme.

5.2 Introduction

Data assimilation is a means of converting a sparse set of observations into a highly resolved estimate of the state of the system using a numerical model as a dynamic interpolator. The Kalman filter provides an optimal estimate of the present state of the system, albeit at computational expense proportional to the cube of the number of model state variables. Although other methods of data assimilation such as variational techniques have been successfully applied in the tropical Pacific (some recent examples include Bennett et al. 2000; Vossepoel et al. 2002; Vialard et al. 2003; Borovikov et al. 2005), the ability to realistically simulate the large scale, low frequency equatorial dynamics with low-order numerical models has made the tropical Pacific ocean particularly well suited for Kalman filtering experiments.

Early Kalman filter schemes applied to the tropical Pacific assimilated monthly sea surface height anomalies (SSHA) from island tide gauges (Miller and Cane 1989; Miller et al. 1995; Cane et al. 1996; Chan et al. 1996) or dynamic height anomalies (DHA) estimated from expendable bathythermograph (XBT) profiles in the waveguide (Miller et al. 1995; Reverdin et al. 1996) into finite difference models of the linearized shallow water equations with equatorial β-plane and long-wave approximations (e.g., Cane and Patton 1984). These studies focused on the reduction of SSHA errors on interannual and intraseasonal time scales.

Recent tropical Pacific Kalman filter implementations have introduced more sophisticated, nonlinear general circulation models (GCMs) with assimilation windows smaller than a month, enabling the assimilation of higher frequency Topex/Poseidon SSHA (Fukumori et al. 1999; Verron et al. 1999; Gourdeau et al. 2000; Dewitte et al. 2003; Parent et al. 2003) and subsurface temperature

measurements from the multi-decadal Tropical Atmosphere Ocean (TAO) Project (McPhaden 1993; Keppenne and Rienecker 2003; Keppenne et al. 2005). Daily to weekly assimilation windows require high frequency wind forcing such as winds derived from scatterometer measurements (Dewitte et al. 2003; Keppenne and Rienecker 2003; Parent et al. 2003) or model reanalyses (Fukumori et al. 1999). These high resolution winds should resolve the relatively small scale features in the tropical Pacific wind field that are coupled to the equatorial cold tongue surface temperatures and the tropical instability waves (TIWs) that perturb the cold tongue frontal boundaries (Chelton et al. 2001). These westward propagating waves have periods of 17 to 33 days in the tropical Pacific (Lyman et al. 2005b and references therein), are most active during La Niña, and are nearly suppressed during El Niño (Baturin and Niiler 1997). To our knowledge, the impact of data assimilation on TIWs has not been adequately studied.

In this study, a reduced state space Kalman filter (RKF) has been developed for the equatorial Pacific during the period August 1999 to July 2004 with 5-day wind forcing and a 5-day assimilation window chosen to resolve and correct TIWs in the model. The goal of this study is to gauge whether the assimilation of 5-day TAO DHA into a nonlinear GCM can improve the structure of temperature and zonal currents in the cold tongue on interannual to intraseasonal timescales and simultaneously improve the statistics of the simulated TIWs. The limitations of anomaly-for-anomaly assimilation in a model whose seasonal cycle may be biased or out-of-phase in the cold tongue and a few degrees away from the equator will also be explored.

The paper is organized as follows. The RKF and its essential components are described in Section 5.3. The performance of the RKF is evaluated in Section 5.4 via quantitative comparisons to observations, analysis of the prior and posterior errors, and the statistics of the sequence of model-data misfits. In Section 5.5, the impact of the assimilation on the structure of temperature and zonal currents in the cold tongue and the properties of the model TIWs are analyzed. The sensitivity of these results to the number of degrees of freedom in the reduced state space is also explored. In Section 5.6, the addition of an autoregressive model to the RKF innovation sequence and the impact on the model bias is discussed. Section 5.7 summarizes the results of this cold tongue assimilation experiment and discusses the limitations of anomaly-for-anomaly assimilation.

5.3 Data Assimilation Scheme

5.3.1 RKF Equations. The assimilation scheme used in this study has evolved from the Kalman filter methodology of Miller and Cane (1989) and Miller et al. (1995) and numerically solves equations (10)-(13)

$$\mathbf{x}^{\mathbf{f}}(\mathbf{t}_i) = \mathbf{M}\mathbf{x}^{\mathbf{a}}(\mathbf{t}_{i-1}) \tag{7}$$

$$\mathbf{x}^{\mathbf{t}}(\mathbf{t}_i) = \mathbf{M}\mathbf{x}^{\mathbf{t}}(\mathbf{t}_{i-1}) + \eta(\mathbf{t}_{i-1}) \tag{8}$$

$$\mathbf{y}_i^{\mathbf{o}} = \mathbf{H}\mathbf{x}^{\mathbf{t}}(\mathbf{t}_i) + \epsilon_i \tag{9}$$

$$\mathbf{x}^{\mathbf{a}}(\mathbf{t}_i) = \mathbf{x}^{\mathbf{f}}(\mathbf{t}_i) + \mathbf{K}_i(\mathbf{y}_i^{\mathbf{o}} - \mathbf{H}\mathbf{x}^{\mathbf{f}}(\mathbf{t}_i)) \equiv \mathbf{x}^{\mathbf{f}}(\mathbf{t}_i) + \mathbf{K}_i\mathbf{d}_i \tag{10}$$

$$\mathbf{K}_i = \mathbf{P}^{\mathbf{f}}(\mathbf{t}_i)\mathbf{H}^{\mathbf{T}}(\mathbf{H}\mathbf{P}^{\mathbf{f}}(\mathbf{t}_i)\mathbf{H}^{\mathbf{T}} + \mathbf{R})^{-1} \tag{11}$$

$$\mathbf{P}^{\mathbf{f}}(\mathbf{t}_i) = \mathbf{M}\mathbf{P}^{\mathbf{a}}(\mathbf{t}_{i-1})\mathbf{M}^{\mathbf{T}} + \mathbf{Q} \tag{12}$$

$$\mathbf{P}^{\mathbf{a}}(\mathbf{t}_i) = (\mathbf{I} - \mathbf{K}_i\mathbf{H})\mathbf{P}^{\mathbf{f}}(\mathbf{t}_i). \tag{13}$$

The notation used here follows the unified notation proposed by Ide et al. (1997). In equations (7)-(10), the vector $\mathbf{x}(\mathbf{t_i})$ with superscript 'f', 't', or 'a' represents the numerical forecast, the true system, or the updated forecast after assimilation, respectively, at time t_i. The model forecast, $\mathbf{x^f}(\mathbf{t_i})$, is given by the forecast update operator, $\mathbf{M}$, which is a linearized approximation of the nonlinear model dynamics and operates on $\mathbf{x^a}(\mathbf{t_{i-1}})$, the best available analysis at time t_{i-1}. The true system, $\mathbf{x^t}(\mathbf{t_i})$, is assumed to differ from the model system by a stationary white process $\eta(\mathbf{t_i})$, with system noise covariance $\mathbf{Q}$. Observations, $\mathbf{y_i^o}$, are related to the true system by the measurement matrix, $\mathbf{H}$, and the white sequence of observation errors $\epsilon_\mathbf{i}$ with covariance $\mathbf{R}$. The innovation sequence or model-data misfit $\mathbf{d_i}$, weighted by the Kalman gain matrix $\mathbf{K_i}$, in (10) is used to correct the model forecast. If all of the information has been extracted from the observations, the innovation sequence should be a white sequence with zero autocorrelation at non-zero lags (Kailath 1968; Daley 1992; Chan et al. 1996). The Kalman gain which describes the relative faith in the model and the data is updated every assimilation cycle by equation (11). The ability of the forecast and analysis error covariances, $\mathbf{P^f}(\mathbf{t_i})$ and $\mathbf{P^a}(\mathbf{t_i})$, respectively, to evolve in time according to equations (12) and (13) distinguishes the Kalman filter from other assimilation techniques.

Matrix operations such as $\mathbf{MP^a}(\mathbf{t_i})\mathbf{M^T}$ and $\mathbf{P^f}(\mathbf{t_i})\mathbf{H^T}(\mathbf{HP^f}(\mathbf{t_i})\mathbf{H^T}+\mathbf{R})^{-1}$ become impractical if the number of state variables (N) is large, as $\mathbf{M}$, $\mathbf{P^a}(\mathbf{t_i})$, and $\mathbf{P^f}(\mathbf{t_1})$ have dimension $N \times N$. Cane et al. (1996) found that using as few as nine truncated multivariate empirical orthogonal functions (EOFs) derived from a long run of the Cane and Patton (1984) model without assimilation were sufficient

to produce results similar to the full state space Kalman filter. Although many different techniques can be utilized to reduce N, an EOF based approach is adopted to reduce the size of the state space for the Kalman filter without changing the number of model state variables (Cane et al. 1996). The Kalman gain, measurement matrix, forecast update operator, and forecast and analysis error covariances are then updated in the reduced state space spanned by m multivariate EOFs (described in Section 5.3.4.1). The matrix of EOFs, $\mathbf{X}$, is then used to project the reduced state space correction to the forecast into the model state space via

$$\mathbf{x^a(t_i) = x^f(t_i) + XK_i d_i}. \tag{14}$$

Given values for $\mathbf{M}$, $\mathbf{Q}$, $\mathbf{H}$, and $\mathbf{R}$ and an initial estimate of $\mathbf{P^a(t_0)}$ the RKF given by equations (11)-(14) can be solved for every assimilation cycle. Within an assimilation run, $\mathbf{H}$ and $\mathbf{R}$ change only in response to missing data.

Implicit in the above equations is the assumption that the observations and models are unbiased estimates of the true state of the ocean. Given the well-documented cold bias and seasonal cycle errors in the equatorial upwelling region (Stockdale et al. 1998 and references therein), present models of the tropical Pacific do not satisfy this criteria. To treat unbiased quantities, the RKF operates on 5-day anomalies from the model seasonal cycle and assimilates 5-day anomalies from the observed seasonal cycle. Removing the seasonal cycle allows the model physics to be represented by the linearized forecast update operator, $\mathbf{M}$. An improperly specified seasonal cycle can lead to a non-white, i.e., colored, innovation sequence. Chan et al. (1996) found that a colored innovation sequence in a tropical Pacific

data assimilation scheme with a linear ocean model can be whitened by modeling the innovation process as an autoregressive process.

5.3.2 Data.

5.3.2.1 Wind Forcing and Climatology: The wind stress data were obtained from the SeaWinds scatterometer aboard the QuikSCAT satellite (Chelton and Freilich 2005) which was launched June 19, 1999. The QuikSCAT wind stress fields from August 1999 to July 2004 are binned into a 5-day x 1° zonal x 1° meridional grid with 8-day x 4° zonal x 2° meridional loess smoothing (Schlax and Chelton 1992). The filtering properties of these loess parameters are similar to those of 4.8-day x 2.4° x 1.2° block averages. The high-frequency wind stress enables the development of a 5-day error model and assimilation window. The QuikSCAT winds resolve the intense bands of wind stress divergence and curl in the waveguide and thus are capable of providing a high level of realism to numerical simulations of the tropical Pacific (e.g., Perez 2005; Perez et al. 2005).

Several monthly climatologies are used to supply forcing to the model surface boundary. These monthly fields include Interannual Satellite Cloud Climatology Project (ISCCP) cloud cover data, Earth Radiation Budget Experiment (ERBE) solar radiation, Oberhuber (1988) precipitation, and European Center for Medium Range Weather Forecasting (ECMWF 1994) estimates of wind speed, air temperature, and humidity at sea level. The ECMWF wind speed climatologies are only used in the heat flux specification (Section 5.3.3.1). Levitus temperature and salinity (Levitus et al. 1994) initialize the model and provide forcing at the lateral boundaries. All climatological fields have been linearly interpolated from a 2° zonal x 2° meridional grid to match the 1° zonal x 1° meridional resolution of the wind

forcing. Cubic spline interpolation (identical to the temporal interpolation used by the model) converts the monthly climatologies into 5-day climatologies.

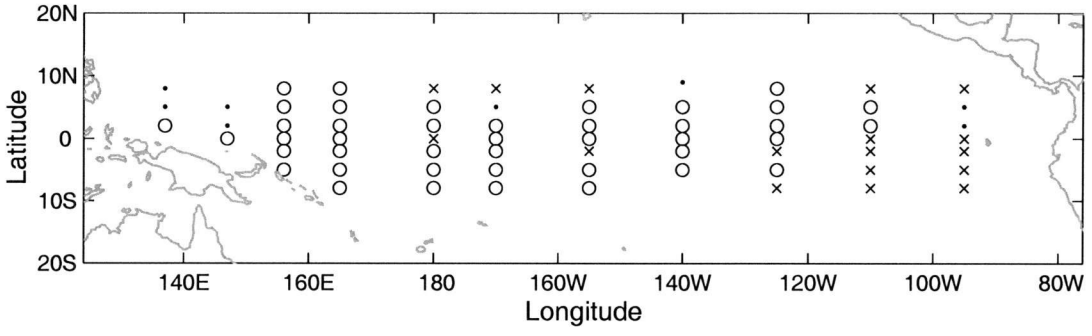

Figure 45. Map of the 42 TAO moorings from which DHA are assimilated (circles) during the August 1999 to July 2004 period. The x-marks indicate the 17 locations that are used for validation and the 8 dots indicate TAO locations not used in this study.

5.3.2.2 Assimilated and Withheld Data: In addition to the wind stress and climatological data used to force the model, observations are required for assimilation and validation. TAO DHA are assimilated into the model during the five-year period of QuikSCAT wind forcing. Using the UNESCO equation of state for seawater (Millero and Poisson 1981), TAO estimates daily specific volume anomalies based on vertical profiles of temperature with salinity inferred from local temperature-salinity (T-S) properties (Conkright et al., 2002). The specific volume anomalies are vertically integrated to generate dynamic heights (DH) relative to 500 decibars (db) at the TAO moorings (Figure 45). Errors in the TAO DH stem from the use of T-S relationships, the limited vertical resolution of the thermistor chain moorings (quadrature error) and gap filling through regression analysis of missing data between 300 and 500 m depth (Johnson and McPhaden 1993; Busalacchi et al. 1994). These combined errors range from 3 to 4 dynamic cm (dyn cm) in the west

to 2 to 3 dyn cm in the east (Busalacchi et al., 1994) and may decrease meridionally from 8°S to 8°N (as in Figure 9 from Vossepoel et al. 1999).

To prepare the data for use in the RKF, 5-day averages of daily TAO DH are computed when there are five consecutive daily measurements. The seasonal cycle of the TAO DH is estimated by stacking together the five years of 5-day values and passing the resulting seasonal cycle through two 60-day running mean low-pass filters. This seasonal cycle is then removed from the data to produce 5-day DHA. Data are assimilated at a given TAO mooring if less than 25% of the 5-day averages are missing during this five-year period and if the correlation between the model and TAO seasonal cycle is greater than 0.6. Only 42 TAO moorings satisfied both criteria and are used in the RKF (circles in Figure 45). Locations that satisfy the first criterion alone are used for scheme validation (17 moorings denoted by x-marks in Figure 45).

TAO measurements such as withheld DH, temperature profiles, 20°C isotherm depths, and ADCP velocities along the equator are used to validate the RKF performance. Merged altimetric sea level anomalies available on a 7-day x 1/3° x 1/3° grid are used to compare the SSHA signatures of TIWs as the TAO zonal spacing of 15° is too sparse to detect the westward propagation. The altimeter products were produced by Ssalto/Duacs as part of the Environment and Climate EU Enact project (EVK2-CT2001-00117) and distributed by the Archiving, Validation and Interpretation of Satellite Oceanographic data (AVISO) program, with support from the French Space Agency.

5.3.3 Ocean Model Coupled to Atmospheric Mixed Layer. The ocean GCM is the Gent and Cane (1989) nonlinear, reduced gravity, β-plane model.

Recent upgrades to the model include the addition of salinity as a dynamic variable (as in Murtugudde and Busalacchi 1998) and coupling to an advective atmospheric mixed layer model (Seager et al. 1995; Murtugudde et al. 1996). This mixed layer model requires the specification of solar radiation, cloud cover, wind speed, and the air temperature and humidity at sea level provided from the climatologies listed in Section 5.3.2.1. We'll refer to the Gent and Cane (1989) model as the GC model and the version with an advective atmospheric mixed layer as the GCAML model. Both the GC and GCAML have been successfully applied to the study of equatorial Pacific cold tongue and TIWs (Kessler et al. 1998; Jochum and Murtugudde 2004), used in wind forcing studies (Chen et al. 1999; Hackert et al. 2001; Perez 2005; Perez et al. 2005), and in data assimilation studies (Verron et al. 1999; Gourdeau et al. 2000; Ballabrera-Poy et al. 2005). The GCAML version used in this study resembles that of Hackert et al. (2001) and significant departures from that implementation are described below.

5.3.3.1 Model Features: In addition to dynamic fields such as zonal velocity, meridional velocity, layer thickness, salinity, and temperature, the GCAML model has been modified to calculate DH relative to 500 db prognostically from the model temperature and salinity, matching in all other respects the processing applied by TAO (Section 5.3.2.2). The model domain spans the entire tropical Pacific from 124°E to 76°W and 30°S to 30°N. No-slip conditions are specified on the eastern and western boundaries. At the northern and southern boundaries, free-slip conditions are specified and there is a gradual relaxation to Levitus climatology over a 5° wide sponge layer.

Table 7. Sample layer distributions and the fixed ratio of the k^{th} layer thickness to the total active layer thickness, s_k for $k > 1$, given an active layer depth of 400 m.

$h_{k=1,15}$	$s_{k=1,15}$
50	
10	0.0286
10	0.0286
10	0.0286
10	0.0286
10	0.0286
10	0.0286
10	0.0286
20	0.0571
20	0.0571
40	0.1143
40	0.1143
40	0.1143
60	0.1714
60	0.1714

5.3.3.2 Resolution: Resolution is chosen to minimize the size of the model state space for the data assimilation experiments while retaining a realistic representation of the cold tongue, equatorial current system (ECS), and the meridional and vertical shears that generate TIWs (Philander 1978; Cox 1980; McCreary and Yu 1992; Donohue and Wimbush 1998; Lyman et al. 2005b). Given that TIWs have zonal wavelengths of 1000 to 2000 km (Qiao and Weisberg 1995), a uniform zonal grid spacing of 1° is chosen. Meridional resolution of 0.25° to 0.4° in the equatorial waveguide was found to be sufficient to produce realistic TIWs with the GC (Kessler et al. 1998) and GCAML (Jochum and Murtugudde 2004) model. Hence, the meridional grid has 0.33° resolution in the equatorial waveguide and stretches to 1° resolution at the poleward boundaries.

The model active region is defined by specifying a bottom density, ρ_{btm}, by selecting the temperature and salinity of the base of the active region, T_{btm} and S_{btm}, respectively. As ρ_{btm} is increased, the slope of the active layer base decreases and the layers approach z-levels and penetrate deeper into the water column. Therefore, a deeper active layer base requires an increase of NZ, the number of layers, to maintain sufficient vertical resolution in the upper ocean. A vertical resolution study of the GCAML using ECMWF climatological wind forcing by Perez (2005) compared five values for ρ_{btm} ranging from 1026.28 $kg\ m^{-3}$ to 1027.55 $kg\ m^{-3}$ and $NZ = 11, 15$, and 20. It was found that the parameters $\rho_{btm} = 1027.00\ kg\ m^{-3}$ (which corresponds to $T_{btm} = 9°C$, $S_{btm} = 34.85$ psu, and a nominal depth of 600 m) and $NZ = 15$, and the initial layer distribution given in Table 7 best resolved the upper 500 m of the water column without sacrificing the efficiency inherent to the model reduced gravity configuration. Specifically, this configuration produced the

best Equatorial Undercurrent (EUC) compared with 1988 - 2004 TAO ADCP zonal velocities along the equator, and the best DH and 20°C isotherm depths at the TAO moorings in the waveguide. Less sensitivity was found in the strength of currents whose cores lie above the thermocline, specifically the eastward flowing North Equatorial Countercurrent (NECC) and the westward flowing South Equatorial Current (SEC). For $\rho_{btm} = 1027.00\ kg\ m^{-3}$, increasing the number of layers to 20 did not improve the model performance significantly.

5.3.4 RKF Components.

5.3.4.1 Reduced State Space: The reduced state space is obtained from a GCAML run without assimilation driven by the 5 years of QuikSCAT winds (NODA). The multivariate EOFs are constructed from the deviations of the full model fields from an identical GCAML run with seasonal cycle QuikSCAT winds (SEAS). Both runs were spun up for the 30 years preceding July 1999 with QuikSCAT seasonal cycle forcing. The seasonal cycle QuikSCAT winds were generated by fitting an annual cycle and five harmonics to the available QuikSCAT winds. Originally designed for monthly wind forcing, the GC/GCAML models have a 360-day calendar year. Rather than reprogramming the model calendar to accept 5-day forcing in a 365.25-day year, we have modified the wind forcing from a 365.25-day to a 360-day year by folding in every 73^{rd} 5-day record into the transition from July to August. In other words, the 5-day record that spans the July-August transition is averaged with the two adjacent 5-day records, thereby compressing 15 days into 10 days. This compression is also applied to the climatological fields and the assimilated and withheld data and gives 360 records during the August 1999 to July 2004 period.

The full model state space is therefore represented by $360 \times N$ (N =16089 horizontal grid points x 15 layers x 5 diagnostic variables) state variables. Since the rank of this matrix can be no larger than 360, this system has no more than 360 degrees of freedom and the size of the state space can be reduced from $O(10^6)$ to $O(10^2)$ or smaller.

The two singular value decompositions (SVDs) used to reduce the model state space have the form

$$\mathbf{A_{NODA} - A_{SEAS}} = \mathbf{U_1 D_1 V_1^T} \quad (15)$$

$$\left(\frac{\mathbf{(U_1 D_1)_{u,k}}}{\sigma_\mathbf{u}} \; \frac{\mathbf{(U_1 D_1)_{v,k}}}{\sigma_\mathbf{v}} \; \frac{\mathbf{(U_1 D_1)_{h,k}}}{\sigma_\mathbf{h}} \; \frac{\mathbf{(U_1 D_1)_{S,k}}}{\sigma_\mathbf{S}} \; \frac{\mathbf{(U_1 D_1)_{T,k}}}{\sigma_\mathbf{T}}\right) = \mathbf{U_2 D_2 V_2^T} \quad (16)$$

The first step is a univariate step applied to the seasonal cycle deviations of each model variable (u, v, h, S, T) and each layer $k = 1, 15$ retaining enough singular vectors to capture 99% of the original variance. The resulting EOF amplitudes are combined for a multivariate step via field-specific normalization factors $(\sigma_u, \sigma_v, \sigma_h, \sigma_S, \sigma_T)$ whose values are given by the overall L^2 norm of the field-specific $\mathbf{D_1}$ (Table 8). Keeping $m = 44, 80, 139$, and 226 of the singular vectors from the multivariate step captures approximately 80, 89, 95, and 98% of the original variance, respectively. The matrix $\mathbf{X}$ in (14) which transforms back into the full state space is given by

$$\mathbf{X} = \mathbf{V_2^T}\left(\sigma_\mathbf{u}(\mathbf{V_1^T})_\mathbf{u,k} \; \sigma_\mathbf{v}(\mathbf{V_1^T})_\mathbf{v,k} \; \sigma_\mathbf{h}(\mathbf{V_1^T})_\mathbf{h,k} \; \sigma_\mathbf{S}(\mathbf{V_1^T})_\mathbf{S,k} \; \sigma_\mathbf{T}(\mathbf{V_1^T})_\mathbf{T,k}\right). \quad (17)$$

Similarly, projections onto the reduced state space can by obtained by applying the appropriate $\mathbf{V_1}/\sigma$ to the seasonal cycle deviations and then multiplying by $\mathbf{V_2}$.

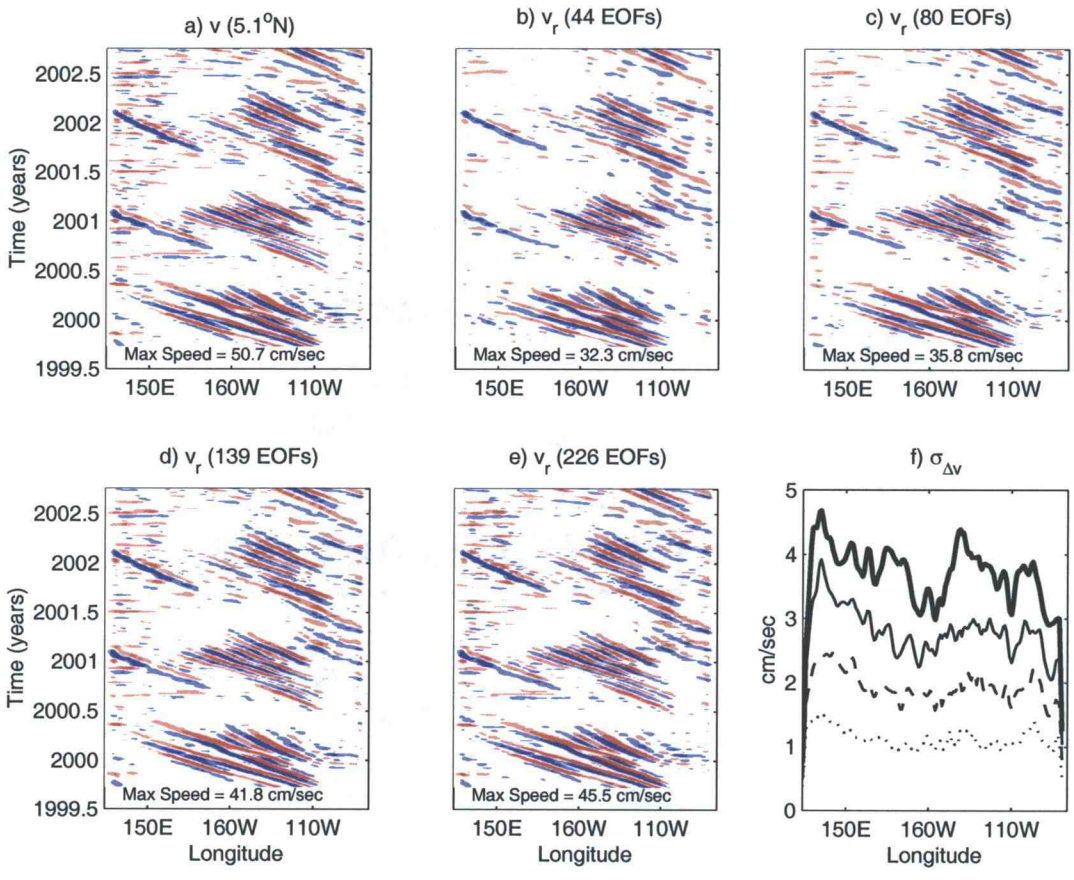

Figure 46. Reduced state space representation of surface layer meridional velocity from the first three years of the QuikSCAT wind driven GCAML run along 5.1°N. A 50-day high pass filter was applied to the a) meridional velocity (v) and the reconstructed meridional velocity (v_r) keeping b) 44, c) 80, d) 139, and e) 226 EOFs. Red and blue indicate northward and southward velocity, respectively. (f) The standard deviation of the difference between the v and v_r along 5.1°N for 44 (thick solid), 80 (thin solid), 139 (dashed), and 226 (dotted) EOFs.

Table 8. Normalization values used in multivariate step of the state space reduction.

$\sigma_{Variable}$	Value
σ_u	0.081 $m\ s^{-1}$
σ_v	0.032 $m\ s^{-1}$
σ_h	3.45 m
σ_S	0.064 psu
σ_T	0.981 °C

Large fluctuations in meridional velocity have been observed between 2° and 6°N associated with the westward propagation of tropical instability vortices (Kennan and Flament 2000). To determine if the reconstructed fields are capable of reproducing these large amplitude meridional velocity fluctuations, 50-day high-pass filtered surface meridional velocity (v_r) along 5.1°N for various values of m are compared with that of the original v for the first three years of the simulation (Figure 46). The surface layer meridional velocity structure and westward propagation are well reconstructed along 5.1°N with as few as 44 EOFs, although the amplitudes of the reconstructed velocities are weaker than the original fields. As the number of EOFs increases, the difference between v and v_r decreases as marked by the standard deviation, $\sigma(v - v_r)$, along 5.1°N (lower right panel of Figure 46).

5.3.4.2 Monte Carlo Simulations: Early tropical Pacific assimilation schemes applied to linear shallow water models have constructed a forecast error model with the assumptions that 1) the model errors were dominated by wind stress

errors, 2) the wind stress errors were white in time with homogenous anisotropic Gaussian structure of the form

$$< e(\vec{x_0}, t_0)e(\vec{x_1}, t_1) >= \sigma^2 \exp(-(x_1 - x_0)^2/L_x^2 - (y_1 - y_0)^2/L_y^2)\delta(t_1 - t_0), \quad (18)$$

and 3) the meridional winds could be neglected according to the long wave approximation (Miller and Cane 1989; Miller et al. 1995; Cane et al. 1996; Chan et al. 1996). In these formulations σ, L_x, and L_y represented the error amplitude and the zonal and the meridional decorrelation length scales, respectively, and were held constant. Random wind perturbations generated with these error models drove Monte Carlo simulations from which initial estimates of the model error covariance and system noise covariance matrix were generated.

More recent Monte Carlo simulations allow the error amplitude to vary spatially such that the wind stress error covariance has the form

$$< e(\vec{x_0}, t_0)e(\vec{x_1}, t_1) >= W(\vec{x_0}; \vec{x_1}) \exp(-(x_1 - x_0)^2/L_x^2 - (y_1 - y_0)^2/L_y^2)\delta(t_1 - t_0). \quad (19)$$

The amplitude of the forcing error variance, W, can be proportional to the point-by-point variance of the difference between the wind stress anomalies from two independent wind products as in Miller et al. (1995), the square of the standard deviation of small scale variability in the component wind stress (Kaplan et al., 2004), or the sample covariance of the winds used in forcing the model (Fukumori et al. 1999). Both components of the wind stress can be given independent error covariances structures with different scalings as in Kaplan et al. (2004).

The approach of Miller et al. (1995) is taken to construct a spatially-varying wind error amplitude for the QuikSCAT wind stress using a comparable wind product. Due to similar spatial coverage and overlapping time records, 1° x 1° wind speed ($10 - m$) measurements from the Special Sensor Microwave/Imager (SSMI) (Meissner et al. 2001) flown by the Defense Meteorological Satellite Program are used to estimate errors in the QuikSCAT wind speed on monthly time scales. The QuikSCAT and SSMI quality control methodologies have developed different means to exclude land, rain, and ice contaminated measurements (Meissner et al. 2001; Chelton and Freilich 2005). The removal of these contaminated measurements give the monthly mean estimates a fair-weather (i.e., non-raining conditions) bias over the ITCZ. Assuming the errors in QuikSCAT and SSMI are independent of one another, areas with large rms differences between QuikSCAT and SSMI should correspond to areas of large wind error amplitudes.

The seasonal cycle deviations are computed by removing an annual cycle and five higher harmonics from the five-year QuikSCAT and SSMI records. The standard deviations of the QuikSCAT and SSMI seasonal cycle deviations have much in common with high variability outside of the waveguide away from the Americas, in a narrow equatorial band between 140°W and 90°W, and off of the southwest coast of Mexico associated with wind jets through gaps in the Sierra Madre mountains (Figure 47). In the waveguide, the largest variability QuikSCAT-SSMI seasonal cycle deviations occurs over the ITCZ and in the western Pacific (lower panel of Figure 47). Large SSMI rainfall seasonal cycle deviations from the same five-year period are collocated with these areas of high QuikSCAT-SSMI variability (contours in the lower panel of Figure 47). Outside of the waveguide, less variance is explained

by the seasonal cycles of the winds and the variance of the wind speed difference is also large.

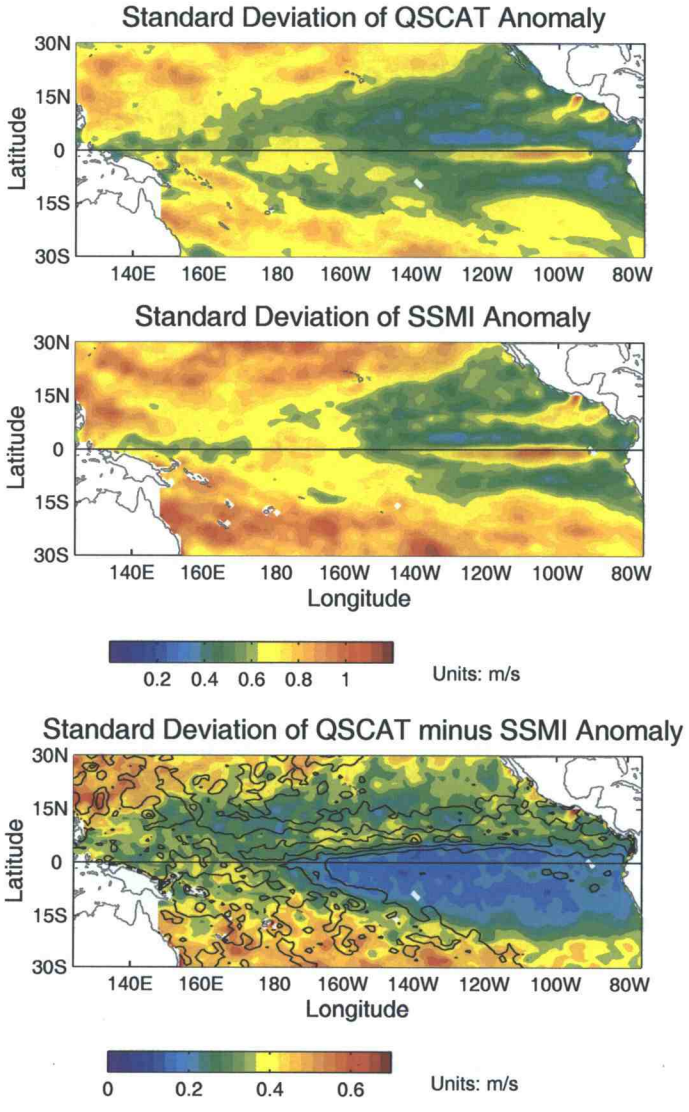

Figure 47. Five-year standard deviation of the monthly QuikSCAT (upper panel) and SSMI (center panel) seasonal cycle deviations of wind speed. Lower panel: five-year standard deviation of the difference between the QuikSCAT and SSMI seasonal cycle deviations of wind speed with contours of the five-year standard deviation of monthly SSMI seasonal cycle deviations of rainfall overlaid. The contour interval is 0.1 $mm\ hour^{-1}$.

To generate the random wind perturbations for the Monte Carlo simulations, two Gaussian random variables with zero mean and unit variance are constructed every five days at each gridpoint, $e^{\theta}(\vec{x},t)$ and $e^{r}(\vec{x},t)$, which represent the correction to the direction and amplitude of the wind stress, respectively. The directional errors, $d\theta$, are scaled so that the standard deviation is 2°. At each location, the wind stress amplitude correction is scaled by the five-year standard deviation of the differences between the QuikSCAT and SSMI wind speed seasonal cycle deviations, $V(\vec{x})$ (lower panel of Figure 47). This error structure is then scaled by 1.88 such that the random deviations combined with seasonal cycle visit the range of values present in the five-year QuikSCAT record. For example, the nominal wind stress errors along 5°N were 0.4 $dyn\ cm^{-2}$.

To generate the appropriate spatial decorrelation scales, the array of wind stress amplitude errors, $V_{i,j}e^{r}_{i,j}$ or $\mathbf{VE^r}$, with dimension $nx \times ny$ must be multiplied by two Cholesky matrices

$$\mathbf{d\tau} = \mathbf{C_x} \times \mathbf{VE^r} \times \mathbf{C_y}. \tag{20}$$

The $\mathbf{C_x}$ matrix has dimension $nx \times nx$ and is the Cholesky decomposition of the positive definite matrix $\mathbf{R_x}$ (e.g., $\mathbf{C_x} \times \mathbf{C_x^T} = \mathbf{R_x}$). Likewise, the $\mathbf{C_Y}$ matrix has dimension $ny \times ny$ and is the Cholesky decomposition of $\mathbf{R_y}$. The $(i,j)^{th}$ entry of $\mathbf{R_x}$ and $\mathbf{R_y}$ have the form

$$(R_x)_{i,j} = \exp(-(x_i - x_j)^2/L_x^2), \tag{21}$$

$$(R_y)_{i,j} = \exp(-(y_i - y_j)^2/L_y^2) \tag{22}$$

where $L_x = 10°$ and $L_y = 4°$. The zonal and meridional wind stress used to force the Monte Carlo simulations are

$$\tau^x(\vec{x},t) = (|T_s(\vec{x},t)| + d\tau(\vec{x},t))\cos(\Theta_s(\vec{x},t) + d\theta(\vec{x},t)), \quad (23)$$

$$\tau^y(\vec{x},t) = (|T_s(\vec{x},t)| + d\tau(\vec{x},t))\sin(\Theta_s(\vec{x},t) + d\theta(\vec{x},t)). \quad (24)$$

Here $|T_s|$ and Θ_s represent the magnitude and direction of the deterministic 5-day QuikSCAT seasonal cycle wind stress and $d\tau$ and $d\theta$ represent the randomly generated wind corrections.

5.3.4.3 Monte Carlo Markov Chain: Five Monte Carlo simulations of 5-year length were performed with different random perturbations to the QuikSCAT seasonal cycle winds (23) and (24). Within the simulations, the SEAS model fields are subtracted from the randomly forced model fields. These deviations are then projected onto our reduced state space using 139 of the multivariate singular vectors (Section 5.3.4.1). Each Monte Carlo simulation then produces a time series of model EOF amplitudes given random perturbations in the wind forcing. These amplitudes correspond to $\mathbf{U_2D_2}$ in (16). Assuming that the amplitudes evolve as a Markov process, 5-day lagged autoregressions similar to Cane et al. (1996) are applied to generate $\mathbf{M}$ and $\mathbf{Q}$. These equations have the form

$$\mathbf{A_k(t+1)} = \sum_{\mathbf{j=1}}^{\mathbf{m}}(\mathbf{M_{jk}A_j(t)}) + \mathbf{r_k(t+1)} \quad (25)$$

$$\mathbf{y} = \mathbf{A_k(t+1)} \quad (26)$$

$$\mathbf{x} = \mathbf{A_k(t)} \tag{27}$$

$$\mathbf{Q} = \frac{\mathbf{y^T y - M^T x^T y}}{\mathbf{N-1}} = \frac{\mathbf{r^T y}}{\mathbf{N-1}} \tag{28}$$

where $\mathbf{A_k(t)}$ is the amplitude of the k^{th} EOF at time t. The resulting $\mathbf{M}$ and $\mathbf{Q}$ matrices have dimension 139 × 139, although it may not be necessary to retain all 139 EOFs. If a second Markov process is applied to the residuals, $\mathbf{r_k(t)}$, the second order regression coefficients are not significantly different from zero. This confirms little color remains in $\mathbf{r_k(t)}$ and the evolution of $\mathbf{A_k}$ is well modeled by the Markov process $\mathbf{M}$. In all five runs, there is a dramatic fall off in the diagonal entries of $\mathbf{M}$ and an increased growth in the condition number of $\mathbf{M}$ after 44 EOFs. We therefore contrast assimilation runs with only 44 EOFs (ASSIM44) with runs with 139 EOFs (ASSIM139) to test the sensitivity of the assimilation scheme to the number of singular vectors used in the forecast error model.

$\mathbf{M}$ and $\mathbf{Q}$ are generated for each Monte Carlo simulation and averaged. These two matrices can then be used to get an initial equilibrium value for $\mathbf{P^a_{eq}} = \mathbf{P^f_{eq}}$ (Miller and Cane 1989) by setting $\mathbf{P^f(t_0)}$ equal to the average covariance of the amplitudes from the five Monte Carlo simulations and iterating (12) using $\mathbf{P^a(t_{i-1}) = P^f(t_{i-1})}$. The series $|\mathbf{P^f(t_{i+1}) - P^f(t_i)}|/|\mathbf{P^f(t_i)}|$ converges to less than 10^{-6} within 5.5 and 10.8 years (or 395 and 779 5-day steps) for $m = 44$ and 139, respectively.

5.3.4.4 Generation of H and R: The measurement matrix, $\mathbf{H}$, projects incremental changes to the amplitude of the reduced state space singular vectors into incremental changes of the 5-day DHA. $\mathbf{H}$ has dimension 42 x m, and the product $\mathbf{HP^f(t_i)H^T}$ projects $\mathbf{P^f(t_i)}$ from the reduced state space into DHA error covariances

at the 42 assimilated TAO locations (Figure 45). The assimilated observations are numbered sequentially from south to north and west to east such that location 1 corresponds to 8°S, 165°E, location 2 corresponds to 8°S, 180°, and location 42 corresponds to 8°N, 125°W.

Given the estimated errors in the western and eastern segments of the TAO array described in Section 5.3.2.2, the observation error covariance, **R**, is constructed such that the errors equal 3.5 dyn cm along 137°E and 2.5 dyn cm along 95°W with linearly decreasing values in between. It is also assumed that the errors at the 42 TAO locations are independent of one another (e.g., off diagonal entries, $R_{j,k}$, are zero). Relaxing this assumption does not significantly alter the assimilation results (not shown).

5.4 Performance of the Assimilation Scheme

The success of the RKF can be determined by making quantitative comparisons to withheld observations and analyzing the evolution of the forecast and analysis error covariances and the statistics of the innovation sequence. The evolution of the prior and posterior error covariance matrices are byproducts of the RKF and provide error bars for the model seasonal cycle anomalies as demonstrated by Miller (1990) and Miller et al. (1995).

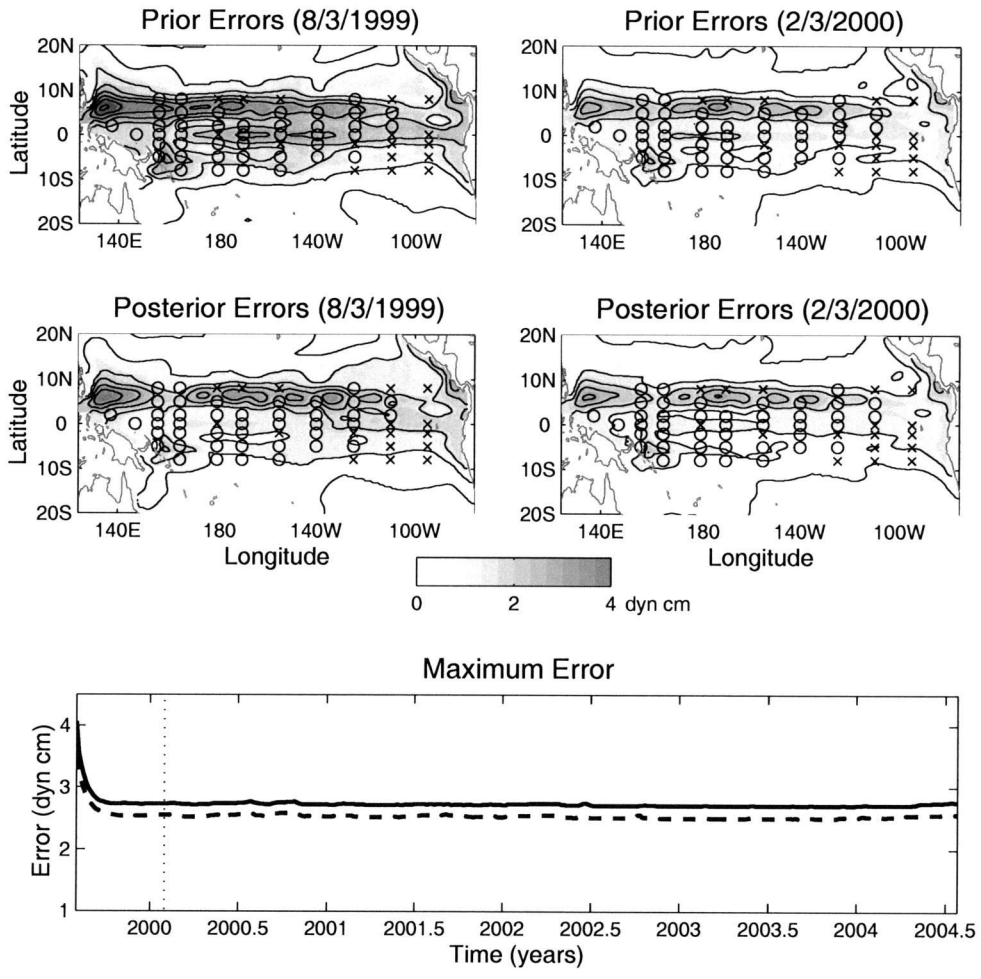

Figure 48. Prior and posterior DHA errors for the ASSIM44 run on August 3, 1999 and February 3, 2000. The x-marks and circles correspond to withheld and assimilation TAO locations, respectively. The contour interval is 0.5 dyn cm. The maximum prior (solid line) and posterior (dashed line) errors are plotted as a function of time for the 5-year assimilation run in the lower panel.

5.4.1 Evolution of Error Covariances. The square root of the diagonal of $(\mathbf{HP^f(t_i)H^T})$ and $(\mathbf{HP^a(t_i)H^T})$ for $m = 44$ at all gridpoints between 20°S and 20°N shows that the maxima of the prior and posterior errors are concentrated in zonal bands in the equatorial waveguide and off the coast of central America (Figure 48). On August 3, 1999, the prior errors are relatively small in the eastern Pacific coincident with areas where the correlation of the observed and unassimilated

model seasonal cycle was less than 0.6 (x-marks in Figure 48). Had data been assimilated at those locations, the RKF would have given those observations little weight relative to the other observations and the results would be qualitatively similar. After the first assimilation cycle, the magnitude of the errors were greatly reduced at the assimilated locations (lower left panel in Figure 48). As demonstrated by the February 3, 2000 errors, the assimilation reduces the errors in the waveguide leaving only large errors centered along 6°N and off the central American coast. In the first two months of assimilation, the maximum prior and posterior errors decrease rapidly to 2.7 and 2.5 dyn cm, respectively, and remain fairly constant for the remainder of the 5-year run with the exception of small jumps associated with gaps in the assimilated data (bottom panel of Figure 48).

5.4.2 Data Comparisons with Error Bars. Comparisons of 5-day DH at the 42 assimilated and 17 withheld TAO stations demonstrate the presence of an overall NODA-data bias that exceeds 10 dyn cm almost everywhere (black line in the upper panel of Figure 49). The elevated NODA DH at the TAO moorings is consistent with a model thermocline that is too deep and an upper ocean water column that is too fresh relative to the unbiased Levitus initialization. Based on the deviations from Levitus climatology, the NODA DH is biased by an average of 7.4 and 5.9 dyn cm due to thermal and salinity biases, respectively, at the TAO moorings. The salinity bias is more important south of the ITCZ (8°S to 2°N) and west of 140°W. Although Verron et al. (1999) and Gourdeau et al. (2000) mention deficiencies in the mean SSH of GC model and climatological drift from the Levitus initialization, to our knowledge this ca. 15 dyn cm has not been quantified in the GC or GCAML model. Parent et al. (2003) found a 20 cm SSH bias in the tropical

Pacific waveguide in simulations with the OPA model (Madec et al. 1998) and were able to reduce the bias via assimilation of altimetric SSHA plus a mean SSH estimated from TAO observations instead of assimilating anomalies.

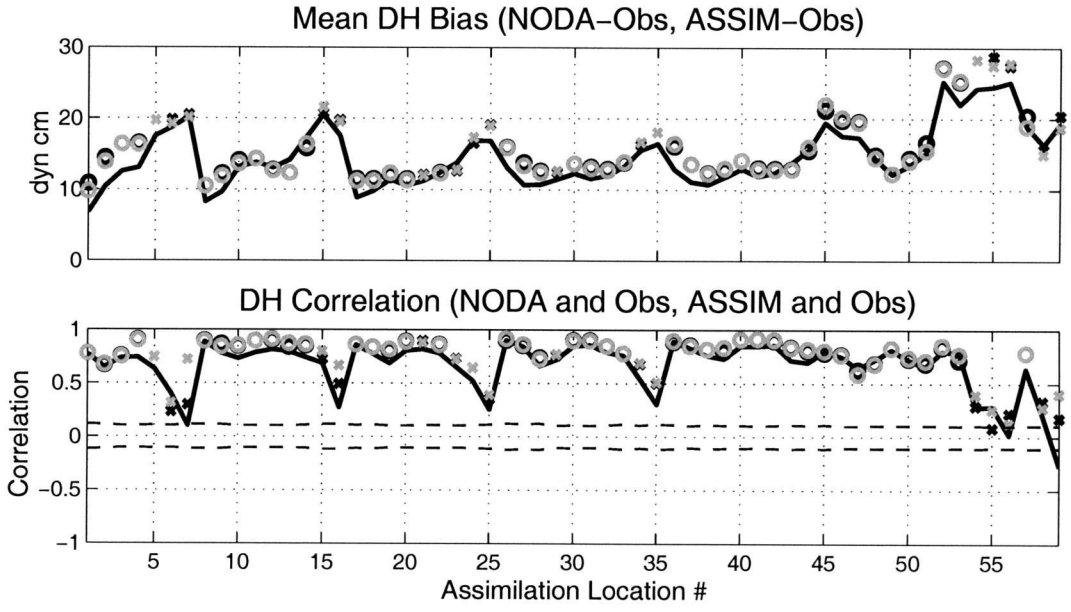

Figure 49. Five-year mean DH bias (upper panel) and correlation (lower panel) between the NODA run (black line), ASSIM44 (black symbols), and ASSIM139 (gray symbols) runs and the TAO observations. The withheld (x-marks) and assimilated (circles) observations are numbered sequentially from west to east and south to north such that location 1 and 59 correspond to 8°S, 165°E and 8°N, 125°W, respectively. The 95% confidence intervals are plotted as dashed lines about zero correlation using the number of TAO observations at each location.

The innovation sequence has no knowledge of the DH bias, as anomalies from the seasonal cycle are assimilated. The salinity and temperature biases, however, are certainly present in the model and are dynamically important. As seen in Figure 49, the assimilation tends to increase the bias in DH with largest increases along 8°S and 8°N. Despite this bias, the correlation between the ASSIM44 and ASSIM139 DHs with the observed DHs (circles in lower panel of Figure 49) are higher than the correlation between the NODA and observed DHs at the assimilated locations. The

majority of the withheld TAO stations between 8°S and 2°N also have increased correlation after assimilation (x-marks in the lower panel of Figure 49).

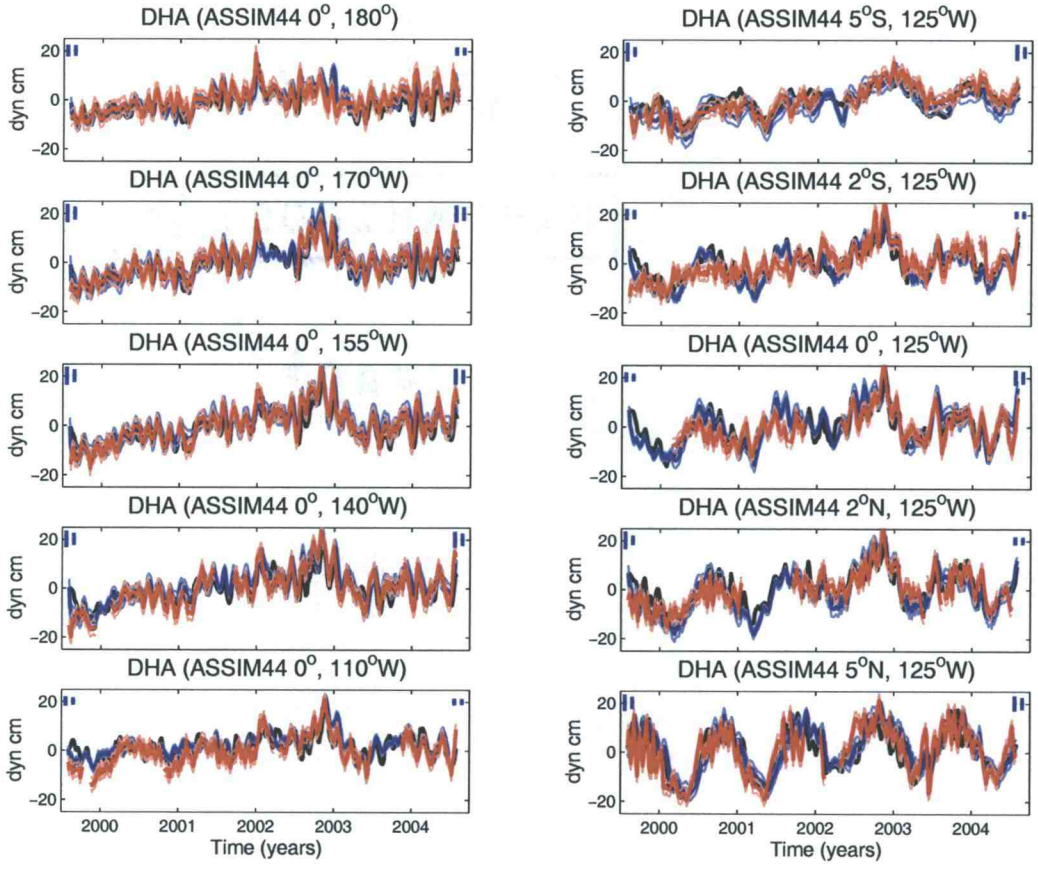

Figure 50. Time series of TAO (red), NODA (black), and ASSIM44 (blue) 5-day DHA along 0° between the dateline and 110°W (left panels) and along 125°W between 5°S and 5°N (right panels). The light red lines indicate the assumed observation error as described in Section 2.4.4. The light blue lines indicate the prior error bars. The pair of error bars in each panel indicate the prior and posterior errors for August 3, 1999 (right hand corner) and July 28, 2004 (left hand corner). Note that data is not assimilated at 0°, 180°; 0°, 110°W; and, 2°S, 125°W.

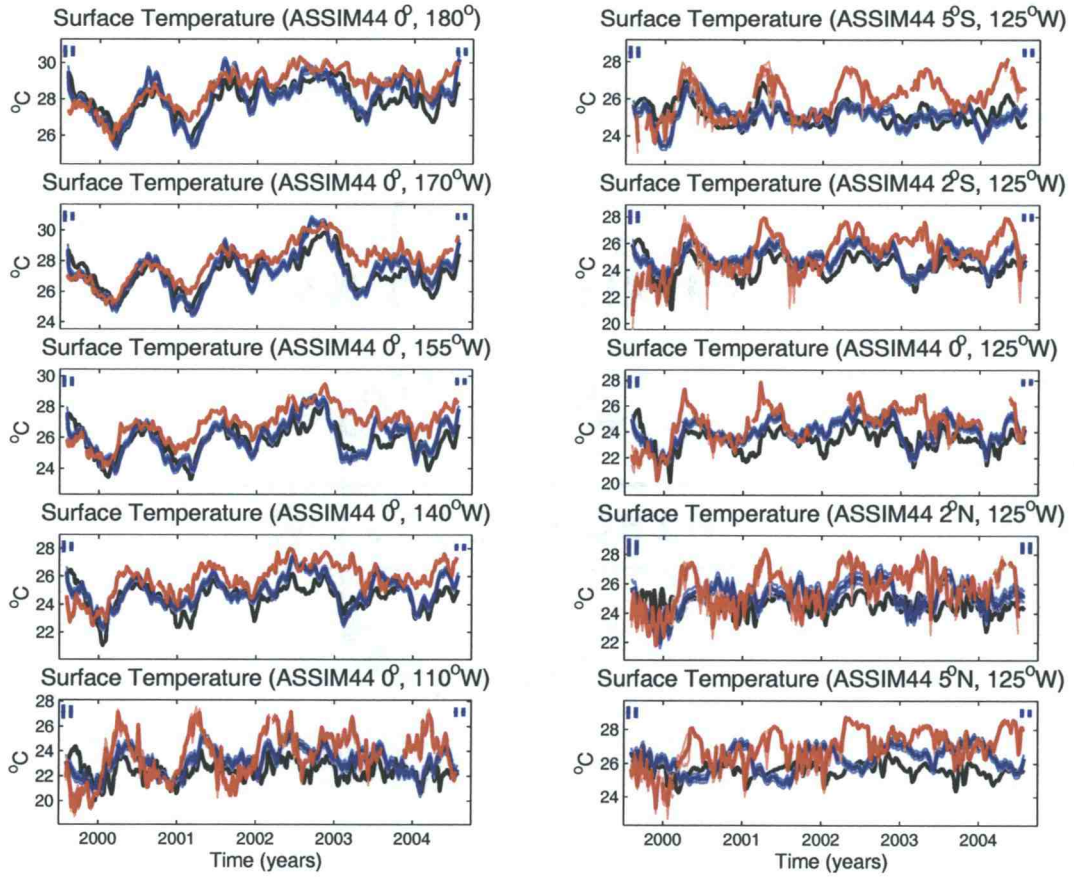

Figure 51. Similar to Figure 50, except for 5-day surface mixed layer temperature. The TAO temperature measurements have been averaged for the vertical range of the surface mixed layer for each 5-day average. The light red lines indicate observation error based on the standard deviation of the temperature measurements over the depth range and the instrument noise divided by the number of samples.

The time series of DHA at the assimilated and withheld TAO moorings along the equator between the dateline and 110°W (left panels of Figure 50) and along 125°W between 5°S to 5°N (right panels of Figure 50) demonstrate that assimilation does in fact increase the agreement between the model and observations. In addition, the posterior error bars from the RKF decrease, as expected, over time and show that most of the differences between the ASSIM44 run and TAO DHA are not significant. The corrections to the 5-day DHA are smaller closer to the equator

(2°S to 2°N) than along 5°S and 5°N. Along 5°S and 5°N, the tendency is for the assimilation to decrease the amplitude and modify the phase of the TIWs.

The impact of assimilation on the cold tongue surface mixed layer temperature is illustrated in Figure 51. Note that the observed surface mixed layer temperatures are estimated by averaging the available TAO temperature measurements in the depth range covered by the model surface mixed layer. Therefore, the observed error bars are given by the standard deviation of the temperatures averaged over the depth range and an estimate of the RMS instrument noise 0.05°C divided by the square root of the number of vertical measurements.

Assimilation with 44 EOFs reduces the model cold tongue cold bias by an average of 0.4°C for the time series in Figure 51. The decrease in the bias is accompanied by an increase in the correlation between ASSIM44 and TAO compared with NODA and TAO, except at 125°W, 5°S and 5°N. These first two years of the simulation overlap with the La Niña event which commenced in the summer of 1998 and terminated in the spring of 2001 based on the NOAA Climate Prediction Center Oceanic Niño Index (ONI, Figure 52). Despite the decreased bias and increased correlation, the observed and ASSIM44 time series disagree in phase after the La Niña event. Under warm conditions associated with the May 2002 to March 2003 El Niño (Figure 52), the annual signal of the observed surface mixed layer temperature is weakened (Figure 51). The ASSIM44 run corrects the 5-day DHA in such a way that the annual cycle of the surface mixed layer temperature is incorrectly amplified during the last three years (Figure 51). Along 125°W, the ASSIM44 and TAO surface mixed layer temperatures overlap within the posterior error bars during the summer and fall. There is less reduction of the cold tongue bias in the ASSIM139

run, and the correlations between ASSIM139 and the TAO surface mixed layer temperature are typically lower than the ASSIM44 and TAO (not shown).

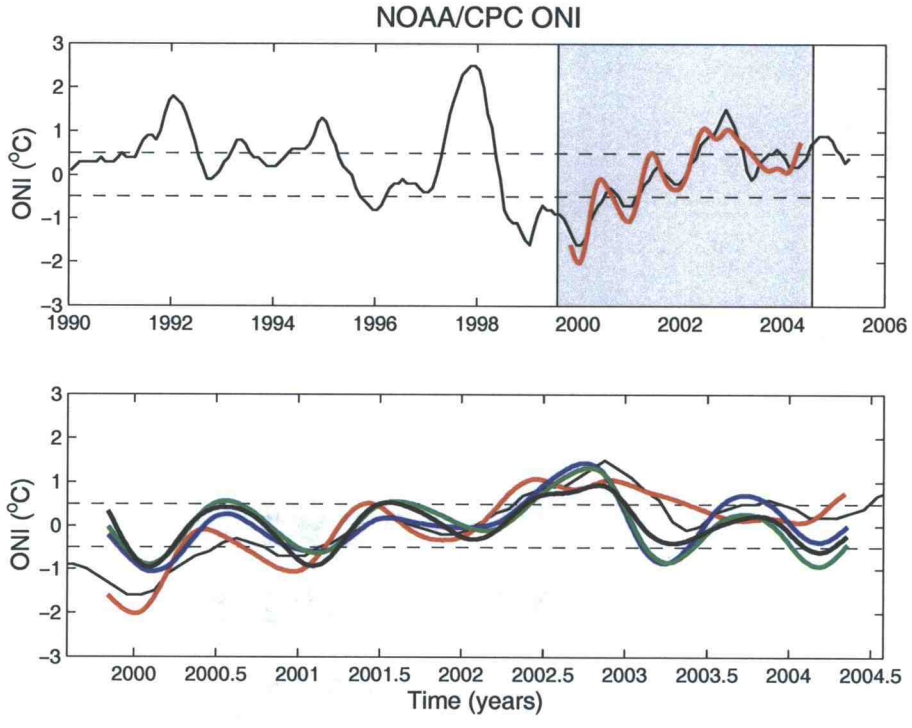

Figure 52. Oceanic Niño Index (ONI) produced by the NOAA Climate Prediction Center from a 3-month running mean of ERSST.v2 SST anomalies from 1971-2000 base period in the Niño 3.4 region (5°N to 5°S, 120° to 170°W) computed for each month (black line). Cold and warm episodes occur when the threshold of −0.5° and 0.5°C are surpassed for 5 consecutive points. Lower panel shows detail of the shaded region in upper panel with the Niño 3.4 surface mixed layer temperature anomalies computed from the 5-years of TAO (red line), the NODA (heavy black line), ASSIM44 (blue line), and ASSIM139 (green line) runs overlaid.

The 90-day low-passed surface mixed layer temperature anomalies in the Niño 3.4 region serve as an approximate ONI index for the NODA, ASSIM44, ASSIM139, and TAO observations during the five-year period (Figure 52). The ONI and TAO index have a correlation of 0.92 and the ONI and model correlations are 0.64 (NODA), 0.74 (ASSIM44), and 0.54 (ASSIM139). The lack of improvement in the ASSIM139 surface mixed layer temperature and ONI implies that the state space

is overfit with 139 EOFs. In addition, the relationship of the surface mixed layer temperatures to DH may be more complex than is represented by the reduced state space.

Along the equator, the TAO ADCP measurements of zonal velocity can be used to compare the strength of the EUC in layer 7 of the model (Figure 53). The ADCP data are available in 5 meter vertical bins. At each location, zonal velocity is vertically averaged over the depth range of layer 7 and the errors are approximated by the standard deviation of the zonal velocities averaged over the depth range and an estimate of the RMS instrument noise 5 $cm\ s^{-1}$ divided by the square root of the number of vertical measurements. The NODA layer 7 zonal velocity has highest correlation with the TAO measurements east of the dateline. The poor agreement west of the dateline is due to the model EUC core being too shallow in the western Pacific. The ASSIM44 run removes some of the bias in the western Pacific but is not able to adjust the vertical placement of the EUC core significantly. The NODA run simulates the strength of the EUC in layer 7 fairly well in the central Pacific and the ASSIM44 run does not make significant corrections to the zonal velocity. Although the ASSIM44 run overcorrects the EUC at 110°W and is positively biased relative to the TAO velocity, the differences between ASSIM44 and TAO are mostly within the posterior error bars at 170° and 140°W. The ASSIM139 run has significantly decreased the mean bias relative to the ASSIM44-TAO and NODA-TAO mean bias and the differences between the ASSIM139 and TAO zonal velocities are mostly within the error bars at 170°, 140°, and 110°W (not shown). The increase in EUC agreement as the number of EOFs increases demonstrates that the relationship

between zonal velocities and DH are well represented by the reduced state space along the equator.

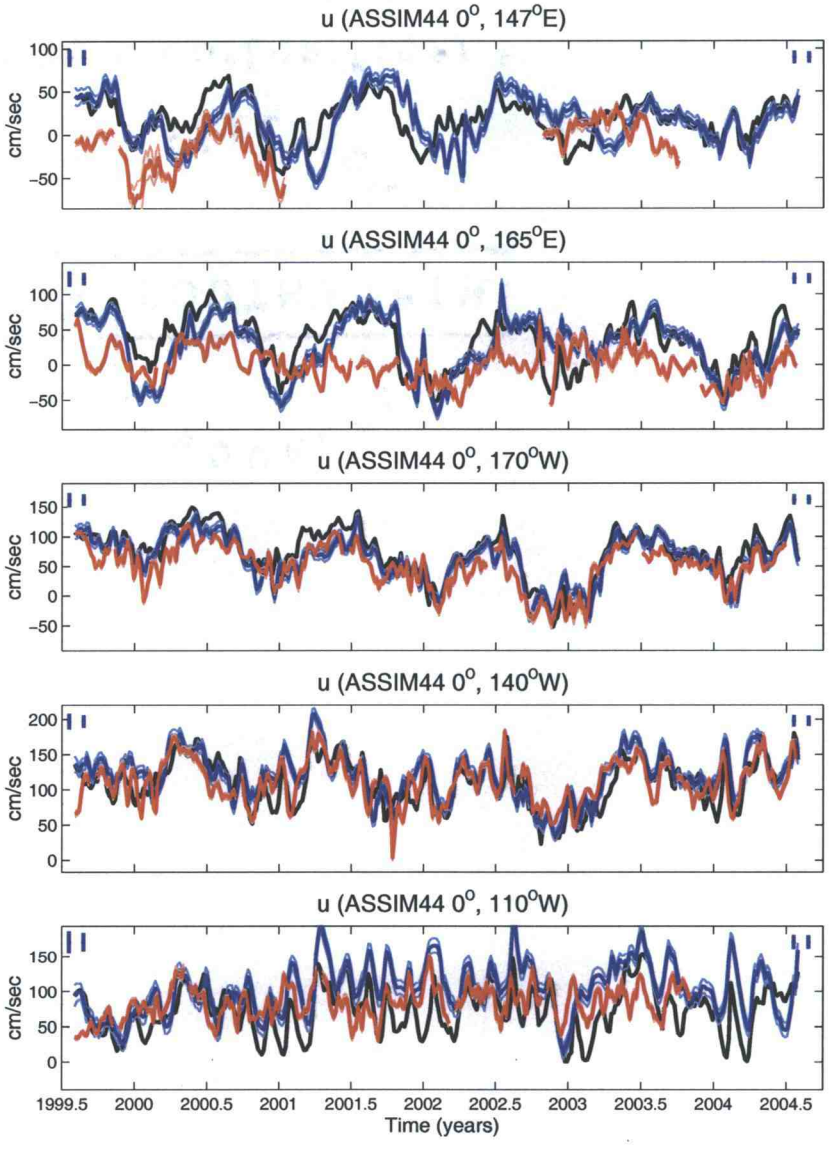

Figure 53. Similar to Figure 50, except for 5-day layer 7 zonal velocity along 0° between 147°E and 110°W. The TAO ADCP measurements have been interpolated to the local depth of layer 7 for each 5-day average. The light red lines indicate observation error based on the standard deviation of the zonal velocity measurements over the depth range and the instrument noise divided by the number of samples.

5.4.3 Statistics of the Innovation Sequence. The five-year innovation sequences for the ASSIM44 and ASSIM139 runs are biased as demonstrated by the five-year mean in Figure 54. The biases, however, are smaller than 2 dyn cm and there is negligible difference between the ASSIM44 and ASSIM139 mean innovation. The innovations have large variability along 5° and 8°N (ca. 6 dyn cm), and relatively uniform variability (ca. 3.5 dyn cm) between 8°S and 2°N (Figure 54). Because the mean innovation biases for ASSIM44 and ASSIM139 are everywhere smaller than the standard error, these biases may not be significant. The innovation sequences do not resemble white processes as demonstrated for 8°S, 155°W and 5°N, 155°W (lower panels in Figure 54). At 5°N, 155°W, seasonally varying information linked to the presence of TIWs colors the innovation sequence.

One consequence of the hypotheses underlying the RKF is that the quantity $\mathbf{J_i} = \mathbf{d_i^T}(\mathbf{HP^f}(\mathbf{t_i})\mathbf{H^T} + \mathbf{R})^{-1}\mathbf{d_i}$ is a χ^2_ν distributed random variable with ν degrees of freedom given by the number of observations for a given assimilation cycle (cf. Miller and Cane 1996; Bennett 2002). A χ^2_ν distributed variable should fall outside the 95 and 99% confidence limits (dotted and dashed lines in Figure 55, respectively) approximately 18 and 4 times, respectively, during the 5-year run. The ASSIM44 and ASSIM139 runs clearly exceed these limits more often than this (Figure 55). These excursions, however, have seasonal modulation and are coincident with phase and amplitude errors in the model representation of the TIWs (Figures 50 and 54). The innovations pass the χ^2-test for several consecutive months in the spring and early summer during the 5-year run. The ASSIM44 run fails the χ^2-test more often than the run retaining 139 EOFs. Partitioning this test into assimilated TAO locations between 8°S-2°N and 5°-8°N reveals that both the ASSIM44 and

ASSIM139 runs nearly pass the χ^2-test when the TAO stations along 5° and 8°N are excluded (Figure 55). The failure of the χ^2-test between 5° and 8°N can be attributed to TIWs on the northern flank of the cold tongue.

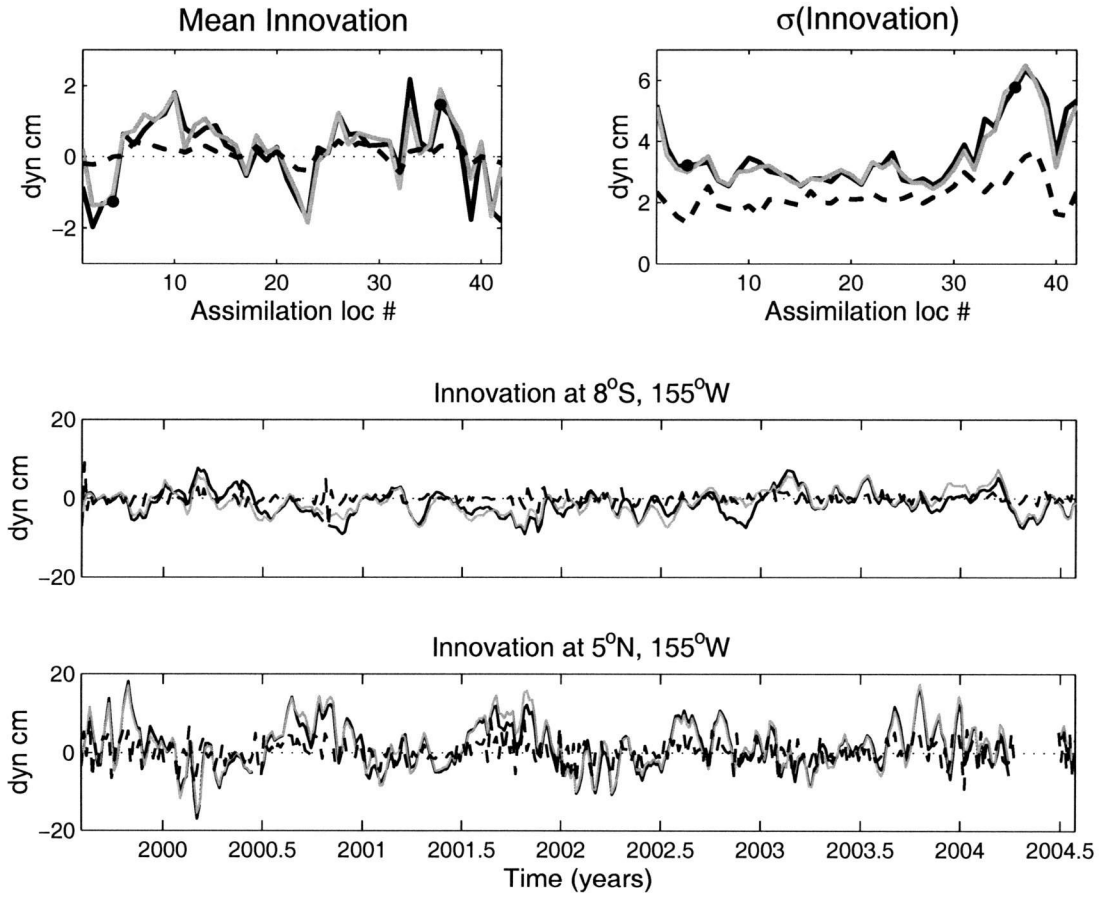

Figure 54. Mean and standard deviation of the 5-year innovation sequence for ASSIM44 (black line), ASSIM139 (gray line) and ASSIM44-AR (dashed line) for the 42 TAO assimilation locations. The innovation sequences are compared at 8°S, 155°W and 5°N, 155°W. Those two locations appear as black dots on the mean and standard deviation plots.

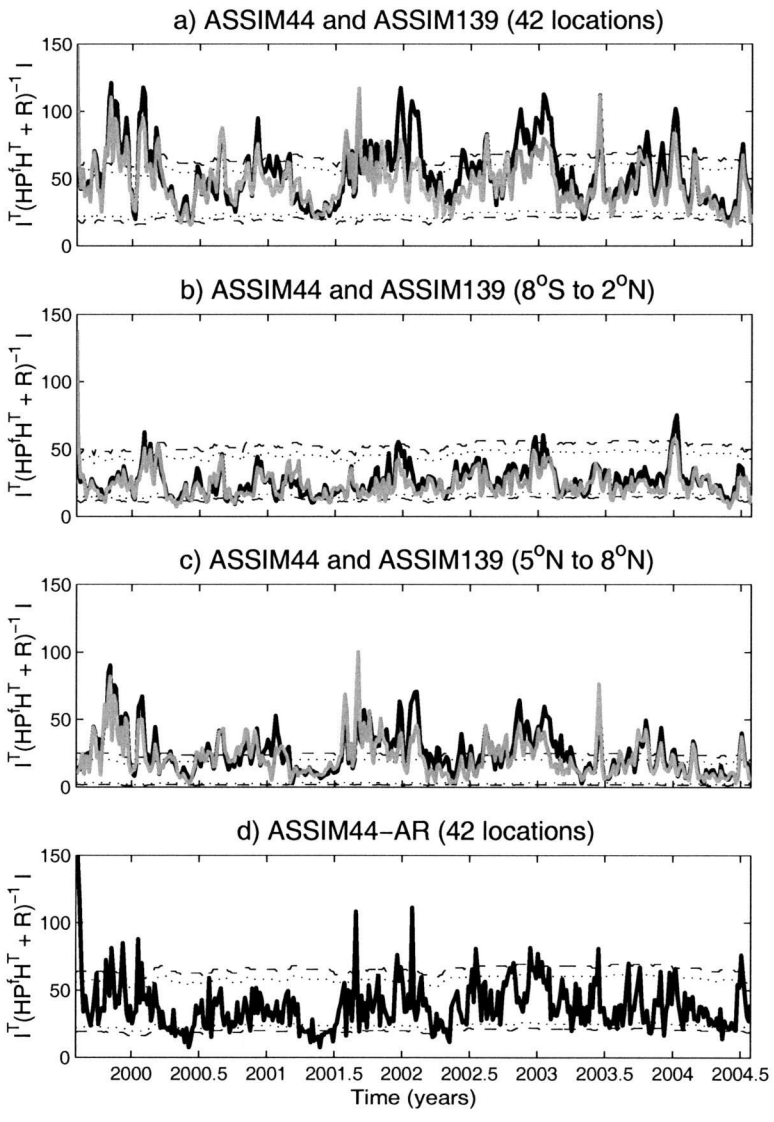

Figure 55. χ^2 hypothesis test for the ASSIM44 (black line) and ASSIM139 (gray line) runs at a) the 42 TAO assimilation locations, b) the locations between 8°S and 2°N, c) the locations along 5° and 8°N, and d) the ASSIM44-AR (black line) run at the 42 TAO assimilation locations. The dotted lines represent 2.5 and 97.5% confidence intervals and the dashed lines represent 0.5 and 99.5% confidence intervals, respectively.

5.5 Impact on the Equatorial Pacific Cold Tongue

5.5.1 Modifications to the Thermocline and ECS. The five-year mean and standard deviation of the cold tongue SST, thermocline depth, and zonal currents are all modified by the assimilation of 5-day TAO DHA. In this section, we compare the mean and standard deviation of the TAO, NODA, ASSIM44, and ASSIM139 temperature and zonal velocity structure at the TAO moorings along the equator and 125°W.

As mentioned in Section 5.4.2, the surface mixed layer temperatures are too cold and the thermocline (as marked by the 20°C isotherm) is too deep and diffuse in the NODA run compared with the TAO thermocline along the equator (Figure 56). Both the ASSIM44 and ASSIM139 run deepen the thermocline between the dateline and 95°W, but only the ASSIM44 significantly increases the surface mixed layer temperatures such that the cold bias is decreased along the equator. The standard deviation of temperature is much weaker in the NODA run than observed by TAO (right panels of Figure 56). Both the ASSIM44 and ASSIM139 runs have increased variability near the thermocline compared with NODA and TAO; however, none of the model runs produce the high variability seen by TAO in the surface mixed layer between 130° and 95°W and have difficulty reproducing the high variability between 100 and 200 m depth, west of 160°W. Along 125°W, the ASSIM44 and to a lesser extent the ASSIM139 runs reduce the surface mixed layer temperature bias between 2°S and 8°N and deepens the thermocline everywhere except 5°S (left panels in Figure 57). The depth of TAO maximum variability is well matched by the model runs and the assimilation acts to increase the temperature variability in those layers (right panels in Figure 57).

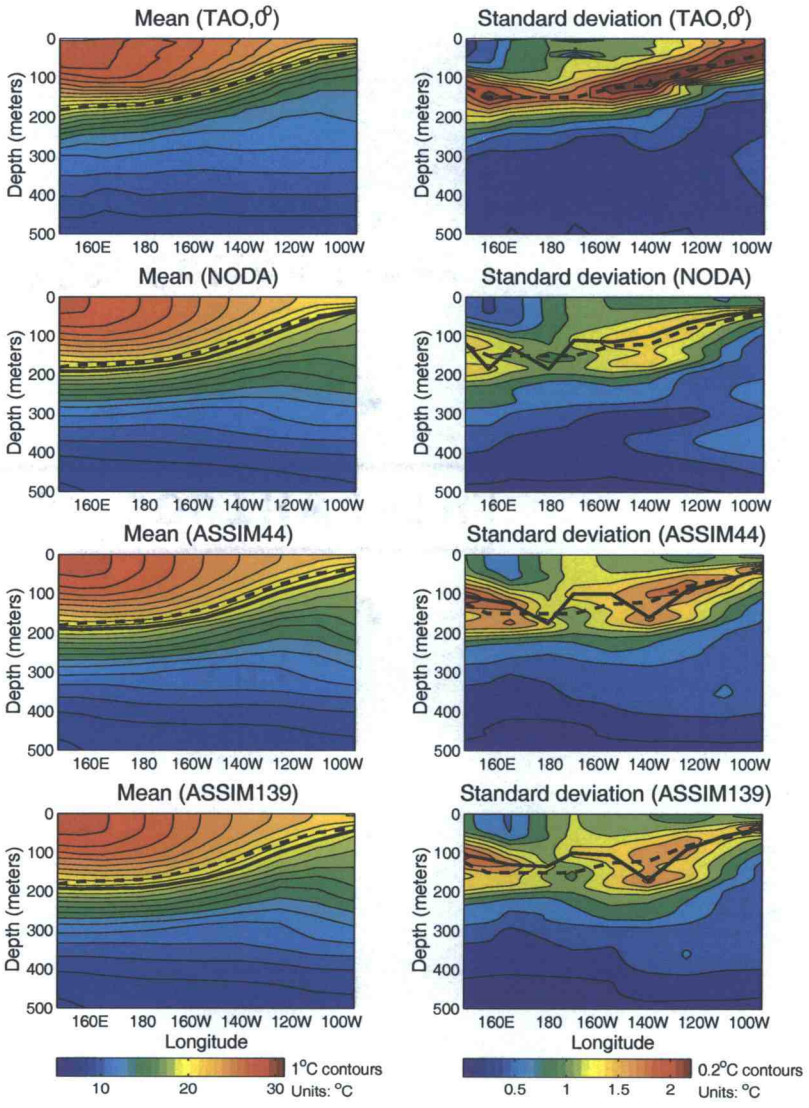

Figure 56. Five-year mean (left panels) and standard deviation (right panels) of temperature along the equator for TAO, NODA, ASSIM44, and ASSIM139. The dashed and solid lines on the left panels correspond to the TAO and model (NODA, ASSIM44, or ASSIM139) mean 20°C isotherm depth. The dashed and solid lines on the right panels correspond to the maximum TAO and model temperature variability.

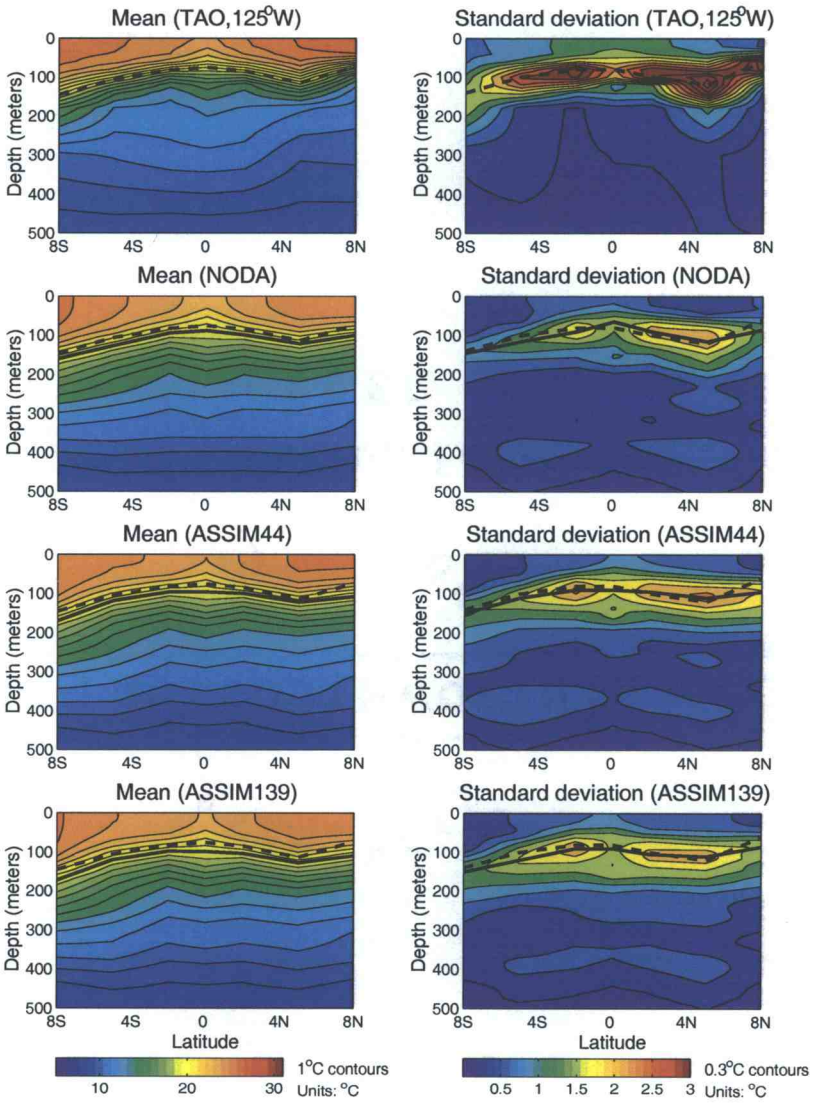

Figure 57. Similar to Figure 56, except along 125°W.

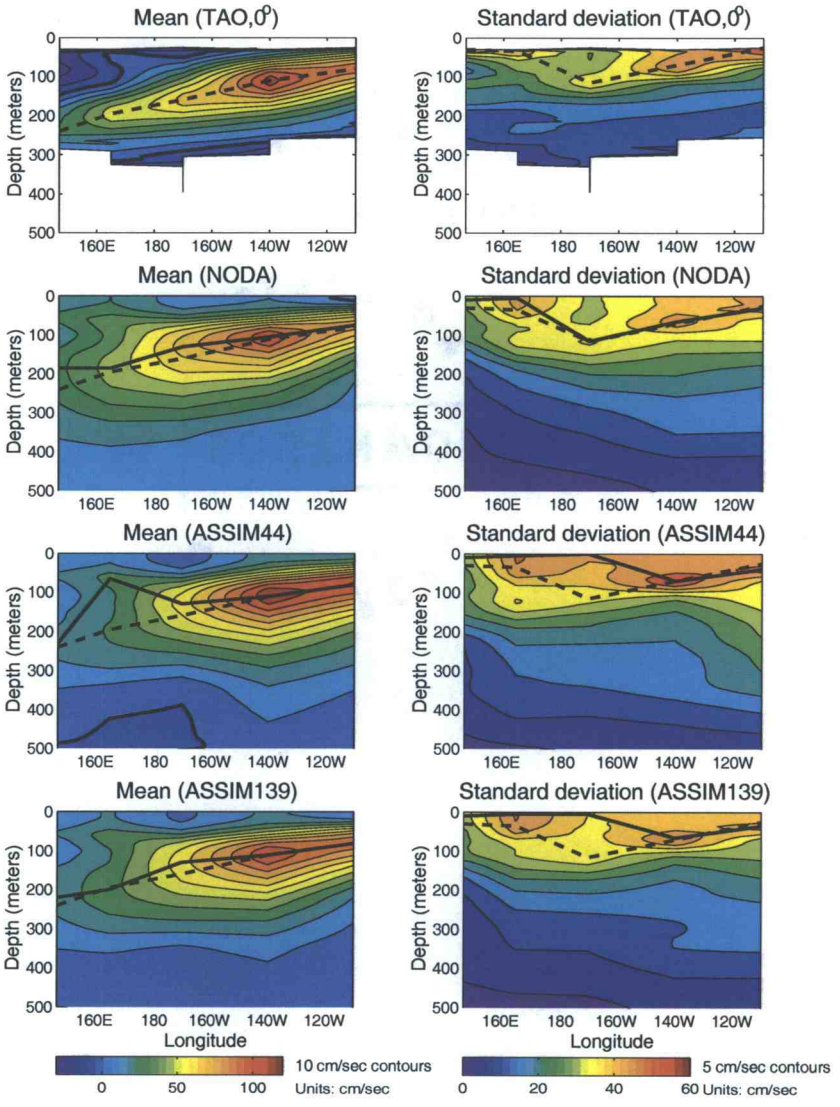

Figure 58. Five-year mean (left panels) and standard deviation (right panels) of zonal velocity along the equator for TAO, NODA, ASSIM44, and ASSIM139. The thick contour corresponds to the zero mean zonal velocity contour in the left panels. The dashed and solid lines on the left panels correspond to the maximum TAO and model (NODA, ASSIM44, or ASSIM139) mean zonal velocity. The dashed and solid lines on the right panels correspond to the maximum TAO and model zonal velocity variability.

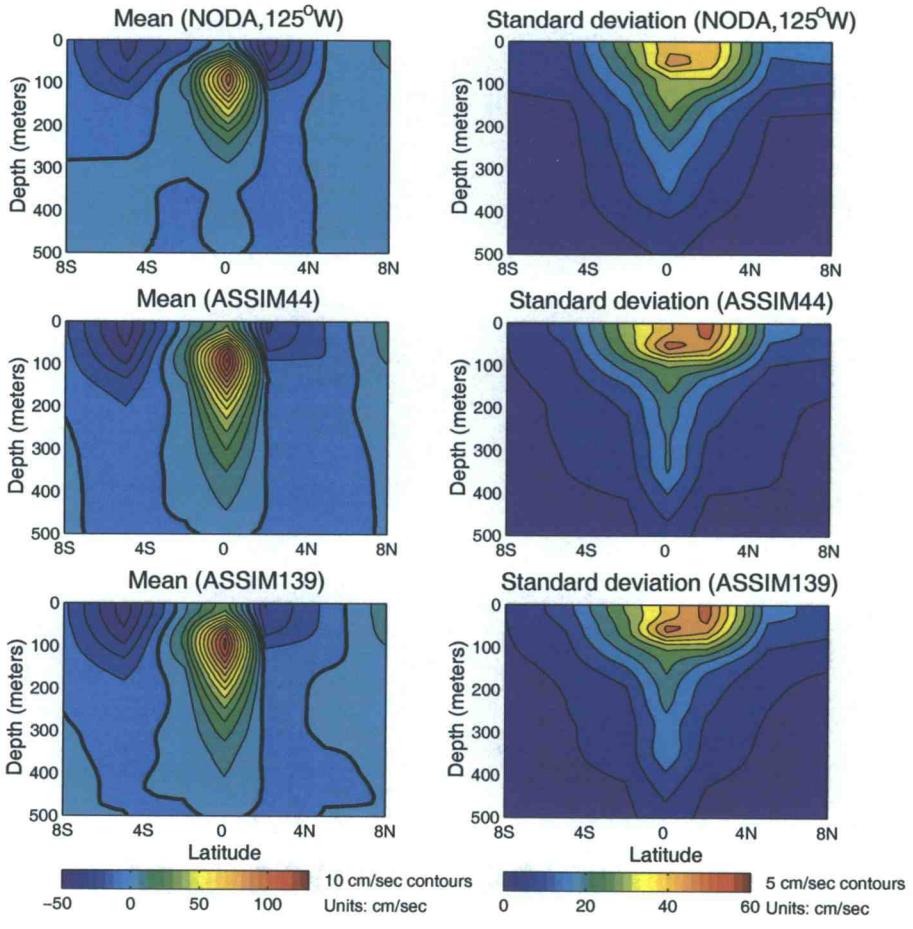

Figure 59. Similar to Figure 58, except along 125°W. Note: TAO zonal velocities are not available along 125°W.

The mean zonal currents along the equator and 125°W are plotted in Figures 58 and 59, respectively. TAO observations of the vertical structure of zonal velocity are only available along the equator (upper panels of Figure 58). The comparison of the model and TAO zonal velocities demonstrates that the model EUC is too broad and the mean SEC is near zero along the equator in all three model runs (left panel of Figure 58). Assimilation increases the strength of the eastward flowing EUC and the ASSIM139 EUC core depth compares best with the TAO EUC core. Both the ASSIM44 and ASSIM139 runs have higher variability than the NODA run along the

equator (right panels of Figure 58). Along 125°W, the assimilation acts to increase the vertical extent of the EUC (left panels of Figure 59) with increased variability near the surface along 2°N between the EUC and the northern branch of the SEC (SECN, right panels of Figure 59). The ASSIM44 and ASSIM139 runs also intensify the south branch of the SEC (SECS) along 5°S and decrease the meridional shear along 5°N between the SECN and the NECC. This weakening of the SECN-NECC shear is consistent with the decrease in the intensity of the model TIWs on the northern flank of the cold tongue (Lyman et al. 2005a).

5.5.2 Cold Tongue Evolution and TIWs. In this section the intraseasonal to interannual variability of the cold tongue and the behavior of the TIWs are compared for the observations and the NODA, ASSIM44, and ASSIM139 runs. In Figure 60, select 5-day averages of NODA surface mixed layer temperature are shown in the cold tongue region during November 3, 2000 and March 23, 2001 (black contours). The differences between the ASSIM44 and the NODA run are overlaid for the same time period.

In the second year of the simulation, the cold tongue (marked by the 25°C contour in Figure 60) began its westward penetration in the fall, reached its maximum extent (175°W) at the end of February, and began its decline in March. The reintensification of the cold tongue occurred in June and July (not shown). TIWs present on the northern and southern flanks of the cold tongue were most pronounced between December and January during this TIW season. While this pattern is very similar to the preceding year, the cold tongue evolution is disrupted during the warm conditions associated with the May 2002 to March 2003 El Niño

(Figure 52). Under these conditions, the annual cycle of the cold tongue is modified and the cold tongue only penetrates as far as 160°W.

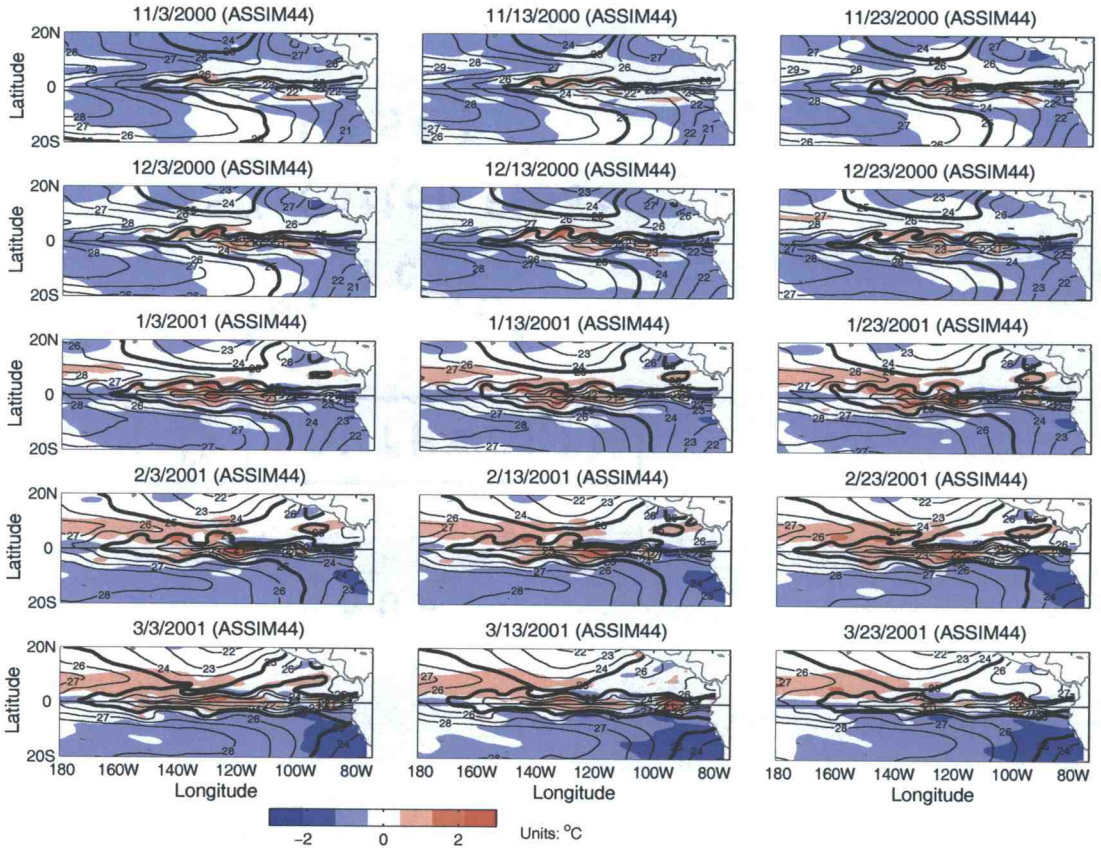

Figure 60. Select 5-day averages of SST between November 3, 2000 and March 23, 2001 for the NODA run (black contours) with the difference between ASSIM44 and NODA SST overlaid as color contours between the dateline and 76°W, and 20°S to 20°N. The thick black contour corresponds to 25°C.

Along the equator, the assimilation of TAO DHA warms the surface mixed layer temperature and reduces the model cold tongue cold bias (Figure 60). During this TIW season, the assimilation warms the cool perturbations and cools the warm perturbations shifting the ASSIM44 TIW crests and troughs out of phase with the NODA waves. The amplitudes of the modified TIWs tend to be smaller than the NODA TIW amplitudes. These patches of large positive and negative differences

between ASSIM44 and NODA surface mixed layer temperature propagate westward with the TIWs. Outside of the waveguide, the assimilation cools the water near the South American coast by approximately 2°C and warms the water on the northern flank of the cold tongue under the ITCZ by 1°C by the end of March 2001. Although the overall pattern is the same for the ASSIM139 run (not shown), the magnitude of the deviations from the NODA run are reduced and the shifted TIWs are somewhat weaker.

To further evaluate the impact of the RKF on the TIW amplitudes and interannual modulation, $x - t$ diagrams of 50-day high-pass filtered SSHA along 5°N are compared for the AVISO observations, NODA, and the assimilated runs (Figure 61). The observed TIW amplitudes are much stronger than seen in all of the model runs and have been scaled by 0.75 and subsampled onto the model 1° grid, to enable the comparison of the TIW amplitudes as a function of longitude and time. During the five-year study period, the NODA TIWs have large amplitudes but the least realistic structure in that the waves extend coherently eastward to the eastern boundary, and exhibit little seasonality. The TIWs observed by AVISO extend east to 85°W at the beginning of each TIW season. Later in the season, they extend east only to 100°W. The ASSIM44 and ASSIM139 SSHA have much weaker amplitude TIWs than NODA and AVISO due to the modification of the phase of the TIWs (as demonstrated in Figure 60), but the seasonality and the $x - t$ structure with large SSHA amplitudes west of 110°W are better correlated with the observed TIWs (upper panel of Figure 61).

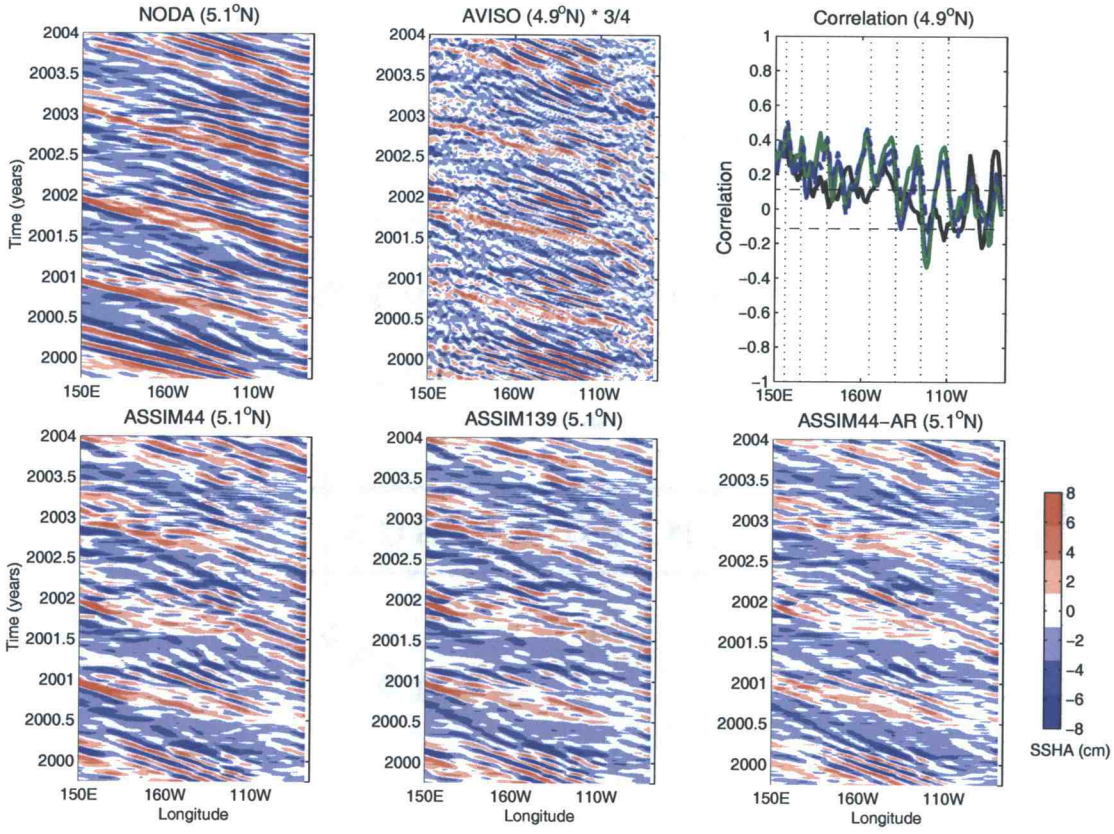

Figure 61. A comparison of $x - t$ diagrams of 50-day high-pass filtered SSHA for the NODA and assimilated runs and the AVISO observations near 5.0°N. The AVISO SSHA have been scaled by 0.75. The cross-correlations between the AVISO data and NODA (black line), ASSIM44 (blue line), ASSIM139 (green line), and ASSIM44-AR (blue dashed line) are plotted in the upper right panel.

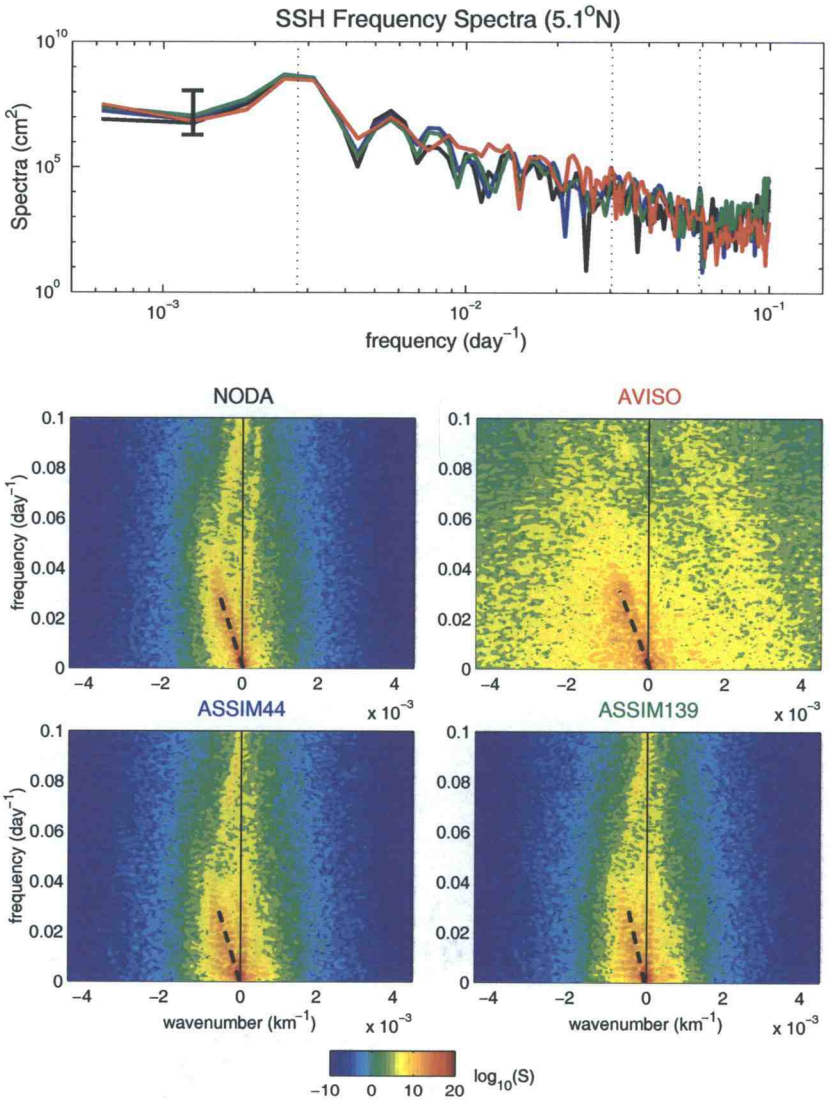

Figure 62. A comparison of SSHA spectra for the NODA (black line), ASSIM44 (blue line), and ASSIM139 (green line) runs and the AVISO (red line) observations near 5.0°N. Top panel compares the spectra as a function of frequency for wavenumber $k = 0$. The dashed lines correspond to the annual period, 33 days, and 17 days and the error bar reflects the 90% confidence interval. The lower four panels compare the wavenumber-frequency spectra with the color contours representing the common logarithm of the spectra.

The wavenumber-frequency spectra along 5°N show the significant improvements made to the SSHA by assimilation (Figure 62). For zero wavenumber, assimilation increases the interannual and intraseasonal SSHA variability and there is increased variability in the TIW frequency band corresponding to 33 and 17 days, respectively (top panel of Figure 62). A linear regression is used to estimate the slope of maximum westward propagating spectral energy (negative wavenumber and positive frequency) in the model and observed wavenumber-frequency spectra (lower panels of Figure 62). The spread of spectral energy about the fitted line (dashed line in lower panels of Figure 62) is small for the NODA run compared with AVISO and the assimilated runs. Average westward propagation speeds estimated from slope of the dashed lines are 39.2 ± 2.2 (AVISO), 46.5 ± 1.3 (NODA), 50.9 ± 4.2 (ASSIM44), and 67.7 ± 6.7 $cm\ s^{-1}$ (ASSIM139). Although assimilation increases the propagation speed, the ASSIM44 and NODA westward phase speeds may not be significantly different.

5.6 Autoregressive Model of the Innovations

An assimilation scheme has been constructed that improves the analysis of the interannual and intraseasonal variability of the DH (and SSH) during the five-year study period. In Section 5.4, it was demonstrated that color remained in the innovation sequence for the ASSIM44 and ASSIM139 runs. The error model was constructed with the assumption that the model errors were dominated by temporally uncorrelated errors in the wind forcing. The assumption that the wind errors are white in time may not be valid for an RKF constructed from a nonlinear GCM with a 5-day assimilation window and wind forcing. Additional errors not

incorporated in the forecast error model may arise from the improper specification of the heat and salt flux at the model boundaries (Section 5.3.2.1), the computation of TAO DH using salinity from T-S climatologies (Section 5.3.2.2), and the construction of the model and observed seasonal cycles from a five-year record (Section 5.3.4.1). Determining the form of the individual errors requires a longer record of QuikSCAT winds and the existence of interannual heat and salt flux data with adequate realism. In lieu of obtaining these individual error estimates, an autoregressive process can be added to the RKF as in Chan et al. (1996) to study the effects of whitening the innovation sequence on our assimilation run with 44 EOFs (ASSIM44-AR).

The innovation sequence $\mathbf{d_i}$ in (14) is replaced by

$$\mathbf{d_i'} = \mathbf{d_i} - \mathbf{a_1 d_{i-1}} - \mathbf{a_2 d_{i-2}} \tag{29}$$

where a second-order (10-day) autoregressive process has been removed from the innovations at each assimilation location. Although additional whitening can be achieved at some of the assimilated stations by using a higher order autoregressive model (e.g., a one-month autoregressive process), only the $k = 1$ and 2 autoregressive coefficients were significantly different from zero for the majority of the 42 assimilated TAO locations. The coefficients, a_1 and a_2, used to compute $\mathbf{d_i'}$ in the ASSIM44-AR run vary meridionally with a_1 smallest near the equator and largest along 8°S and 8°N and a_2 positive when a_1 is small (Table 9). To account for the removal of the color of the innovations, the observation error covariance $\mathbf{R}$ is reduced by 1 (dyn cm)^2 at all 42 assimilated locations.

Table 9. Coefficients[1] for the second-order autoregressive model of the innovation sequence.

TAO location	a_1	a_2	TAO location	a_1	a_2
8°S, 165°E	1.259	-0.428	0°, 140°W	0.930	-0.206
8°S, 180°	1.267	-0.416	0°, 125°W	0.841	-0.024[2]
8°S, 170°W	1.301	-0.528	2°N, 137°E	1.053	-0.216
8°S, 155°W	1.241	-0.327	2°N, 156°E	0.631	0.066
5°S, 156°E	1.033	-0.266	2°N, 165°E	0.459	0.193
5°S, 165°E	0.772	-0.158	2°N, 180°	0.598	0.111
5°S, 180°	0.719	0.004[2]	2°N, 170°W	0.602	-0.040[2]
5°S, 170°W	0.673	0.132	2°N, 155°W	0.662	-0.090
5°S, 155°W	0.931	-0.069	2°N, 140°W	0.701	-0.188
5°S, 140°W	1.184	-0.301	2°N, 125°W	0.708	-0.221
5°S, 125°W	1.182	-0.322	2°N, 110°W	0.739	-0.240
2°S, 156°E	0.860	-0.117	5°N, 156°E	1.098	-0.173
2°S, 165°E	0.490	0.286	5°N, 165°E	1.081	-0.336
2°S, 180°	0.649	0.171	5°N, 180°	1.096	-0.287
2°S, 170°W	0.647	0.147	5°N, 155°W	1.187	-0.398
2°S, 140°W	0.459	0.101	5°N, 140°W	1.191	-0.556
0°, 147°E	0.833	-0.129	5°N, 125°W	1.072	-0.608
0°, 156°E	0.775	-0.090	5°N, 110°W	0.953	-0.149

Table 9. (continued)

TAO location	a_1	a_2	TAO location	a_1	a_2
0°, 165°E	0.734	-0.162	8°N, 156°E	0.939	-0.070
0°, 170°W	0.906	-0.275	8°N, 165°E	1.398	-0.499
0°, 155°W	0.781	-0.212	8°N, 125°W	1.377	-0.549

[1]Coefficients are estimated from a jackknife [Chatfield, 1996] applied to the full five years and two 2.5 year partitions of the ASSIM44 run.

[2]These autoregressive coefficients are not significantly different from zero.

The resulting 5-year mean bias in the innovation sequence is everywhere less than 0.4 dyn cm for the ASSIM44-AR run (upper panels of Figure 54). The variability of the ASSIM44-AR innovation sequence is relatively uniform across the 42 TAO locations with smaller variability than the ASSIM44 and ASSIM139 innovation sequence. Comparison of the ASSIM44 and ASSIM44-AR innovation sequences at 8°S, 155°W and 5°N, 155°W (lower panels of Figure 54) reveals that much of the seasonal and TIW-like variability has been removed from the time series by simply adding a second-order autoregressive model to the innovations. The lagged autocorrelations of the ASSIM44 and ASSIM139 runs (Figure 63) have significant correlation for lags up to a month. For the ASSIM44-AR run, most of the autocorrelation for non-zero lag has been removed and falls within the confidence intervals (bottom panel of Figure 63) which implies that the RKF with second-order autoregressive model is nearly optimal (Kailath 1968; Daley 1992; Chan et al. 1996; Miller and Cane 1996). The ASSIM44-AR innovation sequence also passes the χ^2-test more often than the ASSIM44 and ASSIM139 innovations (bottom panel of Figure 55).

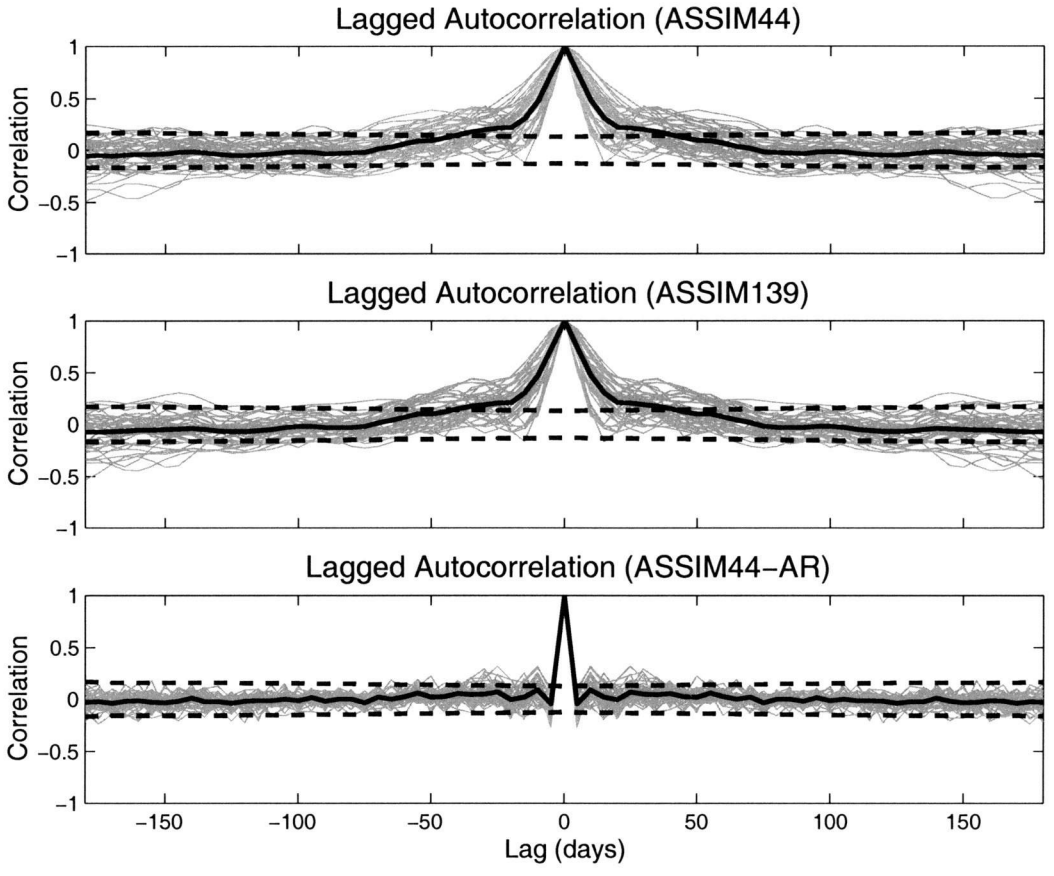

Figure 63. Autocorrelation of the 5-year innovation sequence as a function of lag in days for ASSIM44 (top panel), ASSIM139 (middle panel), and ASSIM44-AR (bottom panel) for the 42 TAO assimilation locations (grey lines). The thick black line represents the mean lagged correlation for all 42 TAO locations. The 95% confidence intervals are plotted as dashed lines about zero correlation using the minimum number of samples for each lag.

The nearly optimal ASSIM44-AR run produces DHA time series much like the ASSIM44 run (not shown). Quantitatively, the ASSIM44-AR and TAO DH correlations are significantly larger at the withheld moorings along 110° and 95°W. The removal of biases in the innovations limits the ability of the ASSIM44-AR to make large corrections to biased model fields such as surface mixed layer temperature; but, the phasing errors in the assimilated cold tongue seasonal cycle are significantly reduced (Figure 64). As was shown for the ASSIM44 and ASSIM139

run (upper panel of Figure 62), the ASSIM44-AR run increases the interannual and intraseasonal SSHA variability. Although the ASSIM44-AR TIW amplitudes are weaker than the ASSIM44 and ASSIM139 amplitudes (which themselves are weaker than the NODA and AVISO amplitudes), the $x - t$ structure is still well correlated with that of AVISO (Figure 61) and is the only run with an average westward propagation speed that agrees within the error bars with the AVISO phase speed ($43.4 \pm 2.0\ cm\ s^{-1}$ compared with $39.2 \pm 2.2\ cm\ s^{-1}$).

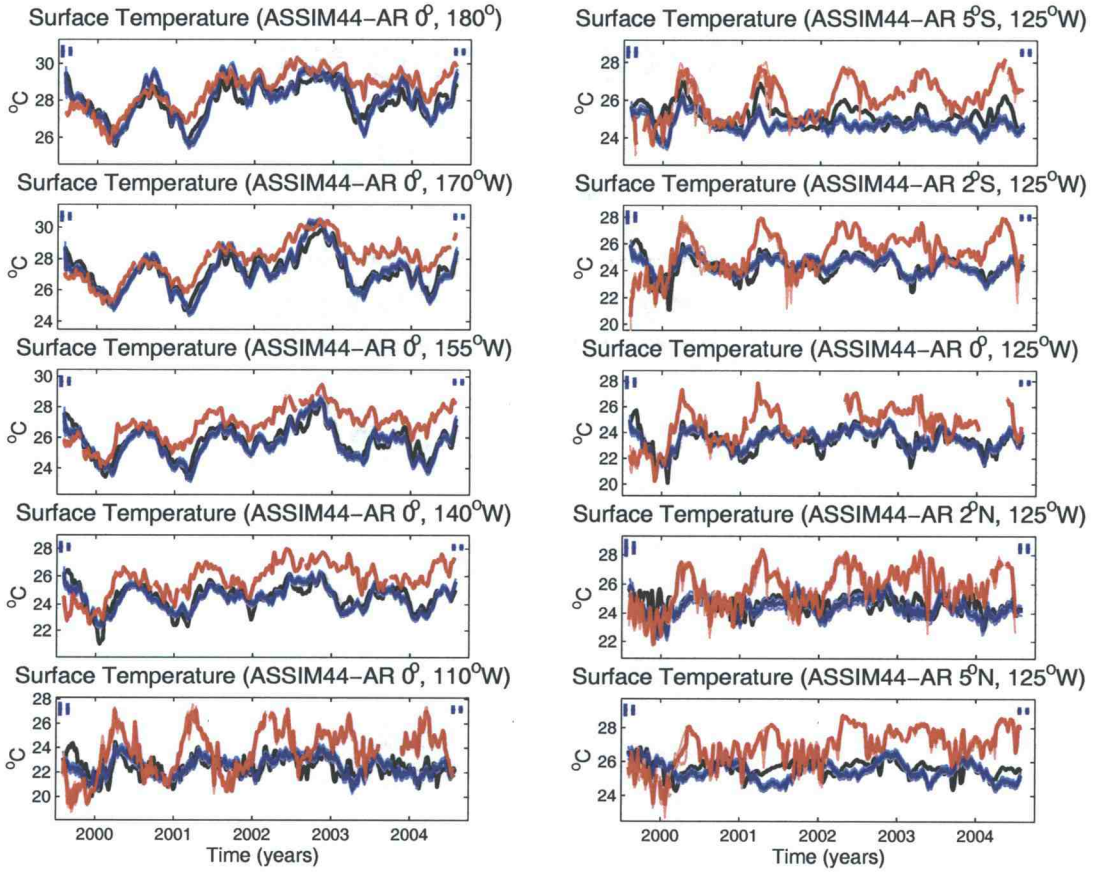

Figure 64. Same as Figure 51, except for the ASSIM44-AR run.

5.7 Summary and Conclusions

An assimilation scheme was developed with the goal of obtaining a better representation of the temperature and zonal currents in the equatorial Pacific cold tongue on interannual to intraseasonal timescales and simultaneously improving the statistics of the simulated TIWs during August 1999 to July 2004. The RKF developed for this study applied sophisticated assimilation and validation techniques developed from two decades of tropical Pacific Kalman filter experiments to a nonlinear GCM forced with high-frequency winds. The RKF passed the rigorous χ^2 test for the assimilated locations between 8°S and 2°N. The failure of the χ^2 test between 5° and 8°N was attributed to seasonally modulated color in the innovation sequence associated with TIWs on the northern flank of the cold tongue.

As expected, the assimilation of 5-day TAO DHA improved the interannual and intraseasonal variability of the DHA in the cold tongue. The 15 dyn cm model mean DH bias described in Section 5.4.2, however, was not reduced by this anomaly-for-anomaly assimilation approach. Bias correction algorithms (e.g., Keppenne et al. 2005) or the assimilation of SSH rather than anomalies (Parent et al. 2003) can be applied to reduce model forecast biases. While these techniques are successful, they do not remove the source of the biases from the model physics.

The RKF was able to reduce the mean surface mixed layer temperature cold bias, increase the variability of the thermocline, and increase the strength of the EUC core in the cold tongue. The RKF corrections, however, amplified the seasonal cycle of surface mixed layer temperature in the cold tongue during the observed suppression of the seasonal cycle associated with warm El Niño conditions (Figures 51 and 52). Although there is some documentation of problems with the

GC seasonal cycle in the eastern Pacific (e.g., Murtugudde et al. 1996; Gourdeau et al. 2000), most GC and GCAML studies have focused on validating the model surface mixed layer temperature and thermocline depth variability and not the seasonal cycles themselves. In the context of anomaly-for-anomaly data assimilation in a reduced state space configuration, these seasonal cycle errors turn out to be rather important.

A 5-day assimilation window and QuikSCAT wind forcing were chosen to resolve and correct the TIWs that perturb the cold tongue frontal boundaries. Although the seasonality, zonal structure, phase, and spread of spectral energy were in better agreement with the AVISO observations after assimilation, the RKF decreased the amplitudes of the TIWs and increased the averaged westward phase speeds (Figures 61 and 62). The decrease in SECN-NECC shear after assimilation (Figure 59) is consistent with weaker amplitude TIWs (Lyman et al. 2005a). Preliminary experiments indicate that the TAO zonal spacing may be too sparse and the assimilation of AVISO SSHA measurements along additional locations in the eastern Pacific (e.g., 5° downstream or upstream of TAO) would improve the TIW amplitudes and propagation in the assimilated runs.

It was demonstrated that assimilation in a reduced state space spanned by 139 EOFs was generally less successful than assimilation with 44 EOFs. Although the ASSIM139 run produced a less biased EUC compared with the TAO ADCP measurements (Figure 53), the model thermal biases remained large (Figures 56 and 57), and the simulated TIWs were faster and weaker than the ASSIM44 run (Figure 61). This may be due to the lack of dynamic relavance of the higher modes and the limited degrees of freedom as observations were only assimilated at 42

locations (Cane et al. 1996). Increasing the number of assimilated locations by adding AVISO SSHA measurements, as suggested above, might necessitate retaining 139 EOFs.

The incorporation of a second-order (10-day) autoregressive model effectively whitened the innovation sequence producing a nearly optimal RKF (Figures 54 and 63). This autoregressive approach developed by Chan et al. (1996) for a linear ocean model, improved the interannual and intraseasonal evolution of DH and surface mixed layer temperatures and improved the westward propagation speed of the TIWs in the nonlinear GCAML model. The removal of biases in the innovations, however, limited the ability of the RKF to make large corrections to the pre-existing cold tongue thermal biases (Figures 51 and 64). In other words, the assimilation is not able to reduce the model bias in a way that further decreases the agreement between the model and observed seasonal cycles.

Preliminary experiments which assimilate AVISO SSHA rather than TAO DHA produce colored innovations similar to the ASSIM44 run. This implies that errors in the innovation sequence due to the computation of TAO DH with salinity from T-S climatologies are not responsible for generating this second-order autoregressive process. Closer scrutiny must be given to the specification of heat and salt fluxes at the model boundaries and their role in producing forecast biases and color in the innovation sequences before anomaly-for-anomaly assimilation schemes can be optimized for nonlinear GCMs.

5.8 Acknowledgments

We thank Michael G. Schlax for preparing the QuikSCAT wind stress and Larry W. O'Neill for providing the SSMI wind speed and rainfall data used in this study. We also thank Eric C. Hackert for insightful comments on implementing the GCAML and Dudley B. Chelton for helpful comments on the focus of this article. Many thanks to the TAO Project Office and the AVISO program for the online distribution of data used in the assimilation and for RKF validation. The authors were supported by the National Oceanic and Atmospheric Administration Office of Global Programs under award NA16GP2016.

5.9 References

Ballabrera-Poy, J., E. Hackert, R. Murtugudde, and A. J. Busalacchi, 2005: An observing system simulation experiment for an optimal moored instrument array in the tropical Indian Ocean, *J. Climate,* submitted.

Baturin, N. G., and P. P. Niiler, 1997: Effects of instability waves in the mixed layer of the equatorial Pacific, *J. Geophys. Res.,* **102,** 27 771-27 793.

Bennett, A. F., 2002: *Inverse Modeling of the Ocean and Atmosphere,* 234 pp., Cambridge University Press, New York.

Bennett, A. F., B. S. Chua, D. E. Harrison, and M. J. McPhaden, 2000: Generalized inversion of Tropical Atmosphere-Ocean (TAO) data using a coupled model of the tropical Pacific, *J. Climate,* **13,** 2770-2785.

Borovikov, A., M. M. Rienecker, C. L. Kepenne, and G. C. Johnson, 2005: Multivariate error covariance estimates by Monte-Carlo simulation for assimilation studies in the Pacific Ocean, *Mon. Wea. Rev.,* in press.

Busalacchi, A. J., M. J. McPhaden, J. Picaut, 1994: Variability in the equatorial Pacific sea surface topography during the verification phase of the TOPEX/Poseidon mission, *J. Geophys. Res.,* **99,** 24 725-24 738.

Cane, M. A., and R. J. Patton, 1984: A numerical model for low-frequency equatorial dynamics, *J. Phys. Oceanogr.,* **14,** 1853-1863.

Cane, M. A., A. Kaplan, R. N. Miller, B. Tang, E. C. Hackert, and A. J. Busalacchi, 1996: Mapping tropical Pacific sea level: Data assimilation via a reduced state space Kalman filter, *J. Geophys. Res.,* **101,** 22 599-22 617.

Chatfield, C., 1996: *The Analysis of Time Series: An Introduction,* 5th ed., 283 pp., Chapman and Hall, London, UK.

Chelton, D. B., and M. H. Freilich, 2005: Scatterometer-based assessment of 10-m wind analyses from the operational ECMWF and NCEP numerical weather prediction models, *Mon. Wea. Rev.,***133,** 409-429.

Chelton, D. B., S. K. Esbensen, M. G. Schlax, N. Thum, M. H. Freilich, F. J. Wentz, C. L. Gentemann, M. J. McPhaden, and P. S. Schopf, 2001: Observations of coupling between surface wind stress and sea surface temparature in the eastern tropical Pacific, *J. Climate,***14,** 1479-1498.

Chen, D., W. T. Liu, S. E. Zebiak, M. A. Cane, Y. Kushnir, and D. Witter, 1999: Sensitivity of the tropical Pacific Ocean simulation to the temporal and spatial resolution of wind forcing, *J. Geophys. Res.,* **104,** 11 261-11 271.

Chan, N. H., J. B. Kadane, R. N. Miller, and W. Palma, 1996: Estimation of tropical sea level anomaly by an improved Kalman filter, *J. Phys. Oceanogr.,* **26,** 1286-1303.

Conkright, M. E., R. A. Locarnini, and H. E. Garcia, 2002: *World ocean atlas 2001: Objective analyses, data statistics, and figure, CD Rom documentation,* National Oceanographic Data Center, Silver Spring, MD.

Cox, M. D., 1980: Generation and propagation of 30-day waves in a numerical model of the Pacific, *J. Phys. Oceanogr.,* **10,** 1168-1186.

Daley, R., 1992: The Lagged innovation covariance: A performance diagnostic for atmospheric data assimilation, *Mon. Weath. Rev.,* **120,** 178-196.

Dewitte, B., S. Illig, L. Parent, Y. duPenhoat, L. Gourdeau, and J. Verron, 2003: Tropical Pacific baroclinic mode contribution and associated long waves for the 1994-1999 period from an assimilation experiment with altimetric data, *J. Geophys. Res.,* **108,** 3121, doi:10.1029/2002JC001362.

Donohue, K. A., and M. Wimbush, 1998: Model results of flow instabilities in the tropical Pacific Ocean, *J. Geophys. Res.,* **103,** 21,401-21,412.

European Centre for Medium-Range Weather Forecasts, 1994: The description of the ECMWF/WCRP Level III-A Global Atmospheric Data Archive, *Tech. Attach.,* 72 pp., Reading, England, U. K.

Fukumori, I., R. Raghunath, L.-L. Fu, and Y. Chao, 1999: Assimilation of TOPEX/Poseidon altimeter data into a global ocean circulation model: How good are the results? *J. Geophys. Res.,* **104,** 25,647-25,665.

Gent, P. R., and M. A. Cane, 1989: A reduced gravity, primitive equation model of the upper equatorial ocean, *J. Comp. Physics,***81,** 444-480.

Gourdeau, L., J. Verron, T. Delcroix, A. J. Busalacchi, and R. Murtugudde, 2000: Assimilation of TOPEX/Poseidon altimetric data in a primitive equation model of the tropical Pacific Ocean during the 1992-1996 El Niño Southern Oscillation period, *J. Geophys. Res.,* **105,** 8473-8488.

Hackert, E. C., A. J. Busalacchi, and R. Murtugudde, 2001: A wind comparison study using an ocean general circulation model for the 1997-1998 El Niño, *J. Geophys. Res.,* **106,** 2345-2362.

Ide, K., P. Courtier, M. Ghil, and A. C. Lorenc, 1997: Unified notation for data assimilation: operational, sequential, and variational, *J. Met. Soc. Japan,***75,** 181-189.

Jochum, M., and R. Murtugudde, 2004: Internal variability of the tropical Pacific Ocean, *Geophys. Res. Lett.,* **31,** L14309, doi: 10.1029/2004GL020488.

Johnson, E. J., and M. J. McPhaden, 1993: Structure of intraseasonal Kelvin waves in the equatorial Pacific ocean, *J. Phys. Oceanogr.,* **23,** 608-625.

Kailath, T., 1968: An innovations control approach to least square estimation - Part I: Linear filtering in additive white noise, *IEEE Trans. Automat. Control.,***13,** 646-655.

Kaplan, A., M. A. Cane, D. Chen, D. L. Witter, and R. E. Cheney, 2004: Small-scale variability and model error in tropical Pacific sea level, *J. Geophys. Res.,* **109,** C02001, doi:10.1029/2002JC001743.

Kennan, S. C., and P. J. Flament, 2000: Observations of a Tropical Instability Vortex, *J. Phys. Oceanogr.,* **30,** 2277-2301.

Keppenne, C. L., and M. M. Rienecker, 2003: Assimilation of temperature into an isopycnal ocean general circulation model using a parallel ensemble Kalman filter, *J. Marine Sys.,***40-41,** 363-380.

Keppenne, C. L., M. M. Rienecker, N. P. Kurkowski, and D. A. Adamec, 2005: Ensemble Kalman filter assimilation of temperature and altimeter data with bias correction and application to seasonal prediction, *Nonlinear Proc. in Geophys.,***12,** 491-503.

Kessler, W. S., L. M. Rothstein, and D. Chen, 1998: The annual cycle of SST in the eastern tropical Pacific, diagnosed in an ocean GCM, *J. Climate,***11,** 777-799.

Levitus, S., T. Boyer, J. Antonov, R. Burgett, 1994: *World ocean atlas 1994, Temperature, NOAA Atlas NESDIS,* vol. 4, 129 pp., Natl. Oceanic and Atmos. Admin., Silver Spring, MD.

Lyman, J. M., D. B. Chelton, R. A. deSzoeke, and R. M. Samelson, 2005a: Tropical instability waves as a resonance between equatorial Rossby waves, *J. Phys. Oceanogr.,* **35,** 232-254.

Lyman, J. M., G. C. Johnson, and W. S. Kessler, 2005b: Structure of 17-day versus 33-day tropical instability waves in the equatorial Pacific, *J. Phys. Oceanogr.,* revised.

Madec, G., P. Delecluse, M. Imbard, C. Levy, 1998: OPA 8.1 general circulation model reference manual, *Notes de l'IPSL no. 11,* 91 pp. Université P. et M. Curie, Paris.

McCreary, J. P, and Z. Yu, 1992: Equatorial dynamics in a 2.5-layer model, *Prog. Oceanogr.,***29,** 61-132.

McPhaden, M. J., 1993: TOGA-TAO and the 1991-1993 El Niño Southern Oscillation event, *Oceanogr.,***6,** 36-44.

Meissner, T., D. Smith, and F. Wentz, 2001: A 10-year intercomparison between collocated SSM/I oceanic surface wind speed retrievals and global analyses, *J. Geophys. Res.,* **106,** 11 731-11 742.

Miller, R. N., 1990: Tropical data assimilation experiments with simulated data: the impact of the Tropical Ocean and Global Atmosphere Thermal Array for the Ocean, *J. Geophys. Res.,* **95,** 11 461-11 482.

Miller, R. N., and M. A. Cane, 1989: A Kalman filter analysis of sea level heights in the tropical Pacific, *J. Phys. Oceanogr.,* **19,** 773-790.

Miller, R. N., and M. A. Cane, 1996: Tropical data assimilation: theoretical aspects, in *Modern Approaches to Data Assimilation in Ocean Modeling,* edited by P. Malanotte-Rizzoli, pp. 207-233, Elsevier Sci., New York.

Miller, R. N., A. J. Busalacchi, and E. C. Hackert, 1995: Sea surface topography fields of the tropical Pacific from data assimilation. *J. Geophys. Res.,* **100,** 13 389-13 425.

Millero, F. J., and A. Poisson, 1981: International one-atmosphere equation of state of seawater, *Deep-Sea Res.,***28,** 625-629.

Murtugudde, R., and A. J. Busalacchi, 1998: Salinity effects in a tropical ocean model, *J. Geophys. Res.,* **103,** 3283-3300.

Murtugudde, R., R. Seager, and A. J. Busalacchi, 1996: Simulation of the tropical oceans with an ocean GCM coupled to an atmospheric mixed-layer model, *J. Climate,***9,** 1795-1815.

Oberhuber, J., 1988: An atlas based on 'COADS' Data Set, *Rep. 15.,* Max-Planck-Inst. für Meterol., Hamburg, Germany.

Parent, L., C.-E. Testut, J.-M. Brankart, J. Verron, P. Brasseur, and L. Gourdeau, 2003: Comparative assimilation of Topex/Poseidon and ERS altimeter data and of TAO temperature data in the tropical Pacific ocean during 1994-1998, and the mean sea-surface height issue, *J. Mar. Res.,***40-41,** 381-401.

Perez, R. C., D. B. Chelton, and R. N. Miller, 2005: The effects of wind forcing and background mean currents on the latitudinal structure of equatorial Rossby waves, *J. Phys. Oceanogr.,* **35,** 666-682.

Perez, R. C., 2005: Numerical and assimilative studies of the equatorial Pacific cold tongue. Ph.D. thesis, Oregon State University, Corvallis, Oregon.

Philander, S. G. H., 1978: Instabilities of zonal equatorial currents, Part 2, *J. Geophys. Res.,* **83,** 3679-3682.

Qiao, L., and R. H. Weisberg, 1995: Tropical instability wave kinematics: Observations from the Tropical Instability Wave Experiment, *J. Geophys. Res.,* **100,** 8677-8693.

Reverdin, G., A. Kaplan, M. A. Cane, 1996: Sea level from temperature profiles in the tropical Pacific Ocean, 1975-1982, *J. Geophys. Res.,* **101,** 18 105-18 119.

Schlax, M. G., and D. B. Chelton, 1992: Frequency domain diagnostics for linear smoothers, *J. Amer. Stat. Assoc.,***87,** 1070-1081.

Seager, R., M. Blumenthal, and Y. Kushnir, 1995: An advective atmospheric mixed layer model for ocean modeling purposes: Global simulation of surface heat fluxes, *J. Climate.,***8,** 1951-1964.

Stockdale, T. N., A. J. Busalacchi, D. E. Harrison, and R. Seager, 1998: Ocean modeling for ENSO, *J. Geophys. Res.,* **103,** 14 325-14 355.

Verron, J., L. Gourdeau, D. T. Pham, R. Murtugudde, and A. J. Busalacchi, 1999: An extended Kalman filter to assimilate satellite altimeter data into a nonlinear numerical model of the tropical Pacific Ocean: method and validation, *J. Geophys. Res.,* **104,** 5441-5458.

Vialard, J., A. T. Weaver, D. L. T. Anderson, and P. Delecluse, 2003: Three- and four-dimensional variational assimilation with a general circulation model of the tropical Pacific Ocean. Part II: physical validation, *Mon. Wea. Rev.,***131,** 1379-1395.

Vossepoel, F. C., G. Burgers, and P. J. van Leeeuwen, 2002: Effects of correcting salinity with altimeter measurements in an equatorial Pacific ocean model, *J. Geophys. Res.,* **107,** 8001, doi:10.1029/2001JC000816.

6 Impact of a reduced state space Kalman filter on the equatorial Pacific cold tongue mixed layer heat budget

Renellys C. Perez, and R. N. Miller

To be submitted to

Journal of Geophysical Research, Oceans

or

Journal of Climate

6.1 Abstract

A four-dimensional multivariate data assimilation scheme is applied to the tropical Pacific to determine whether the cold tongue surface mixed layer temperature balance of a nonlinear GCM could be improved by the assimilation of Tropical Atmosphere Ocean dynamic height anomalies during August 1999 to July 2004. The differences in the unassimilated and assimilated model runs are compared in 3 regions covering the zonal extent of the cold tongue (165°E to 80°W) and extending from 1.5°S to 1.5°N. Comparisons are made to sea surface temperature and horizontal temperature gradients from the Reynolds et al. (2002) blended satellite/in-situ data set and horizontal advection estimated at 3 equatorial Tropical Ocean Atmosphere moorings: 170°, 140°, and 110°W. The assimilation scheme provides prior and posterior error bars that determine whether the model and observations are significantly different. The dominant terms in 5-year mean temperature balance of the unassimilated model run are entrainment and net surface flux. The second order balance is maintained by the zonal and meridional advection and diffusion. Despite the decrease in positive (warming) high-frequency horizontal advection associated with TIWs, assimilation does not alter the mean balance significantly as there is a compensatory decrease in magnitude of the cooling by the low-frequency horizontal advection. Both the unassimilated and assimilated tendencies have annual cycles that are too weak in the eastern Pacific giving rise to cold tongue sea surface temperatures that are too cold in the spring and summer months and during the 2002-2003 El Niño event. The low annual amplitude of the model tendency is related to errors in the simulated net surface flux, vertical entrainment and diffusion.

6.2 Introduction

The eastern equatorial Pacific is characterized by a "cold tongue" of water which seasonally extends westward from South America along the equator to the central Pacific (Mitchell and Wallace 1992), finds its strongest expression during La Niña events and is weakened during El Niño events (Wallace et al. 1989; Deser and Wallace 1990). At select Tropical Atmosphere Ocean (TAO; McPhaden 1993) equatorial moorings between 165°E and 110°W, Wang and McPhaden (WM; 1999) found that the mean temperature balance in the cold tongue mixed layer is largely controlled by the net surface flux adjusted for penetrative radiation (41 $W\ m^{-2}$), vertical entrainment ($-61\ W\ m^{-2}$), meridional (28 $W\ m^{-2}$) and zonal advection ($-8\ W\ m^{-2}$). Zonal and meridional advection become important when heat fluxes are analyzed a few degrees away from the equator and on average export heat from the cold tongue (e.g., Swenson and Hansen 1999).

La Niña conditions strengthen the South Equatorial Current (SEC) and Equatorial Undercurrent (EUC) (Johnson et al. 2002), generating enhanced latitudinal shear between the eastward flowing North Equatorial Countercurrent (NECC) and the north branch of the westward flowing SEC (SECN), and increased vertical shear between the SEC and the eastward flowing EUC. Tropical instability waves (TIWs), which likely result from the meridional and vertical shears in the equatorial current system (see Lyman et al. 2005 for a review of TIW literature), are most active during La Niña and nearly supressed during El Niño (Baturin and Niiler 1997). Both observed (Hansen and Paul 1984; Bryden and Brady 1989; Baturin and Niiler 1997; WM 1999; Swenson and Hansen 1999; WM 2000) and modeled (Kessler et al. 1998; Vialard et al. 2001; Jochum and Murtugudde 2005) TIWs in the Pacific

produce equatorward oceanic eddy heat flux on par with the large-scale advective heat flux away from the equator. Hence, TIWs play an important role in the cold tongue heat balance and more observations and numerical studies are needed to quantify the mean and ENSO modulated variability inherent to the TIW heat flux.

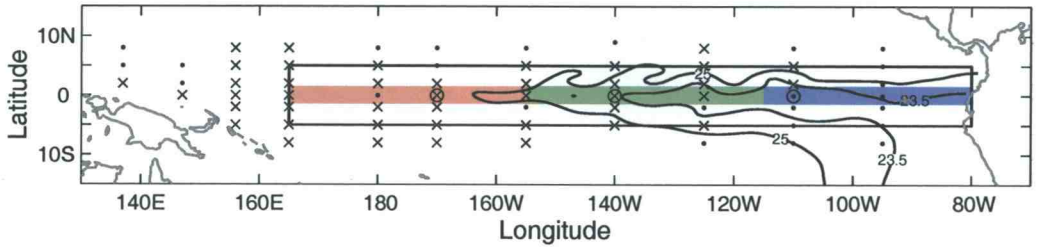

Figure 65. 20-25 Dec 2000 average of the 23.5 and 25°C isotherms from the NODA run with the heat budget box-average boundaries overlaid in red (Region 1), green (Region 2), and blue (Region 3). The x-marks and dots denote the assimilated and withheld TAO moorings, respectively, of Perez and Miller (2005). The circles identify the locations of TAO ADCPs used for validation of the model and assimilated heat budget terms. The larger box indicates the area in which the spatial structure of the mean SST and temperature balances are analyzed in Figures 66 to 68.

In Perez and Miller (2005) a reduced state space Kalman filter (RKF) was developed to improve the three-dimensional structure of temperature and zonal currents in the equatorial Pacific cold tongue in a nonlinear general circulation model. Output from the unassimilated (NODA) model run which is described in Section 6.3.1 was compared with the output from the model when 5-day dynamic height anomalies from 42 TAO moorings were assimilated in the equatorial Pacific waveguide (x-marks in Figure 65). A 5-day assimilation cycle and a Monte Carlo Markov Chain model of the forecast errors were constructed to resolve and correct TIWs in the model. The Kalman filter machinery operated in a reduced state space spanned by the number of Empirical Orthogonal Functions (EOFs) required to

capture a significant percentage of the model variance. This truncation of the model state space by 4 to 5 orders of magnitude is required to minimize the computational expense of the Kalman filter operations.

Perez and Miller (2005) determined that keeping 44 EOFs (80% of the model variance) in the assimilation scheme increased the intraseasonal to interannual variability of dynamic height in the equatorial Pacific cold tongue, reduced the model thermal biases, and generated more realistic TIWs than the assimilation run with 139 EOFs (95% of the model variance). Removing color from the sequence of model-data misfits with a second-order (10-day) autoregressive model nearly optimized the Perez and Miller (2005) assimilation scheme with 44 EOFs (hereafter referred to as the ASSIM44-AR run) and improved the cold tongue evolution and the phase and westward propagation of the TIWs. Unlike the assimilation runs without an autoregressive model, the ASSIM44-AR run was not able to make large corrections to the pre-existing cold tongue thermal biases in the model and reduced the variability of model surface mixed layer temperature (hereafter SST) slightly in the eastern Pacific. This is evident from comparison of the 5-year mean and standard deviations of model and SST from the Reynolds et al. (2002) blended satellite-in situ dataset (Reynolds SST) from 5°S to 5°N between 165°E and the eastern boundary (Figure 66). The NODA and ASSIM44-AR cold tongue SSTs are too cold (ca. 1.5°C) and exhibit far less variability than the observed SST in the cold tongue. The Reynolds SST are a few tenths of a degree warmer than the temperature averaged over the surface mixed layer (WM 1999) and will therefore be warmer than the model SSTs (e.g., the vertically homogenous temperatures in the model surface mixed layer). This small bias, however, does not account for the

1.5°C cold tongue bias in the model or the phasing errors in the model seasonal cycle which limited the number of TAO observations assimilated in the eastern Pacific (Figure 65; Perez and Miller 2005). Note that Reynolds SST may exhibit less variability than reality due to smoothing described in Section 6.3.2.2.

In this study, the temperature budget terms from ASSIM44-AR run will be compared with those from the NODA run in the surface mixed layer to determine whether the assimilation of TAO dynamic height anomalies into a nonlinear GCM improved the cold tongue temperature budget. The numerical model, equations governing the temperature balance, and the strategy for the model and data comparisons are detailed in Section 6.3. In Section 6.4, spatial and temporal variations of the cold tongue temperature balance are compared for the NODA and ASSIM44-AR runs. Assimilation improved the phase propagation and zonal structure of the model TIWs but significantly weakened the amplitudes in Perez and Miller (2005). As the reduction of TIW amplitudes was most pronounced in the ASSIM44-AR run, the terms in the temperature balance associated with TIW fluxes will also be compared in Section 6.4. Temperature fluxes along the equator between 170° and 110°W will be compared with available observations in Section 6.4. The time series of prior and posterior errors that are byproducts of the Kalman filter will be used to provide error bars (Miller 1990; Miller et al. 1995) for terms in the ASSIM44-AR temperature balance to diagnose whether the model and observed tendency and horizontal advection are significantly different and examine why thermal biases and low variability characterize the model cold tongue. In Section 6.6, the results from this study are summarized and conclusions about the impact of data assimilation on the GCAML temperature budget are made.

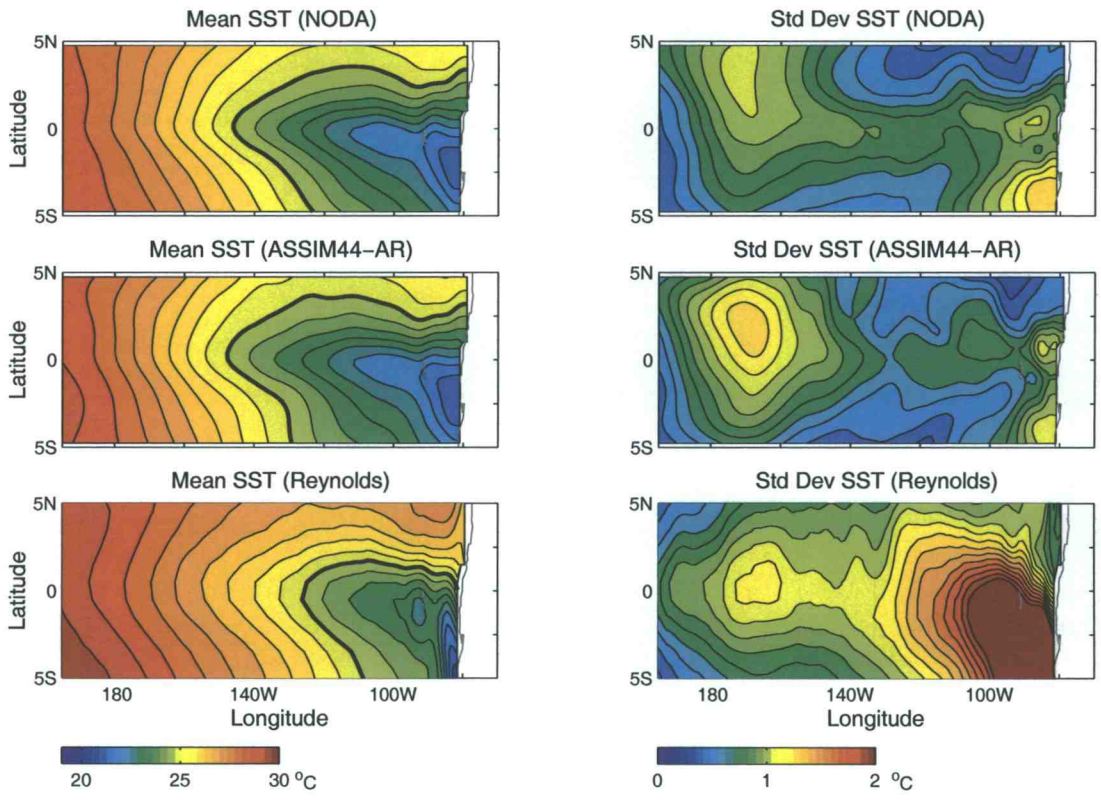

Figure 66. August 1999 to July 2004 mean (left panels) and standard deviation (right panels) of the NODA (upper panels) and ASSIM44-AR (middle panels) 5-day SST from 5°S to 5°N between 165°E and the eastern boundary. The mean and standard devation from the same time period of the 7-day Reynolds SST time series are plotted in the bottom panels. The thick black contour in the left panels corresponds to 25°C.

6.3 Numerical Model and Heat Flux Comparisons

6.3.1 Numerical Model. The numerical model used in this heat flux study is the Gent and Cane (1989) nonlinear, reduced gravity, β-plane model coupled to an advective atmospheric mixed layer (Seager et al. 1995; Murtugudde et al. 1996). The model implementation summarized below is that of Perez and Miller (2005) and is hereafter referred to as the GCAML model. The model domain spans

the entire tropical Pacific from 124°E to 76°W and 30°S to 30°N. No-slip conditions are specified on the eastern and western boundaries. At the northern and southern boundaries, free-slip conditions are specified and the model temperature and salinity are gradually relaxed to Levitus climatology (Levitus et al. 1994) over a 5° wide sponge layer. The model has a uniform zonal grid with 1° resolution and a stretched meridional grid with 0.33° resolution in the equatorial waveguide and 1° resolution at the poleward boundaries. The vertical layers consist of a wind-driven surface mixed layer and 14 σ-like layers which vary in fixed proportion to the thickness of the active layer. The active layer base is defined by a bottom temperature and salinity, 9°C and 34.85 psu, respectively, and has a nominal depth of 600 m. For every time step (4 hours), the model has been modified to calculate dynamic height relative to 500 db prognostically from the model temperature, salinity, and layer thicknesses (Perez and Miller 2005).

High-resolution winds from the SeaWinds scatterometer aboard the QuikSCAT satellite (Chelton and Freilich 2005) during August 1, 1999 to July 31, 2004 were used to force the model. The QuikSCAT winds were binned onto a 5-day x 1° zonal x 1° meridional grid and a 8-day x 4° zonal x 2° meridional loess smoother (Schlax and Chelton 1992) was applied. The model was spun up from rest with seasonal cycle forcing and Levitus climatology provided the initial values of temperature, salinity, and layer thickness. In addition to Levitus, several monthly climatologies available on a 2° zonal x 2° meridional grid are used to specify the heat and rain fluxes at the model surface. These monthly fields include Interannual Satellite Cloud Climatology Project (ISCCP) cloud cover data, Earth Radiation Budget Experiment (ERBE) solar radiation, Oberhuber (1988) precipitation, and European Center for

Medium Range Weather Forecasting (ECMWF 1994) estimates of wind speed, air temperature, and humidity at sea level. As the GCAML model requires that all forcing fields have the same temporal and spatial grid, the climatological fields were linearly interpolated from 2° grid to a 1° grid and the monthly climatologies were converted into 5-day climatologies via cubic spline interpolation. The model was spun up for the 30 years preceding August 1, 1999 with seasonal cycle winds obtained by fitting an annual cycle and five harmonics to the five-year QuikSCAT wind stress record. The output from the model driven with the real QuikSCAT winds during August 1, 1999 to July 31, 2004 was stored as 5-day averages.

6.3.2 GCAML heat budget. The GCAML model surface mixed layer heat budget is given by

$$\rho C_p h\left(\frac{\partial T}{\partial t} + u\frac{\partial T}{\partial x} + v\frac{\partial T}{\partial y} + \frac{w_e}{h}\frac{\partial T}{\partial s}\right) = Q + D \tag{30}$$

where local changes in heat depend on the zonal and meridional advection of heat, vertical entrainment at the base of the mixed layer computed by the Chen et al. (1994) hybrid mixing scheme, net surface heat flux from the atmosphere Q, and a diffusion term D which represents numerical horizontal diffusion by the Shapiro (1971) filter. The net surface heat flux is the sum of the incoming shortwave solar radiation, evaporative or latent heat, outgoing longwave radiation, and sensible heat flux minus the heat lost from the mixed layer due to penetrative radiation. The individual atmospheric heat flux terms are computed using the surface climatological fields described in Section 6.3.1, GCAML surface mixed layer temperatures (hereafter SST), and the advective atmospheric mixed layer model of Seager et al. (1995).

Heat fluxes are converted to temperature fluxes by dividing by $\rho C_p = 4.12\ 10^{-6}$ J m^{-3} °C^{-1}, the value used internally by the model, and the 5-day averages of model surface mixed layer thickness, h. Although the model updates the heat budget every time step, only 5-day averages of the net surface heat flux, entrainment, zonal and meridional advection are directly output by the model. The tendency term $\frac{\partial T}{\partial t}$, is estimated from the 5-day model averages of temperature using centered (10-day) differences. The residual ($D/\rho C_p h$) or diffusion term also includes truncation errors from use of centered differences and nonlinear interactions introduced by dividing the heat flux by 5-day averages of h to estimate the temperature flux. All terms affecting the temperature balance are displayed such that positive (negative) values indicate warming (cooling) tendency.

The time series of GCAML SST and horizontal velocity are decomposed into a high-frequency component and a seasonal to interannual component such that the nonlinear horizontal temperature advection terms can be separated into

$$u\frac{\partial T}{\partial x} = u_l\frac{\partial T_l}{\partial x} + u_h\frac{\partial T_l}{\partial x} + u_l\frac{\partial T_h}{\partial x} + u_h\frac{\partial T_h}{\partial x} \quad (31)$$

$$v\frac{\partial T}{\partial y} = v_l\frac{\partial T_l}{\partial y} + v_h\frac{\partial T_l}{\partial y} + v_l\frac{\partial T_h}{\partial y} + v_h\frac{\partial T_h}{\partial y}. \quad (32)$$

To obtain the low-frequency signal (u_l and T_l), the model temperature and velocity are passed through 2 running mean filters with 60-day windows which corresponds to a filter cutoff of approximately 135 days. The high-frequency data, u_h and T_h, are merely the residuals of $u - u_l$ and $h - h_l$, respectively. In Section 6.4, the low-frequency (LF) advection terms, $-u_l\frac{\partial T_l}{\partial x}$ and $-v_l\frac{\partial T_l}{\partial y}$, are compared with the high-frequency (HF) terms, $-(u\frac{\partial T}{\partial x} - u_l\frac{\partial T_l}{\partial x})$ and $-(v\frac{\partial T}{\partial y} - v_l\frac{\partial T_l}{\partial y})$, from (2) and (3).

The temperature gradients that are used to compute the HF and LF advection terms are compute using centered (2° zonal and 0.67° meridional in the waveguide) differences.

6.3.2.1 Definition of Regions for Spatially-Averaged Flux Estimates: Spatially-averaged temperature fluxes are computed in three cold tongue regions which extend from 1.5°S and 1.5°N (colored boxes in Figure 65) for the GCAML runs. The first box has zonal boundaries along 165°E and 155°W and overlaps with the westward penetrating equatorial Pacific cold tongue only during the winter and spring months (as marked by the 25°C isotherm in Figure 65). Large SST variability associated with TIWs has been observed in the equatorial Pacific approximately within the longitudinal range of the second box, 155°W to 115°W, using measurements from the Tropical Rainfall Measuring Mission Microwave Imager (Chelton et al. 2000). The third box with zonal boundaries along 115°W and 80°W is influenced by the cold tongue throughout the entire five-year record and overlaps with the region where TIWs have been observed forming (e.g., Chelton et al. 2000). As will be discussed in Section 6.4, the meridional boundaries of the three boxes were defined to isolate the fluxes affecting the cold tongue temperature balance near the equator and exclude the impact of those temperature fluxes on the warm water surrounding the cold tongue.

6.3.2.2 TAO/Reynolds Heat Flux Comparisons: The GCAML temperature flux terms are compared with available observations along the equator between 170°W and the eastern boundary. Four TAO ADCP moorings (circles in Figure 65) are contained within the 3 box-average regions defined above: 165°E and 170°W (Region 1), 140°W (Region 2), and 110°W (Region 3). In Region 1, however,

the heat budget is only analyzed at 170°W as it is more likely to overlap with the cold tongue. While vertical temperature profiles are also available at these sites, the zonal and meridional spacing of the TAO moorings along the equator, $10 - 15°$ and 2°, respectively, are too large to estimate zonal and meridional temperature gradients reliably.

Following the approach of WM (1999; 2000; 2001), weekly Reynolds SST are used to estimate horizontal temperature gradients and the tendency term. Reynolds SST is available globally on a 1° zonal x 1° meridional grid and measurements from 165.5°E to 80.5°W and 1.5°S to 1.5°N are used in the model-data comparisons in Regions 1 to 3. As Reynolds SST incorporates in situ measurements from the TAO array, the two data sets are very similar at the TAO moorings and the SST uncertainty is assumed to be 0.3°C along the equator (Reynolds et al. 2002; WM 1999). The weekly Reynolds time series has been linearly interpolated to 5-day intervals and the horizontal gradients are combined with TAO surface mixed layer zonal and meridional velocity to produce 5-day time series of zonal and meridional advection, respectively, at 170°, 140°, and 110°W.

WM (1999; 2000; 2001) found that the meridional gradients of Reynolds SST varied with the type of differencing method utilized and determined that a 1° upwind differencing scheme and 1.3 scaling were required for the meridional gradients. The meridional scaling was introduced to better match the meridional gradients observed by TAO (using a 2° upwind scheme) and thereby counter the effects of the smoothing applied to the Reynolds dataset (WM 1999; 2000; 2001) which Chelton and Wentz (2005) estimate is on the order of 1000 km. The zonal gradients were relatively insensitive to the differencing methodology applied given longitudinal scales of 4° to

10° and 4° (WM 2000; 2001) and 6° (WM 1999) centered differences were used. For this model comparison study, however, it was decided to take simple (1°) centered differences of the Reynolds SST and not introduce a meridional scaling in the box average regions and at the three TAO moorings.

To compute the TAO mixed layer zonal and meridional currents, a 5-year time series of mixed layer depth (MLD) was generated at the 3 moorings. Using the 5-day time series of TAO temperature profiles, the MLD is the depth at which the linearly interpolated temperature is 0.5°C less than the TAO SST. The MLD was computed for all TAO moorings between 180° and 95°W and the stations surrounding 170°, 140°, and 110°W were only used to fill gaps and generate a continuous 5-year record. As the GCAML h can not exceed 100 m or fall below 10 m, these bounds were also imposed on the TAO MLD. The MLD uncertainty is assumed to be 10 m (WM 1999; 2000).

To generate zonal and meridional mixed layer currents, it was necessary to linearly extrapolate the velocities from the upward looking TAO ADCPs as most of the measurements above 30 m depth were removed due to sidelobe contamination (Plimpton et al. 1997; WM 1999). This is done by estimating the 10 m vertical shear between the shallowest measurements (e.g., 30 and 40 m) and using the shear to fill in the missing near-surface values (e.g., between 10 and 30 m). These currents were then averaged over the MLD to obtain mixed layer zonal and meridional velocity measurements. The linear extrapolation described above may introduce biases of several $cm\ sec^{-1}$ to the mixed layer velocity (WM 1999) and a 5 $cm\ sec^{-1}$ rms error has been assumed for the velocity which is then divided by the square root of the number of vertical measurements average over the mixed layer to produce the

error bars. The uncertainty in the observed zonal and meridional advection were computed using

$$\sigma_{zonal} = \left(\left(\sigma_u \frac{\partial T}{\partial x} \right)^2 + \left(u \sigma_{\frac{\partial T}{\partial x}} \right)^2 \right)^{1/2} \quad (33)$$

$$\sigma_{meridional} = \left(\left(\sigma_v \frac{\partial T}{\partial y} \right)^2 + \left(v \sigma_{\frac{\partial T}{\partial y}} \right)^2 \right)^{1/2} \quad (34)$$

where the zonal and meridional SST gradient errors were both assumed to be constant and values comparable to WM (2000) were chosen (2.3×10^{-4}°C km^{-1}).

In the WM (1999; 2000; 2001) studies, estimates of the net surface heat flux were also generated using available shortwave and longwave radiation observations, bulk formulas, and a parameterization for the penetrative radiation. The cumulative flux due to vertical entrainment and diffusion was then obtained as the residual of the horizontal material derivative (tendency plus horizontal advection) minus the net atmospheric flux (including the effects of penetrative radiation). In a more recent paper by McPhaden (2002), the vertical advection/entrainment term was computed using an estimate of the vertical velocity and the temperature differential between the surface and 20 m. Although the calculations of net surface heat flux and vertical entrainment are not repeated in this paper, the comparisons of the observed and modeled tendency and horizontal advection terms will be put into the context of the WM (1999; 2000; 2001) and McPhaden (2002) results in Section 6.5.

6.4 NODA and ASSIM44-AR Cold Tongue Temperature Balance

The 5-year mean temperature balance in the NODA run is maintained to first-order by the net surface flux and vertical entrainment in a narrow band

along the equator with largest values between 115°W and 95°W (upper panels of Figure 67). The next largest term is the mean LF meridional advection which has equatorially asymmetric minima along 1°N and 1.3°S and acts to cool the cold tongue. The pattern of larger amplitudes on the northern flank of the cold tongue is consistent with a stronger model SEC north of the equator and larger meridional temperature gradients (Perez and Miller 2005). The mean LF zonal advection is small compared with the LF meridional advection with alternating positive and negative values on the northern flank of the cold tongue between 105°W and the eastern boundary and broad regions of cooling north and south of the equator along 2°N and 4°S, respectively. The mean HF zonal and meridional advection terms associated with TIW eddy fluxes are positive and act to warm the equatorial Pacific cold tongue. The HF zonal advection is equatorially asymmetric with largest value along 1°N between 135°W to 85°W. The HF meridional advection is maximum along the equator with largest values between 135°W to 85°W. Spatially averaging from 5°S to 5°N and 165°E to the eastern boundary, the contribution to the temperature balance from the HF terms is less than half that of the LF terms in the NODA run. However, averaging over such a large box diminishes the HF meridional advection contribution by TIWs which simulateously warm the cold tongue and cool the warm water surrounding the cold tongue. As expected, the 5-year mean of the tendency term is near zero in the NODA run (lower left panel in Figure 67). The mean residual temperature flux (lower right panel in Figure 67) is positive near the northern flank of the cold tongue along 0.6°N and negative along 2°N and 2°S coincident with extrema in the LF zonal and meridional advection terms.

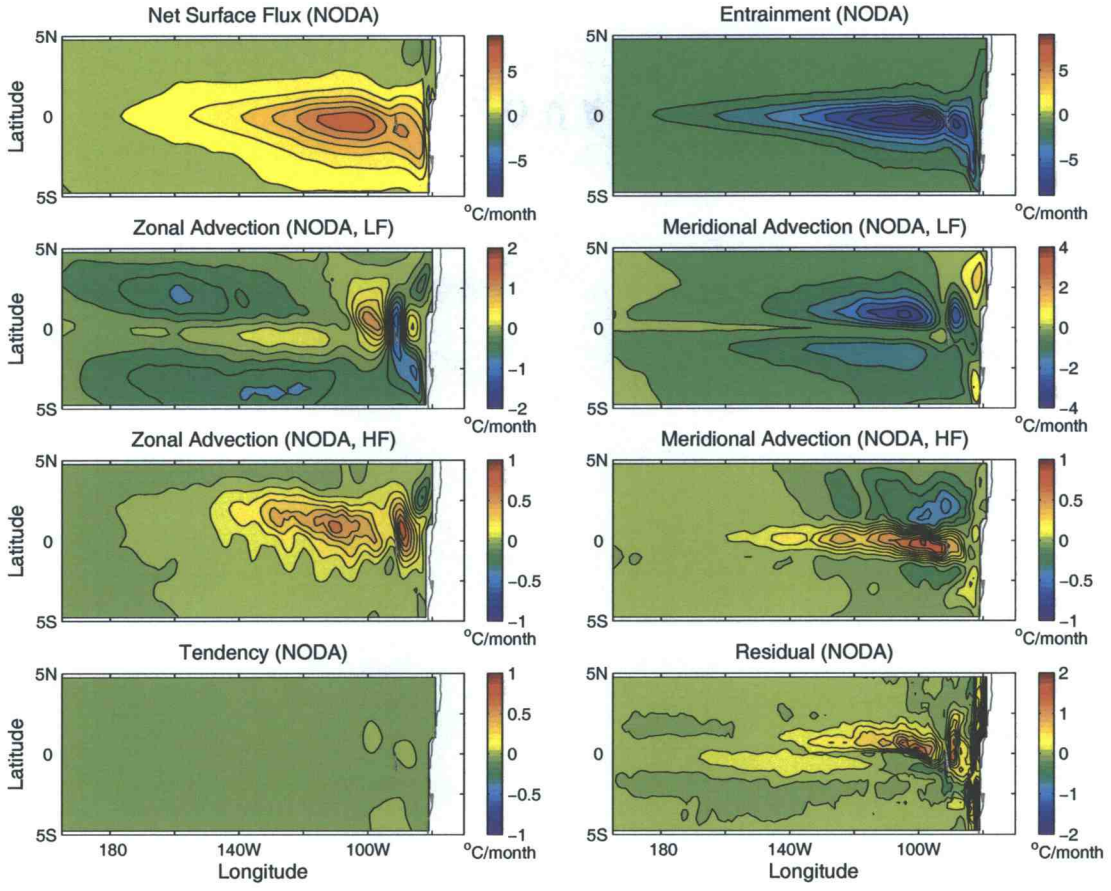

Figure 67. August 1999 to July 2004 mean of the NODA temperature flux terms (net surface flux, entrainment, LF zonal and meridional advection, HF zonal and meridional advection, tendency, and the residual or diffusion term) 5°S to 5°N between 165°E and the eastern boundary.

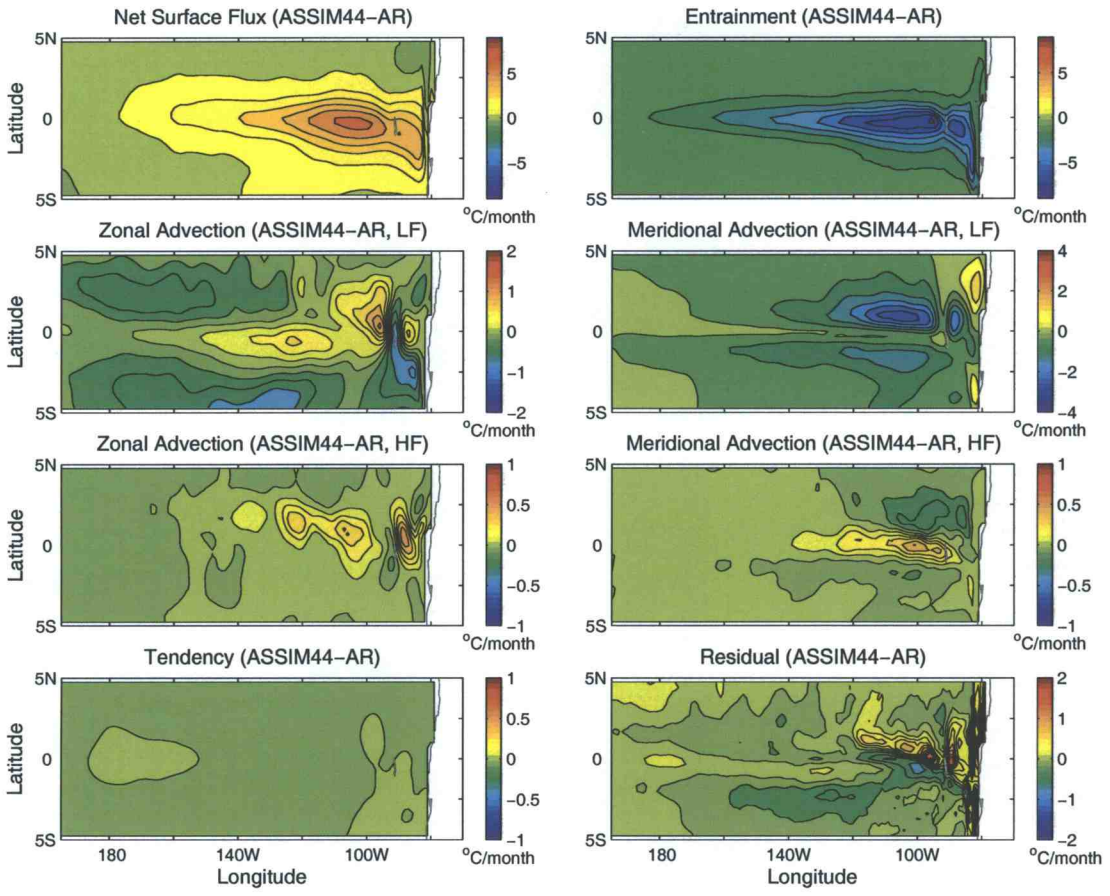

Figure 68. Similar to Figure 67, except for the ASSIM44-AR run.

Although assimilation does not alter which terms play a significant role in the mean temperature balance, the magnitudes of the mean net surface flux, vertical entrainment, and meridional advection decrease slightly in the eastern Pacific for the ASSIM44-AR run (Figure 68). The decreased LF meridional advection in the ASSIM44-AR run coincides with a decrease in the strength of the SECN, decreased meridional shear between the SECN and NECC, and weaker TIWs (Perez and Miller 2005). The mean LF zonal advection along the equator increases with

largest (warming) values along 0.6°S between 125°W and 115°W associated with the strengthening of the EUC which surfaces when the cold tongue subsides in the spring and summer months. The weak TIW amplitudes of the ASSIM44-AR run decrease the mean HF zonal and meridional advection terms significantly and supply less heat to the cold tongue. The 5-year mean tendency increased slightly for the ASSIM44-AR run, but is still very close to zero (lower left panel in Figure 68). The mean ASSIM44-AR residual (lower right panel in Figure 68) has larger meridional gradients across the cold tongue northern front in the eastern Pacific than the NODA run and increased cooling of the water surrounding the cold tongue along 2°S and 2°N between the dateline and 110°W.

To further examine the spatial and temporal variability of the cold tongue heat balance, the 5-year time series of SST (Figure 69) and the temperature budget terms (Figures 70 to 75) spatially-averaged over the three regions defined in Section 6.3.2.1 are compared for the NODA and ASSIM44-AR runs. Note that the range of the y-axis for plots of a particular temperature flux is the same throughout the three regions to facilitate comparisons of spatial variations. Table 10 compares the 5-year mean and standard deviations of SST and the temperature flux terms in the three regions. The contribution of the HF and LF zonal and meridional advection terms are also evaluated in the three regions for the NODA and ASSIM44-AR runs (Table 11 and Figures 76 and 77). Defining the regions in this way will exclude the heating and cooling that occurs poleward of 1.5° in order to focus on the direct impact of the TIWs on the cold tongue temperature balance.

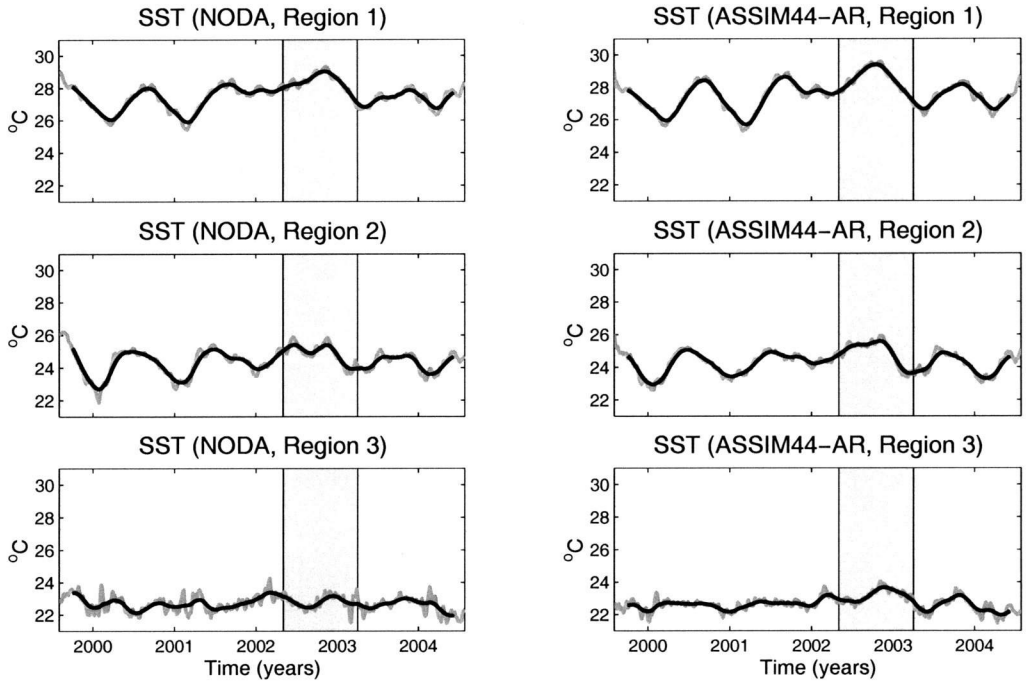

Figure 69. August 1999 to July 2004 time series of NODA (left panels) and ASSIM44-AR (right panels) SST averaged over Region 1, 2, and 3 (defined in Section 2.2.1). The gray and black lines correspond to the 5-day record and the same record with 60-day low-pass filtering, respectively. The gray shaded area indicates the 2002-2003 El Niño event.

6.4.1 Region 1. In Region 1, the mean NODA temperature budget (Figure 70 and Table 10) is balanced by net surface flux (0.92 °C month^{-1}) and entrainment (-0.81 °C month^{-1}). The mean total (not decomposed into LF and HF signals) zonal and meridional advection and tendency term are of secondary importance but all act to cool Region 1, whereas the residual term acts to warm Region 1. Entrainment and meridional advection exhibit little seasonal and interannual variability in Region 1 (black lines in Figure 70 and Table 10), although meridional advection becomes positive and the magnitude of the entrainment decreases during the 2002-2003 El Niño. The seasonal fluctuations of the tendency

term (black line in the lower left panel of Figure 70) are highly correlated (0.88) with the seasonal fluctuations of zonal advection (black line in the center left panel of Figure 70) with positive values (warming) consistent with the warmer SST of the 2002-2003 El Niño (Figure 69).

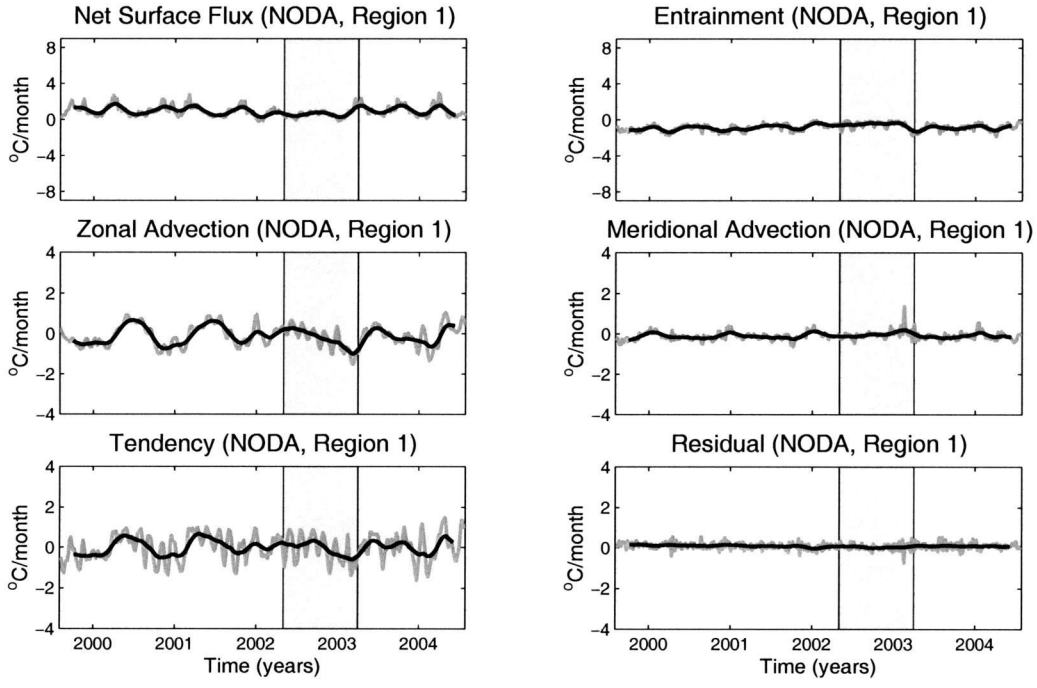

Figure 70. August 1999 to July 2004 time series of NODA temperature flux terms (net surface flux, entrainment, zonal and meridional advection, and the residual or tendency term) averaged over 165°E to 155°W and 1.5°S to 1.5°N (Region 1). The gray and black lines correspond to the 5-day record and the same record with 60-day low-pass filtering, respectively. The gray shaded area indicates the 2002-2003 El Niño event.

The 5-year mean ASSIM44-AR temperature balance in Region 1 (Figure 71 and Table 10) is still maintained to first order by the net surface flux and entrainment and both terms have increased in magnitude to 1.01 °C month^{-1} and −0.88 °C month^{-1}, respectively. The mean ASSIM44-AR total zonal advection is unchanged (−0.12 °C month^{-1}) and the mean meridional advection and residual

terms are closer to zero than their NODA counterparts (Table 10). Although the 5-year mean SST is essentially the same, the ASSIM44-AR SST is much cooler than the NODA SST at the beginning of the assimilation run and is warmer than the NODA SST during much of the 2002-2003 El Niño (Figure 69). Unlike the eastern Pacific, assimilation introduces more seasonal to interannual variability to all of the temperature flux terms in Region 1 (Figure 71), with largest increases in the 5-year standard deviations of residual term, net surface flux, and zonal advection. As a result, the variability of SST is increased in Region 1 by 0.13 °C over the 5-year period (Table 10). The high (0.88) correlation between the seasonal fluctuations of the tendency and mean zonal advection terms (black lines in Figure 71) still holds for the ASSIM44-AR run.

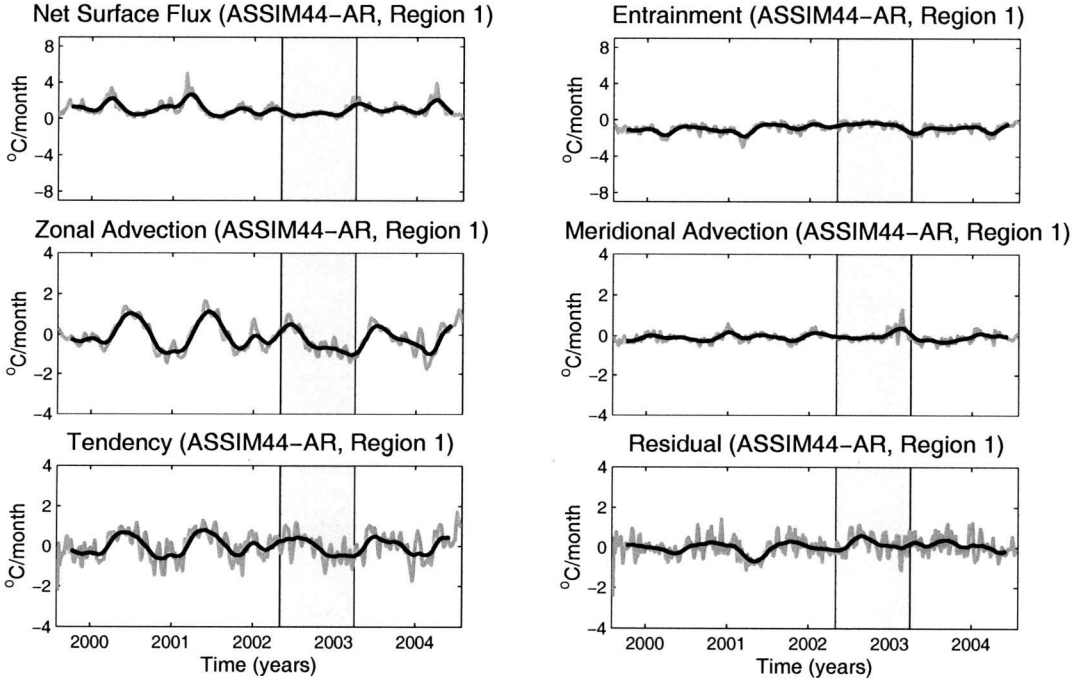

Figure 71. Similar to Figure 70, except for the ASSIM44-AR run.

Table 10. Five-year mean (standard deviations) of the SST (°C) and temperature flux terms (°C month^{-1}) in Region 1, 2, and 3 for the NODA and ASSIM44-AR run.

Term	Region 1	Region 2	Region 3
NODA			
SST	27.55 (0.81)	24.42 (0.78)	22.69 (0.49)
Net Surface Flux	0.92 (0.58)	2.85 (1.81)	4.17 (1.99)
Entrainment	−0.81 (0.40)	−2.73 (1.49)	−4.21 (2.08)
Zonal Advection	−0.12 (0.53)	0.12 (0.52)	0.43 (0.42)
Meridional Advection	−0.09 (0.20)	−0.52 (0.38)	−0.76 (1.06)
Tendency	−0.01 (0.65)	−0.02 (0.78)	−0.01 (1.29)
Residual	0.08 (0.17)	0.26 (0.34)	0.36 (0.98)
ASSIM44-AR			
SST	27.57 (0.94)	24.36 (0.73)	22.66 (0.47)
Net Surface Flux	1.01 (0.74)	2.71 (1.74)	3.93 (1.99)
Entrainment	−0.88 (0.52)	−2.46 (1.37)	−3.70 (1.98)
Zonal Advection	−0.12 (0.69)	0.21 (0.51)	0.39 (0.37)
Meridional Advection	−0.06 (0.22)	−0.47 (0.36)	−0.79 (1.00)
Tendency	0.00 (0.66)	−0.01 (0.66)	−0.01 (0.82)
Residual	0.04 (0.48)	0.00 (0.60)	0.15 (1.20)

6.4.2 Region 2. In Region 2 (Figure 72 and Table 10), the mean NODA temperature balance is maintained to first order by the net surface flux (2.85 °C month^{-1}), entrainment (−2.73 °C month^{-1}), and meridional advection (−0.52 °C month^{-1}). The mean total zonal advection is still small compared to the other terms but is now positive (warming the cold tongue) and the mean residual term is large (0.26 °C month^{-1}) acting to warm Region 2. Note that the mean net surface flux in Region 2 is nearly 3 times that of Region 1 and SST is on average 3.13°C cooler (Figure 69 and Table 10). The variability of the Region 2 temperature flux terms are larger than in Region 1, except for zonal advection and the SST variability has decreased slightly (Figures 69 and 72 and Table 10). Seasonal variations in the tendency term remain strongly correlated (0.58) to the seasonal variations in zonal advection (Figure 72). During the 2002-2003 El Niño, the decrease in amplitude of the annual cycle of the temperature flux terms (Figures 70 and 72) and SST (Figure 69) is more pronounced than for Region 1. The large HF fluctuations in meridional advection (middle right panel of Figure 72) associated with TIW events during the 1999-2001 La Niña events and in early 2004 will be discussed in more detail in Section 6.4.4.

Although the magnitude of the mean temperature flux terms decreased slightly (Table 10), the ASSIM44-AR run maintains the same balance between net surface flux (2.71 °C month^{-1}), entrainment (−2.46 °C month^{-1}), and meridional advection (−0.47 °C month^{-1}). The strength of the mean zonal advection term has increased and assimilation shifts the mean residual essentially to zero. As in Region 1, the ASSIM44-AR SST is cooler than the NODA run at the beginning of the simulation and slightly warmer during the 2002-2003 El Niño (Figure 69) and the seasonal

variations in the tendency term are still highly correlated (0.64) with the seasonal variations of zonal advection (black lines in Figure 73). Although the HF fluctuations in meridional advection (gray line in middle right panel of Figure 73) are smaller than the NODA run consistent with a decrease in TIW amplitudes, the HF variations of the residual term have increased (gray line in lower right panel of Figure 73).

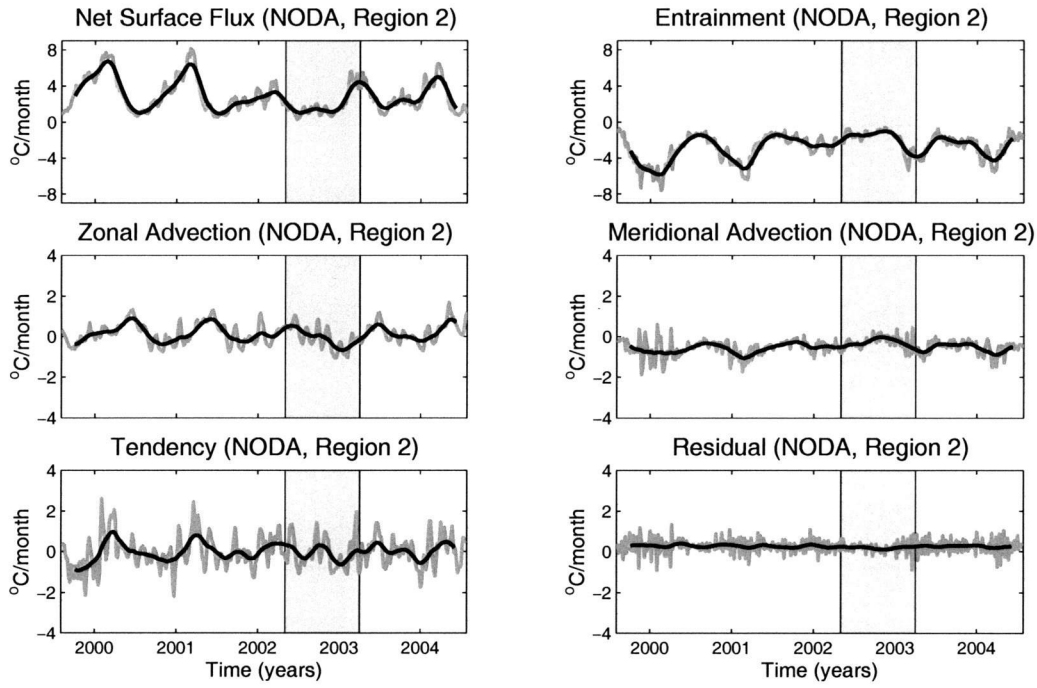

Figure 72. August 1999 to July 2004 time series of NODA temperature flux terms (net surface flux, entrainment, zonal and meridional advection, and the residual or tendency term) averaged over 155°W to 115°W and 1.5°S to 1.5°N (Region 2). The gray and black lines correspond to the 5-day record and the same record with 60-day low-pass filtering, respectively. The gray shaded area indicates the 2002-2003 El Niño event.

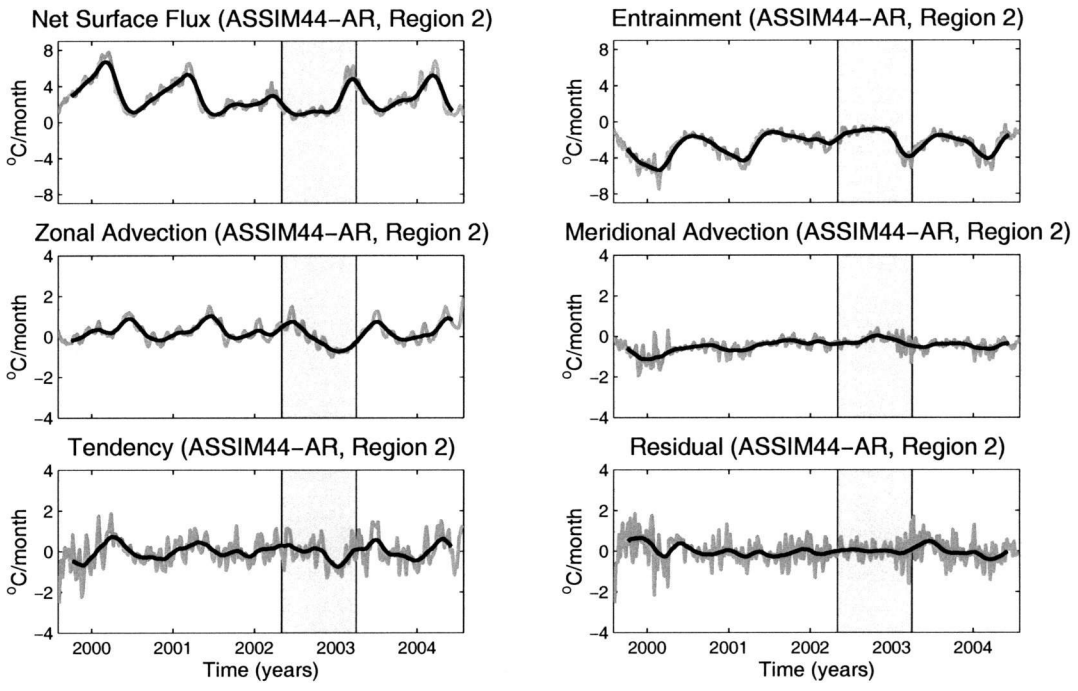

Figure 73. Similar to Figure 72, except for the ASSIM44-AR run.

6.4.3 Region 3. In the NODA run, the mean net surface flux and vertical entrainment terms, 4.17 and -4.21 °C month^{-1}, respectively, are clearly the dominant terms in the Region 3 temperature balance (Figure 74 and Table 10). Mean meridional advection is the next largest term balanced by the sum of mean zonal advection and the residual term (Table 10). Although most of the temperature flux terms have increased variability, the SST variability has decreased along with the mean SST from Region 2 to Region 3 (Table 10). The mean residual term is much larger in Region 3 consistent with the increase in the residual near the eastern boundary (Figure 67) and the HF fluctuations have large amplitudes (gray lines in lower panel of Figure 74). The tendency time series (seasonal plus HF fluctuations)

is highly correlated (0.67) with the meridional advection time series (gray lines in Figure 74).

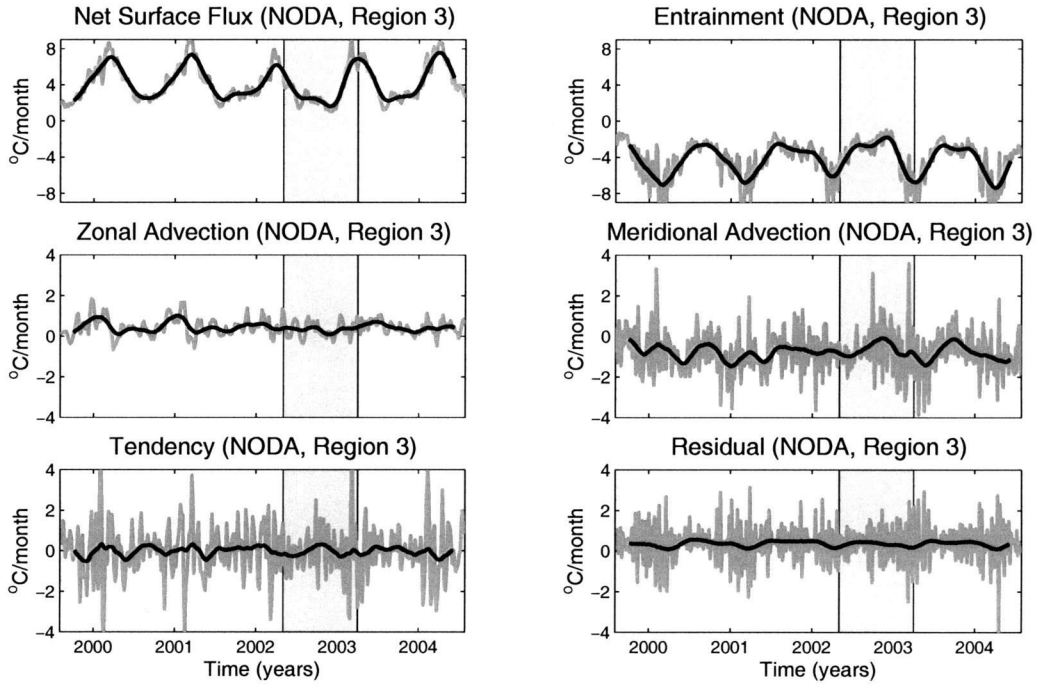

Figure 74. August 1999 to July 2004 time series of NODA temperature flux terms (net surface flux, entrainment, zonal and meridional advection, and the residual or tendency term) averaged over 115°W to 80°W and 1.5°S to 1.5°N (Region 3). The gray and black lines correspond to the 5-day record and the same record with 60-day low-pass filtering, respectively. The gray shaded area indicates the 2002-2003 El Niño event.

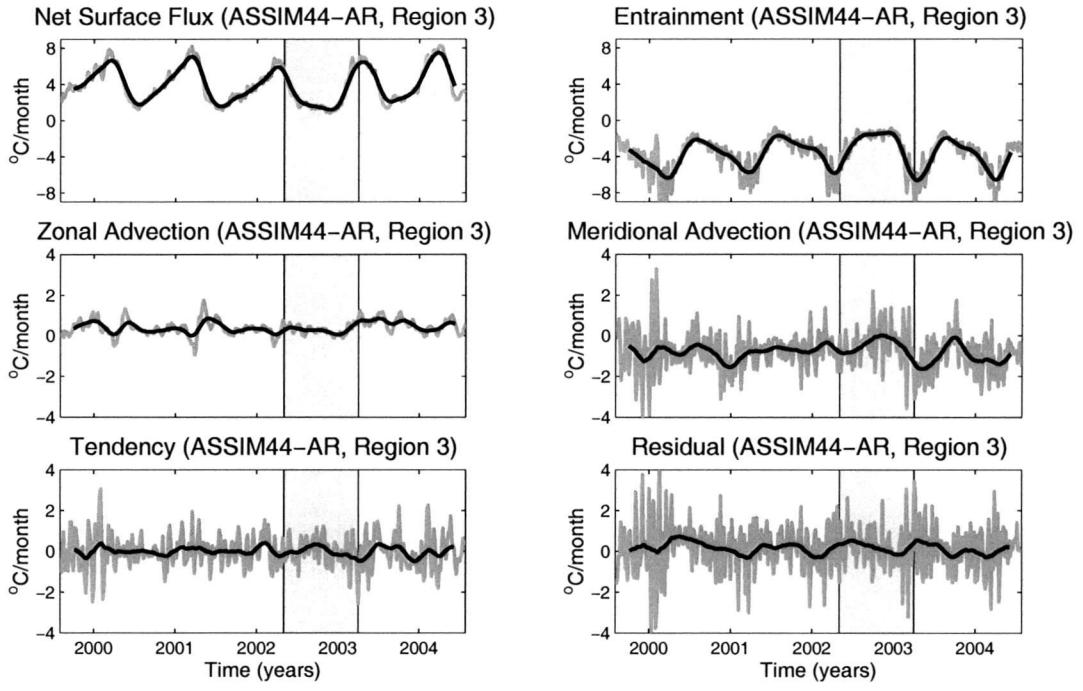

Figure 75. Similar to Figure 74, except for the ASSIM44-AR run.

The dominant terms balancing temperature are essentially the same for the ASSIM44-AR run with a significant decrease in the 5-year mean residual flux compared with the NODA run (Table 10). As is the case for the NODA run, the magnitude of the mean zonal and meridional advection are largest in the east (Region 3). The amplitude of the ASSIM44-AR HF fluctuations in the tendency, entrainment, and meridional advection terms have all decreased compared to the NODA run (gray lines in Figure 75). In contrast, the magnitude of the HF fluctuations of the residual temperature flux has increased dramatically and the residual time series is anticorrelated (-0.76) with the meridional advection (gray lines in Figure 75).

Table 11. Five-year mean (standard deviations) of the LF and HF zonal and meridional temperature advection terms (°C month^{-1}) in Region 1, 2, and 3 for the NODA and ASSIM44-AR run.

Term	Region 1	Region 2	Region 3
NODA			
Zonal Advection (LF)	-0.12 (0.42)	-0.02 (0.46)	0.12 (0.18)
Zonal Advection (HF)	0.00 (0.28)	0.15 (0.34)	0.32 (0.35)
Meridional Advection (LF)	-0.12 (0.10)	-0.69 (0.32)	-1.05 (0.41)
Meridional Advection (HF)	0.04 (0.15)	0.12 (0.32)	0.18 (0.97)
Total Mean (HF:LF)	−0.17	−0.38	−0.54
ASSIM44-AR			
Zonal Advection (LF)	-0.11 (0.58)	0.16 (0.43)	0.24 (0.20)
Zonal Advection (HF)	-0.02 (0.29)	0.06 (0.25)	0.17 (0.28)
Meridional Advection (LF)	-0.07 (0.13)	-0.56 (0.29)	-0.92 (0.40)
Meridional Advection (HF)	0.02 (0.15)	0.07 (0.25)	0.08 (0.88)
Total Mean (HF:LF)	0.00	−0.33	−0.37

6.4.4 HF versus LF. The horizontal advection time-series decomposed into LF and HF signals (as described in Section 6.3.2) are compared here for the NODA (Figure 76) and ASSIM44-AR (Figure 77) runs in Regions 1 to 3. This decomposition allows the examination of the contributions of TIWs and seasonal to interannual variations to the total zonal and meridional advection terms displayed in Figures 70 to 75.

In the NODA run, the HF zonal advection in Regions 2 and 3 acts to warm the cold tongue on average (gray lines in Figure 76 and Table 11). The mean LF zonal advection is very small and negative (cooling) in Regions 1 and 2 and positive (warming) in Region 3 as we are excluding the large westward LF zonal advection of heat outside of 1.5°S and 1.5°N boundaries (Figure 67), and the surfacing of the EUC changes the sign of the LF zonal advection along the equator in the spring and summer months (black lines in Figure 76). Regions 2 and 3 have large LF meridional advection away from the equator (black lines in Figure 76) and large positive HF meridional advection along the equator (Figure 68) which is weakened by the spatial averaging process (Table 11). The ratio of mean HF zonal plus meridional advection towards the cold tongue to mean LF zonal plus meridional advection away from the cold tongue (e.g., the cumulative role of TIWs relative to seasonal and interannual advection of heat) is largest in Region 3 (0.54). With the exception of the LF zonal advection, the 5-year standard deviation increases eastward from Region 1 to Region 3 (Table 11). As expected, the HF meridional fluctuations are largest during the cool (La Niña) periods (gray lines in Figure 76).

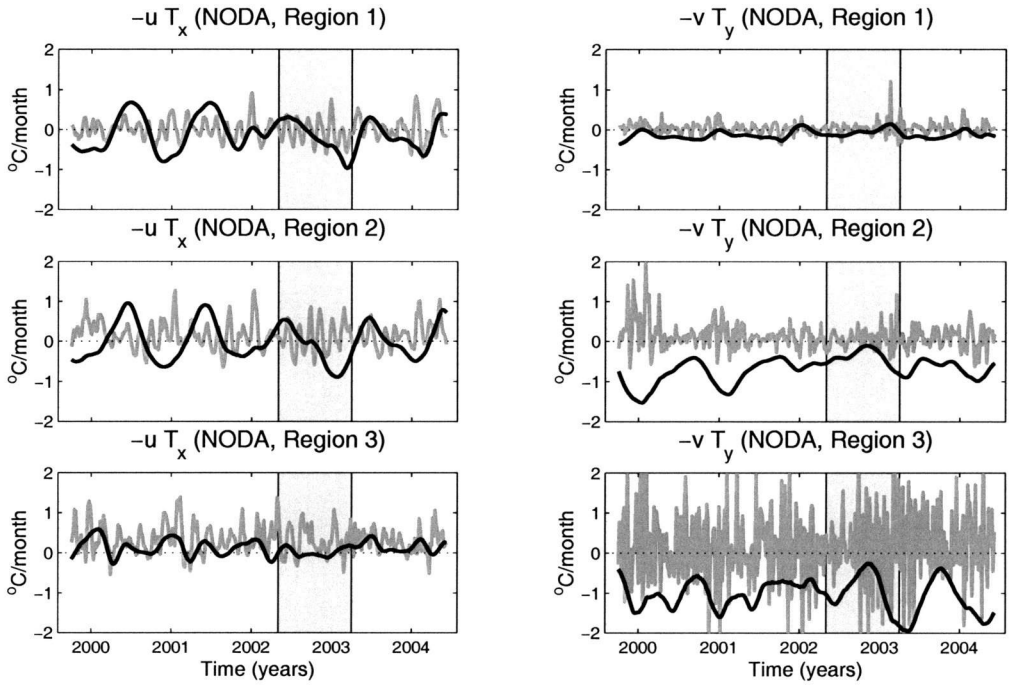

Figure 76. August 1999 to July 2004 time series of the NODA LF zonal and meridional advection terms (black line) with the HF terms overlaid as gray lines for Regions 1, 2, and 3. The gray shaded area indicates the 2002-2003 El Niño event.

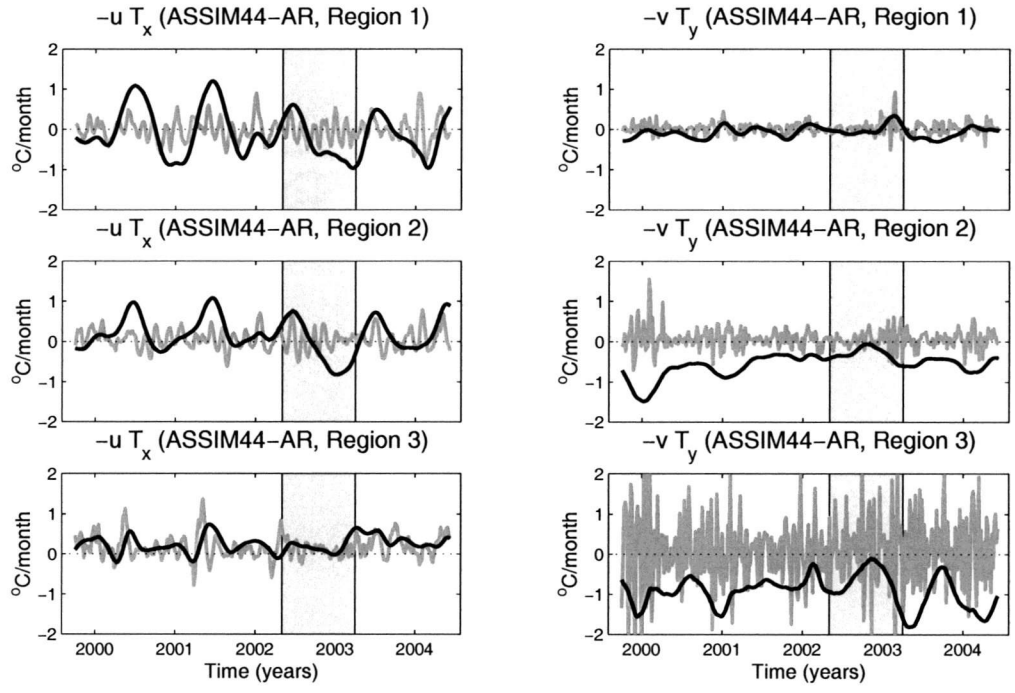

Figure 77. Similar to Figure 76, except for the ASSIM44-AR run.

Assimilation increased the mean LF zonal advection by strengthening the EUC in Regions 2 and 3 which compensates for the decrease in the mean LF meridional advection (black lines in Figure 77 and Table 11). The decreased mean and variability of HF zonal and meridional advection in all three regions corresponds to weaker TIWs in the ASSIM44-AR run (gray lines in Figure 77 and Table 11). The large decrease between the ASSIM44-AR and NODA ratio of mean HF horizontal advection to LF horizontal advection in Region 3 relative to Region 2 (Table 11) is consistent with the damping of the TIW amplitudes east of 110°W in the ASSIM44-AR run to better align the TIWs with those observed by altimetry (Perez and Miller 2005). Note that one of the main differences between the ASSIM44-AR and NODA temperature budgets in Regions 1 to 3 is the strong HF damping of SST

by the residual term (Figures 71, 73, and 75). Whether this damping improved the HF correlations with the temperature fluxes estimated from observations will be discussed in Section 6.5.

Based on the comparisons in this section, the NODA and ASSIM44-AR net surface flux is largely balanced by the entrainment and the tendency (HF + LF) has the highest correlation with the horizontal advection terms in Regions 1 to 3. In the transition from Region 1 to Region 3, the term highly correlated with the tendency shifts from the LF and HF zonal advection terms to the HF meridional and HF zonal advection terms, with the LF meridional advection term having little impact on the evolution of SST tendency. This does not imply that the other flux terms do not play a role in the heat balance (e.g., in Region 3 entrainment is strongly correlated with meridional advection), but it does say that the largest correlations between individual terms in the heat balance and tendency occur for the horizontal advection terms. Based on these findings, the comparisons of the NODA and ASSIM44-AR with TAO/Reynolds temperature fluxes in Section 6.5 focus on the tendency and horizontal advection terms to investigate whether these terms dominate at the 3 TAO moorings along the equator.

6.5 Comparisons with Observations

6.5.1 Spatially-Averaged Comparisons with Reynolds SST. From comparisons of the spatially-averaged time series of NODA, ASSIM44-AR, and Reynolds SST in Regions 1 to 3 (left panels in Figure 78), the eastward progression from high (greater than 0.7) to low (less than 0.2) model-data correlation and the eastward increase of the 5-year mean bias (Table 12) are apparent. While

the variability in the Reynolds SST increases from Region 1 to 3 (Figure 78 and Table 12), the opposite is true in the NODA and ASSIM44-AR runs. In all 3 regions, the agreement between the model and observed SST is better prior to the disruption of the annual cycle by the 2002-2003 El Niño event (left panels in Figure 78).

The eastward decrease in correlation between NODA and ASSIM44-AR with Reynolds also holds for the tendency term (right panels in Figure 78), although the correlations are higher in Region 3 (ca. 0.4) than was the case for SST. The magnitude of the eastward increase in the variability of the NODA and Reynolds tendency is similar (Table 12). However, the seasonal variability of the NODA and ASSIM44-AR tendency in Region 3 is nearly three times smaller than the observed seasonal variability and is compensated by larger HF variability (not shown). Assimilation, decreases the variability of the model tendency by 0.12 and 0.37°C month^{-1} in Regions 2 and 3, respectively, which provides a better match to the observed HF variability.

The NODA and ASSIM44-AR zonal gradients have high (greater than 0.7) correlation with the Reynolds zonal gradient in Regions 1 and 2 (left panels in Figure 79). The 5-year mean zonal gradient in the NODA and ASSIM44-AR runs also compare well with the Reynolds mean gradient in Regions 1 and 2 (Table 12). Although there is still significant correlation (0.5) in Region 3, the NODA and ASSIM44-AR runs clearly have difficulty reproducing the disruption of the annual cycle that appears in the Reynolds zonal gradients after the 2002-2003 El Niño. As a result, the 5-year mean NODA and ASSIM44-AR zonal gradient in Region 3 has a different sign than the mean Reynolds zonal gradient (Table 12).

In Regions 1 and 3, the meridional gradient correlation is generally high (greater than 0.6) between Reynolds and the NODA and the ASSIM44-AR run (right panels in Figure 79). However, the best agreement between the NODA, ASSIM44-AR, and Reynolds 5-year mean and standard deviation of the meridional gradient occurs in Region 3 (Table 12) where there is a large mean meridional gradient of ca. 5°C/1000 km.

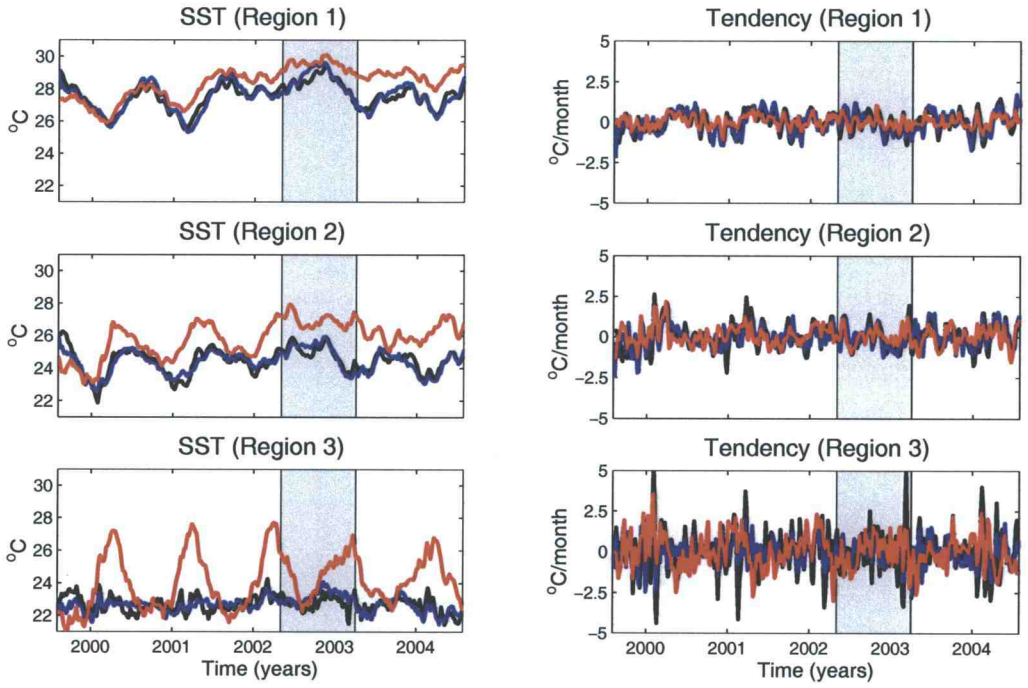

Figure 78. August 1999 to July 2004 time series of the NODA (black line) and ASSIM44-AR (blue line) SST (left panels) and tendency (right panels) in Regions 1, 2, and 3 with Reynolds SST (red line) and tendency overlaid. The gray shaded area indicates the 2002-2003 El Niño event.

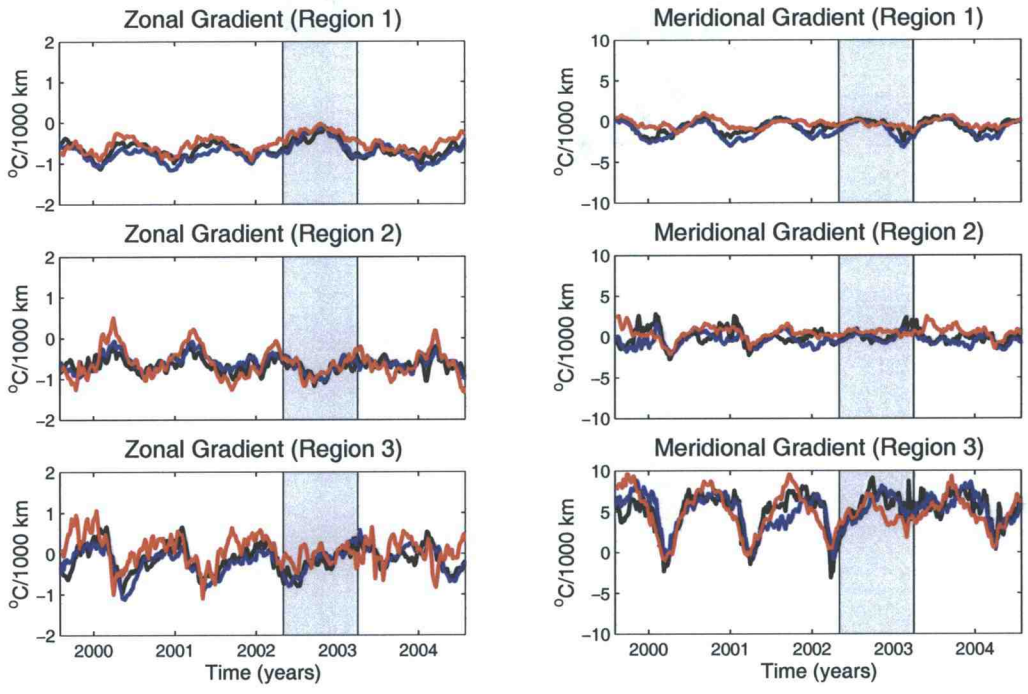

Figure 79. Similar to Figure 78, except for zonal (left panels) and meridional (right panels) temperature gradients.

Table 12. Comparison of five-year mean (standard deviations) of the model and Reynolds SST (°C), tendency (°C month^{-1}), and horizontal gradients (°C/1000 km) in Region 1, 2, and 3.

Term	Region 1	Region 2	Region 3
NODA			
SST	27.55 (0.81)	24.42 (0.78)	22.69 (0.49)
Tendency	−0.01 (0.65)	−0.02 (0.78)	−0.01 (1.29)
Zonal Gradient	−0.66 (0.19)	−0.66 (0.18)	−0.14 (0.33)
Meridional Gradient	−0.70 (0.75)	−0.04 (0.89)	5.09 (2.34)
ASSIM44-AR			
SST	27.57 (0.94)	24.36 (0.73)	22.66 (0.47)
Tendency	0.00 (0.66)	−0.01 (0.66)	−0.01 (0.82)
Zonal Gradient	−0.73 (0.22)	−0.62 (0.20)	−0.18 (0.32)
Meridional Gradient	−1.09 (0.96)	−0.43 (0.71)	5.02 (2.10)
REYNOLDS			
SST	28.37 (1.00)	25.81 (1.10)	24.09 (1.65)
Tendency	0.03 (0.49)	0.03 (0.80)	0.00 (1.38)
Zonal Gradient	−0.53 (0.20)	−0.61 (0.35)	0.07 (0.37)
Meridional Gradient	−0.38 (0.50)	0.46 (0.76)	4.86 (2.41)

6.5.2 Temperature Flux Comparisons along the Equator.

6.5.2.1 SST, MLD, and Horizontal Velocity: The Reynolds tendency and zonal and meridional gradients are now combined with current measurements at the 170°, 140°, and 110°W TAO moorings to estimate the tendency, zonal and meridional advection along the equator. In this series of plots the observed uncertainty (Section 6.3.2.2) and ASSIM44-AR prior error bars (Miller 1990; Miller et al. 1995) are plotted as thin red and blue lines, respectively, surrounding the observations and assimilated results. Note that the error bars from the assimilation scheme represent the errors in the deviations from the model seasonal cycle and therefore do not account for model biases.

The Reynolds and model SST comparisons at the 3 moorings are similar to the spatially-averaged Reynolds SST described for Regions 1 to 3 (Section 6.5.1), with 5-year mean bias, low variability, and a divergence of the simulated and observed SST after the 2002-2003 El Niño event (left panels of Figure 80 and Table 13). Although the NODA and ASSIM44-AR run often overlap within the error bars, the differences between the model and data SST exceed the uncertainty in the observations and the ASSIM44-AR run for most of the 5-year record.

The right panel of Figure 80, compares the model h (surface mixed layer thickness) to the MLD time series computed for at the 3 TAO moorings. The 5-year mean TAO MLDs (Table 13) computed here agree well with the mean MLDs computed by McPhaden (2002), 71 (170°W), 45 (140°W), and 21 m (110°W). The model and observed MLD differences are smallest (MLDs overlap within the errorbars) at 110°W and are largest at 170°W related to the increasing importance of salinity in the western Pacific (right panels of Figure 80 and Table 13). The

variability at 140° and 110°W (Table 13) is similar to that of TAO, but is too weak at 170°W. The MLD increases significantly at 140° and 110°W during the 2002-2003 El Niño event, consistent with the MLD increase observed by WM (2001) during the 1997-1998 El Niño.

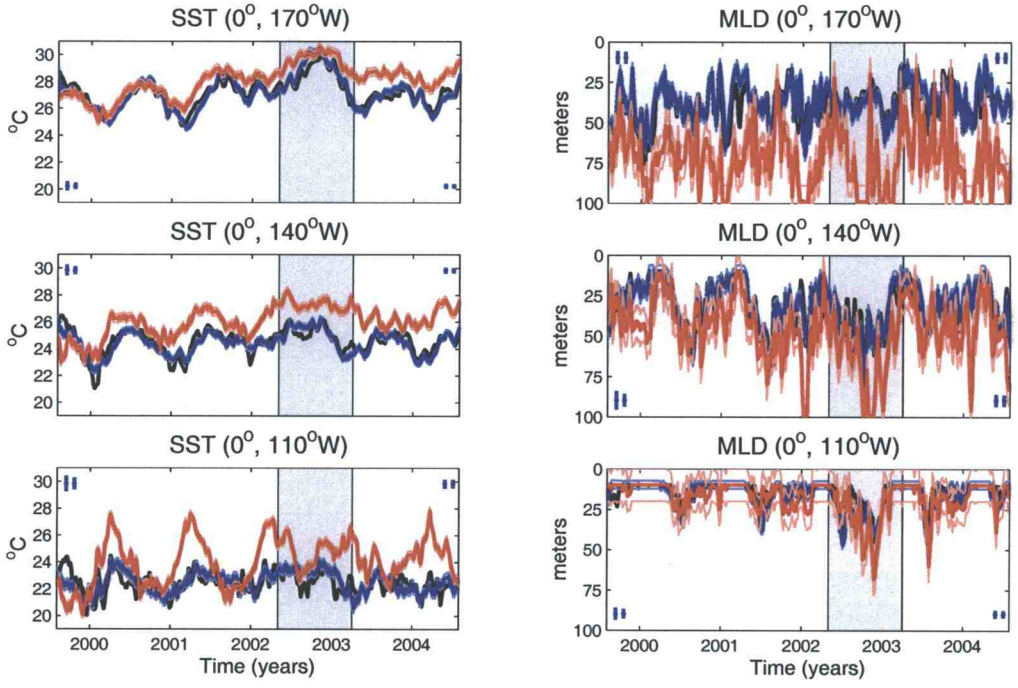

Figure 80. August 1999 to July 2004 time series of the NODA (black line) and ASSIM44-AR (blue line) SST (left panels) and surface mixed layer depth (right panels) at 3 TAO moorings along the equator with TAO/Reynolds SST and mixed layer depths (red lines) overlaid. The light red lines indicate the assumed observation error. The light blue lines indicate the prior error bars for the ASSIM44-AR run. The pair of error bars in each panel indicate the prior and posterior errors for August 3, 1999 (right hand corner) and July 28, 2004 (left hand corner). Note that data was not assimilated at 0°, 110°W.

Table 13. Comparison of five-year mean (standard deviations) of the model and TAO/Reynolds SST (°C), MLD (m), and velocity ($cm\ s^{-1}$) at the 3 TAO moorings.

Term	170°W	140°W	110°W
NODA			
SST	27.15 (1.07)	24.51 (0.94)	22.43 (0.78)
MLD	37.98 (11.09)	31.22 (14.61)	14.69 (7.53)
u	4.19 (33.85)	9.94 (42.13)	−4.07 (46.47)
v	1.65 (7.94)	1.95 (9.48)	5.53 (11.50)
ASSIM44-AR			
SST	27.11 (1.27)	24.40 (0.86)	22.45 (0.77)
MLD	37.14 (10.90)	31.23 (14.91)	15.89 (8.58)
u	7.28 (39.94)	22.37 (40.81)	12.60 (44.26)
v	1.93 (6.02)	2.03 (7.46)	5.46 (9.42)
REYNOLDS/TAO			
SST	28.05 (1.21)	26.04 (1.13)	24.00 (1.72)
MLD	72.49 (18.00)	46.28 (19.16)	17.79 (10.25)
u	−5.30 (29.19)	3.20 (41.96)	−2.71 (56.76)
v	−0.72 (12.07)	−2.20 (22.20)	−0.36 (29.50)

The time series of TAO mixed layer zonal velocity agrees well with the NODA and ASSIM44-AR zonal velocity time series (left panels of Figure 81) with smallest correlation at 110°W for the NODA and ASSIM44-AR runs (0.55 and 0.58, respectively). As noted in Section 6.4, assimilation strengthens the EUC which increases the 5-year mean zonal velocity at the three TAO moorings (Table 13) and as a consequence increases the mean LF zonal advection along the equator (Table 11).

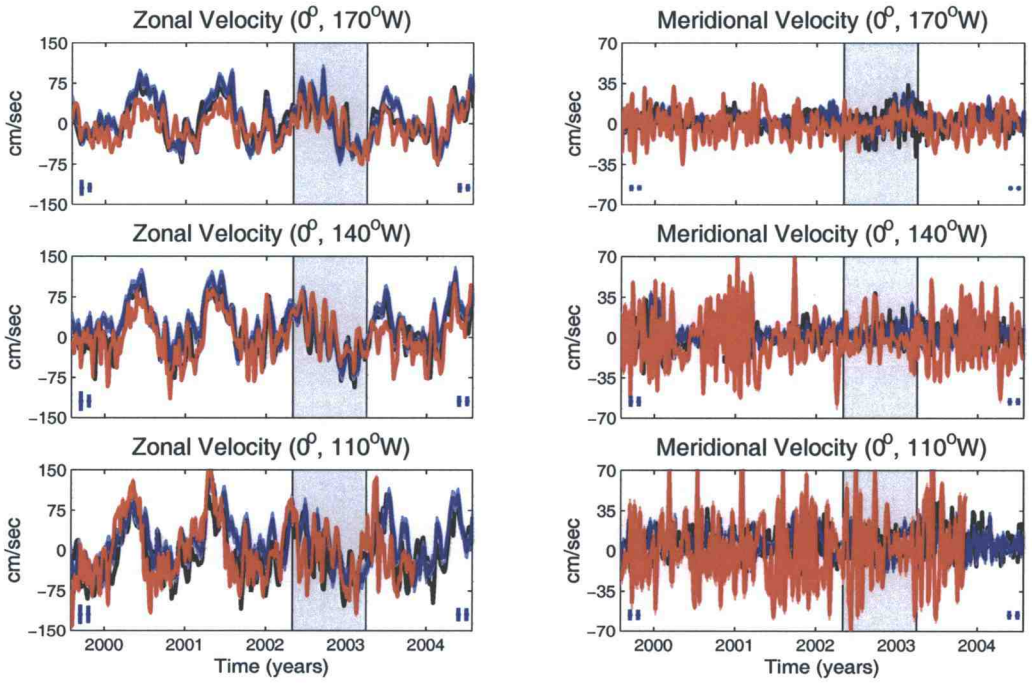

Figure 81. Similar to Figure 80, except for surface mixed layer zonal velocity and meridional velocity.

The magnitude of the 5-year mean TAO, NODA, and ASSIM44-AR meridional velocity are less than 6 $cm\ s^{-1}$ at the three TAO moorings (Table 13). While the LF TAO zonal velocity has a fairly robust annual signal along the equator, the LF meridional velocity has a weak annual cycle relative to the HF fluctuations associated

with TIWs (right panels in Figure 81 and Table 13; WM 1999) and the seasonal cycle is therefore susceptible to the biases introduced from the linear extrapolation process. The uncertainty in both the model and observed LF meridional velocity poses a problem as it is sufficient to change the sign of the LF meridional advection at the 3 TAO moorings. Apart from errors in the LF evolution, the NODA and ASSIM44-AR HF meridional velocity fluctuations are significantly weaker than observed at 140° and 110°W where TIWs are active (right panels Figure 81 and Table 13).

6.5.2.2 Zonal and Meridional Advection: The total TAO/Reynolds zonal and meridional advection time series are compared with the NODA and ASSIM44-AR zonal and meridional advection at the 3 TAO sites (Figure 82). While there is significant correlation between the model and observed zonal advection at 170° and 140°W (greater than 0.5 and 0.25, respectively), the 5-year mean NODA and ASSIM44-AR zonal advection are positively biased at 170°W by approximately 0.26°C month^{-1} (Table 14). Although the model generates realistic spatially-averaged meridional temperature gradients in Regions 1 to 3 (Figure 79), the sensitivity of the meridional gradients to the differencing technique employed along the equator (WM 1999; 2000; 2001) and the biases in the TAO meridional velocity described above make it difficult to validate the NODA and ASSIM44-AR meridional advection (right panels in Figure 82).

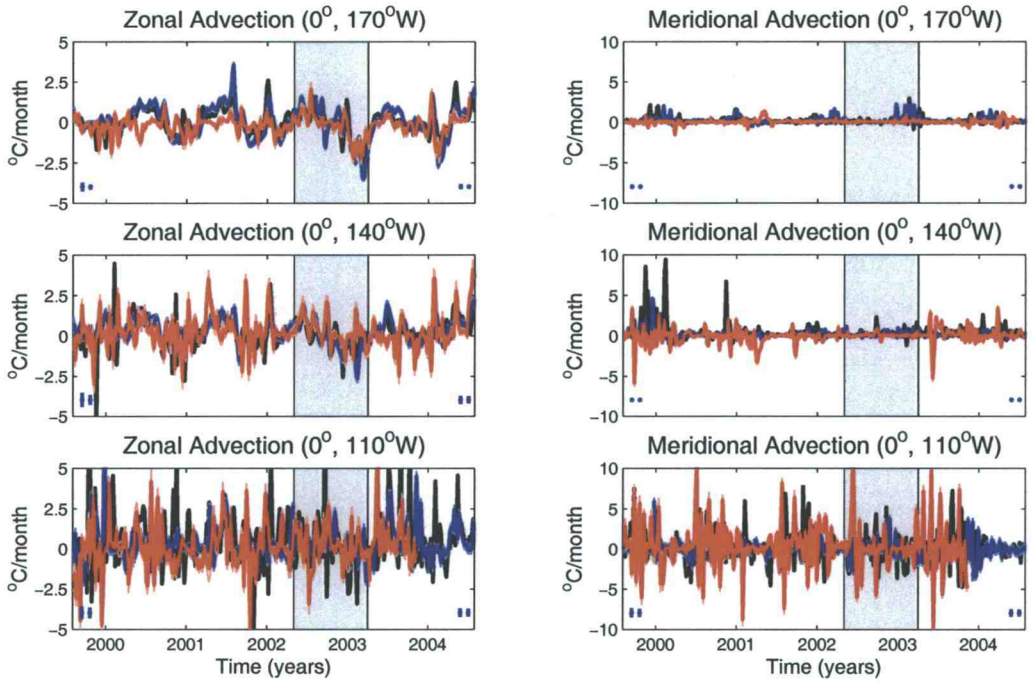

Figure 82. Similar to Figure 80, except for zonal and meridional temperature advection.

Table 14. Comparison of five-year mean (standard deviations) of the model and TAO/Reynolds heat flux terms (°C month^{-1}) at the 3 TAO moorings.

Term	170°W	140°W	110°W
NODA			
Net Surface Flux	1.26 (0.82)	2.93 (2.08)	6.39 (2.54)
Entrainment	-1.66 (0.85)	-3.69 (2.33)	-6.84 (3.46)
Zonal Advection	0.04 (0.75)	0.16 (0.87)	0.45 (1.71)
Meridional Advection	0.16 (0.38)	0.36 (1.06)	0.15 (1.78)
Tendency	0.00 (0.98)	-0.02 (1.20)	-0.01 (1.97)
Residual	0.20 (0.49)	0.22 (1.10)	-0.17 (2.06)
Net + Ent + Res	-0.20 (0.72)	-0.54 (1.28)	-0.61 (2.46)
ASSIM44-AR			
Net Surface Flux	1.37 (1.00)	2.98 (2.14)	6.00 (2.70)
Entrainment	-1.70 (0.96)	-3.28 (1.90)	-5.66 (3.07)
Zonal Advection	0.03 (1.00)	0.24 (0.70)	0.28 (1.01)
Meridional Advection	0.18 (0.41)	0.18 (0.48)	-0.01 (1.02)
Tendency	0.01 (0.94)	-0.01 (0.89)	-0.02 (1.13)
Residual	0.14 (0.79)	-0.14 (0.91)	-0.64 (2.31)
Net + Ent + Res	-0.19 (0.81)	-0.43 (0.99)	-0.28 (1.71)

Table 14. (continued)

Term	170°W	140°W	110°W
REYNOLDS/TAO			
Zonal Advection	-0.23 (0.60)	0.24 (1.02)	0.09 (1.39)
Meridional Advection	0.02 (0.27)	-0.04 (0.88)	0.30 (2.71)
Tendency	0.04 (0.73)	0.04 (1.21)	0.01 (2.02)
Net + Ent/Diff	0.25 (0.75)	-0.16 (1.45)	-0.37 (3.24)

In Figures 83 and 84, the LF and HF zonal and meridional advection contributions are compared at the 3 TAO sites. The skill of the NODA and ASSIM44-AR LF zonal advection is demonstrated by the greater than 0.6 correlation with TAO/Reynolds LF zonal advection along 170° and 140°W (left panel of Figure 83). The amplitude of the zonal advection seasonal fluctuations, however, are typically larger than observed and the LF zonal advection warms the equator on average whereas the TAO/Reynolds LF zonal advection cools the cold tongue. The impact of bias and phasing errors in meridional velocity is apparent at 110°W (lower right panel of Figure 83) where the LF TAO/Reynolds meridional advection has a different sign than the LF NODA and ASSIM44-AR meridional advection and acts to warm the cold tongue. Note that the uncertainty in these measurements is large enough that the ASSIM44-AR and observed LF meridional advection may not be significantly different.

The NODA HF zonal and meridional advection terms reproduce the interannual modulation of the TIWs, but phasing errors in the TIWs produce low model-data

correlations (Figure 84). Assimilation reduces the variability in the HF horizontal advection terms consistent with a decrease in the TIW amplitudes in the east. Although assimilation improved the TIW phasing and increased the correlation with observed sea surface height anomalies west of 125°W in the Perez and Miller (2005) assimilation experiments, the correlation between ASSIM44-AR and TAO/Reynolds HF meridional advection (e.g., meridional temperature advection by TIWs) is not similarly improved at 140° and 110°W. This indicates that the relationship of model SST to the other fields in the reduced state space may be more complex than is represented by the Perez and Miller (2005) RKF.

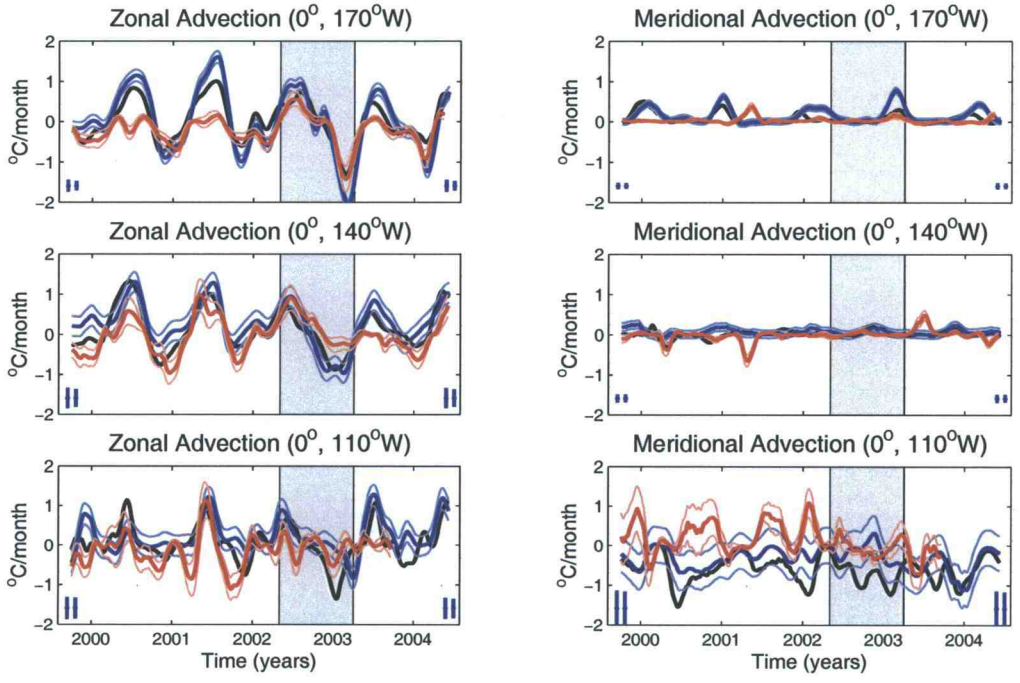

Figure 83. Similar to Figure 82, except for the LF zonal and meridional temperature advection. The pair of error bars in each panel indicate the prior and posterior errors for October 3, 1999 (right hand corner) and June 8, 2004 (left hand corner).

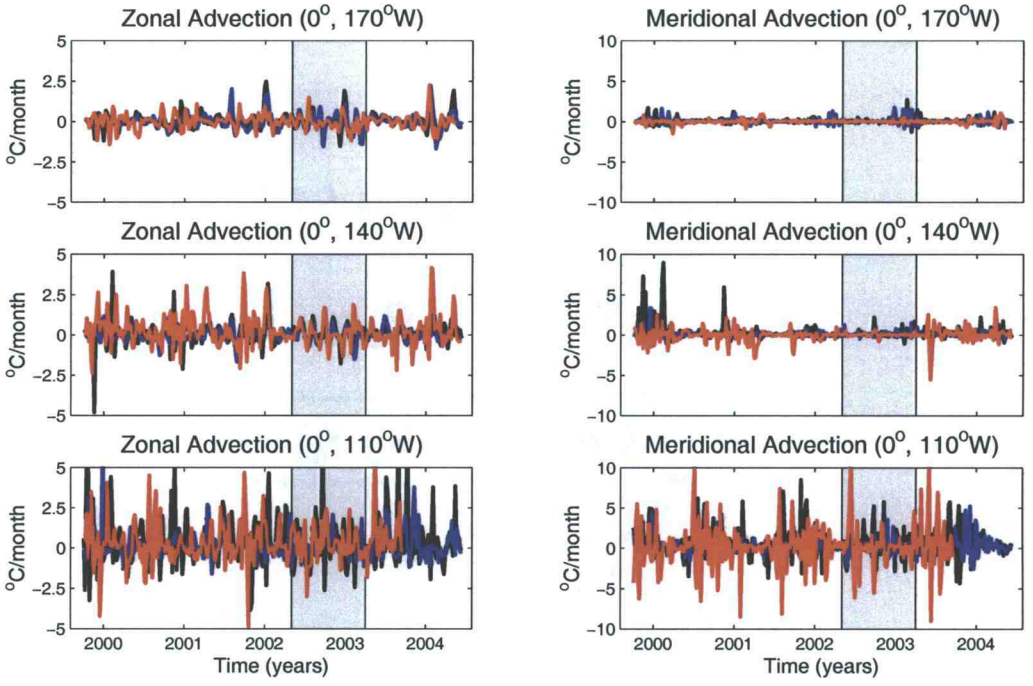

Figure 84. Similar to Figure 82, except for the HF zonal and meridional advection and without the error bars.

6.5.2.3 Tendency and Horizontal Material Derivative: The model and TAO/Reynolds tendency and horizontal material derivative (or the combination of net surface flux, entrainment, and the diffusion/residual) agree fairly well along the equator (Figure 85). The correlations between the observed and simulated tendency range between 0.22 and 0.53 with largest values at 170°W. The model-data correlations for the horizontal material derivative are smaller. This is because the balance between tendency and zonal and meridional advection is different in the TAO/Reynolds observations than for the NODA and ASSIM44-AR runs. There is significant correlation at 170° and 140°W between the TAO/Reynolds tendency and zonal advection, 0.42 and 0.27, respectively, and very little correlation at 110°W with either the zonal or meridional advection term. In contrast, both the

NODA and ASSIM44-AR tendency have high correlation with zonal advection (greater than 0.6) at 170°W. The ASSIM44-AR correlation at 140° and 110°W between the tendency and zonal and meridional advection is small and in better agreement with the observations. The model tendency in the east (140° and 110°W) is not highly correlated with the cumulative temperature flux by vertical entrainment and diffusion. This differs from the findings of WM (2000) where the interannual tendency variations were strongly correlated with the interannual variations of vertical entrainment and diffusion (computed as a residual) in the east. Vertical entrainment computed directly from TAO measurements in a later study by McPhaden (2002) explained a significant percentage of the intraseasonal tendency variance at 140° and 110°W.

Despite the lower correlations with zonal and meridional advection, the LF TAO/Reynolds tendency evolution agrees well with the LF model tendency evolution and the seasonal to interannual variability of the observed tendency is well reproduced by the model at 170° and 140°W (Figure 86). At 110°W, however, the amplitude of the tendency seasonal cycle is much stronger for TAO/Reynolds than it is in the model. In other words, the observed seasonal warming along the equator is more intense than is permitted by the model physics in the eastern Pacific.

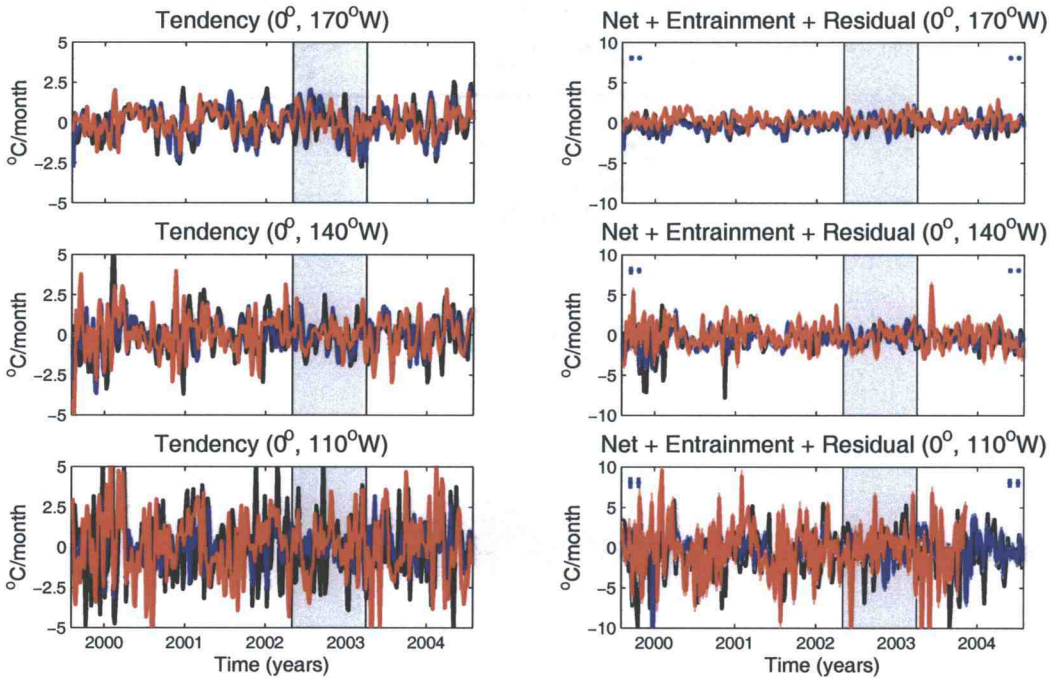

Figure 85. Similar to Figure 80, except for the tendency and horizontal material derivative (or the sum of the net surface flux, entrainment, and the residual terms).

The differences between the model and observed LF horizontal material derivative are enhanced because of differences in the LF meridional advection in the east (Figure 86). Combining the horizontal advection terms with the tendency term does not decrease the large annual variations at 110°W that are missing in the NODA and ASSIM44-AR runs. This suggests that the missing variability in the model temperature flux is in the net surface flux, entrainment, or diffusion.

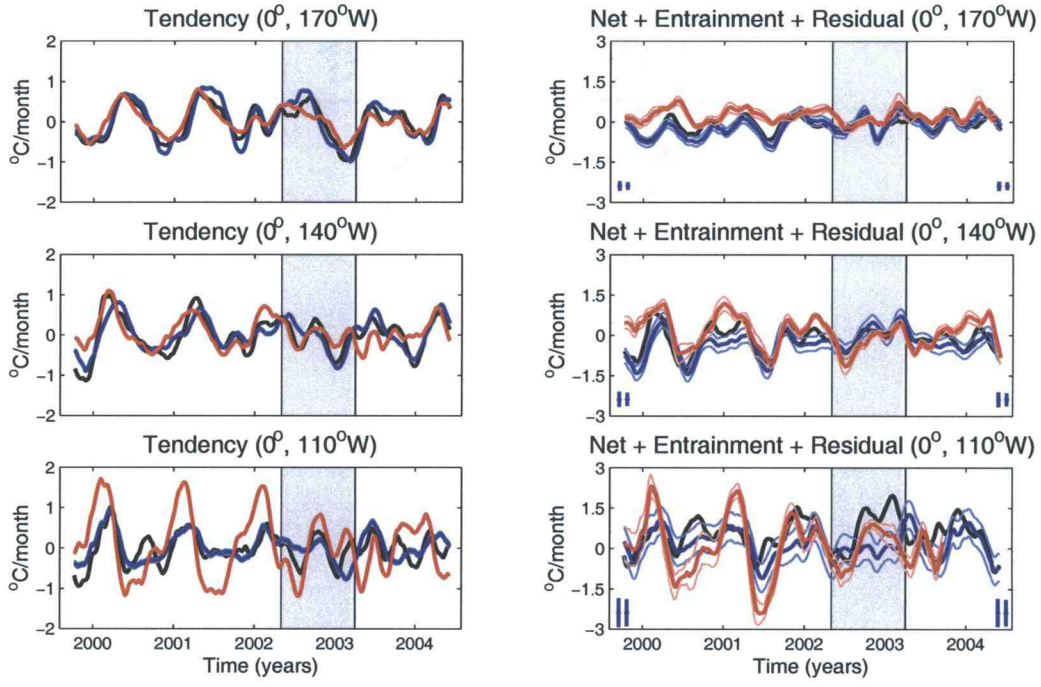

Figure 86. Similar to Figure 85, except for the 60-day low-pass filtered tendency and the LF horizontal material derivative. The pair of error bars in each panel indicate the prior and posterior errors for October 3, 1999 (right hand corner) and June 8, 2004 (left hand corner).

On average, the net cooling from entrainment and diffusion (e.g., the horizontal material derivative) exceeds the net warming from the atmospheric by 0.20 (170°W), 0.54 (140°W), and 0.61°C month^{-1} (110°W) in the NODA run (Table 14). Assimilation decreases the 5-year mean net cooling by entrainment and diffusion such that the 5-year mean horizontal material derivative is −0.19 (170°W), −0.43 (140°W), and −0.28°C month^{-1} (110°W). The 5-year mean TAO/Reynolds horizontal material derivative acts to warm the equator at 170°W by 0.25°C month^{-1} and the net cooling at 140°W and 110°W is 0.16 and 0.37°C month^{-1}, respectively. The same quantities estimated from mean WM (1999) temperature fluxes find that net cooling by entrainment and diffusion exceeds the net surface flux at 140° and

110°W by 0.89 and 1.53°C month^{-1}, respectively. The net cooling in WM (1999) by entrainment/diffusion, however, is computed as a residual and balances the mean meridional advection which is much larger than estimated during the time period investigated in this study.

6.6 Summary and Conclusions

This paper sets out to determine whether the assimilation of TAO dynamic height anomalies in the equatorial waveguide could improve the temperature budget of a nonlinear GCM in the equatorial Pacific cold tongue. The assimilated (ASSIM44-AR) and unassimilated (NODA) seasonal to interannual temperature fluxes and eddy fluxes associated with TIWs were compared in three regions covering the zonal extent of the cold tongue and extending from 1.5°S to 1.5°N. It was determined that the fundamental temperature balance in both the NODA and ASSIM44-AR runs is maintained between the mean net surface flux and vertical entrainment. The secondary balance between mean zonal and meridional advection and the mean residual also remains essentially the same for both runs. When the horizontal advection is decomposed into LF and HF components, it is evident that the significant reduction in warming by the TIW eddy fluxes in the ASSIM44-AR run is compensated by a decrease in the net cooling by the seasonal to interannual zonal and meridional advection. The decrease in the ASSIM44-AR HF meridional advection in Region 3 is negatively correlated with the increase of HF fluctuations in the residual term (i.e., the assimilated TIWs are damped by the diffusion term). Although the ASSIM44-AR SST was cooler during the 1999-2001 La Niña conditions and warmer during the 2002-2003 El Niño in Regions 1 to 3, assimilation did not

modify the average SST significantly. Assimilation introduced more variability to the SST and temperature fluxes in the westernmost region (Region 1), however, the SST variability in the east decreased which lowered the model agreement with Reynolds SST observations. For both model runs, the terms in the temperature balance highly correlated with the SST tendency transitioned from HF and LF zonal advection in Region 1 to HF meridional and HF zonal advection in Region 3.

The second focus of this paper was to determine why the NODA and ASSIM44-AR SST seasonal cycle in the eastern Pacific are so different (e.g., too cold and characterized by low variability) from the observed SST seasonal cycle along the equator. The ASSIM44-AR run was selected for this heat flux study specifically because the corrections to the SST were small and the prior and posterior error bars that are byproducts of the assimilation scheme can be used to quantitatively determine whether the model-data differences are significant. In comparisons with the observed SST and tendency in Section 6.5, it was determined that the amplitudes of the NODA and ASSIM44-AR seasonal cycle are too weak in Region 3 and at the 110°W TAO mooring. There is less warming of the cold tongue during the winter/spring in the model than observed and therefore the temperatures in the spring/summer are too cold. The model and observed SST agree within the error bars during the fall and winter months. Combining the tendency and horizontal advection terms (material horizontal derivative) did not remove the large seasonal cycle differences in the east. Therefore, the inaccuracies in the model SST seasonal cycle must derive from problems in the seasonal cycle of net surface flux, entrainment, or the residual (diffusion) term. Note that at 170°, 140°, and 110°W,

the NODA and ASSIM44-AR horizontal material derivative was significantly correlated with vertical entrainment.

Based on the results in Section 6.5 and comparisons to WM (1999; 2000; 2001) and McPhaden (2002), the largest uncertainties in the LF and HF horizontal advection of temperature are in the LF meridional advection term. This presents a challenge for heat flux studies which estimate the vertical entrainment and diffusion as a residual of the net surface flux and the horizontal material derivative. Although the dominant balance between net surface flux and vertical entrainment in this study is consistent with the WM (1999) findings, the mean net surface flux (Table 14) forcing the model is much larger than WM (1999) values estimated using the tuned Da Silva et al. (1994) surface marine atlas 0.32 ± 0.15 (170°W), 0.75 ± 0.28 (140°W), and 1.91°C month^{-1} (110°W). A notable difference in the GCAML model heat budget and that of WM (1999) is that their parameterization of penetrative radiation allows for more heat to penetrate the mixed layer. In a model sensitivity study by Murtugudde et al. (2002), it was found that the constant attenuation depth used in the GCAML (17 m) is realistic during La Niña events and less appropriate during warm El Niño events (a possible explanation for the deviation of our simulation during the 2002-2003 El Niño). The incorporation of attentuation depths which vary in space and time by Murtugudde et al. (2002) allowed more heat to penetrate the layers below the mixed layer and decreased the upwelling and entrainment, thereby increasing the SST in the cold tongue. Given the uncertainty in the net surface flux, future data assimilation studies in the equatorial Pacific must develop forecast error models that include errors in the atmospheric heat flux applied to the surface mixed layer.

6.7 Acknowledgments

We thank the TAO Project Office and International Research Institute for Climate Prediction Data Library for the online distribution of data used in the model-data temperature flux comparisons. Thank you to Dudley B. Chelton for helpful comments that improved the focus of the article. The authors were supported by the National Oceanic and Atmospheric Administration Office of Global Programs under award NA16GP2016.

6.8 References

Baturin, N. G., and P. P. Niiler, 1997: Effects of instability waves in the mixed layer of the equatorial Pacific, *J. Geophys. Res.,* **102,** 27 771-27 793.

Bryden, H., and E. C. Brady, 1989: Eddy momentum and heat fluxes and their effects on the circulation of the equatorial Pacific Ocean. *J. Mar. Res.,* **47,** 55-79.

Chelton, D. B., F. J. Wentz, C. L. Gentemann, R. A. deSzoeke, and M. G. Schlax, 2000: Satellite microwave SST observations of transequatorial Tropical Instability Waves. *Geophys. Res. Lett.,* **21,** 1239-1242.

Chelton, D. B., and M. H. Freilich, 2005: Scatterometer-based assessment of 10-m wind analyses from the operational ECMWF and NCEP numerical weather prediction models, *Mon. Wea. Rev.,***133,** 409-429.

Chelton, D. B., and F. J. Wentz, 2005: Global high-resolution satellite observations of sea-surface temperature for numerical weather prediction and climate research. *Bull. Amer. Meteor. Soc.,* **86,** 1097-1115.

Chen, D., L. M. Rothstein, and A. J. Busalacchi, 1994: A hybrid vertical mixing scheme and its application to tropical ocean models. *J. Phys. Oceanogr.,* **24,** 2156-2179.

da Silva, A. M., C. C. Young, and S. Levitus, 1994: *Atlas of surface marine data 1994.* Vol.1, *Algorithms and Procedures,* NOAA Atlas NESDIS 6, U.S. Department of Commerce, 83 pp.

Deser, C. S., and J. M. Wallace, 1990: Large-scale atmospheric circulation features of warm and cold episodes in the tropical Pacific. *J. Climate,* **3,** 1254-1281.

European Centre for Medium-Range Weather Forecasts, 1994: The description of the ECMWF/WCRP Level III-A Global Atmospheric Data Archive, *Tech. Attach.,* 72 pp., Reading, England, U. K.

Gent, P. R., and M. A. Cane, 1989: A reduced gravity, primitive equation model of the upper equatorial ocean, *J. Comp. Physics,***81,** 444-480.

Hansen, D. V., and C. A. Paul, 1984: Genesis and effects of long waves in the equatorial Pacific. *J. Geophys. Res.,* **89,** 10 431-10 440.

Jochum, M., and R. Murtugudde, 2005: Temperature advection by Tropical Instability Waves. *J. Phys. Oceanogr.,* . In press.

Johnson, G. C., B. M. Sloyan, W. S. Kessler, and K. E. McTaggart, 2002: Direct measurements of upper ocean currents and water properties across the tropical Pacific Ocean during the 1990s. *Prog. Oceanogr.,* **52,** 31-61.

Kessler, W. S., L. M. Rothstein, and D. Chen, 1998: The annual cycle of SST in the eastern tropical Pacific, diagnosed in an ocean GCM, *J. Climate,***11,** 777-799.

Levitus, S., T. Boyer, J. Antonov, R. Burgett, 1994: *World ocean atlas 1994, Temperature, NOAA Atlas NESDIS,* vol. 4, 129 pp., Natl. Oceanic and Atmos. Admin., Silver Spring, MD.

Lyman, J. M., G. C. Johnson, and W. S. Kessler, 2005: Structure of 17-day versus 33-day tropical instability waves in the equatorial Pacific. *J. Phys. Oceanogr.,* revised.

McPhaden, M. J., 1993: TOGA-TAO and the 1991-1993 El Niño Southern Oscillation event, *Oceanogr.,***6,** 36-44.

Miller, R. N., 1990: Tropical data assimilation experiments with simulated data: the impact of the Tropical Ocean and Global Atmosphere Thermal Array for the Ocean, *J. Geophys. Res.,* **95,** 11 461-11 482.

Miller, R. N., A. J. Busalacchi, and E. C. Hackert, 1995: Sea surface topography fields of the tropical Pacific from data assimilation. *J. Geophys. Res.,* **100,** 13 389-13 425.

Mitchell, T. P., and J. M. Wallace, 1992: The annual cycle in equatorial convection and sea surface temperature. *J. Climate,* **5,** 1140-1156.

Murtugudde, R., R. Seager, and A. J. Busalacchi, 1996: Simulation of the tropical oceans with an ocean GCM coupled to an atmospheric mixed-layer model, *J. Climate,***9,** 1795-1815.

Murtugudde, R., J. Beauchamp, C. R. McClain, M. Lewis, and A. J. Busalacchi, 2002: Effects of penetrative radiation on the upper tropical ocean circulation. *J. Climate,* **15,** 470-486.

Oberhuber, J., 1988: An atlas based on 'COADS' Data Set, *Rep. 15.,* Max-Planck-Inst. für Meterol., Hamburg, Germany.

Plimpton, P. E., H. P. Freitag, and M. J. McPhaden, 1997: ADCP velocity errors from pelagic fish schooling around equatorial moorings. *J. Atmos. Oceanic Technol.,* **14,** 1212-1223.

Perez, R. C., and R. N. Miller, 2005: Impact of a reduced state space Kalman filter on the equatorial Pacific cold tongue and tropical instability waves. *Submitted to J. Geophys. Res.*

Reynolds, R., W., N. A. Rayner, T. M. Smith, and W. Wang, 2002: An improved in situ and satellite SST analysis for climate. *J. Climate,* **15,** 1609-1625.

Schlax, M. G., and D. B. Chelton, 1992: Frequency domain diagnostics for linear smoothers, *J. Amer. Stat. Assoc.,***87,** 1070-1081.

Seager, R., M. Blumenthal, and Y. Kushnir, 1995: An advective atmospheric mixed layer model for ocean modeling purposes: Global simulation of surface heat fluxes, *J. Climate.,***8,** 1951-1964.

Shapiro, R., 1971: The use of linear filtering as a parameterization of atmospheric diffusion. *J. Atmos. Science,* **28,** 523-531.

Swenson, M. S., and D. V. Hansen, 1999: Tropical Pacific Ocean mixed layer heat budget: The Pacific cold tongue. *J. Phys. Oceanogr.,* **29,** 69-81.

Vialard, J., C. Menkes, J.-P. Boulanger, P. Delecluse, E. Guilyardi, M. J. McPhaden, and G. Madec, 2001: A model study of oceanic mechanisms affecting equatorial Pacific sea surface temperature during the 1997-98 El Niño. *J. Phys. Oceanogr.,* **31,** 1649-1675.

Wallace, J. M., T. P. Mitchell, and C. S. Deser, 1989: The influence of sea surface temperature on surface wind in the eastern equatorial Pacific: Seasonal and interannual variability. *J. Climate,* **2,** 1492-1499.

Wang, W., and M. J. McPhaden, 1999: The surface-layer heat balance in the equatorial Pacific Ocean. Part I: The mean seasonal cycle. *J. Phys. Oceanogr.*, **29,** 1812-1831.

Wang, W., and M. J.McPhaden, 2000: The surface-layer heat balance in the equatorial Pacific Ocean. Part II: Interannual variability. *J. Phys. Oceanogr.*, **30,** 2989-3008.

Wang, W., and M. J. McPhaden, 2001: Surface layer temperature balance in the equatorial Pacific during the 1997-1998 El Niño and 1998-1999 La Niña. *J. Climate,* **14,** 3393-3407.

7 Summary and Conclusions

A four-dimensional multivariate data assimilation scheme has been developed in the tropical Pacific with the goal of obtaining a better understanding of the physical processes that dominate the surface mixed layer temperature (SST) balance of the equatorial Pacific cold tongue from August 1999 to July 2004. The Kalman filter methodology applied in this dissertation evolved from early Kalman filter schemes that assimilated monthly sea surface height anomalies (SSHA) from Pacific island tide gauges (Miller and Cane 1989; Miller et al. 1995; Cane et al. 1996; Chan et al., 1996) or dynamic height anomalies (DHA) estimated from temperature profiles in the waveguide (Miller et al. 1995; Reverdin et al. 1996) into low-order numerical models. These seminal assimilation experiments focused on the reduction of SSHA errors in the equatorial Pacific on intraseasonal to interannual time scales. In this study, the Kalman filter was applied to a more sophisticated nonlinear general circulation model of the equatorial Pacific, the Gent and Cane (1989) model, with an emphasis on high-frequency phenomena such as tropical instability waves (TIWs) and low-frequency signals associated with the annual cycle and the El Niño Southern Oscillation.

The Gent and Cane (1989) model has been successfully applied to the study of equatorial Pacific cold tongue and TIWs (Kessler et al. 1998; Jochum and Murtugudde 2004), used in wind forcing studies (Chen et al. 1999; Hackert et al. 2001), and in previous data assimilation studies (Verron et al. 1999; Gourdeau et al. 2000; Ballabrera-Poy et al. 2005). In Chapter 2, a relatively coarse resolution implementation of the Gent and Cane (1989) model with Seager et al. (1988) surface heat flux was used in an equatorial Rossby wave process study. It was demonstrated

that realisitic background currents were essential for reproducing the observed Rossby wave asymmetry. In the presence of an asymmetric equatorial current system (ECS), the asymmetric time-varying wind forcing supplied by QuikSCAT seasonal cycle winds served as a secondary and weaker mechanism for the Rossby wave asymmetry, and the inclusion of realistic coastline geometry produced equatorially asymmetric Rossby wave phase speeds similar to the phase speeds estimated from observations.

In Chapter 3, a wind sensitivity study was performed using the version of the model described in Chapter 2 that extends the 1997-1998 El Niño study of Hackert et al. (2001) to the August 1999 to July 2001 period when La Niña conditions prevailed. A model seasonal cycle was generated with FSU, ECMWF, and QuikSCAT seasonal cycle winds and the simulated cold tongue, ECS, TIWs, and annual equatorial Rossby waves were compared with available observations in the waveguide. The highest level of realism in the equatorial Pacific cold tongue was achieved with QuikSCAT wind forcing. It was determined that the consistency of the error statistics over time and high quality of the QuikSCAT wind stress forcing make them the best available choice for the data assimilation experiments in Chapters 5 and 6.

The heat flux formulation of the Gent and Cane (1989) model was upgraded to the Seager et al. (1995) atmospheric mixed layer model for the Chapters 4 to 6. This model upgrade (hereafter the GCAML model) provided the opportunity to increase the horizontal resolution in the waveguide from 2.4° longitude by 0.6° latitude to 1° longitude by 0.33° latitude and increase the vertical resolution in the upper 500 m of the water column (Chapter 4). Based on the spatial structure of the

mean dynamic heights (DH) and the ECS in the waveguide and the assimilation constraints on the number of model state variables, it was determined that a bottom density of 1027.0 $kg\ m^{-3}$ and 15 vertical layers were suitable values for the base of the model active layer. The Chapter 4 vertical resolution study also revealed that spatially-varying model-data DH biases of approximately 15 dyn cm were present in the waveguide for all of the vertical layer configurations tested. Forced by climatological heat and salt fluxes, the model drifted away from the Levitus (1994) initialization and developed significant biases in temperature and salinity such that the thermocline was too deep or the water column was too fresh. These biases were responsible for the positive DH bias in the equatorial waveguide.

In Chapter 5, the GCAML model and high-resolution QuikSCAT winds were combined with 5-day DHA at 42 Tropical Atmosphere Ocean (TAO; McPhaden 1993) moorings in a series of assimilation experiments. Using a Monte Carlo Markov Chain model and the assumption that model forecast errors are dominated by errors in the wind, the Kalman filter machinery was constructed in a reduced state space spanned by Empirical Orthogonal Functions (EOFs). Operating as designed, the assimilation of TAO DHA improved the intraseasonal and interannual variability of the DHA in the cold tongue. The assimilation runs with 44 and 139 EOFs (ASSIM44 and ASSIM139, respectively) also passed the rigorous χ^2 test for the assimilated TAO locations between 8°S and 2°N, but not at latitudes north of 2°N. Assimilation also reduced the mean SST cold bias, increased the variability near the thermocline, and increased the strength of the EUC core in the cold tongue. The 15 dyn cm model mean DH bias described in Chapter 4, however, was not reduced by this anomaly-for-anomaly assimilation approach.

The 5-day assimilation window was designed to resolve and correct the TIWs that perturb the cold tongue frontal boundaries. In the assimilated runs, the seasonality, zonal structure, phase, and spectral properties of the TIWs were better correlated with the observed TIWs, but the amplitudes were reduced and the westward phase speeds increased. Preliminary experiments indicate that the TAO zonal spacing may be too sparse and the assimilation of gridded altimetry SSHA measurements along additional locations in the eastern Pacific (e.g., 5° downstream or upstream of TAO) would improve the TIW amplitudes and propagation in the assimilated runs.

Despite the improvements to the model described above, assimilation of TAO DHA incorrectly amplified the SST seasonal cycle in the cold tongue during the observed suppression of the seasonal cycle associated with warm El Niño conditions (Chapter 5). Although there is some documentation of problems with the model seasonal cycle in the eastern Pacific (e.g., Murtugudde et al. 1996; Gourdeau et al. 2000), most Gent and Cane modeling studies have focused on validating the model SST and thermocline depth variability and not the seasonal cycles themselves. In the context of anomaly-for-anomaly data assimilation, these model seasonal cycle errors turned out to be rather important. For this reason, a second-order (10-day) autoregressive model was introduced to remove color from the sequence of model-data misfits (or innovation sequence) resulting from an improperly specified seasonal cycle and TIW phasing errors. This nearly optimized assimilation scheme with 44 EOFs (ASSIM44-AR run) passed the χ^2-test more often than the ASSIM44 and ASSIM139 runs, improved the cold tongue evolution, and the westward propagation speed of the TIWs. The removal of biases in the innovations, however, limited the ability of

the RKF to make large corrections to the pre-existing cold tongue thermal biases and decreased the amplitude of the TIWs.

Chapter 6 set out to determine whether the seasonal to interannual temperature fluxes and eddy fluxes associated with TIWs in the equatorial Pacific cold tongue are improved by the ASSIM44-AR run. It was determined that the fundamental temperature balance between 1.5°S and 1.5°N in both the unassimilated (NODA) and ASSIM44-AR runs was maintained between the mean net surface flux and vertical entrainment. The secondary balance between mean zonal and meridional advection and the mean residual also remained essentially the same for both runs. When the ASSIM44-AR horizontal advection was decomposed into low-frequency and high-frequency signals, the reduction in warming by the TIW eddy fluxes in the cold tongue was compensated by a decrease in the net cooling of the cold tongue by the seasonal to interannual zonal and meridional advection.

Although the ASSIM44-AR SST was cooler during the 1999-2001 La Niña conditions and warmer during the 2002-2003 El Niño along the equator, assimilation did not modify the mean SST significantly. Assimilation introduced more variability to the SST and temperature fluxes in the central Pacific, however, the SST variability in the east decreased thereby lowering the model agreement with observations. The ASSIM44-AR run was selected for this heat flux study specifically because the corrections to the SST were small and the prior and posterior error bars that are byproducts of the assimilation scheme can be used to determine quantitatively whether the model-data differences are significant. In comparisons with observed SST and tendency in Chapter 6, it was determined that the amplitudes of the NODA and ASSIM44-AR seasonal fluctuations are too weak in the eastern Pacific

(and well outside the error bars). There is less warming of the cold tongue during the winter/spring in the model than observed and therefore the temperatures in the spring/summer are too cold. Combining the tendency and horizontal advection terms (material horizontal derivative or net surface flux plus entrainment and diffusion) did not remove the large seasonal cycle differences in the east. Therefore, the inaccuracies in the model SST seasonal cycle must derive from problems in the seasonal cycle of net surface flux, entrainment, or the diffusion (residual) term.

Due to uncertainties in several of the model and observed temperature fluxes discussed in Chapter 6, many questions remain about the exact cause of errors in the model SST. One notable difference in the net surface flux supplied to the model surface mixed layer and that of the observational studies such as Wang and McPhaden (1999; 2000; 2001) is that the model parameterization of penetrative radiation allows less heat to penetrate the surface mixed layer in the east. Murtugudde et al. (2002) found that the constant attenuation depth used in the GCAML model (17 m) is realistic during La Niña events and less appropriate during warm El Niño events and that the incorporation of attentuation depths which vary in space and time allowed more heat to penetrate the layers below the mixed layer and decreased the upwelling and entrainment, thereby increasing the SST in the cold tongue.

In this study, errors in the net surface flux were linked to errors in the model SST seasonal cycle (Chapter 6) and the mean DH biases that arose from the climatological drift in the model from the Levitus initialization (Chapter 4). The incorporation of high-quality QuikSCAT wind stress may have invalidated the traditional data assimilation assumption that the largest forecast errors are in the surface wind

forcing. Closer scrutiny must therefore be given to the specification of surface heat fluxes such that the model DH biases and cold tongue seasonal cycle errors are removed. In addition, a forecast error model must be constructed that incorporates the colored noise introduced by heat flux errors before anomaly-for-anomaly assimilation schemes can truly be optimized for nonlinear GCMs.

Bibliography

Ballabrera-Poy, J., E. Hackert, R. Murtugudde, and A. J. Busalacchi, 2005: An observing system simulation experiment for an optimal moored instrument array in the tropical Indian Ocean, *J. Climate,* submitted.

Baturin, N. G., and P. P. Niiler, 1997: Effects of instability waves in the mixed layer of the equatorial Pacific. *J. Geophys. Res.,* **102,** 27 771- 27 793.

Bennett, A. F., 2002: *Inverse Modeling of the Ocean and Atmosphere,* 234 pp., Cambridge University Press, New York.

Bennett, A. F., B. S. Chua, D. E. Harrison, and M. J. McPhaden, 2000: Generalized inversion of Tropical Atmosphere-Ocean (TAO) data using a coupled model of the tropical Pacific, *J. Climate,* **13,** 2770-2785.

Bonjean F., and G. S. E. Lagerloef, 2002: Diagnostic model and analysis of the surface currents in the tropical Pacific ocean. *J. Phys. Oceanogr.,* **32,** 2938-2954.

Borovikov, A., M. M. Rienecker, C. L. Kepenne, and G. C. Johnson, 2005: Multivariate error covariance estimates by Monte-Carlo simulation for assimilation studies in the Pacific Ocean, *Mon. Wea. Rev.,* in press.

Bourassa, M. A., S. R. Smith, and J. J. O'Brien, 2001: A new FSU winds and flux climatology. 11th Conference on Interations of the Sea and Atmosphere, San Diego, CA, Amer. Meteor. Soc., 912.

Bourassa, M. A., S. R. Smith, and J. J. O'Brien, 2002: Assimilation of scatterometer and in situ winds for regularly gridded products. 6th Symposium on Integrated Observing Systems, Orlando, FL, Amer. Meteor. Soc., xx.

Bryden, H., and E. C. Brady, 1989: Eddy momentum and heat fluxes and their effects on the circulation of the equatorial Pacific Ocean. *J. Mar. Res.,* **47,** 55-79.

Busalacchi, A. J., and J. J. O'Brien, 1980: The seasonal variability in a model of the tropical Pacific. *J. Phys. Oceanogr.,* **10,** 1929-1951.

Busalacchi, A. J., M. J. McPhaden, J. Picaut, 1994: Variability in the equatorial Pacific sea surface topography during the verification phase of the TOPEX/Poseidon mission. *J. Geophys. Res.,* **99,** 24 725-24 738.

Cane, M. A., and R. J. Patton, 1984: A numerical model for low-frequency equatorial dynamics, *J. Phys. Oceanogr.,* **14,** 1853-1863.

Cane, M. A., A. Kaplan, R. N. Miller, B. Tang, E. C. Hackert, and A. J. Busalacchi, 1996: Mapping tropical Pacific sea level: Data assimilation via a reduced state space Kalman filter. *J. Geophys. Res.,* **101,** 22 599-22 617.

Chan, N. H., J. B. Kadane, R. N. Miller, and W. Palma, 1996: Estimation of tropical sea level anomaly by an improved Kalman filter, *J. Phys. Oceanogr.,* **26,** 1286-1303.

Chang, P., and S. G. H. Philander, 1989: Rossby wave packets in baroclinic mean currents. *Deep Sea Res.,* **36,** 17-37.

Chatfield, C., 1996: *The Analysis of Time Series: An Introduction,* 5th ed., 283 pp., Chapman and Hall, London, UK.

Chelton, D. B., 2005: The impact of SST specification on ECMWF surface wind stress fields in the eastern tropical Pacific. *J. Climate,* **18,** 530-550.

Chelton, D. B., and M. H. Freilich, 2005: Scatterometer-based assessment of 10-m wind analyses from the operational ECMWF and NCEP numerical weather prediction models. *Mon. Wea. Rev.,* **133,** 409-429.

Chelton, D. B., and F. J. Wentz, 2005: Global high-resolution satellite observations of sea-surface temperature for numerical weather prediction and climate research. *Bull. Amer. Meteor. Soc.,* **86,** 1097-1115.

Chelton, D. B., R. A. De Szoeke, M. G. Schlax, K. El Naggar, and N. Siwertz, 1998: Geographical variability of the first baroclinic Rossby radius of deformation. *J. Phys. Oceanogr.,* **28,** 443-460.

Chelton, D. B., F. J. Wentz, C. L. Gentemann, R. A. deSzoeke, and M. G. Schlax, 2000: Satellite microwave SST observations of transequatorial Tropical Instability Waves. *Geophys. Res. Lett.,* **21,** 1239-1242.

Chelton, D. B., S. K. Esbensen, M. G. Schlax, N. Thum, M. H. Freilich, F. J. Wentz, C. L. Gentemann, M. J. McPhaden, and P. S. Schopf, 2001: Observations of coupling between surface wind stress and sea surface temparature in the eastern tropical Pacific, *J. Climate,***14,** 1479-1498.

Chelton, D. B., M. G. Schlax, J. M. Lyman, and G. C. Johnson, 2003: Equatorially trapped waves in the presence of meridionally sheared baroclinic flow in the Pacific Ocean. *Prog. Oceanogr.,* **56,** 323-380.

Chen, D., L. M. Rothstein, and A. J. Busalacchi, 1994a: A hybrid vertical mixing scheme and its application to tropical ocean models. *J. Phys. Oceanogr.,* **24,** 2156-2179.

Chen, D., A. J. Busalacchi, and L. M. Rothstein, 1994b: The roles of vertical mixing, solar radiation, and wind stress in a model simulation of the sea surface temperature seasonal cycle in the tropical Pacific Ocean. *J. Geophys. Res.,* **99,** 20 345-20 359.

Chen, D., W. T. Liu, S. E. Zebiak, M. A. Cane, Y. Kushnir, and D. Witter, 1999: Sensitivity of the tropical Pacific Ocean simulation to the temporal and spatial resolution of wind forcing. *J. Geophys. Res.,* **104,** 11 261-11 271.

Conkright, M. E., R. A. Locarnini, and H. E. Garcia 2002: *World ocean atlas 2001: Objective analyses, data statistics, and figure, CD Rom documentation,* National Oceanographic Data Center, Silver Spring, MD.

Cox, M. D., 1980: Generation and propagation of 30-day waves in a numerical model of the Pacific. *J. Phys. Oceanogr.,* **10,** 1168-1186.

Daley, R., 1992: The Lagged innovation covariance: A performance diagnostic for atmospheric data assimilation, *Mon. Weath. Rev.,* **120,** 178-196.

da Silva, A. M., C. C. Young, and S. Levitus, 1994: *Atlas of surface marine data 1994.* Vol.1, *Algorithms and Procedures,* NOAA Atlas NESDIS 6, U.S. Department of Commerce, 83 pp.

Delcroix, T., J. Picaut, and G. Eldin, 1991: Equatorial Kelvin and Rossby waves evidenced in the Pacific Ocean through Geosat sea level and surface current anomalies. *J. Geophys. Res.,* **96 Suppl.,** 3249-3262.

Delcroix, T., J.-P. Boulanger, F. Masia, and C. Menkes, 1994: Geosat-derived sea level and surface current anomalies in the equatorial Pacific during the 1986-1989 El Niño and La Niña. *J. Geophys. Res.*, **99,** 25 093-25 107.

Deser, C. S., and J. M. Wallace, 1990: Large-scale atmospheric circulation features of warm and cold episodes in the tropical Pacific. *J. Climate,* **3,** 1254-1281.

De Szoeke, R. A., and D. B. Chelton, 2004: On the wind-driven vertical velocity at the equator. *In preparation for J. Phys. Oceanogr.*

Dewitte, B., and G. Reverdin, 2000: Vertically propagating annual and interannual variability in an OGCM simulation of the tropical Pacific Ocean in 1985-94. *J. Phys. Oceanogr.,* **30,** 1562-1581.

Dewitte, B., S. Illig, L. Parent, Y. duPenhoat, L. Gourdeau, and J. Verron, 2003: Tropical Pacific baroclinic mode contribution and associated long waves for the 1994-1999 period from an assimilation experiment with altimetric data, *J. Geophys. Res.,* **108,** 3121, doi:10.1029/2002JC001362.

Donohue, K. A., and M. Wimbush, 1998: Model results of flow instabilities in the tropical Pacific Ocean. *J. Geophys. Res.,* **103,** 21 401 - 21 412.

Ducet, N., P. Y. Le Traon, and G. Reverdin, 2000: Global high-resolution mapping of ocean circulation from TOPEX/Poseidon and ERS-1 and -2. *J. Geophys. Res.,* **105,** 19 477-19 498.

Eriksen, C. C., M. B. Blumethal, S. P. Hayes, and P. Ripa, 1983: Wind-generated equatorial Kelvin waves observed across the Pacific Ocean. *J. Phys. Oceanogr.,* **13,** 1622-1640.

European Centre for Medium-Range Weather Forecasts (ECMWF), 1994: The description of the ECMWF/WCRP Level III-A Global Atmospheric Data Archive, *Tech. Attach.,* 72 pp., Reading, England, U. K.

Freilich, M. H., D. G. Long, and M. W. Spencer, 1994: SeaWinds: A scanning scatterometer for ADEOS II - science overview. *Proc. Int. Geosci. Rem. Sens. Symposium,* Vol. II, Pasadena, CA, August 8-12, 960-963.

Fu, L.-L., J. Vazquez, and C. Perigaud, 1991: Fitting dynamic models to the Geosat sea level observations in the tropical Pacific ocean. Part I: A free wave model. *J. Phys. Oceanogr.,* **21,** 798-809.

Fukumori, I., R. Raghunath, L.-L. Fu, and Y. Chao, 1999: Assimilation of TOPEX/Poseidon altimeter data into a global ocean circulation model: How good are the results? *J. Geophys. Res.,* **104,** 25,647-25,665.

Gent, P. R., and M. A. Cane, 1989: A reduced gravity, primitive equation model of the upper equatorial ocean. *J. Comp. Physics,* **81,** 444-480.

Gourdeau, L., J. Verron, T. Delcroix, A. J. Busalacchi, and R. Murtugudde, 2000. Assimilation of TOPEX/Poseidon altimetric data in a primitive equation model of the tropical Pacific Ocean during the 1992-1996 El Niño Southern Oscillation period. *J. Geophys. Res.,* **105,** 8473-8488.

Hackert, E. C., A. J. Busalacchi, and R. Murtugudde, 2001: A wind comparison study using an ocean general circulation model for the 1997-1998 El Niño. *J. Geophys. Res.,* **106,** 2345-2362.

Hansen, D. V., and C. A. Paul, 1984: Genesis and effects of long waves in the equatorial Pacific. *J. Geophys. Res.,* **89,** 10 431-10 440.

Hayes, S. P., L. J. Mangum, J. Picaut, A. Sumi, and K. Takeuchi, 1991: TOGA-TAO: A moored array for real-time measurements in the tropical Pacific Ocean. *Bull. Amer. Meteor. Soc.,* **72,** 339-347.

Ide, K., P. Courtier, M. Ghil, and A. C. Lorenc, 1997: Unified notation for data assimilation: operational, sequential, and variational, *J. Met. Soc. Japan,***75,** 181-189.

Jochum, M., and R. Murtugudde, 2004: Internal variability of the tropical Pacific Ocean. *Geophys. Res. Lett.,* 31, L14309, doi: 10.1029/2004GL020488.

Jochum, M., and R. Murtugudde, 2005: Temperature advection by Tropical Instability Waves. *J. Phys. Oceanogr.,* . In press.

Johnson, E. J., and M. J. McPhaden, 1993: Structure of intraseasonal Kelvin waves in the equatorial Pacific ocean, *J. Phys. Oceanogr.,* **23,** 608-625.

Johnson, G. C., and M. J. McPhaden, 1999: Interior pycnocline flow from the subtropical to the equatorial Pacific Ocean. *J. Phys. Oceanogr.,* **29,** 3073-3089.

Johnson, G. C., B. M. Sloyan, W. S. Kessler, and K. E. McTaggart, 2002: Direct measurements of upper ocean currents and water properties across the tropical Pacific Ocean during the 1990s. *Prog. Oceanogr.,* **52,** 31-61.

Kailath, T., 1968: An innovations control approach to least square estimation - Part I: Linear filtering in additive white noise, *IEEE Trans. Automat. Control.,***13,** 646-655.

Kaplan, A., M. A. Cane, D. Chen, D. L. Witter, and R. E. Cheney, 2004: Small-scale variability and model error in tropical Pacific sea level, *J. Geophys. Res.,* **109,** C02001, doi:10.1029/2002JC001743.

Kelly, K. A., and L. Thompson, 2002: Scatterometer winds explain damped Rossby waves. *Geophys. Res. Lett.,* **29,** 52,1-4, doi:10.129/2002GL015595.

Kennan, S. C., and P. J. Flament, 2000: Observations of a Tropical Instability Vortex, *J. Phys. Oceanogr.,* **30,** 2277-2301.

Keppenne, C. L., and M. M. Rienecker, 2003: Assimilation of temperature into an isopycnal ocean general circulation model using a parallel ensemble Kalman filter, *J. Marine Sys.,***40-41,** 363-380.

Keppenne, C. L., M. M. Rienecker, N. P. Kurkowski, and D. A. Adamec, 2005: Ensemble Kalman filter assimilation of temperature and altimeter data with bias correction and application to seasonal prediction, *Nonlinear Proc. in Geophys.,***12,** 491-503.

Kessler, W. S., 1990: Observations of long Rossby waves in the northern tropical Pacific. *J. Geophys. Res.,* **95,** 5183-5217.

Kessler, W. S., and J. P. McCreary, 1993: The annual wind-driven Rossby wave in the subthermocline equatorial Pacific. *J. Phys. Oceanogr.,* **23,** 1192-1207.

Kessler, W. S., L. M. Rothstein, and D. Chen, 1998: The annual cycle of SST in the eastern tropical Pacific, diagnosed in an ocean GCM. *J. Climate,* **11,** 777-799.

Kessler, W. S., G. C. Johnson, and D. W. Moore, 2003: Sverdrup and nonlinear dynamics of the Pacific Equatorial Currents. *J. Phys. Oceanogr.,* **33,** 994-1008.

Kraus, E. B., and J. S. Turner, 1967: A one-dimensional model of the seasonal thermocline. Part II. The general theory and its consequences. *Tellus,* **19,** 98-105.

Kummerow, C., W. Barnes, T. Kozu, J. Shiue, and J. Simpson, 1998: The Tropical Rainfall Measuring Mission (TRMM) sensor package. *J. Atmos. Oceanic Technol.,* **15,** 808-816.

Lagerloef, G. S. E., G. T. Mitchum, R. B. Lukas, and P. P. Niiler, 1999: Tropical Pacific near-surface currents estimated from altimeter, wind and drifter data. *J. Geophys. Res.,* **104,** 23 313-23 326.

Large, W. G., and S. Pond, 1982: Sensible and latent heat flux measurements over the ocean. *J. Phys. Oceanogr.,* **12,** 464-482.

Legler, D.M., and J.J. O'Brien, 1988: Tropical Pacific wind stress analysis for TOGA, IOC Time series of ocean measurements, IOC Technical Series 33, Volume 4, UNESCO.

Levitus, S., 1982: *Climatological atlas of the world ocean.* National Oceanic and Atmospheric Administration, 173 pp.

Levitus, S., T. Boyer, J. Antonov, R. Burgett, 1994: *World ocean atlas 1994, Temperature, NOAA Atlas NESDIS,* vol. 4, 129 pp., Natl. Oceanic and Atmos. Admin., Silver Spring, MD.

Lukas, R., and E. Firing, 1985: The annual Rossby wave in the central equatorial Pacific Ocean. *J. Phys. Oceanogr.,* **15,** 55-67.

Lyman, J. M., D. B. Chelton, R. A. deSzoeke, and R. M. Samelson, 2005a: Tropical instability waves as a resonance between equatorial Rossby waves. *J. Phys. Oceanogr.,* **35,** 232-254.

Lyman, J. M., G. C. Johnson, and W. S. Kessler, 2005b: Structure of 17-day versus 33-day tropical instability waves in the equatorial Pacific. *J. Phys. Oceanogr.,* revised.

Madec, G., P. Delecluse, M. Imbard, C. Levy, 1998: OPA 8.1 general circulation model reference manual, *Notes de l'IPSL no. 11,* 91 pp. Université P. et M. Curie, Paris.

Matsuno, T., 1966: Quasi-geostrophic motions in the equatorial area. *J. Meteorol. Soc. Jpn.,* **44,** 25-43.

McCreary, J. P., and Z. Yu, 1992: Equatorial dynamics in a 2.5-layer model. *Prog. Oceanogr.,* **29,** 61-132.

McCreary, J. P., P. Lu, and Z. Yu, 2002: Dynamics of the Pacific subsurface countercurrents. *J. Phys. Oceanogr.,* **32,** 2379-2404.

McPhaden, M. J., 1993: TOGA-TAO and the 1991-1993 El Niño Southern Oscillation event, *Oceanogr.,***6,** 36-44.

Meyers, G., 1979: On the annual Rossby wave in the tropical North Pacific. *J. Phys. Oceanogr.,* **9,** 663-674.

Meissner, T., D. Smith, and F. Wentz, 2001: A 10-year intercomparison between collocated SSM/I oceanic surface wind speed retrievals and global analyses, *J. Geophys. Res.,* **106,** 11 731-11 742.

Miller, R. N., 1990: Tropical data assimilation experiments with simulated data: the impact of the Tropical Ocean and Global Atmosphere Thermal Array for the Ocean, *J. Geophys. Res.,* **95,** 11 461-11 482.

Miller, R. N., and M. A. Cane, 1989: A Kalman filter analysis of sea level heights in the tropical Pacific. *J. Phys. Oceanogr.,* **19,** 773-790.

Miller, R. N., and M. A. Cane, 1996: Tropical data assimilation: theoretical aspects, in *Modern Approaches to Data Assimilation in Ocean Modeling,* edited by P. Malanotte-Rizzoli, pp. 207-233, Elsevier Sci., New York.

Miller, R. N., A. J. Busalacchi, and E. C. Hackert, 1995: Sea surface topography fields of the tropical Pacific from data assimilation. *J. Geophys. Res.,* **100,** 13 389-13 425.

Millero, F. J., and A. Poisson, 1981: International one-atmosphere equation of state of seawater. *Deep-Sea Res.,* **28,** 625-629.

Mitchell, T. P., and J. M. Wallace, 1992: The annual cycle in equatorial convection and sea surface temperature. *J. Climate,* **5,** 1140-1156.

Moore, D. W., 1968: Rossby waves in an equatorial ocean. Ph.D. dissertation, Harvard University, Cambridge, MA, 207 pp.

Moore, D. W., and S. G. H. Philander, 1977: Modeling of the tropical oceanic circulation. *The Sea,* E. D. Goldberg, I. N. McCave, J. J. O'Brien, and J. H. Steele, Eds., Vol. 6, Wiley-Interscience, 319-361.

Murtugudde, R., and A. J. Busalacchi, 1998: Salinity effects in a tropical ocean model. *J. Geophys. Res.,* **103,** 3283-3300.

Murtugudde, R., R. Seager, and A. J. Busalacchi, 1996: Simulation of the tropical oceans with an ocean GCM coupled to an atmospheric mixed-layer model. *J. Climate,* **9,** 1795-1815.

Murtugudde, R., J. Beauchamp, C. R. McClain, M. Lewis, and A. J. Busalacchi, 2002: Effects of penetrative radiation on the upper tropical ocean circulation. *J. Climate,* **15,** 470-486.

Oberhuber, J., 1988: An atlas based on 'COADS' Data Set, *Rep. 15.,* Max-Planck-Inst. für Meterol., Hamburg, Germany.

Parent, L., C.-E. Testut, J.-M. Brankart, J. Verron, P. Brasseur, and L. Gourdeau, 2003: Comparative assimilation of Topex/Poseidon and ERS altimeter data and of TAO temperature data in the tropical Pacific ocean during 1994-1998, and the mean sea-surface height issue, *J. Mar. Res.,***40-41,** 381-401.

Perez, R. C., 2005: Numerical and assimilative studies of the equatorial Pacific cold tongue. Ph.D. thesis, Oregon State University, Corvallis, Oregon.

Perez, R. C., and R. N. Miller, 2005: Impact of a reduced state space Kalman filter on the equatorial Pacific cold tongue and tropical instability waves. *Submitted to J. Geophys. Res.*

Perez, R. C., D. B. Chelton, and R. N. Miller, 2005: The effects of wind forcing and background mean currents on the latitudinal structure of equatorial Rossby waves. *J. Phys. Oceanogr.*, **35,** 666-682.

Philander, S. G. H., 1978: Instabilities of zonal equatorial currents, Part 2. *J. Geophys. Res.*, **83,** 3679-3682.

Philander, S. G. H., 1979: Equatorial waves in the presence of the equatorial undercurrent. *J. Phys. Oceanogr.*, **9,** 254-262.

Plimpton, P. E., H. P. Freitag, and M. J. McPhaden, 1997: ADCP velocity errors from pelagic fish schooling around equatorial moorings. *J. Atmos. Oceanic Technol.*, **14,** 1212-1223.

Price, J. F., R. A. Weller, and R. Pinkel, 1986: Diurnal cycling: Observations and models of the upper ocean response to diurnal heating, cooling, and wind mixing. *J. Geophys. Res.*, **91,** 8411-8427.

Qiao, L., and R. H. Weisberg, 1995: Tropical instability wave kinematics: Observations from the Tropical Instability Wave Experiment. *J. Geophys. Res.*, **100,** 8677-8693.

Reverdin, G., A. Kaplan, M. A. Cane, 1996: Sea level from temperature profiles in the tropical Pacific Ocean, 1975-1982, *J. Geophys. Res.*, **101,** 18 105-18 119.

Reynolds, R., W., N. A. Rayner, T. M. Smith, and W. Wang, 2002: An improved in situ and satellite SST analysis for climate. *J. Climate,* **15,** 1609-1625.

Rossow, W. B., and R. A. Schiffer, 1991: ISCCP cloud data products. *Bull. Am. Meteorol. Soc.*, **72,** 2-20.

Schlax, M. G., and D. B. Chelton, 1992: Frequency domain diagnostics for linear smoothers. *J. Amer. Stat. Assoc.*, **87,** 1070-1081.

Seager, R., S. E. Zebiak, and M. A. Cane, 1988: A model of the tropical Pacific sea surface temperature climatology. *J. Geophys. Res.*, **93,** 1265-1280.

Seager, R., M. Blumenthal, and Y. Kushnir, 1995: An advective atmospheric mixed layer model for ocean modeling purposes: Global simulation of surface heat fluxes. *J. Climate,* **8,** 1951-1964.

Seager, R., R. Murtugudde, A. Clement, C. Herweijer, 2003: Why is there an evaporative minimum at the equator? *J. Climate,* **16,** 3793-3802.

Shapiro, R., 1971: The use of linear filtering as a parameterization of atmospheric diffusion. *J. Atmos. Science,* **28,** 523-531.

Stockdale, T. N., A. J. Busalacchi, D. E. Harrison, and R. Seager, 1998: Ocean modeling for ENSO, *J. Geophys. Res.,* **103,** 14 325-14 355.

Susanto, R. D., Q. Zheng, and X.-H. Yan, 1998: Complex singular value decomposition analysis of equatorial waves in the Pacific observed by TOPEX/Poseidon altimeter. *J. Atmos. Oceanic Technol.,* **15,** 764-774.

Swenson, M. S., and D. V. Hansen, 1999: Tropical Pacific Ocean mixed layer heat budget: The Pacific cold tongue. *J. Phys. Oceanogr.,* **29,** 69-81.

Verron, J., L. Gourdeau, D. T. Pham, R. Murtugudde, and A. J. Busalacchi, 1999: An extended Kalman filter to assimilate satellite altimeter data into a nonlinear numerical model of the tropical Pacific Ocean: method and validation. *J. Geophys. Res.,* **104,** 5441-5458.

Vialard, J., A. T. Weaver, D. L. T. Anderson, and P. Delecluse, 2003: Three- and four-dimensional variational assimilation with a general circulation model of the tropical Pacific Ocean. Part II: physical validation, *Mon. Wea. Rev.,***131,** 1379-1395.

Vialard, J., C. Menkes, J.-P. Boulanger, P. Delecluse, E. Guilyardi, M. J. McPhaden, and G. Madec, 2001: A model study of oceanic mechanisms affecting equatorial Pacific sea surface temperature during the 1997-98 El Niño. *J. Phys. Oceanogr.,* **31,** 1649-1675.

Vossepoel, F. C., G. Burgers, and P. J. van Leeeuwen, 2002: Effects of correcting salinity with altimeter measurements in an equatorial Pacific ocean model, *J. Geophys. Res.,* **107,** 8001, doi:10.1029/2001JC000816.

Wallace, J. M., T. P. Mitchell, and C. S. Deser, 1989: The influence of sea surface temperature on surface wind in the eastern equatorial Pacific: Seasonal and interannual variability. *J. Climate,* **2,** 1492-1499.

Wang, W., and M. J. McPhaden, 1999: The surface-layer heat balance in the equatorial Pacific Ocean. Part I: The mean seasonal cycle. *J. Phys. Oceanogr.,* **29,** 1812-1831.

Wang, W., and M. J.McPhaden, 2000: The surface-layer heat balance in the equatorial Pacific Ocean. Part II: Interannual variability. *J. Phys. Oceanogr.,* **30,** 2989-3008.

Wang, W., and M. J. McPhaden, 2001: Surface layer temperature balance in the equatorial Pacific during the 1997-1998 El Niño and 1998-1999 La Niña. *J. Climate,* **14,** 3393-3407.

White, W. B., 1977: Annual forcing of baroclinic long waves in the tropical North Pacific Ocean. *J. Phys. Oceanogr.,* **7,** 50-61.

Yu, X., and M. J. McPhaden, 1999: Seasonal variability in the equatorial Pacific. *J. Phys. Oceanogr.,* **29,** 925-947.

Zheng, Q., X. -H. Yan, C. -R. Ho, and C. -K. Tai, 1994: The effects of shear flow on propagation of Rossby waves in the equatorial oceans. *J. Phys. Oceanogr.,* **24,** 1680-1686.